

NORTHEASTERN UNIVERSITY  
Graduate School of Arts and Sciences

Dissertation Title: Massive  $\pi^0\pi^0$ ,  $\pi^0\pi^-$ , and  $\pi^0\pi^+$  Production from 515 GeV/c  
 $\pi^-$  Collisions with Beryllium and Copper Targets

Author: Paoti Chang

Department: Physics

Approved for Dissertation Requirements of the Doctor of Philosophy Degree

David Gershnik

8/24/94

Michael T. Vaughn

24 Aug 94

G. Aloni

24 Aug 94

Michael J. Klebaner

8/24/94

Thesis Committee

Date

William J. Farnham

8/24/94

Head of Department

Date

Graduate School Notified of Acceptance

K. O'Neil

Dean

25 Aug 94

Date

Copy Deposited in Library

Susan York  
Signed

August 25, 1994  
Date

FERMILAB  
LIBRARY

Shaw  
Ref  
Hitt 5084  
Doc 31314052

Massive  $\pi^0\pi^0$ ,  $\pi^0\pi^-$ , and  $\pi^0\pi^+$  Production  
from 515 GeV/c  $\pi^-$  Collisions with  
Beryllium and Copper Targets

A dissertation presented

by

Paoti Chang

to

The Department of Physics

In partial fulfillment of the requirements  
for the degree of

Doctor of Philosophy

in the field of

Physics

Northeastern University  
Boston, Massachusetts

August 1994

Massive  $\pi^0\pi^0$ ,  $\pi^0\pi^-$ , and  $\pi^0\pi^+$  Production  
from 515 GeV/c  $\pi^-$  Collisions with  
Beryllium and Copper Targets

by

Paoti Chang

**ABSTRACT**

This thesis presents the measurement of high mass  $\pi^0\pi^0$  and  $\pi^0\pi^\pm$  production by a 515 GeV/c  $\pi^-$  beam on Be and Cu targets at Fermilab experiment E706. The data correspond to an integrated luminosity of  $\sim 8.6$  events/pb on Be and of  $\sim 1.4$  events/pb on Cu for the 1990 fixed target run. These high mass di- $\pi$  states, produced near  $90^\circ$  in the  $\pi^-$ -nucleus center of mass frame, cover the mass range from 4 to 18 GeV/ $c^2$  with the parton-parton scattering angle up to  $\cos\theta^* = 0.5$ . This thesis reports the mass differential di- $\pi$  cross sections as well as the study of the di- $\pi$  angular correlations in comparison with QCD predictions. Results from the structure of particles produced in association with these  $\pi$ 's are also discussed. A nuclear enhancement of the di- $\pi$  events is observed and the results are presented in comparison with the data from other experiments.

Submitted in partial fulfillment of the requirements  
for the degree of Doctor of Philosophy in Physics  
in the Graduate School of Arts and Sciences of  
Northeastern University, August 1994

## ACKNOWLEDGEMENTS

Many people have influenced me in the course of my studies. I would like to gratefully acknowledge the help of some of them here although this document could not fully express my gratitude and respect for them.

First and foremost, I want to thank my parents and my wife, Wen-ling, for their patience, sacrifice, and support during these years. Without them, this thesis would never have been accomplished. Thanks Mom and Dad for allowing me to do what I like, including coming to the States to study for such a long time. Thank you Wen-ling for going through this process with me as I pursue my professional goals in a foreign country. It must have been as demanding for you as it has been for me. Our unborn baby also deserves credit in pushing me to (finally) finish my thesis in the past six months. Thanks, my child, no matter if you are a boy or a girl.

Many thanks to my thesis advisor, David Garelick, as well as Michael Glaubman, George Alverson, and William Faissler for their continual support and encouragement. Professor Garelick, in particular, gave me the greatest academic freedom to do whatever interested me. Our spokesman, Paul Slattery, has been nothing less than inspiring. He shows up almost at every Friday meeting and gives us valuable suggestions. In addition, I would like to thank Fred Lobkowicz, Tom Ferbel, Gene Engels, Paul Shepard, Sudhindra Mani, Joey Huston, William Toothacker, and Carl Bromberg for their contributions to this experiment. (Carl, I have not forgot B physics yet.)

For such a complicated experiment, E706 would not have been a reality without some of the most dedicated and hardworking people. George Ginther deserves the highest credit, not only in the completion of this thesis but also in the achievements of this experiment. Thank you George for taking many hours per week from your busy schedule to discuss my physics analyses and to share your wisdom with me. Marek Zilenski directed me in studying the nuclear dependence of this thesis. I would like to thank him for his guidance and support, especially for answering my very igno-

rant questions about QCD theory. Special thanks to Takahiro Yasuda, James Dunlea, Edward Pothier, Christopher Lirakis, Dane Skow, Vijay Kapoor, David Brown, Dhammika Weerasundara, Carlos Yosef, and Keith Hartman for teaching me about the techniques both in software and hardware. Keith (Casey), I will never forget my sense of awkwardness in my first project: grounding the straw chamber 1.

As for my fellow second run graduate students, I sincerely thank you for creating such a wonderful learning environment. You have made the various meetings fruitful with your generous inputs. It is also you that made this experiment an enjoyable learning experience. I appreciate the outstanding work of E706 trackers: Woo-hyun Chung, Steve Blusk, Andre Maul, and John Bacigalupi. I am also indebted to the marvelous job done by the LAC group: Nikos Varelas, Rob Roser, Lucyna de Barbaro, Wiesiek Dlugosz, George Osborne, and Michael Begel. Thank you my fellow Northeasterner, Wiesiek, for showing me the analysis code to measure cross sections. Do you still miss (as I do) the sesame beef we had together in Crystal City? Many thanks to Lee Sorrell from whom I learned the E706 trigger system. To tell the truth, three thousand histograms were not easy for me to swallow. I would like to thank four other people: to Leonard Apanasevich, for helping me with Monte Carlo events; to Vishnu Zutshi, for sharing the idea of muon rejection; to David Striley, for his contributions on the Cerenkov detector; to John Kuehler, for providing the photon conversion corrections. Every Thursday night is game time for basketball. Steve and Lenny, I hope we still have chances to play one-on-one sometime in the future.

Special thanks to "soccer punch" Daniel Ruggiero, whose humor makes our life more colorful. Thank you Mr. Shi for taking care of our Fastbus electronics and for giving me an opportunity to talk in my mother tongue. Again but not least, thank you George and Wen-ling for editing and proofreading the drafts of this thesis.

This thesis is dedicated to my mother.

# Contents

<b>Abstract</b>	<b>i</b>
<b>Acknowledgements</b>	<b>ii</b>
<b>Table of Contents</b>	<b>iv</b>
<b>1 Introduction</b>	<b>1</b>
1.1 A Brief Historic Review . . . . .	1
1.2 QCD and Parton Model . . . . .	4
1.3 Di- $\pi$ Production . . . . .	7
1.3.1 Kinematic Variables . . . . .	8
1.3.2 Angular Correlations . . . . .	11
1.4 Nuclear Dependence . . . . .	15
<b>2 The Experiment</b>	<b>18</b>
2.1 The Beam Line . . . . .	18
2.2 Beam Hodoscope, Interaction Counters and E706 Target . . . . .	22
2.3 The Tracking System . . . . .	23
2.3.1 The Silicon Strip Detector (SSD) System . . . . .	23
2.3.2 The MW9AN Dipole Magnet . . . . .	26
2.3.3 The Proportional Wire Chamber (PWC) System . . . . .	26
2.3.4 Read Out Electronics for SSD and PWC . . . . .	32
2.3.5 Straw Chamber System . . . . .	34

2.9	A bundle of straw tubes. . . . .	35
2.10	The gantry and cryostat of the LAC . . . . .	37
2.11	A side view of single EMLAC layer. . . . .	38
2.12	Exploded view of the electromagnetic calorimeter . . . . .	41
2.13	An exploded view of a cookie. . . . .	43
2.14	The first readout board of a HALAC readout pair of boards. Each triangle pad was read out on the edges. The second readout board of the pair had the same design as the first one, but was read out in alternate rows which did not have a triangle pad in the first readout board of the pair. . . . .	44
2.15	The Forward Calorimeter . . . . .	45
3.1	The E706 data acquisition system. . . . .	47
3.2	Layout of counters in the trigger system. . . . .	51
3.3	The E706 $P_T$ Summing Module . . . . .	54
3.4	The Pretrigger High Turn-on Curves. (a) Turn-on efficiency versus $\pi^0$ $P_T$ in inner region, (b) Turn-on efficiency versus $\pi^0$ $P_T$ in outer region, (c) Turn-on efficiency versus trigger $P_T$ in inner region, (d) Turn-on efficiency versus trigger $P_T$ in outer region. . . . .	58
3.5	The Single Local High turn-on curves of four different regions in a typical octant. Smaller section numbers correspond to sum-of-8 pairs with smaller radial locations. . . . .	59
3.6	The Pretrigger Low Turn-on Curves. . . . .	61
3.7	The Local low Turn-on Curves in Four Different Regions of an Octant. . . . .	62
4.1	$\chi^2$ per degree of freedom for PWC tracks. (a) 13 hit, (b) 14 hit, (c) 15 hit, (d) 16 hit. . . . .	67
4.2	Distribution of the number of hits used for PWC tracks . . . . .	68

4.3	The time-to-distance curves for straw chambers in four different modules. The curves are almost flat at small TDC time due to the inefficiency in getting the proper time measurement when charged particles hit close to the wire. If the measured TDC time is less than 20 ns (cutoff value), the hit position is assigned to the wire position. . . . .	71
4.4	$\sigma$ versus $r$ . The straw $\sigma$ (gaussian width) is measured by fitting the residual of the straw hits to the straw tracks at a certain radial position.	73
4.5	$\sigma$ 's of $\Delta X$ , $\Delta Y$ , and $\Delta YSL$ vs $P$ for PWC-SSD pairs. $\sigma$ 's are the fitted gaussian width of $\Delta X$ , $\Delta Y$ , and $\Delta YSL$ distributions. The function $f$ is fitted to the data points. . . . .	77
4.6	$\sigma$ 's of $\Delta X$ , $\Delta Y$ , and $\Delta YSL$ vs $P$ for STRAW-SSD pairs. $\sigma$ 's are the fitted gaussian width of $\Delta X$ , $\Delta Y$ , and $\Delta YSL$ distributions. The function $f$ is fitted to the data points. . . . .	78
4.7	The estimated momentum versus the momentum measured from the linked tracks. The top plot is a scatter plot and the bottom one is a contour plot. . . . .	79
4.8	$\Delta X$ distributions in different $Z$ . Solid line is for positively charged tracks and dash line is for negatively charged tracks. . . . .	80
4.9	$\pi^+\pi^-$ mass spectrum . . . . .	88
4.10	$\mu^+\mu^-$ mass spectrum . . . . .	88
4.11	The twelve neighbors of the peak pad (center pad). The first neighbors are labeled as pads 1, 2, and 3. The second neighbors contained pads 4, 5, and 6. The rest were the third neighbors. . . . .	89
5.1	(a) $Y$ -slope difference, (b) $ZX$ intersection, (c) $Y$ -slope difference after $ZX$ intersection cut, (d) $ZX$ intersection after $Y$ -slope difference cut.	92
5.2	The differences between tracks' projections and photons for ZMPs. (a) $\Delta X$ , (b) $\Delta Y$ , (c) $\Delta R^2$ . . . . .	93



5.3	The positions of photons at the front face of the EMLAC. The LAC fiducial cut is applied. . . . .	94
5.4	The positions of electrons at the front face of the EMLAC. The LAC fiducial cut is applied. . . . .	94
5.5	(a) $E/P$ for tracks, (b) $E_f/E_t$ for tracks, (c) $E/P$ for ZMP tracks, (d) $E_f/E_t$ for ZMP tracks. . . . .	96
5.6	The position of $\pi^0$ candidates with $P_T$ above 5 GeV/c. (a) before the offline veto wall cut, (b) after the offline veto wall cut. . . . .	98
5.7	The idea of directionality. If photons come from a target, then $\frac{R_f}{R_b} \simeq \frac{Z_f}{Z_b}$ , implying the directionality is near zero. For muons, the directionality is positive because $R_f \simeq R_b$ . . . . .	100
5.8	$P_T$ versus directionality. (a) Veto walls fired in the same quadrant, (b) Veto walls did not fire in the same quadrant. . . . .	101
5.9	The two-photon mass spectrum with $P_T$ ranging from 7 to 9 GeV/c: (a) Two Gamma trigger, (b) Single Local High trigger. . . . .	102
5.10	Two photon mass distribution with $P_T$ above 4 GeV/c. Dash line is after applying the asymmetry cut. . . . .	104
5.11	Asymmetry distribution of $\pi^0$ 's at $P_T \geq 2$ GeV/c. (a) After the side band subtraction, (b) Before the side band subtraction, (c) Asymmetry distribution for the side bands of $\pi^0$ 's. . . . .	106
5.12	The definition of $\pi^0$ mass region and the sideband region. Region A is the $\pi^0$ region while region B and C are the sideband regions. The minimum $P_T$ for each $\pi^0$ is 2 GeV/c. . . . .	107
5.13	PWC Y impact parameter over the predicted value in four different momentum regions. The function of the fit is a second order polynomial plus a gauss function. p6 is the gaussian width. . . . .	109

5.14	STRAW Y impact parameter over the predicted value in four different momentum regions. The function of the fit is a second order polynomial plus a gauss function. $p_6$ is the gaussian width. . . . .	110
5.15	The $P_T$ and rapidity spectrum of charged tracks. (a) $P_T$ distribution on semi-logarithmic scale, (b) rapidity distribution. The long tail in the $P_T$ spectrum and the spike at $-1$ in rapidity indicate that some tracks do not have proper momentum measurement. . . . .	112
5.16	The generated Z position of MC tracks. Each track combines with a high $P_T$ $\pi^0$ in the same event to form a high mass state above 20 GeV/ $c^2$ . Since the total energy in the hadron-hadron center of momentum frame is 31 GeV, it's very unlikely to have dihadron mass greater than 20 GeV/ $c^2$ . The momenta of these tracks are probably not properly measured. . . . .	113
5.17	The distribution of number of hits in the first PWC module. (a) All tracks with $P_T$ greater than 1.5 GeV/c, (b) The mass of $\pi^0$ s and charged tracks are greater than 20 GeV/ $c^2$ . . . . .	115
5.18	Charged track $P_T$ distribution after different cuts for 1990 data. (a) PWC1 cut, (b) LAC cut, (c) kinematic cut, (d) PWC1, LAC, and kinematic cuts. . . . .	116
5.19	The reconstructed $P_T$ distribution (dashed) compared to the generated distribution (solid) in the MC data. (a) Before the cuts, (b) After the cuts. . . . .	117
5.20	The top two plots are the distributions of $\frac{\Delta P}{P_m^2}$ for (a) PWC tracks and (b) Straw tracks, while the bottom two are the distributions of $\frac{\Delta P}{P_e^2}$ for (c) PWC tracks and (d) Straw tracks. . . . .	120

5.21	Uncorrected $\pi^0$ and $\eta$ mass as a function of time during the 1990 run. Both masses are normalized to their nominal values. Beam days was counted when there were beams in those days. The reference day is 31-May-1990. There was a 7-day shutdown, indicated in the vertical lines in (b), during 1990 run. During this shutdown period, the measured $\pi^0$ mass did not change. This beam-off time was, therefore, subtracted from the fit in (a) to correct this time-dependent effect. . . . .	121
5.22	E/P as a function of "beam days" for charged hadrons. The dashed line represents a fit to the data points in Fig. 5.21. . . . .	122
5.23	Radial dependence of the reconstructed $\pi^0$ mass over the nominal value in octants 1 through 4. . . . .	124
5.24	Radial dependence of the reconstructed $\pi^0$ mass over the nominal value in octants 5 through 8. . . . .	125
5.25	Radial dependence of the reconstructed $\pi^0$ and $\eta$ mass over their nominal values. . . . .	126
5.26	The invariant mass of (a) $\gamma e^+e^-$ and (b) $e^+e^-e^+e^-$ . The $P_T$ cut for the $\gamma e^+e^-$ sample is 3 GeV/c, while the $P_T$ cut for the four electron sample is 1 GeV/c. . . . .	128
6.1	Distribution of the reconstructed primary vertices in the di- $\pi$ events. The Silicon SSD planes are labeled Si. No photon conversion correction is applied. . . . .	131
6.2	X-Y positions of reconstructed primary vertices. The square corresponds to the effective area of the beam hodoscope. The circle in the upper plot shows the shape of Be targets, and the truncated circle in the lower plot indicates the effective region of Cu targets. . . . .	132

6.3	The ratio of the number of $\pi^0$ 's which pass the muon cuts in $\pi^0 P_T$ between 4 to 9 GeV/c. Sideband subtraction is applied when counting the number of $\pi^0$ 's. The function $f$ is fitted to these points and implemented to correct for the event losses caused by the muon cuts for high $P_T$ $\pi^0$ 's ( $P_T > 9$ GeV/c). . . . .	134
6.4	Two photon mass spectrum in the di- $\pi$ events with and without the muon cuts. (a) $9 < P_T < 11$ without the cuts, (b) $11 < P_T$ without the cuts, (c) $9 < P_T < 11$ with the cuts, (d) $11 < P_T$ with the cuts. The number of $\pi^0$ 's is about $10 \pm 4.25$ entries in (c), and $0 \pm 3.464$ events in (d). Therefore, the statistical uncertainty ( $> 30\%$ ) is larger than the systematic uncertainty ( $< 10\%$ ) of the function in Fig. 6.3. . . . .	135
6.5	The average correction factor of the geometrical acceptance vs the mass of two photons. (a) $\pi^0\pi^0$ , (b) $\pi^0\pi^\pm$ . . . . .	138
6.6	$\pi^0$ reconstruction efficiency as a function of $P_T$ and rapidity in the $\pi^-$ -nucleon center of mass frame. . . . .	140
6.7	Charged particle reconstruction efficiency as a function of rapidity in the $\pi^-$ -nucleon center of mass frame. The minimum $P_T$ for each track is 1.5 GeV/c. . . . .	141
6.8	The MC generated and reconstructed mass spectra of di- $\pi$ events. (a) $\pi^0\pi^-$ , (b) $\pi^0\pi^+$ , (c) $\pi^0\pi^0$ . The same kinematic cuts were applied for the generated and the reconstructed events. All the corrections except the trigger correction, the target fiducial correction, and the correction for beam muon contamination were turned on. . . . .	147
6.9	The MC generated and reconstructed mass spectra of (a) $\pi^0\pi^-$ and (b) $\pi^0\pi^+$ . Every charged track corresponds to a generated particle. All corrections were turned off. . . . .	148

6.10	The ratio of the MC generated and reconstructed mass spectra of $\pi^0\pi^\pm$ events. This ratio is around one except at mass greater than 14 GeV/c <sup>2</sup> . The fitted function is used as a correction to measure the $\pi^0\pi^\pm$ cross sections in the real data. . . . .	149
6.11	$\pi^0$ pair mass spectra in $\pi^-$ Be and $\pi^-$ Cu interactions. The spectra rises in the low mass region because of the minimum $P_T$ requirement for each $\pi^0$ (2 GeV/c). After the point (4 GeV/c) that stands for the sum of the $P_T$ of each $\pi^0$ is reached, the spectra are falling as expected.	151
6.12	$\pi^0\pi^\pm$ mass spectra in $\pi^-$ Be and $\pi^-$ Cu interactions. The spectra rises in the low mass region because of the minimum $P_T$ requirement for the $\pi^0$ (4 GeV/c) and the $\pi^\pm$ (1.5 GeV/c). After the point (5.5 GeV/c) that stands for the sum of the $P_T$ of each particle is reached, the spectra are falling as expected. . . . .	152
6.13	The cross section ratio of $\pi^0\pi^+$ and $\pi^0\pi^-$ versus mass of the pairs. . .	153
6.14	The measured $\pi^0\pi^0$ mass differential cross section compared to the generated result from the Herwig event generator. The Herwig result is normalized to the fifth point of the data spectrum. . . . .	155
6.15	The measured $\pi^0\pi^-$ mass differential cross section compared to the generated result from the Herwig event generator. . . . .	156
6.16	The measured $\pi^0\pi^+$ mass differential cross section compared to the generated result from the Herwig event generator. . . . .	157
6.17	The measured $\pi^0\pi^0$ mass differential cross sections using the SINGLE LOCAL HIGH trigger and the TWO GAMMA trigger. . . . .	158
6.18	The measured $\pi^0\pi^-$ mass differential cross section overlapped with the $\pi^0\pi^0$ cross section using the SINGLE LOCAL HIGH trigger. . . . .	160
6.19	The measured $\pi^0\pi^+$ mass differential cross section overlapped with the $\pi^0\pi^0$ cross section using the SINGLE LOCAL HIGH trigger. . . . .	161

6.20	The MC generated $\pi^0\pi^\pm$ mass spectra overlapped with the generated $\pi^0\pi^0$ mass spectrum. . . . .	162
6.21	$\cos\theta^*$ distribution of $\pi^0$ pairs in four different mass regions. . . . .	163
6.22	$\cos\theta^*$ distribution of $\pi^0$ pairs overlapped with the leading-log QCD calculation derived from the Herwig event generator. The fitted function is $\frac{1}{2}[\frac{1}{(1+\cos\theta^*)^a} + \frac{1}{(1-\cos\theta^*)^a}]$ . The parameter $a$ is determined from the experimental data. . . . .	164
6.23	$\cos\theta^*$ distribution of $\pi^0\pi^\pm$ in four different mass regions. . . . .	167
6.24	$\cos\theta^*$ distribution of $\pi^0\pi^\pm$ overlapped with the leading-log QCD calculations derived from the Herwig event generator. The fitted function is $\frac{1}{2}[\frac{1}{(1+\cos\theta^*)^a} + \frac{1}{(1-\cos\theta^*)^a}]$ . The parameter $a$ is determined from the experimental data. . . . .	168
6.25	Azimuthal correlations in $\pi^0\pi^0$ events. $\Delta\phi$ is the angle between the highest $P_T$ $\pi^0$ and the charged particles. For all tracks with (a) $P_T < 0.25$ GeV/c, (b) $P_T > 0.25$ GeV/c, (c) $P_T > 1$ GeV/c, (d) $P_T > 2$ GeV/c. . . . .	170
6.26	Azimuthal Correlations in $\pi^0\pi^0$ Events. $\Delta\phi$ is the angle between the highest $P_T$ $\pi^0$ and photons. For all photons with (a) $P_T < 0.25$ GeV/c, (b) $P_T > 0.25$ GeV/c, (c) $P_T > 1$ GeV/c, (d) $P_T > 2$ GeV/c. . . . .	170
6.27	Azimuthal Correlations in $\pi^0\pi^\pm$ Events. $\Delta\phi$ is the angle between the highest $P_T$ $\pi^\pm$ and the other charged particles. For all tracks with (a) $P_T < 0.25$ GeV/c, (b) $P_T > 0.25$ GeV/c, (c) $P_T > 1$ GeV/c, (d) $P_T > 2$ GeV/c. . . . .	171
6.28	Azimuthal Correlations in $\pi^0\pi^\pm$ Events. $\Delta\phi$ is the angle between the highest $P_T$ $\pi^\pm$ and photons. For all photons with (a) $P_T < 0.25$ GeV/c, (b) $P_T > 0.25$ GeV/c, (c) $P_T > 1$ GeV/c, (d) $P_T > 2$ GeV/c. . . . .	171

- 6.29 Rapidity Correlations in  $\pi^0\pi^0$  Events.  $\Delta Y$  is the rapidity difference between the highest  $P_T$   $\pi^0$  and the charged particles. For all tracks with (a)  $P_T < 0.25$  GeV/c, (b)  $P_T > 0.25$  GeV/c, (c)  $P_T > 1$  GeV/c, (d)  $P_T > 2$  GeV/c. The dash line represents the background of  $\Delta Y$  formed by the leading  $\pi^0$  of the previous event and the particles from the present event. The strong enhancement at zero suggests that there are particles moving in the same direction of the leading particles. . . 173
- 6.30 Rapidity Correlations in  $\pi^0\pi^0$  Events.  $\Delta Y$  is the rapidity difference between the highest  $P_T$   $\pi^0$  and photons. For all photons with (a)  $P_T < 0.25$  GeV/c, (b)  $P_T > 0.25$  GeV/c, (c)  $P_T > 1$  GeV/c, (d)  $P_T > 2$  GeV/c. The dash line represents the background of  $\Delta Y$  formed by the leading  $\pi^0$  of the previous event and the particles of the present event. 174
- 6.31 Rapidity Correlations in  $\pi^0\pi^\pm$  Events.  $\Delta Y$  is the rapidity difference between the highest  $P_T$   $\pi^\pm$  and the charged particles. For all tracks with (a)  $P_T < 0.25$  GeV/c, (b)  $P_T > 0.25$  GeV/c, (c)  $P_T > 1$  GeV/c, (d)  $P_T > 2$  GeV/c. The dash line represents the background of  $\Delta Y$  formed by the leading  $\pi^\pm$  from the previous event and the particles of the present event. . . . . 175
- 6.32 Rapidity Correlations in  $\pi^0\pi^\pm$  Events.  $\Delta Y$  is the rapidity difference between the highest  $P_T$   $\pi^\pm$  and photons. For all photons with (a)  $P_T < 0.25$  GeV/c, (b)  $P_T > 0.25$  GeV/c, (c)  $P_T > 1$  GeV/c, (d)  $P_T > 2$  GeV/c. The dash line represents the background of  $\Delta Y$  formed by the leading  $\pi^\pm$  from the previous event and the particles of the present event. 176
- 6.33 The average number of particles in  $\pi^0$  jets versus the  $P_T$  of the leading  $\pi^0$ . The top plot counts charged particles only, the middle one displays the average number of neutral, and the bottom one includes both neutral and charged particles. . . . . 178

6.34	The average number of particles in $\pi^\pm$ jets versus the $P_T$ of $\pi^\pm$ . The top plot counts charged particles only, the middle one displays the average number of neutral particles, and the bottom plot includes both neutral and charged particles. . . . .	179
6.35	The average fraction of the jet $P_T$ carried by the leading $\pi$ meson, versus the $P_T$ of $\pi$ meson. The leading particle is $\pi^0$ in the plot to the left and $\pi^\pm$ in the one to the right. . . . .	180
6.36	$x_a$ and $x_b$ distributions in $\pi^0\pi^0$ jets. These distributions are weighted by all the correction factors described in Section 6.2. . . . .	181
6.37	$x_a$ and $x_b$ distributions in $\pi^0\pi^\pm$ jets. These distributions are weighted by all the correction factors described in Section 6.2. . . . .	182
6.38	$\alpha$ vs dihadron mass. The top plot shows the results of $\pi^0\pi^0$ and $\pi^0\pi^\pm$ events. The bottom one shows all published data of $\alpha$ as a function of mass. All experiments except E706 measured dihadrons in $+-$ states. FMP (Ref. [40]), CFS (Ref. [39]), and E605 (Ref. [42]) used 400 GeV/c proton beams. Experiment E711 (Ref. [43]) used 800 GeV/c proton beams while Serpukhov (Ref. [41]) used 70 GeV/c proton beams.	185
6.39	$\Delta\phi$ between jet axes for $\pi^-$ -Be and $\pi^-$ -Cu interactions. . . . .	186
6.40	$K_{T\phi}$ distributions in Be, Cu, and Si data. . . . .	187
6.41	Cu-to-Be ratio of the $K_{T\phi}$ distribution in $\pi^0\pi^0$ jets and $\pi^0\pi^\pm$ jets . .	188
6.42	Ratios of the $K_{T\phi}$ distributions for (a) first piece of Be to second piece of Be, (b) first piece of Cu to second piece of Cu, (c) upstream Si to downstream Si. . . . .	189



6.43	$\langle K_{T\phi}^2 \rangle$ as a function of atomic weight for photon-nucleus ( $\gamma$ A) and pion-nucleus ( $\pi$ A) data in E683 experiment. The curves shown are the best power law fits to the form $\langle K_{T\phi}^2 \rangle = C_0 + C_1(A - 1)^\alpha$ . For the photon data the minimum $\chi^2$ fit yields $C_0 = 1.85 \pm 0.10, C_1 = 0.24 \pm 0.10, \alpha = 0.32 \pm 0.08$ , and for pion data the fit yields $C_0 = 3.54 \pm 0.22, C_1 = 0.27 \pm 0.21, \alpha = 0.39 \pm 0.15$ . . . . .	190
6.44	$\sigma^2$ as a function of atomic number for pion-nucleus data in E706 experiment. $\sigma$ is the RMS of the $K_{T\phi}$ distribution. . . . .	191
A.1	The trajectory of charged particle inside the magnet in Z-X plane. . .	200
A.2	The trajectory of charged particle inside the magnet in Z - Y plane .	201
A.3	The illustration of the angle $\eta$ . . . . .	202

# List of Tables

1.1	Three Generations of Elementary Particles . . . . .	3
1.2	Expressions of two body parton-parton scattering . . . . .	10
2.1	SSD wafer parameters. X planes have vertical strips while Y planes have horizontal strips. As described in the text, module 4 has two different regions: 25 $\mu\text{m}$ and 50 $\mu\text{m}$ regions. Therefore, there are two rows for module 4 in this table. . . . .	25
2.2	Regions of Cathode Segmentation in PWC Modules. All cathodes in the same module had identical sizes in each region. The unit is centimeter. . . . .	29
2.3	Orientation and Positions of Garlands. . . . .	30
2.4	Straw Tubes Parameters . . . . .	35
3.1	The DA subsystems which read out the data of their corresponding detectors. . . . .	48
3.2	The statistics of different trigger sets for 1990 Data . . . . .	55
3.3	The twelve combinations of the TWO GAMMA trigger . . . . .	57
6.1	The minimum and maximum values of $\eta_b$ in different $\cos \theta^*$ values with respect to $\pi^0$ 's in $\pi^0\pi^\pm$ events. The negative $\cos \theta^*$ values with respect to $\pi^0$ 's correspond to the positive values with respect to $\pi^\pm$ 's. The $\eta_b$ range is derived from Eqs. 6.11, 6.12, 6.13, and 6.14. . . . .	165

B.1	Invariant differential cross section per nucleon in units nb/(GeV/c <sup>2</sup> ) for $\pi^0\pi^0$ production in 515 GeV/c $\pi^-$ -Be and $\pi^-$ -Cu interactions. The cross sections are integrated from -0.3 to 0.7 in $Y_{cm}$ and from 0 to 0.5 in $\cos\theta^*$ . . . . .	207
B.2	Invariant differential cross section per nucleon in units nb/(GeV/c <sup>2</sup> ) for $\pi^0\pi^-$ production in 515 GeV/c $\pi^-$ -Be and $\pi^-$ -Cu interactions. The cross sections are integrated from -0.4 to 0.8 in $Y_{cm}$ and from 0 to 0.5 in $\cos\theta^*$ . . . . .	208
B.3	Invariant differential cross section per nucleon in units nb/(GeV/c <sup>2</sup> ) for $\pi^0\pi^+$ production in 515 GeV/c $\pi^-$ -Be and $\pi^-$ -Cu interactions. The cross sections are integrated from -0.4 to 0.8 in $Y_{cm}$ and from 0 to 0.5 in $\cos\theta^*$ . . . . .	209
B.4	$\alpha$ values in different $\pi^0\pi^\pm$ masses. Only statistical uncertainty is included. . . . .	210
B.5	$\alpha$ values in different $\pi^0\pi^0$ masses. Only statistical uncertainty is included.	210
B.6	RMS of $K_{T\phi}$ for di- $\pi$ jets in the interactions of different targets. . . .	210

# Chapter 1

## Introduction

This thesis aims to study high mass di- $\pi$  events and their associated jets using a  $\pi^-$  beam incident on Beryllium (Be) and Copper (Cu) targets. The data analyzed in this thesis were taken by experiment E706 at Fermilab during the 1990 fixed target run. This chapter will give a brief introduction to our current understanding of the strong interaction, the physics motivation of this thesis, and the kinematic variables employed.

### 1.1 A Brief Historic Review

“What is the world made of?” “Where are we from?” These questions have been asked at least since the beginning of human history. From the four elements— air, water, fire, and dust—proposed by the ancient Greek philosopher Anaximenes, to more than a hundred chemical elements listed in Mendeleev’s periodic table, human beings have come closer and closer to understanding the building blocks of our universe. Chemists created the idea that all chemicals were composed of atoms. With the discovery of X rays by W. C. Röntgen in 1895, the concept of the atom was gradually confirmed. In 1909, using alpha particles bombarding a thin gold foil, Hans Geiger, Ernest Marsden, and Ernest Rutherford discovered that an atom has a small charged nucleus [1]. Later on, this small nucleus was demonstrated to be composed of protons and neutrons. Protons and neutrons, along with electrons discovered earlier by J.J. Thomson, constitute atoms. By 1926, it was understood that all particles

were from two classes: fermions and bosons. Electrons, protons, and neutrons are fermions ( that is, they have half integral angular momentum or spin), while photons are bosons (which have integral spin).

Since the 1930's, many cosmic-ray experiments revealed the existence of positrons,  $\pi$ 's and  $\mu$ 's[2][3]. Positrons and electrons have the same physical properties but opposite electrical charges. Electrons and muons, which do not feel nuclear forces, are called leptons, whereas protons and neutrons, which are influenced by nuclear forces (strong forces), are named hadrons. With the discovery of subsequent heavier particles such as K's and  $\omega$ 's, scientists tried to explain why there exists so many particle types. In the mean time, quantum electrodynamics (QED), formulated by Richard Feynman, Julian Schwinger, and Sin-itiro Tomonaga, convincingly interpreted electromagnetic interactions between charged particles in the quantum realm. However, an explanation of hadronic interactions was still missing at that time.

In 1964, Murray Gell-Mann and G. Zweig proposed that protons, neutrons, and the other hadrons were not fundamental particles but consisted of tiny, more basic objects, named quarks[4][5]. In the late 1960's, a SLAC<sup>1</sup>-MIT group first detected direct evidence of point-like particles inside protons by scattering electrons from a hydrogen target[6]. Through the "scaling" effect<sup>2</sup> found in that experiment and with the help of the interpretations provided by Feynman and Bjorken, it was concluded that protons contain particles which have spin quantum numbers 1/2. These spin 1/2 particles have been identified as the quarks. The experimental results also showed that the proton momentum was not carried only by these quarks but also by spin 1 particles—gluons. Quarks and gluons are referred to as partons.

According to the current theory, the Standard Model, there are three generations of particles as listed in Table 1.1. Each generation is composed of quarks and leptons, which are all spin 1/2 particles. Quarks, the only particles affected by the strong

---

<sup>1</sup>Stanford Linear Accelerator

<sup>2</sup>In the deep inelastic scattering experiment at SLAC, they discovered that  $\nu W_2$  was independent of  $Q^2$ .

Table 1.1: Three Generations of Elementary Particles

	First				Second				Third			
	u	d	$\nu_e$	e	c	s	$\nu_\mu$	$\mu$	t	b	$\nu_\tau$	$\tau$
Electric Charge	$\frac{2}{3}$	$-\frac{1}{3}$	0	-1	$\frac{2}{3}$	$-\frac{1}{3}$	0	-1	$\frac{2}{3}$	$-\frac{1}{3}$	0	-1
Strong Int.	✓	✓			✓	✓			✓	✓		
EM Int.	✓	✓		✓	✓	✓		✓	✓	✓		✓
Weak Int.	✓	✓	✓	✓	✓	✓	✓	✓	✓	✓	✓	✓

force, carry fractional electronic charges; leptons consist of electrons, muons, and taus, all of which carry one negative unit of electric charge, and their associated neutrinos. Neutrinos do not carry any electric charge and are only involved in the weak interaction. The interactions between two particles are mediated by another class of particles, which can be annihilated and created. These “messengers” include photons for the electromagnetic interaction, W’s and Z’s for the weak interaction, and gluons for the strong interaction.

Quarks must, based on current knowledge, bind to form final states which have integral electric charges. Only two types of final states are confirmed so far: mesons ( $q\bar{q}$ ) and baryons ( $qqq$ ). Mesons, such as pions and kaons, have integral spins, while baryons, such as protons and neutrons, have half integral spins. Since quarks are fermions, the wavefunctions of hadrons should be anti-symmetric. The existence of the  $\Delta^{++}$  baryon leads to a challenge to the theory because it contains three u quarks. Besides, the question why  $qq$ ,  $\bar{q}\bar{q}$ , and  $q$  states do not exist also remains to be answered. These issues were addressed by introducing a new quantum number called color[7]. Supposes that quarks come in three colors and only colorless particles can be seen, then single quark and  $qq$  states will not be observed.

Color is also used to explain the strong interaction. Just as photons mediate the electromagnetic interaction between electrically charged particles, gluons mediate the strong interaction between “color” charged particles. Applying the method used in quantizing the electromagnetic field to the color field, physicists try to explain the strong interaction. This theory is referred to as quantum chromodynamics (QCD).

QCD is a non-Abelian gauge field theory with SU(3) symmetry. According to this theory, eight generators —gluons— can be expressed as eight different bi-color states. Although gluons play the same role as photons do in mediating the interactions, gluons carry color charges whereas photons do not bear electric charges. Therefore, gluons can couple with each other, while photons can not. This characteristics is significant in connecting experimental results and QCD predictions.

## 1.2 QCD and Parton Model

QCD is capable of accounting for two key elements of the strong interaction: asymptotic freedom and confinement[8]. The strong force, unlike the electromagnetic force, becomes stronger with increasing distance between quarks because of the self-couplings of gluons. This feature can be described by the leading order expression for the strong coupling constant:

$$\alpha_s(Q^2) = \frac{12\pi}{(11N_c - 2n_f)\ln(Q^2/\Lambda^2)} \quad (1.1)$$

where  $n_f$  is the number of quark flavors and  $N_c$  is the number of colors.  $Q^2$  represents the momentum transfer and  $\Lambda$  is the momentum scale which can not be calculated by the theory but is determined by experiments. In large momentum transfer processes (smaller distance interactions),  $\alpha_s$  becomes small (asymptotic freedom). On the other hand,  $\alpha_s$  becomes large in the long distance interaction<sup>3</sup>(confinement). Therefore, at some distance between two quarks, the work to pull these two quarks apart is larger than the energy to make quarks and antiquarks. These quarks and antiquarks will combine with each other to form hadrons.

The two body hard scattering in the parton model is illustrated in Fig. 1.1. Parton “a” from hadron A collides with parton “b” from hadron B producing partons c and d which fragment into, respectively, hadrons h1, h2 and other soft hadrons. The cross sections for di-hadron production from hard scattering may be written as follows[9]:

---

<sup>3</sup>From the Heisenberg uncertainty principle,  $\Delta P \Delta X \geq \frac{\hbar}{2\pi}$ . In a long distance interaction (large  $\Delta X$ ),  $\Delta P$  becomes small so that  $Q^2$  is small. The  $\alpha_s$  value, consequently, becomes large.

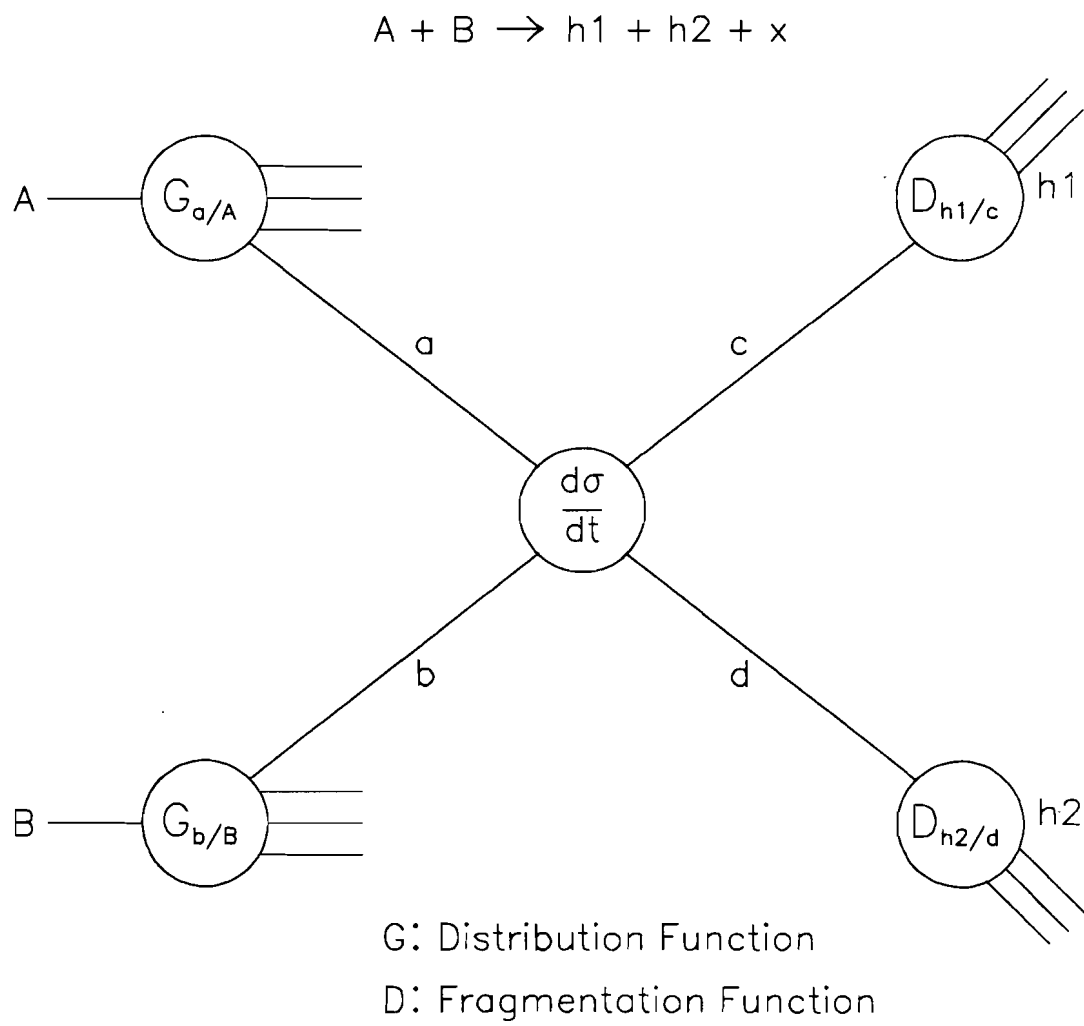


**Figure 1.1: Two body hard scattering.**



$$\frac{d\sigma}{dM^2 dY d\Delta d\cos\theta^*} = \int dz_1 \frac{d\sigma}{dM_{jj}^2 dY_{jj} d\cos\theta^*} \times D_{h1/j1}(z_1) D_{h2/j2}(z_2) \frac{2}{z_1 P_{Tj}(z_1 + z_2)} \quad (1.2)$$

$$(1.3)$$

where  $\Delta = P_{Tj}(z_1 - z_2)$ , and

$$\frac{d\sigma}{dM_{jj}^2 dY_{jj} d\cos\theta^*} = \frac{x_a x_b}{2} \sum_{abcd} G_{a/A}(x_a) G_{b/B}(x_b) \frac{d\sigma}{dt}(ab \rightarrow cd) \quad (1.4)$$

where  $G_{i/H}(x)$  is the parton distribution function, which gives the probability of parton  $i$  carrying a fractional momentum  $x$  from its hadron  $H$ ,  $D_{H/j}(z)$  is the fragmentation function, which indicates the probability of finding hadron  $H$  fragmented from parton  $j$  in momentum fraction between  $z$  and  $z + dz$ .  $M$  and  $Y$  are the effective mass and rapidity of the pairs of hadrons  $h1$  and  $h2$ , respectively.  $M_{jj}$  and  $Y_{jj}$  are the mass and rapidity of dijets. Parton distribution functions and fragmentation functions are determined from experiments and  $\frac{d\sigma}{dt}$ , is calculated via QCD. We can compare the predicted cross sections to the results of experiments. However,  $\frac{d\sigma}{dt}$  is only calculable for large momentum transfer processes, for which  $\alpha_s$  is small and perturbative QCD is appropriate.

When we apply perturbative QCD in calculating cross sections, some singularity problems have to be resolved. The first type of singularities is the mass singularities brought about by the radiated gluons from massless partons. It turns out that the mass singularities in all subprocesses behave the same way. These mass singularity terms can be separated from the calculations and can be assigned to the uncalculated distribution functions and fragmentation functions using the factorization theorem. The remaining finite terms are calculable. Additionally, ultraviolet singularities appear when calculating the loop diagrams. The ultraviolet singularities can be “regulated” by techniques such as dimensional regularization. These steps in removing singularities are often called renormalization. Finally, the soft singularities (infrared divergence) are canceled out when adding all loop diagrams and tree diagrams.

Because mass singularities are factorized, the parton distribution function,  $G$ , and fragmentation function,  $D$ , become dependent on the factorization scale,  $M^2$ . The strong coupling constant  $\alpha_s$  also depends on the momentum scale,  $Q^2$ . If one could calculate the cross sections of all the subprocesses in perturbation theory, the results would be independent of the scales. However, it's still beyond our abilities to do this. High energy phenomenologists are able to calculate the leading logarithmic contribution from each order and use it as an approximation to the cross sections. Lately, the next-to-leading-logarithm contributions have been calculated for some processes. Thus, the calculated cross sections depend on the scales we choose in the leading-logarithm approximation, even including the next-to-leading-logarithm corrections. Nowadays,  $M^2$  is often chosen as  $Q^2$  in large momentum transverse processes and the scale of order  $P_T^2$  are commonly employed.

Parton distribution and fragmentation functions are often obtained from deep-inelastic scattering or  $e^+e^-$  collider experiments at a scale  $Q_0$ . The evolution of these functions from  $Q_0$  to  $Q$  can be derived from theory. Therefore, we can use Eq. 1.2 and parton distribution function and fragmentation function measured from other experiments to calculate the cross sections and compare them to our measurements.

### 1.3 Di- $\pi$ Production

As mentioned in the previous section, in the large momentum transfer processes, perturbative QCD can be applied to obtain predictions. Measuring the cross sections of single or double high  $P_T$  particles plays an important role in testing these QCD calculations. There are two other effects which have to be taken into account in understanding the cross sections in fixed target experiments. The first one is the nuclear enhancement, which is discussed in Section 1.4; the second one is the  $K_T$  effect. The colliding partons might have some initial transverse momentum  $K_T$  with respect to the incoming hadrons. This  $K_T$  effect comes from the Fermi motion of nucleons in a nucleus and causes a smearing in the  $P_T$  spectrum. Since the invariant

cross section falls rapidly in  $P_T$ , even a small  $K_T$  smearing can make a significant increase in the differential cross section for the production of high  $P_T$  mesons. Besides, experiments with single arm triggers will preferentially select those events in which initial partons have already some transverse momentum. However, the cross section of two high  $P_T$  particles forming a high mass state is relatively insensitive to the initial  $K_T$  effect[10][11]. Measuring the cross sections of two high  $P_T$  particles, therefore, provides a good check of QCD independent of  $K_T$  smearing.

Measuring the angular distributions of parton-parton scattering also provides a test of QCD (see Section 1.3.2). Experimentally, dijet events and dihadron events are often used to measure the angular distributions assuming the directions of high  $P_T$  hadrons or jets are close to the directions of their parent partons. In the dihadron case, these two high  $P_T$  hadrons from their parent partons are preferentially produced near  $90^\circ$  in the parton-parton center of momentum frame to form a high mass state. Therefore, the study of massive dihadron (di- $\pi$  in this experiment) production provides at least two QCD tests: cross sections and angular distributions.

$\pi^0$  pairs are the main background of double direct photon production. Direct photons are photons produced from hard scattering processes rather than from the decay products of hadrons. There are only two lowest order Feynman diagrams (see Figure 1.2) in double direct photon production. Therefore, these processes provide a clean test of QCD since no fragmentation functions will be involved in the calculations. Besides, the Born process in Fig. 1.2 can be used to test the fractional charges of quarks[12]. Through the comparison of  $q\bar{q} \rightarrow \gamma\gamma$  and  $q\bar{q} \rightarrow g\gamma$ , one may estimate  $\alpha_s$ [13]. However, detecting double direct photons is very difficult experimentally because the cross section, proportional to  $\alpha^2$ , is very small and the photons from hadron decay, mainly  $\pi^0$ 's, generate substantial backgrounds. The cross section measurement of  $\pi^0$  pairs, consequently, becomes essential for being able to extract the signal of double direct photons.

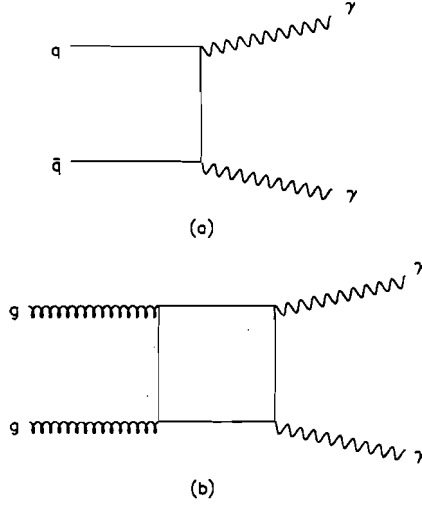


Figure 1.2: The lowest order diagrams of double direct photon production. (a) Born diagram, (b) Box diagram.

### 1.3.1 Kinematic Variables

There are at least 8 different subprocesses, listed in Table 1.2, for di- $\pi$  production. In Table 1.2,  $\hat{s}$ ,  $\hat{t}$ , and  $\hat{u}$  are Mandelstam variables for pointlike scattering. They are defined as follows:

$$\hat{s} = (p_a + p_b)^2 \quad (1.5)$$

$$\hat{t} = (p_a - p_c)^2 \quad (1.6)$$

$$\hat{u} = (p_a - p_d)^2 \quad (1.7)$$

where  $p_i$  is the four-vector momentum of parton  $i$ . In high energy interactions, the sum of  $\hat{s}$ ,  $\hat{t}$ , and  $\hat{u}$  is zero.

It is also useful to define Mandelstam variables for the hadron states. They can be written as

$$s = (p_A - p_B)^2 \quad (1.8)$$

$$t = (p_A - p_C)^2 \quad (1.9)$$

$$u = (p_A - p_D)^2. \quad (1.10)$$

Subprocess	Cross section
$qq' \rightarrow qq'$	$\frac{4}{9} \frac{s^2 + \hat{u}^2}{\hat{t}^2}$
$qq \rightarrow qq$	$\frac{4}{9} \left[ \frac{s^2 + \hat{u}^2}{\hat{t}^2} + \frac{s^2 + \hat{t}^2}{\hat{u}^2} \right] - \frac{8}{27} \frac{s^2}{\hat{t}\hat{u}}$
$q\bar{q} \rightarrow q'\bar{q}'$	$\frac{4}{9} \frac{\hat{t}^2 + \hat{u}^2}{s^2}$
$q\bar{q} \rightarrow q\bar{q}$	$\frac{4}{9} \left[ \frac{s^2 + \hat{u}^2}{\hat{t}^2} + \frac{\hat{u}^2 + \hat{t}^2}{s^2} \right] - \frac{8}{27} \frac{\hat{u}^2}{s\hat{t}}$
$gq \rightarrow gq$	$-\frac{4}{9} \left[ \frac{\hat{s}}{\hat{u}} + \frac{\hat{u}}{\hat{s}} \right] + \frac{s^2 + \hat{u}^2}{\hat{t}^2}$
$q\bar{q} \rightarrow gg$	$\frac{32}{27} \left[ \frac{\hat{t}}{\hat{u}} + \frac{\hat{u}}{\hat{t}} \right] - \frac{8}{3} \frac{\hat{t}^2 + \hat{u}^2}{s^2}$
$gg \rightarrow q\bar{q}$	$\frac{1}{6} \left[ \frac{\hat{t}}{\hat{u}} + \frac{\hat{u}}{\hat{t}} \right] - \frac{3}{8} \frac{\hat{t}^2 + \hat{u}^2}{s^2}$
$gg \rightarrow gg$	$\frac{9}{2} \left[ 3 - \frac{\hat{t}\hat{u}}{s^2} - \frac{s\hat{u}}{\hat{t}^2} - \frac{s\hat{t}}{\hat{u}^2} \right]$

Table 1.2: Expressions of two body parton-parton scattering

For the sake of simplicity, the hadron-hadron center of mass frame is chosen to express these kinematic variables. In this frame, parton four vectors  $p_a$  and  $p_b$  can be given as

$$p_a = \frac{x_a \sqrt{s}}{2} (1, 0, 0, 1) \quad (1.11)$$

and

$$p_b = \frac{x_b \sqrt{s}}{2} (1, 0, 0, -1) \quad (1.12)$$

where the positive  $z$  direction is assumed to be the direction of hadron A, and the intrinsic transverse momenta are neglected.  $x_a$  and  $x_b$  are the fraction of the momentum carried by partons  $a$  and  $b$  inside hadrons A and B, respectively. If parton  $c$  has transverse momentum  $P_T$  and rapidity  $y_c$ , the four-vector  $p_c$  can be written as

$$p_c = P_T (\cosh y_c, 1, 0, \sinh y_c). \quad (1.13)$$

The rapidity  $y$  is defined as

$$y = \frac{1}{2} \ln \frac{E + p_l}{E - p_l} \quad (1.14)$$

where  $p_l$  is the longitudinal momentum. Similarly, the corresponding expression for the four vector of scattered parton  $d$  is applied to  $p_d$ .

$$p_d = P_T (\cosh y_d, -1, 0, \sinh y_d). \quad (1.15)$$

Finally, the Mandelstam variables can be expressed as:

$$\hat{s} = x_a x_b s \quad (1.16)$$

$$\hat{t} = -x_a p_T \sqrt{s} e^{-y_c} \quad (1.17)$$

$$= -x_b p_T \sqrt{s} e^{y_d} \quad (1.18)$$

$$\hat{u} = -x_b p_T \sqrt{s} e^{y_c} \quad (1.19)$$

$$= -x_a p_T \sqrt{s} e^{-y_d}. \quad (1.20)$$

Once the rapidity and  $P_T$  of the out going partons are measured,  $x_a$  and  $x_b$  can be determined from the following equations:

$$x_a = \frac{P_T}{\sqrt{s}} (e^{y_c} + e^{y_d}) \quad (1.21)$$

$$x_b = \frac{P_T}{\sqrt{s}} (e^{-y_c} + e^{-y_d}). \quad (1.22)$$

### 1.3.2 Angular Correlations

Measuring the angular distributions of parton-parton scattering provides a test of QCD. As shown in Table 1.2, there are t-channel, u-channel, and s-channel poles in the cross sections. Therefore, the angular distributions should be sharply peaked in the forward and backward directions<sup>4</sup>. The angular distributions can be parametrized as

$$\frac{d\sigma}{d\cos\theta^*} \bigg/ \frac{d\sigma}{d\cos\theta^*} \bigg|_{\cos\theta^*=0} = \frac{1}{2} \left[ \frac{1}{(1+\cos\theta^*)^a} + \frac{1}{(1-\cos\theta^*)^a} \right]. \quad (1.23)$$

Different subprocesses will give different values of  $a$ . For example,  $a$  is 2.02 for  $gg \rightarrow gg$ , 2.15 for  $gq \rightarrow gq$ , and 2.6 for  $qq \rightarrow qq$ [9]. The final result of the angular distributions is a weighted average in all available subprocesses. Hence, the parameter  $a$  is sensitive to the parton distribution functions and the strong coupling constant.

Experimentally, at least two cuts are needed to get an unbiased  $\cos\theta^*$  distribution. The first bias comes from the steeply falling spectrum of the dihadron cross section

---

<sup>4</sup>In the parton-parton center of mass frame,  $\hat{t} = -2 |p_a| |p_c| (1 - \cos\theta^*)$ , and  $\hat{u} = -2 |p_a| |p_c| (1 + \cos\theta^*)$ . When  $\cos\theta^* = \pm 1$ , the cross sections in Table 1.2 become infinite.

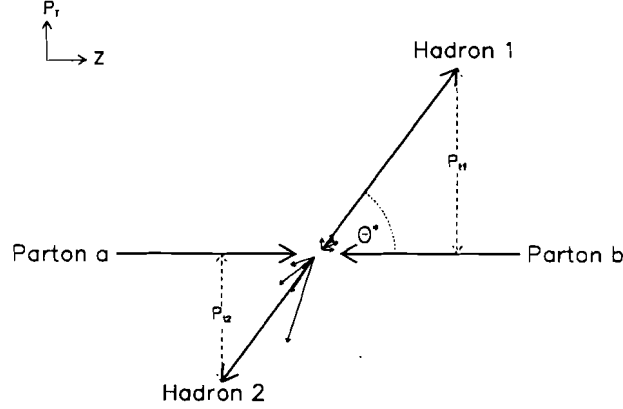


Figure 1.3: The hard scattering in the parton-parton center of mass frame.

in mass. Assuming the intrinsic transverse momentum of the partons is negligible and the leading hadron of a jet (parton) is moving in the direction of that jet, the effective mass of hadron 1 and 2 is

$$\begin{aligned}
 M &= \sqrt{(P_1 + P_2)^2} \\
 &\sim 2\sqrt{|P_1||P_2|} \\
 &\sim \frac{2\sqrt{P_{T1}P_{T2}}}{\sin \theta^*}
 \end{aligned} \tag{1.24}$$

where  $P_{T1}$  and  $P_{T2}$  are the transverse momenta of hadrons  $h1$  and  $h2$ , respectively, and  $\theta^*$  is the angular difference between hadron  $h1$  and the direction of the incoming hadrons. Note that in Eq. 1.24, hadrons  $h1$  and  $h2$  are almost collinear but their transverse momenta are not necessarily equal (see Figure 1.3). At a given mass,  $\sin \theta^*$  increases when  $P_{T1}$  or  $P_{T2}$  increases.

Since  $P_{T1}$  and  $P_{T2}$  are required to be above the threshold values, the kinematic space of  $\theta^*$  is restricted. For example,  $\theta^*$  ranges from  $\theta_1$  ( $\theta_2$ ) to  $90^\circ$  at mass equal to

$M_1$  ( $M_2$ ) in Fig. 1.4. The corresponding  $\cos \theta^*$  ranges from 0 to  $\cos \theta_1$  ( $\cos \theta_2$ ). Since  $M_1$  is smaller than  $M_2$ ,  $\cos \theta_1$  is less than  $\cos \theta_2$ . Therefore, the low mass dihadron pairs are restricted to the low  $\cos \theta^*$  region. The  $\cos \theta^*$  distribution is, consequently, more populated in the low value region, since the dihadron mass has a steeply falling spectrum. In order to have an unbiased sample in measuring  $\cos \theta^*$ , a mass cut must be implemented. From Eq. 1.24 and the appropriate  $\cos \theta^*$  range to investigate, the minimum mass cut can be derived.

The second bias comes from the acceptance of the detectors. Since the detectors in E706 do not have  $4\pi$  coverage, events in some specific kinematic region won't be detected. The  $\theta^*$  variable may be expressed in terms of pseudo-rapidity  $\eta$ .  $\eta$  has the same definition of rapidity  $Y$  but the masses of particles are neglected. Hence,

$$\eta = \frac{1}{2} \ln \frac{E + P_l}{E - P_l} = \frac{1}{2} \ln \frac{1 + \cos \theta}{1 - \cos \theta} \quad (1.25)$$

where  $\cos \theta$  equals  $\frac{P_l}{E}$ .  $\theta$  equals  $\theta^*$  in the parton-parton center of momentum frame. The rapidity transformations between the hadron-hadron and the parton-parton center of momentum frame obey the following equations:

$$\eta'_1 = \eta_1 + \eta_b \quad (1.26)$$

$$\eta'_2 = \eta_2 + \eta_b \quad (1.27)$$

where  $\eta_b$  is the rapidity boost between the prime frame and the unprime frame, and  $\eta_i$  is the pseudo-rapidity of hadron  $i$ . If the prime frame is chosen as the parton-parton center of mass frame,  $\eta'_1$  equals  $-\eta'_2$ . Therefore,  $\eta'_1$  and  $\eta_b$  are derivable from the measured  $\eta_1$  and  $\eta_2$ . In this analysis, the pseudo-rapidity in the hadron-hadron center of momentum frame ranged from  $-0.8$  to  $0.8$  for  $\pi^0$ 's, and  $-1$  to  $2$  for charged particles. Because the observed ranges of  $\eta_1$  and  $\eta_2$  are constrained by our detector acceptance, the distribution of  $\eta_b$  is not uniform in each  $\theta^*$ . For example, the corresponding range of  $\eta_b$  in three  $\cos \theta^*$  values of  $\pi^0$  pairs can be expressed as:

$$\cos \theta^* = \begin{cases} 0 & \Rightarrow -0.8 \leq \eta_b \leq 0.8 \\ 0.3 & \Rightarrow -0.49 \leq \eta_b \leq 0.49 \\ 0.5 & \Rightarrow -0.25 \leq \eta_b \leq 0.25 \end{cases}$$



$$M \sin \theta^* = 2(p_{T1} p_{T2})^{1/2}$$

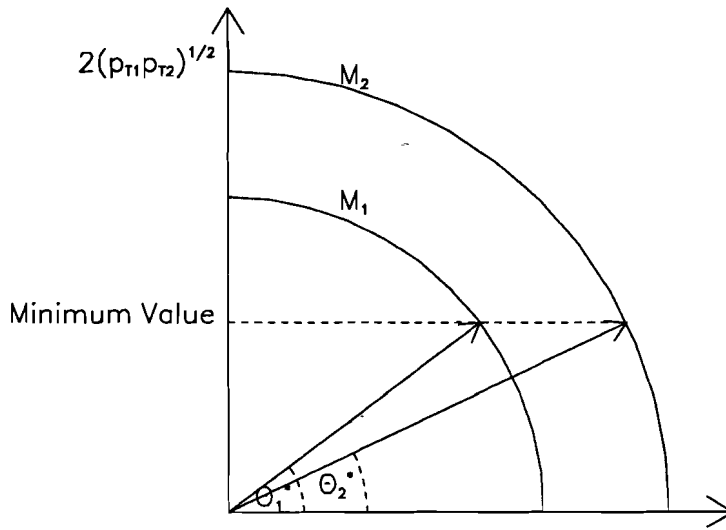


Figure 1.4: A graphical display of the relation between the effective mass  $M$ , the  $P_T$ 's of each hadron, and  $\theta^*$  in dihadron events. The minimal value of  $2(P_{T1} P_{T2})^{1/2}$  is caused by the minimal  $P_T$  requirement for each hadron. The higher the mass, the greater the  $\theta^*$  range.

These  $\eta_b$  ranges, derived from Eqs. 1.26 and 1.27, are purely caused by the detector acceptance. Theoretically,  $\eta_b$  is independent of  $\cos \theta^*$ . Therefore, the rapidity coverage in our detectors favors low  $\cos \theta^*$  value. The  $\eta_b$  cut is necessary in measuring the unbiased  $\cos \theta^*$  distribution.

## 1.4 Nuclear Dependence

Since the first observation of “anomalous nuclear enhancement” in proton-nucleus collisions about twenty years ago [14][15], the cross section for hadron-nucleus collisions is usually parametrized as  $A^\alpha$  times the cross section for hadron-hadron scattering, where  $A$  is the atomic number of the target nucleus. Previous experimental data have shown that  $\alpha$  is generally about  $2/3$  at low  $P_T$  values (below 1 GeV/c), which is due to the interaction of the incident hadron and the nuclear surface. At high  $P_T$  values,  $\alpha$  increases to values greater than 1 at  $P_T$  above 2 GeV/c. Numerous theoretical models have been proposed to explain why  $\alpha$  exceeds 1 in high  $P_T$  interactions. A plausible explanation is that the parton rescatters inside the nuclear matter after a hard scatter[16]. Fig. 1.5 illustrates the idea of the multi-scattering effect. Since high  $P_T$  cross sections have steeply falling spectra, rescattering which results in larger  $P_T$  or higher mass values will have a more significant contribution than will rescattering which contributes to the lower  $P_T$  or lower mass regions. In other words, the entries scattered to the lower  $P_T$  (mass) region from the larger  $P_T$  (mass) region do not have too much impact on the cross section in the lower  $P_T$  (mass) region, but the entries from the lower  $P_T$  (mass) region to the larger  $P_T$  (mass) region play a significant role in enhancing the cross section in the larger  $P_T$  (mass) region. This rescattering effect depends on the number of nucleons in a nucleus. The more nucleons there are, the greater the rescattering effect is and, therefore, the larger increase in cross sections. However, a more comprehensive explanation of the experimental data is still lacking.

In this thesis, we present results on the nuclear dependence in di- $\pi$  production.

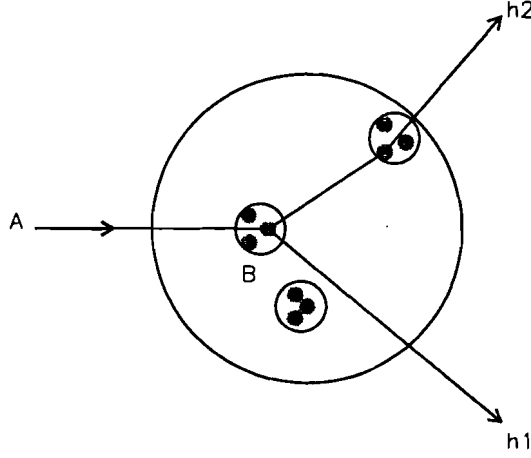


Figure 1.5: Parton rescatters after a hard scatter.

The parameter  $\alpha$  is measured as a function of the effective masses of di- $\pi$ 's. The reconstructed jets in the di- $\pi$  events are also employed to illustrate the nuclear dependence of two different variables,  $\Delta\phi$  and  $K_{T\phi}$ .  $\Delta\phi$  is defined as the azimuthal opening angle between the two jets, while  $K_{T\phi}$  is the average  $P_T$  of the two jets times the sine value of  $\Delta\phi$ . Figure 1.6 illustrates the relations between  $\Delta\phi$  and  $K_{T\phi}$ . In an ideal case, two outgoing partons would be exactly back to back in the hard scattering processes if only there were the leading order contribution and no  $K_T$  effect. Therefore,  $\Delta\phi$  would be  $180^\circ$  and  $K_{T\phi}$  would always be 0. In the real world, we can only reconstruct jets to approximate partons. Therefore, there is a smearing in the  $\Delta\phi$  and the  $K_{T\phi}$  distributions. If we take the intrinsic  $K_T$  and the next order contribution into account, this smearing effect is increased. The distributions of  $K_{T\phi}$  and  $\Delta\phi$  will be even broader if outgoing partons rescatter with nuclear matter after a hard scatter. Hence, the distributions of  $\Delta\phi$  and  $K_{T\phi}$  in different nuclei give us a clearer

picture in investigating the multiple scattering effect. As a result, they provide us with additional insights in understanding hadron-nucleus interactions.

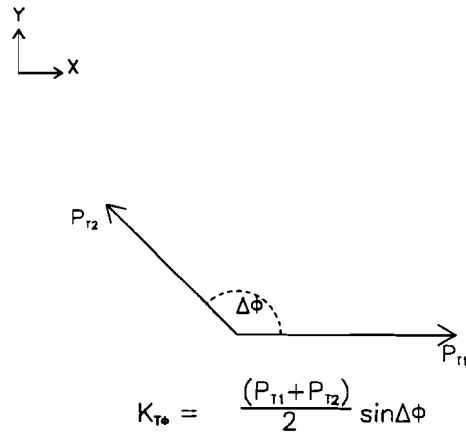


Figure 1.6: The Definitions of  $\Delta\phi$  and  $K_{T\phi}$ .

# Chapter 2

## The Experiment

The Meson West Experiment Hall houses two experiments, E706 and E672. These two experiments share the same detectors and data acquisition system. E672 was designed to study massive dimuon pairs and E706 was designed to study high  $P_T$  photons. Figure 2.1 displays the spectrometer in Meson West. The spectrometer consists of a beam transport system, a charged tracking system, a liquid argon calorimeter, a forward calorimeter, and a dimuon tracking system. The dimuon tracking system, which includes a toroidal magnet and a set of proportional wire chambers before and after the magnet, is used mainly by E672 to tag muons and to trigger on dimuon events. The other apparatus will be described in the following sections.

### 2.1 The Beam Line

Experiment E706 uses a right handed coordinate system. The  $Z$  axis is defined in the nominal beam direction while the  $X$  axis is in the horizontal direction to the west and the  $Y$  axis is in the vertical direction, pointing up.

The Meson beam line was capable of transporting primary beam (800 GeV/c) as well as both positive and negative polarity secondary beams. The 800 GeV proton beam from primary beamline was delivered for about 23 seconds per bunch and was transported into the production target. We called this beam within the 23 second bunch period, a spill. There were about 37 seconds regeneration time between spills. The interaction of the primary beam on the primary target produced a secondary

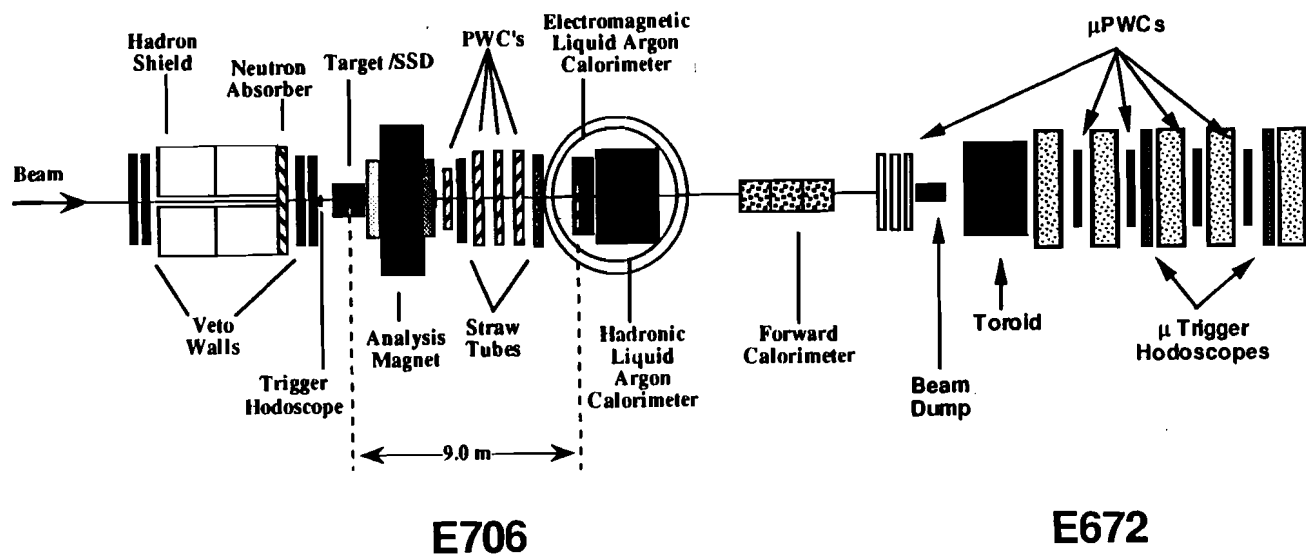


Figure 2.1: The physical layout of the Mwest spectrometer

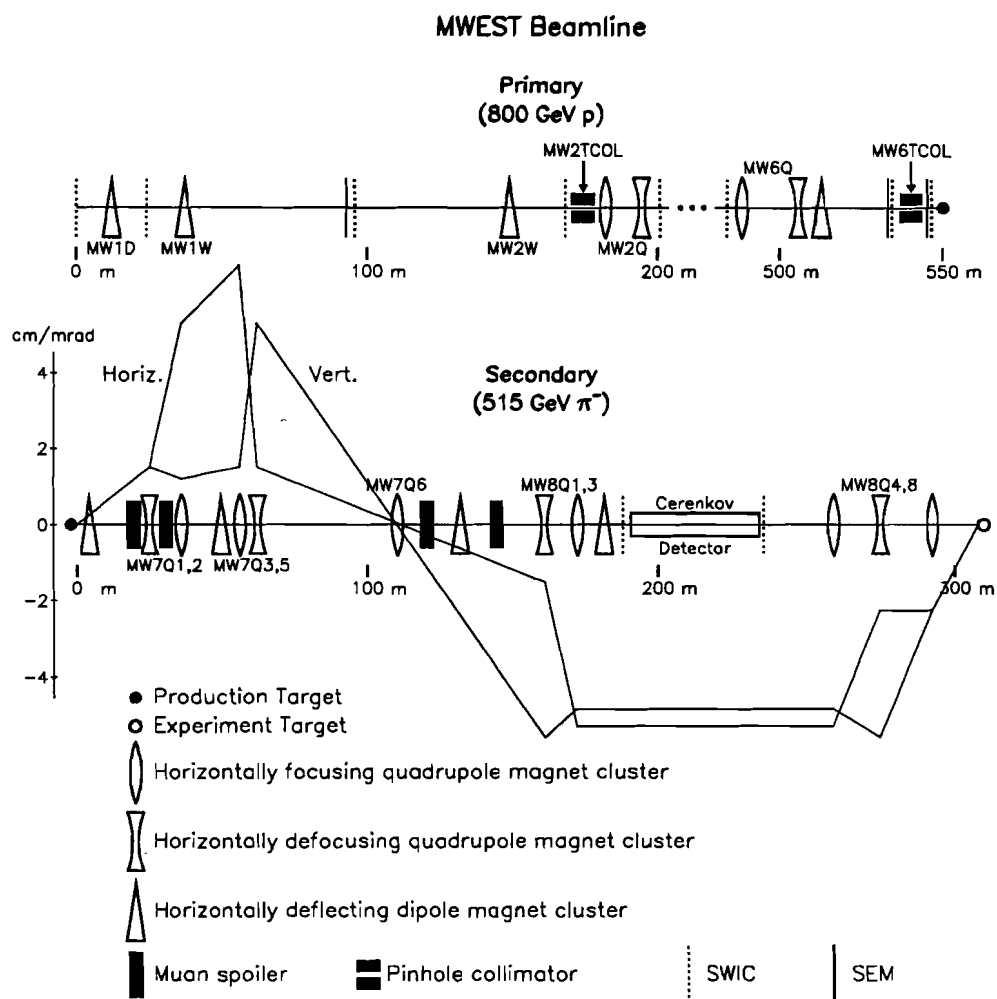


Figure 2.2: The Mwest beam line

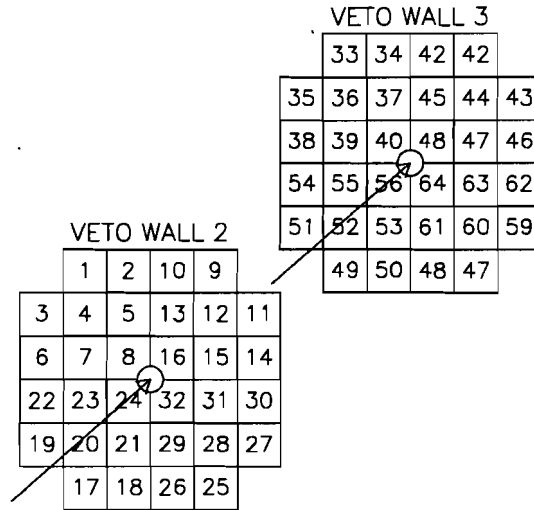


Figure 2.3: The downstream veto walls

beam which was defined by an aperture of the dump magnet, MW6W. By controlling the magnitude and polarity of the secondary beamline magnet currents, we were able to select positive or negative beams of the desired momenta. Although most of the particles in the secondary beam were pions, a 42.1 m long differential Cherenkov counter was available to identify the incident beam particle type. The intensity of the secondary beam was moderated by a set of collimators and its profile was monitored by segmented wire ionization chambers. When the primary production target was removed, a 800 GeV/c proton beam was transported down to the Meson West secondary beamline. Figure 2.2 shows a schematic of the secondary beam line at Meson west.

Those muons and hadrons which came parallel to the beam line could generate a large background in our high  $P_T$  events. Three efforts were made to reduce this



background. First, there were muon spoilers in our beam line. These spoilers had three inches diameter vacuum pipe surrounded with soft steel. The steel was wound with copper coils to make an electromagnet so that the magnetic field was high in the steel and low in the vacuum pipe. The muons of the same sign as the beam particles but outside the vacuum pipe were swept away. Second, a three-meter long iron shield was located in front of the spectrometer to attenuate hadrons near the beam line. Third, three scintillation counter veto walls, one before and two after the hadron shield, were installed to identify the remaining halo muons. Each downstream wall was made from 32 scintillation counters with a hole in the center, while the upstream one contained 10 scintillation counters with a hole of size 14.5 in.  $\times$  12 in. Figure 2.3 shows the geometry of the downstream veto walls.

## 2.2 Beam Hodoscope, Interaction Counters and E706 Target

A beam hodoscope<sup>1</sup>, positioned in front of the experimental target, was set up to identify beam particles incident on the target. The beam hodoscope consisted of three planes (X, Y, and U), each of which covered a  $2 \times 2$  cm<sup>2</sup> area and was composed of 12 scintillating paddles. Right after the three planes of the beam hodoscope was a beam hole counter, which had a 1 cm hole in its center. This beam hole counter, along with the beam hodoscope, were used to define the useful beam. The hodoscope information was read out to check if there were multiple particles in a single RF bucket.

Four interaction counters (SW1,SE1,SW2,SE2), located before and after analysis magnet (see Fig. 3.2), were implemented to detect interactions. SE1 and SW1 were  $7.6 \times 15.2$  cm<sup>2</sup> large and were situated between the silicon detector and the dipole magnet; SE2 and SW2 were  $10.2 \times 20.4$  cm<sup>2</sup> large and were positioned downstream of the magnet.

---

<sup>1</sup>C.Bromberg et al.,Nucl. Instr. and Meth. 200(1982), 245.

The E706 target consisted of two pieces of beryllium, separated by 1 cm, and two pieces of copper just upstream of the first piece of beryllium. In this fixed target experiment, we want to minimize secondary interactions and the probability of photon conversions. That's why we chose beryllium as our target. The 1 cm gap between the beryllium pieces was designed for studying heavy flavor physics. If there is a secondary vertex inside the gap, it is more likely a particle decay rather than a secondary interaction with nuclear target. Nuclear effect can also be studied in fixed target experiments. During the 1990 run, we used the copper targets, which has a large atomic number, for this purpose.

## 2.3 The Tracking System

E706 tracking system was designed to reconstruct the vertices, where the interactions occurred, and to measure the momenta of charged particles. In addition, the tracking system also measured the incident beam direction. The tracking system consisted of 16 planes of silicon microstrip detectors (SSDs), a dipole analyzing magnet, 16 planes of multiwire proportional chambers (PWCs), and 16 planes of straw tubes (drift chambers).

### 2.3.1 The Silicon Strip Detector (SSD) System

With the advanced technology of solid state detectors and the desire for the discrimination of secondary vertices, silicon strip detectors are now widely used in fixed target and collider experiments. E706 SSDs were divided into two parts: the 6 planes of upstream SSDs, which measured the position of beam particles before entering the target, and the 10 planes of downstream SSDs, which not only allowed for determination the positions of vertices but also, along with the PWC-STRAW system, measured the momentum of charged particles.

The 6 upstream SSD planes were grouped into 3 X-Y modules, which had 3 cm  $\times$  3 cm wafers and 50  $\mu$ m wide strips. The 10 downstream SSD planes were grouped

Module	Plane Number	Wafer Size (cm <sup>2</sup> )	Instrumented Region(cm)	Number of Strips	Strip Width ( $\mu$ m)
1 X	1	3 $\times$ 3	$\pm 0.64$	256	50
1 Y	2	3 $\times$ 3	$\pm 0.64$	256	50
2 X	3	3 $\times$ 3	$\pm 0.64$	256	50
2 Y	4	3 $\times$ 3	$\pm 0.64$	256	50
3 X	5	3 $\times$ 3	$\pm 0.64$	256	50
3 Y	6	3 $\times$ 3	$\pm 0.64$	256	50
4 X	7	5 $\times$ 5	$\pm 0.48$ $\pm 0.64$	384 256	25 50
4 Y	8	5 $\times$ 5	$\pm 0.48$ $\pm 0.64$	384 256	25 50
5 X	9	5 $\times$ 5	$\pm 1.28$	512	50
5 Y	10	5 $\times$ 5	$\pm 1.28$	512	50
6 X	11	5 $\times$ 5	$\pm 1.76$	704	50
6 Y	12	5 $\times$ 5	$\pm 1.76$	704	50
7 X	13	5 $\times$ 5	$\pm 2.08$	832	50
7 Y	14	5 $\times$ 5	$\pm 2.08$	832	50
8 X	15	5 $\times$ 5	$\pm 2.5$	1000	50
8 Y	16	5 $\times$ 5	$\pm 2.5$	1000	50

Table 2.1: SSD wafer parameters. X planes have vertical strips while Y planes have horizontal strips. As described in the text, module 4 has two different regions: 25  $\mu$ m and 50  $\mu$ m regions. Therefore, there are two rows for module 4 in this table.

into 5 X-Y modules with 5 cm  $\times$  5 cm wafers. The first downstream module contained 25  $\mu$ m strips in the inner region and 50  $\mu$ m strips in the outer region; the other four contained only 50  $\mu$ m strips. Figure 2.4 shows the geometry of the SSD system. The wafer size, number of strips, and instrumented region of each SSD plane are given in Table 2.1.

The instrumented region (active region) of each plane was not necessarily the same as the size of the wafer. For example, the active region in the X-plane of module 1 was 1.28 cm $\times$ 3 cm and that in the Y-plane of module 1 was 3 cm $\times$ 1.28 cm. Only the last downstream module was fully instrumented.

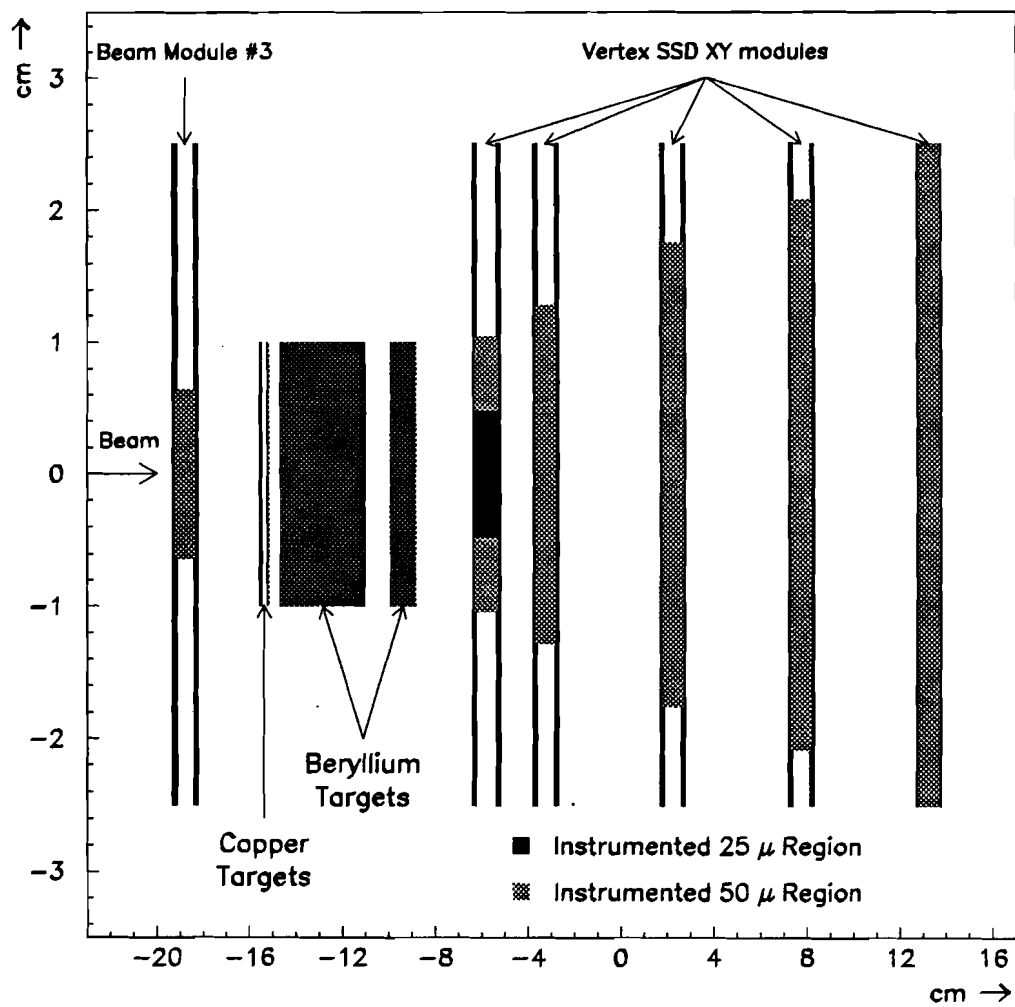


Figure 2.4: The layout of silicon strip detector and 90 target.

### 2.3.2 The MW9AN Dipole Magnet

The MW9AN dipole magnet provided a  $444 \text{ MeV}/c \text{ } P_T$  impulse for all charged particles within its geometrical acceptance. The operating current during our 90-91 data run was 1050 amperes, which generated a 6.2 KG magnetic field in the Y direction. The field was mapped using a nuclear magnetic resonance probe (NMR) at values of 700, 1400, and 2100 amperes. Besides, the value of the field integral was within 1% of the measured value.

With 20 cm thick mirror plates on both ends of MW9AN, 53.03 cm and 360.85 cm respectively in Z positions, the field approached a nearly uniform dipole shape. Both mirror plates had holes in the central region: 35.5 cm wide by 25.3 cm high in the upstream mirror plate and 127.0 cm wide by 91.4 cm high for the downstream one. The transverse center of MW9AN was near zero in X and Y, and the longitudinal coordinate center was around 2 meters from the target. The detailed description of how we locate the center of the magnetic field is given in Section 4.1. Because the current in the magnet generated a large amount of heat, cold water was circulated through the coils to prevent overheating.

### 2.3.3 The Proportional Wire Chamber (PWC) System

The E706 PWC system consisted of four modules and each module contained four anode planes—X, Y, U, and V. Each anode plane was surrounded by two cathode planes. Figure 2.5 illustrates the arrangement of the different planes in each module. The X-Y-Z and U-V-Z each formed a cartesian coordinate system. However, the U-V system had a azimuthal angular difference of  $37^\circ$  with respect to X-Y system. The purpose for this design was to measure the particle's trajectory in 3 dimensions and reduce tracking ambiguities. Although the four modules were almost identical in design, the transverse sizes increased with increasing distance between the module and the target. This design gives a consistent aperture for detecting charged particles coming from the target.

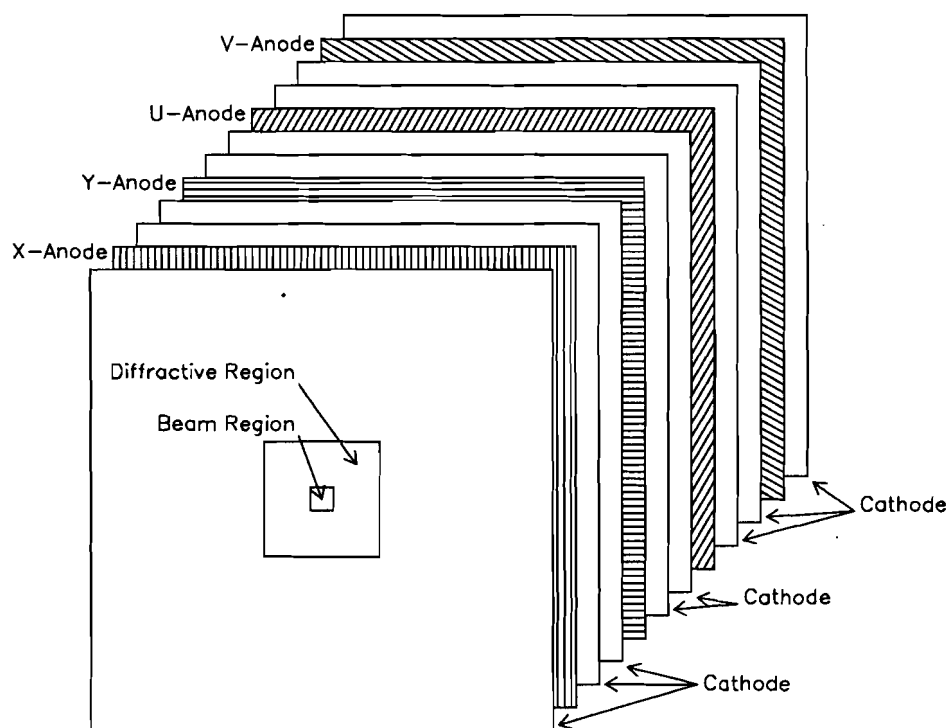


Figure 2.5: Arrangement of sense planes in each PWC module. Each cathode plane was capable of supporting independent high voltages in three regions to decrease the sensitivity in the high rate region.

Table 2.2: Regions of Cathode Segmentation in PWC Modules. All cathodes in the same module had identical sizes in each region. The unit is centimeter.

	Beam		Diffractive		Main	
	X	Y	X	Y	X	Y
Module 1	2.54	2.54	15.2	15.2	162.6	121.9
Module 2	3.81	3.81	20.3	20.3	203.2	203.2
Module 3	3.81	3.81	20.3	20.3	203.2	203.2
Module 4	5.08	5.08	30.5	30.5	243.8	243.8

The active region of each module was roughly the same as the size of the main cathode region of that module. In order to decrease the sensitivity of the high rate central region, each cathode plane was segmented into three electrically independent regions. Table 2.2 gives the sizes of each module in three different regions. The cathodes were constructed of 1.0 mil mylar sheets stretched to a tension of 40 lbs and glued to G-10<sup>2</sup> frames. The cathodes were mounted to supporting frames, which were made of iron for modules 2, 3, and 4 and aluminum for module 1. Aluminum was chosen for frame of module 1 due to its proximity to the dipole magnet.

The anodes were made of 0.8 mil diameter gold-plated tungsten wire, which had a tension 40 grams. The spacing between anode wires was 2.54 mm in each plane. A high-voltage feed wire was connected externally with a feedthrough connector. There were three high voltage wires in this connector, one for each cathode region. The spacing between the cathode and the anode planes was 0.226 inches. A set of garland support structures, made of zig-zagged Kapton, were installed on the cathode planes in order to maintain the distance between the anode wires and the cathode planes. These garlands were mounted perpendicular to the X-wires or Y-wires so that these wires were sandwiched by the garlands. All the orientations and positions of the garlands are shown in Table 2.3. Because the garlands disturbed the electric field between the anodes and the cathodes, a field restoring wire was connected to each garland.

---

<sup>2</sup>G-10 is a glass epoxy material which is often used for printed circuit boards.

Table 2.3: Orientation and Positions of Garlands.

Module	View	Orientation	Positions (cm)
1	X, U	Horizontal	$\pm 2.54, \pm 38.1, \pm 43.2$
1	Y, V	Vertical	$\pm 17.8, \pm 22.9, \pm 58.4, \pm 63.5$
2,3	X, U	Horizontal	$\pm 12.7, \pm 17.8, \pm 43.2, \pm 48.3, \pm 73.7, \pm 78.7$
2,3	Y, V	Vertical	$\pm 12.7, \pm 17.8, \pm 43.2, \pm 48.3, \pm 73.7, \pm 78.7$
4	X, U	Horizontal	$\pm 15.2, \pm 20.3, \pm 50.8, \pm 55.9, \pm 86.4, \pm 91.4$
4	Y, V	Vertical	$\pm 15.2, \pm 20.3, \pm 50.8, \pm 55.9, \pm 86.4, \pm 91.4$

The PWC gas mixture was composed of 80.4% argon, 18% isobutane, 0.1% freon and 1.5% isopropyl alcohol vapor. Noble gases are desirable as ionizing media because they are chemical inert. In the same column in the periodic table, the atoms with larger atomic number are easier to ionize because the outermost shell is farther from the central nucleus. However, noble gases like xenon and krypton are very expensive. Therefore, argon was chosen to be the ionizing media in this experiment. A more detailed description of PWC gas system is given in Ref. [17].

Figure 2.6 shows the high voltage plateau curves for four different PWC modules. The purpose of this measurement is to determine the minimum operating voltage for each module. The method we used to determine the plateau curve is as follows: (1) Record data at various high voltage settings for the test module while leaving all the other modules with relatively high voltages. (2) Reconstruct tracks using the hits in each module, including the test module. (3) Loop all tracks and check if there were hits in the test module. Although this method is somewhat biased because of the hits in the test module participating in track reconstruction, our goal is to measure the “turn on” voltage rather than to measure the absolute chamber efficiency. About 2800 volts was the voltage we used in our 90-91 data. We used step 2 and step 3 to measure the efficiency in the garland region. Figure 2.7 shows the chamber efficiency perpendicular to the garland direction with and without garland high voltage [18]. We can see that the efficiency drops to 50% when the garland high voltage is off. The high voltage value used for the garland was 1500 volts.



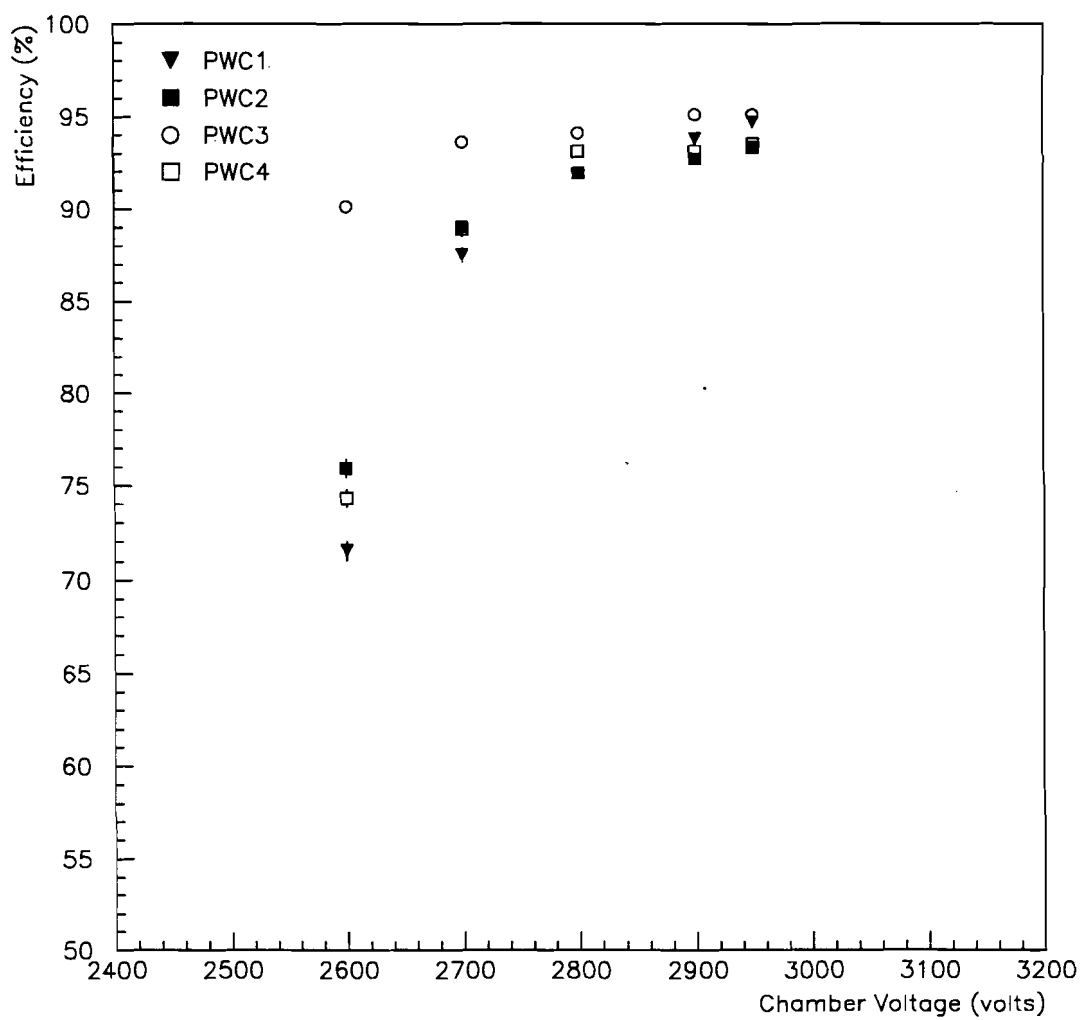


Figure 2.6: PWC Efficiency at several high voltages

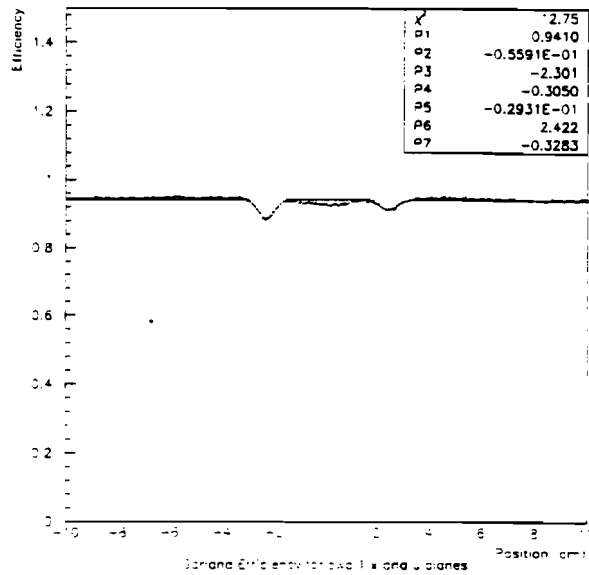
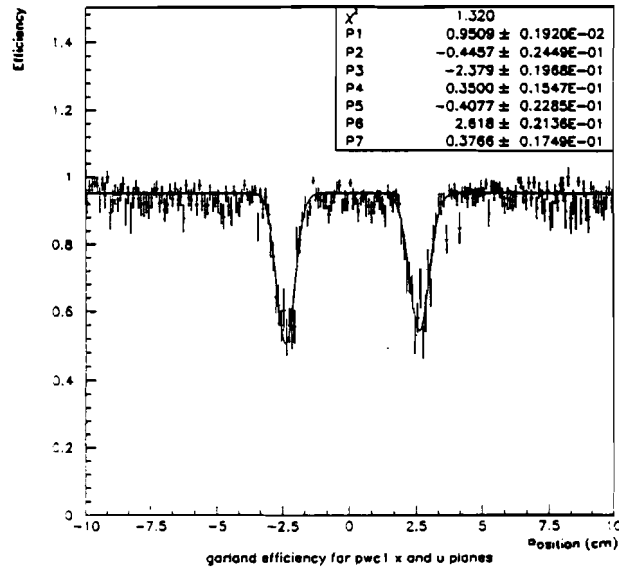


Figure 2.7: PWC Efficiency as a function of position. The top plot is without high voltage supply on the garlands. The bottom one is with 1500 volts supplied on the garlands.

### 2.3.4 Read Out Electronics for SSD and PWC

Signals from the SSDs were first amplified by the preamplifiers before being sent into nano discriminators, while signals from the PWCs went directly to these discriminators. The function of the preamplifiers is to enlarge the signals so that they can fire the nano discriminators since the SSD signals are very small. Beyond the preamplifier stage the readout system for SSD was identical with that for PWC. All the read out electronics except preamplifiers were produced by Nanometric System Inc.

Signals from PWC or SSD after the preamplifier stage were sent to N-277 amplifier and discriminator modules, which had 16 channels in each module with  $330\ \Omega$  input impedance. The threshold was set by an external DC voltage source. The signal above threshold was then transformed into a maximum width 45 ns ECL signal and was transmitted through a 50 ft long ribbon cable to a N-278 latch. The N-278 latches were able to delay signals by a pre-determined value and latch signals which were in coincidence with a 100 ns 'load' pulse generated by the pre-trigger logic. All the latched signals were loaded into 32 bit buffers in the N-278 card. The latched data were read out by N-280 crate controllers when the controllers received a 'read' pulse from the PDP-11 computers. Otherwise, the buffers were reset by a clear signal from trigger system. Each E-278 channel was assigned a wire address which corresponded to a PWC wire or a SSD strip. All the wire maps were loaded into N-280 controllers by a software program. Through these addresses, we were able to tell which wire or strip detected hits in the real events.

All the N-280 modules were serially connected to N-281 CAMAC interface modules. The data from N-280 modules were transmitted through N-281 modules via RS-422 lines. Eventually, the data in the N-281 interface were transferred into a PDP-11 computer and then the data were sent to a micro-vax computer in order to concatenate the data from other systems. Figure 2.8 illustrates the read out electronics for PWC and SSD.

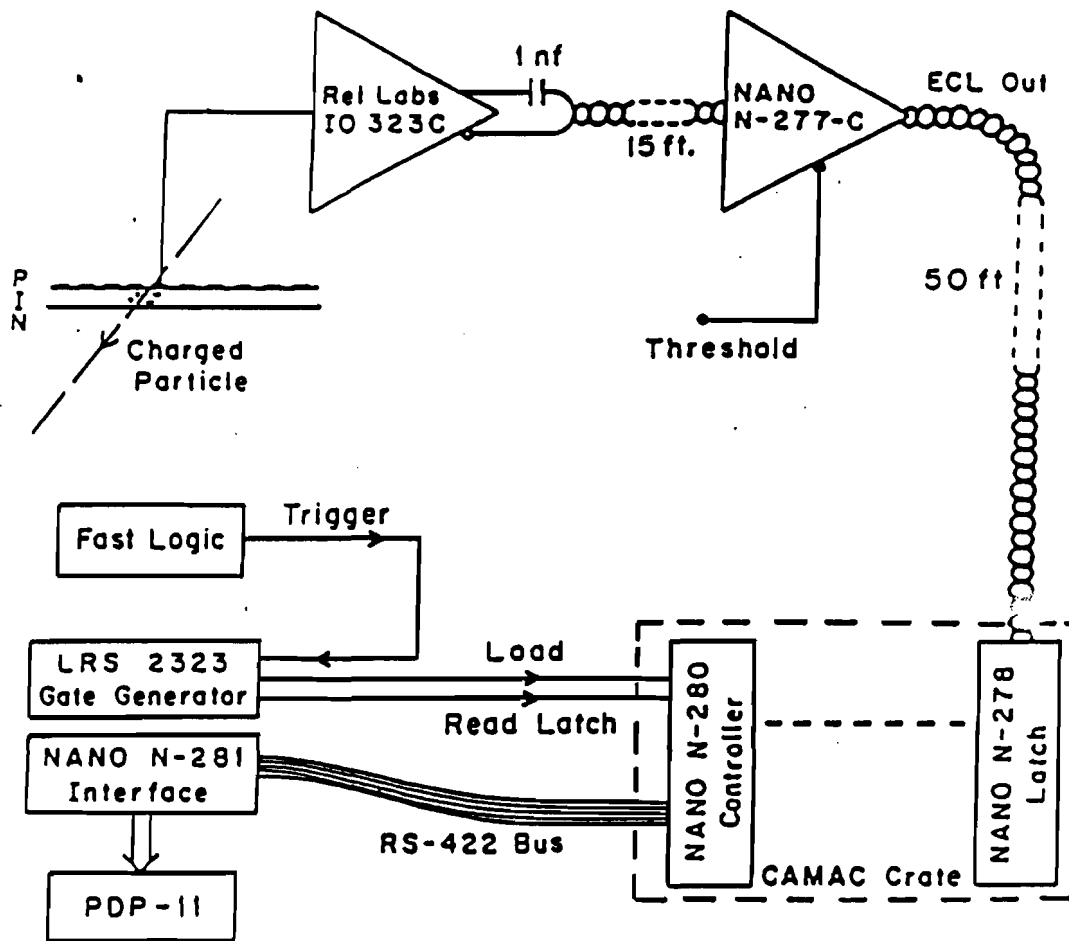


Figure 2.8: The Read Out System for PWC and SSD

### 2.3.5 Straw Chamber System

The 16 straw planes were added after 1988 run in order to reduce the ambiguity in linking downstream and upstream tracks at the center of the magnet and to improve the resolution of the measured momentum. There were two modules of straw chambers in the downstream tracking system. Each module contained 4-X planes and 4-Y planes. The first module was located between PWC module 1 and module 2 and the second module was between PWC module 4 and the calorimetry. Table 2.3.5 shows the numbers and the sizes of the tubes in each plane.

Table 2.4: Straw Tubes Parameters

Module	Number of Tubes	Length of Tubes	Diameter of Tubes
1x (4 planes)	160*4	1.67 m	10.4 mm
1y (4 planes)	128*4	1.26 m	10.4 mm
2x (4 planes)	160*4	2.80 m	15.9 mm
2y (4 planes)	160*4	2.80 m	15.9 mm

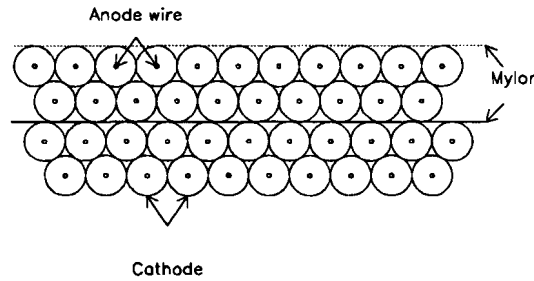
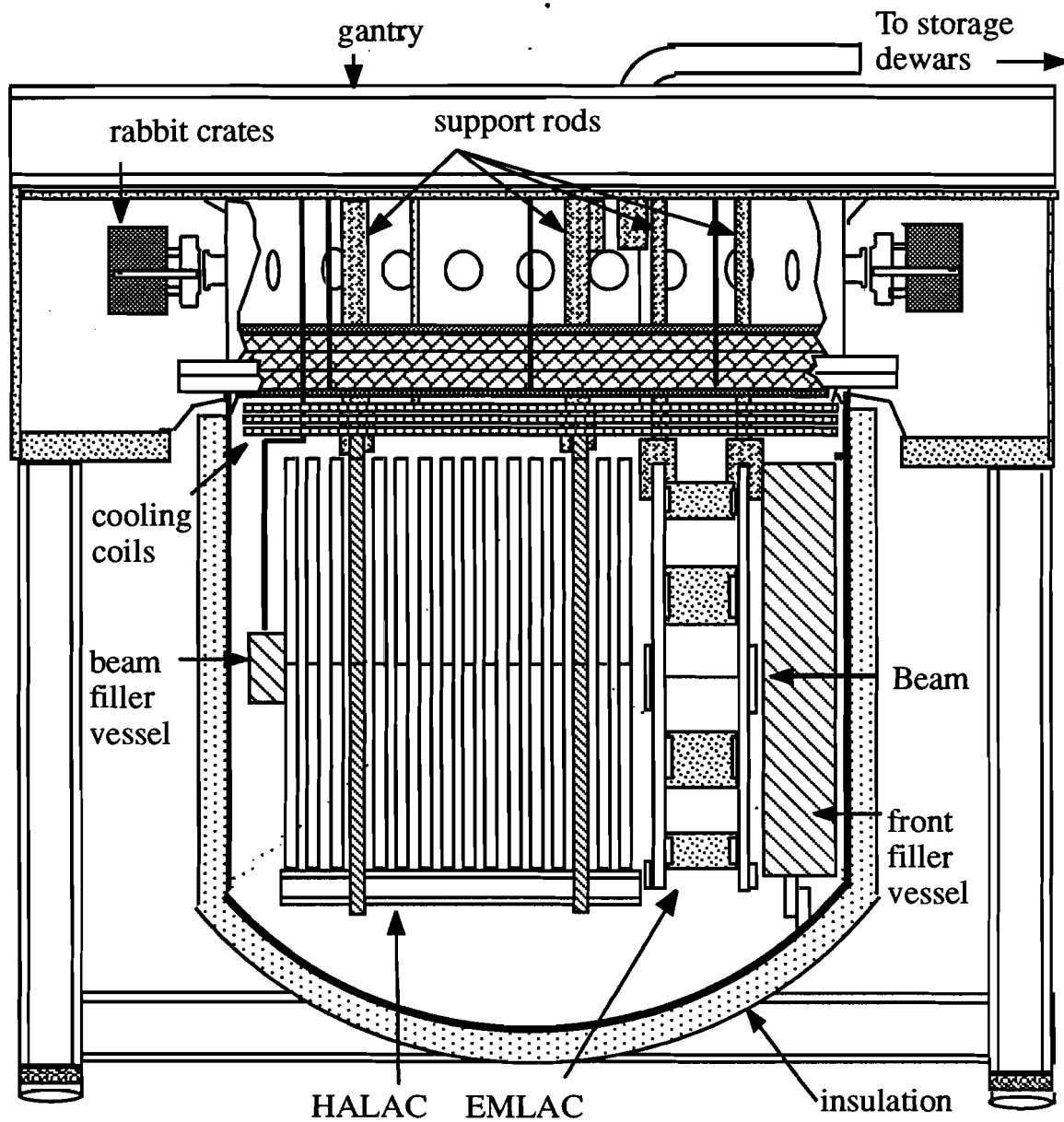


Figure 2.9: A bundle of straw tubes.

The straws were made from two spiral wrapped layers of 0.003 inches mylar. 0.0003 inches of aluminum was coated on the inner surface of the inner layer. The straws were glued together into bundles. There were 16 straw tubes glued in each bundle of module 1, and 10 to 11 tubes in each bundle of module 2. Figure 2.9 shows the geometry of straw tubes in a bundle. After checking the straightness of each bundle and cleaning the interior of each straw tube, all bundles in straw 2 were mounted on an aluminum c-channel frame in each module, while the bundles in straw 1 were simply glued together. The anode wire was made from 20  $\mu\text{m}$  diameter gold plated tungsten wire with a tension of 50 gm. Each anode wire was connected to a high voltage supply, which was 1800 volts for straw 1 and 1700 volts for straw 2. A gas mixture of 50% Argon and 50% Ethane, bubbled through ethyl alcohol at 0°, was used as an ionizing medium. The N-277 readout-discriminator cards were mounted on the chambers and the signals above threshold were transferred to Time-to-Digital Converters (TDCs) via 50 (75) ft long ribbon cables for straw 1 (2). These TDCs were capable of latching the drift time of the straw signals and the outputs were read out through a FASTBUS based system. The construction details for the straw chambers are given in [19].

## 2.4 Liquid Argon Calorimeter

The liquid argon calorimeter, situated downstream of straw chamber 2, plays a central role of this experiment. The purpose of this calorimeter is to detect photons, electrons, neutral and charged hadrons as well as select events which contain high  $P_T$  electromagnetic showers. The calorimeter was composed of two parts: the electromagnetic calorimeter (EMLAC) and the hadron calorimeter (HALAC). They both resided in the same cryostat and used argon as the ionizing medium. In the EMLAC, we used lead as the absorbing material while in HALAC steel plates were chosen. Figure 2.10 shows the layout of the calorimeter in the gantry supporting system. A more detailed description of the design criteria, the cryogenic system, and



Cut View of the LAC

Figure 2.10: The gantry and cryostat of the LAC

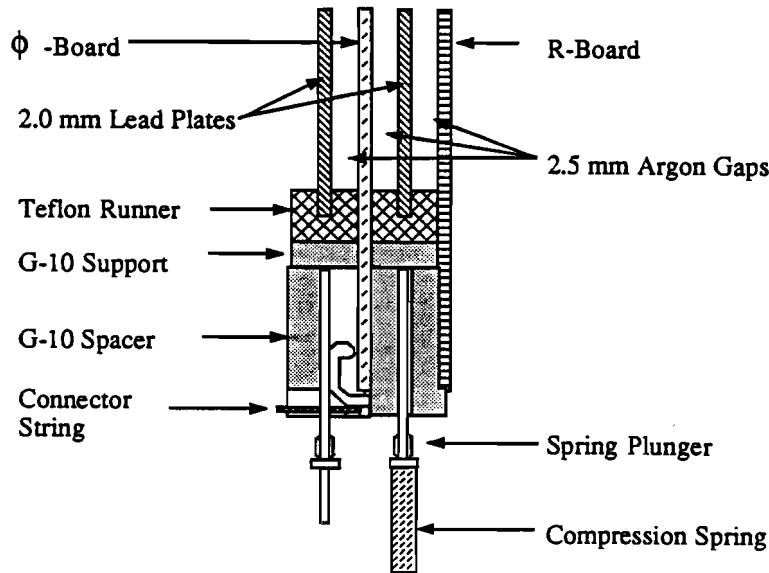


Figure 2.11: A side view of single EMLAC layer.

the construction can be found in Ref. [20].

### 2.4.1 The Electromagnetic Calorimeter

The electromagnetic calorimeter was constructed in four mechanically independent quadrants, each of which contained 33 r signal layers interleaved with 33  $\phi$  signal layers. A 2 mm lead plate was placed in between each r and  $\phi$  pair. The r and  $\phi$  layers were composed of 1.6 mm copper clad G-10 anode boards, which were double sided. The lead plate and each r or  $\phi$  layer were separated by a 2.5 mm liquid argon gap. The relative positions of the r and  $\phi$  layers are illustrated in Fig. 2.11.

When an electron or a photon penetrates through the EMLAC, it first interact with the lead plates to bremsstrahlung photons. These photons then convert to electron pairs via the lead plates. These bremsstrahlung electrons with low energy are



absorbed by lead while the energetic electrons move forward and ionize argon. Therefore, more electrons are produced through ionization. Electrons from ionization, usually low energy, move towards the  $r$  and  $\phi$  boards due to the voltage difference between the lead plates and the anode boards. During this driving path, more electrons in the lead and argon atoms are excited. The EM detector generates a large number of electrons which cause a voltage difference, due to the accumulated charge. The higher the energy of the incident particle, the more electrons are produced. As a result, the accumulated charge is a measure of the energies of photons and electrons, after calibrating the LAC. When electrons reach the anode planes, they will suppress the applied electric field and change the drift characteristics. Two  $1.0 \mu\text{F}$  capacitors were added in connection with each lead plate. These capacitors served as reservoirs of charge to compensate the field suppression.

The EMLAC was divided into two sections: the front section containing the first 11 cells ( $r$  and  $\phi$  layers) and the back section containing the last 22 cells. Since the output wires of each  $r/\phi$  layer in the same  $r/\phi$  position at the front or back section were electronically connected together, we were able to measure the energies in  $r$  and  $\phi$  views of the front and the back sections. There were 254 concentric radial strips in each octant of the front section and 240 strips in the back section. The width of the  $r$  strips in each layers increased as the distance between the target and the layer increased. (That is why we had fewer strips in the back section.) As to the  $\phi$  view, we subdivided the strips into inner and outer segments. In the inner section of each quadrant, there were 92 strips, each subtending  $16.36 \text{ mrad}$  in azimuth; in the outer section, there were 192 strips, each subtending  $8.18 \text{ mrad}$  in azimuth. The inner and outer boundary was about  $56 \text{ mrad}$  in polar angle from the target or about  $40 \text{ cm}$  in the  $r$  position at front of the LAC. The inner-outer  $\phi$  split was intended to improve the energy and position resolutions at large radii. There were 6272 readout channels in the EMLAC. Figure 2.12 displays the exploded view of the EMLAC. The central hole region, radius  $20 \text{ cm}$ , was designed to minimize interactions of the beam and the

detector.

## 2.4.2 The Hadron Calorimeter

The hadron calorimeter, located downstream of the EMLAC, was designed to detect the positions and energies of neutral and charged hadrons. The HALAC had a tower read out structure. There were 53 equilateral triangle pads connected in  $z$  direction for each tower (each channel). The pad size changed with the detector depth to focus on the target. The total number of HALAC channels was 2368.

The HALAC consisted of 53 2.5 cm thick steel absorber plates interleaved with readout cells named cookies. Each cookie was made up of 7 layers, including two high voltage planes interleaved with 3.2 mm G-10 strips, two readout boards, and a support G-10 ribs. Figure 2.13 displays an exploded view of a single cookie. The high voltage planes were made up of 0.08 cm thick G-10, copper clad on both sides, with the inner side held the high voltage and the outer side grounded. After the first high voltage plane there was the first readout board, which was made of 0.08 cm thick G-10. The readout plane contained alternate rows of equilateral triangle pads read out at the edges (see Fig. 2.14). The second readout board, glued to the first one with support ribs in between the two, had a similar structure but read out the pads in different rows. Right after the second readout board was the second high voltage plane. G-10 strips were installed between the first/second high voltage plane and the the first/second readout board in order to obtain constant 0.32 cm gaps between readout pads and high voltage boards. These strips also gave rigidity to the detector planes.

The HALAC was, like the EMLAC, longitudinally divided into two sections, the front section and the back section. The front section contained 14 cookies and 13 steel plates while the back section contained the rest. The height of the hadron pad increased from 10.9 cm in the front section to 13.3 cm in the last readout board in the back section. The pads corresponding to the same X and Y positions in

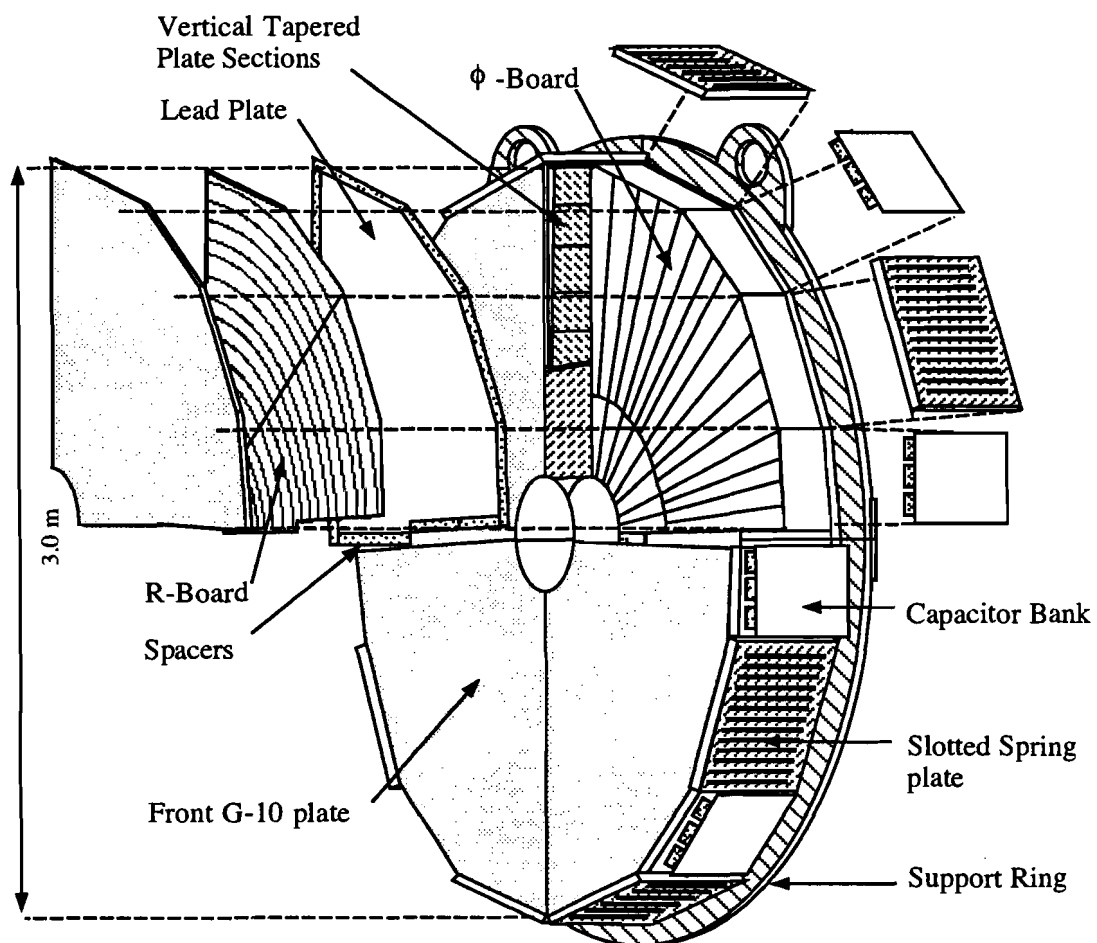


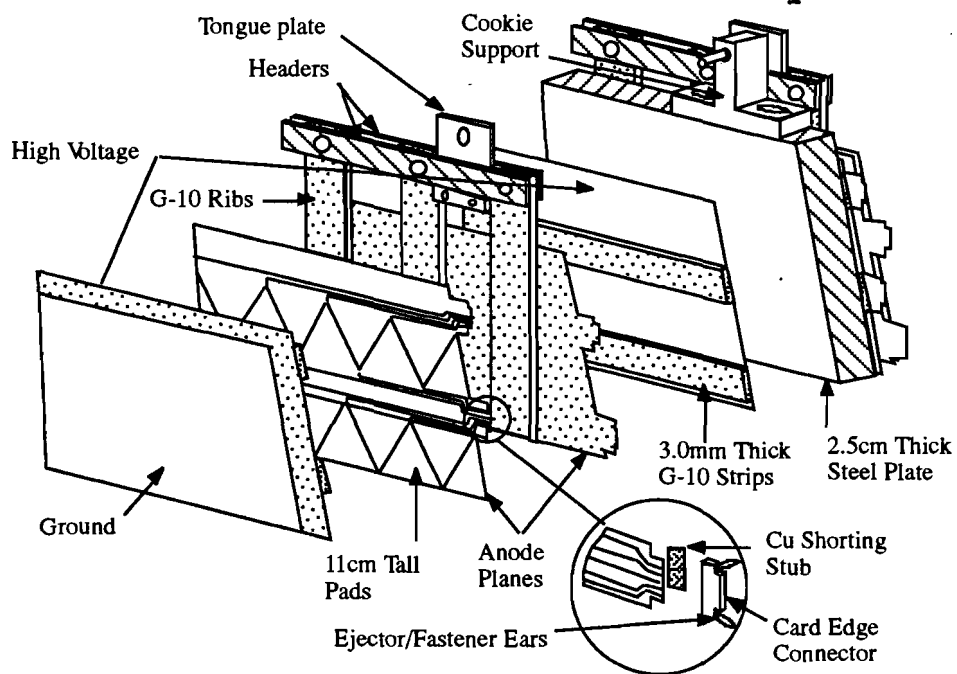
Figure 2.12: Exploded view of the electromagnetic calorimeter

the same section were connected together. Therefore, the positions and energies of hadrons were read out separately in the front and back sections. Reference [22] gives a detailed description of the hardware construction.

## 2.5 Forward Calorimeter

The forward calorimeter (FCAL), located downstream of the LAC at about 17 m from the target, was designed to measure the energy and the  $P_T$  of the beam jets which were not detected by the LAC or the charged tracking system. The FCAL was composed of three identical modules, each of which had 28 circular steel absorber plates. Each absorber was 114 cm large in diameter and 1.9 cm thick. 29 plexipop scintillator sheets were sandwiched between the plates. Each sheet was 4.6 mm thick. A 3.18 cm diameter beam hole was drilled through the center of each plate and sheet. Figure 2.15 shows an expanded view of the FCAL.

Each plate and sheet had a grid of 1 cm diameter holes drilled in them to accommodate the 86.4 cm long wave shifter bars. There were 76 holes on an 11 cm grid. The wave shifter bars were doped with BBQ, an organic dye, which converted ultraviolet light into green light. A phototube was attached at one end of each bar. When hadrons passed through the absorber and scintillator, the light produced was collected by the closest wave shifter rod and was transmitted to its phototube. The phototubes were readout via a flash ADC system. Each ADC continuously digitized at the rate of 80 MHz. The resulting data were stored in a ring buffer in 64 time slices. When a trigger was sent, it caused the digitizing clock to stop and the entire 2.56  $\mu$ s history was read for 15 channels around the interacting time slice. The signal was proportional to the energy deposited. Therefore, we were able to measure the total energy in the FCAL. A more detail discussion can be found in Reference [23].



Exploded View of a HALAC Cell

Figure 2.13: An exploded view of a cookie.

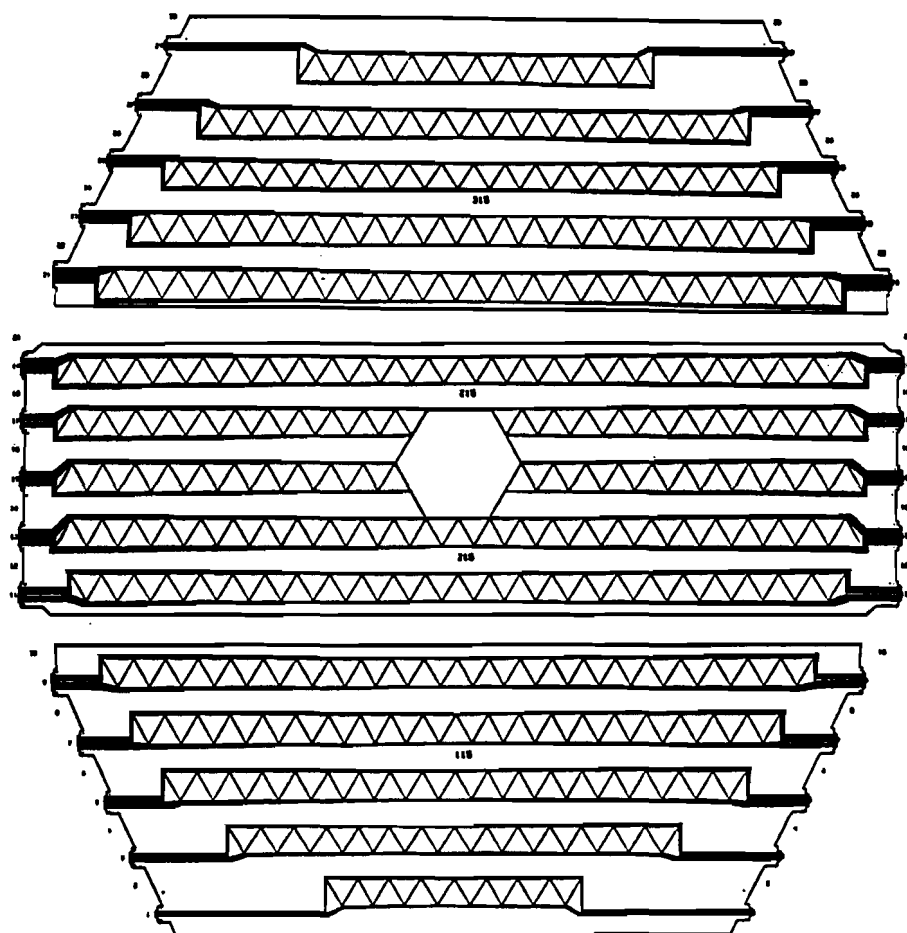


Figure 2.14: The first readout board of a HALAC readout pair of boards. Each triangle pad was read out on the edges. The second readout board of the pair had the same design as the first one, but was read out in alternate rows which did not have a triangle pad in the first readout board of the pair.

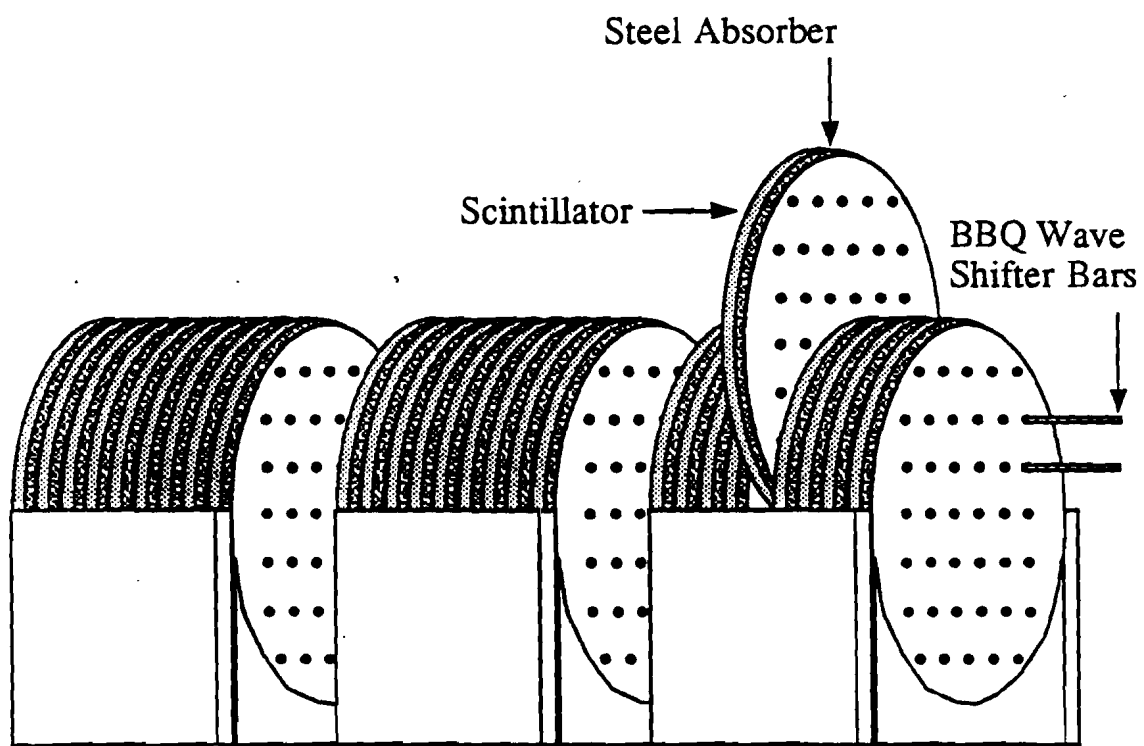


Figure 2.15: The Forward Calorimeter

# Chapter 3

## Data Acquisition and Trigger

This chapter describes the data acquisition system and trigger logic in this experiment. Since this thesis analyzes the data of two different triggers, SINGLE LOCAL HIGH and TWO GAMMA triggers, their trigger design, performance, and the corresponding corrections are discussed separately. The detailed description of the hardware and software designs of the whole DA system is given elsewhere[21][24]. A brief introduction to the E706 DA is presented in this chapter.

### 3.1 Overview of DA

The E706 data acquisition system was rather complex. It was set up to merge the data from different detectors into one output stream, to run and test each apparatus, and to allow non-experts to operate the system. At the top level of the DA system was a  $\mu$ VAX, which was used as a control and event writing machine. Directly under the  $\mu$ VAX were three PDP-11 minicomputers and one fastbus system, each of which controlled the I/O of data from its corresponding devices (see Table 3.1). Figure 3.1 illustrates the entire DA architecture.

The  $\mu$ VAX ran a multilevel program named VAXONLINE, Fermilab's on-line data acquisition package. VAXONLINE, which played a central role of the DA system, consisted of four parts: Global Menu, Event Builder, Output, and Run Control. Global Menu, as its title suggests, displayed the available functions of VAXONLINE and directed the user to other attached process. Event Builder was responsible for



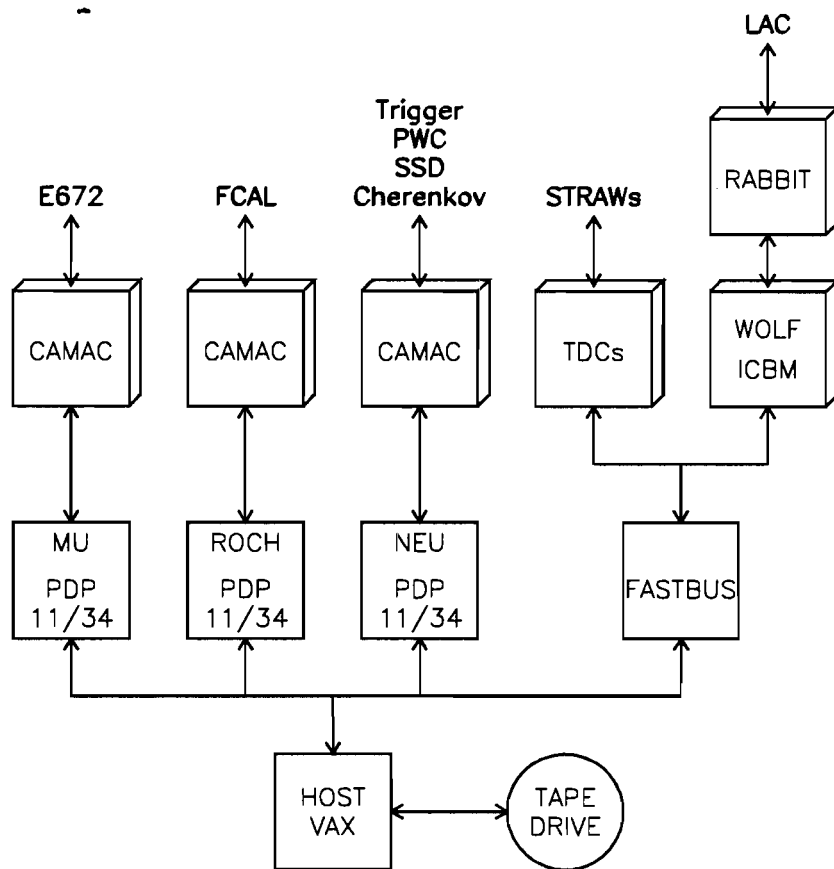


Figure 3.1: The E706 data acquisition system.

DA subsystem	The Corresponding Devices
FASTBUS	LAC and Straw Chambers
PDP NEU	SSD's, PWC's, Trigger
PDP ROCH	FCAL
PDP MU	E672 Muon Chambers

Table 3.1: The DA subsystems which read out the data of their corresponding detectors.

the concatenation of the event fragments delivered by the various DA subsystem. It first whether the event headers for different subsystem were consistent. Once Event Builder confirmed that the data from different apparatus were from the same event, it concatenated data from all sources into one big record. It also wrote its own header for each event. Output took the events from staging pool and wrote them to the specified media, which could be disks, 9 track tape, 8mm cassette, or null. Run Control, a user interface, managed the above processes and initiated the begin run tasks.

A fraction of events was sent to a DEC VAX 780 computer, where the consumer program was running to monitor the apparatus. For example, PLMON, a plane monitoring package, displayed the number of hits per tracking plane and the raw TDC time for straw chamber. The trigger monitor showed the number of events in each trigger per spill. A scaler monitor displayed all the scalers which were read out between spills so that people could calculate the event yields on line. GRREC, the E706 event display package, displayed all the raw tracking hits and the reconstructed results for the entire spectrometers (silicon strip planes, wire chambers, straw tubes, and three calorimeters). GRREC, using DI3000 graphics interface, could help users debug the reconstruction code and test the tracking algorithm as well as monitor the status of spectrometer elements. EMBANK displayed the energy in each LAC strip and listed the energy of each photon in  $r$  and  $\phi$  views.

Occasionally in the beginning of each shift (about 8 hours), a cold start task was initiated for the tracking planes (SSC and PWC) and the LAC (EM and HA). The plane's cold start downloaded the wire map into the Nanometric latches. It

could check the wire addresses and displayed the diagnosis of the electronics for each channel. Therefore, we would be able to know which nano latches or nano cards needed to be replaced. The LAC cold start was to record pedestals for individual ADC channels and to measure the gains of the LAC amplifiers. The pedestal task used a software trigger to sample the signal in each channel. Each channel was digitized 128 times and the averaged value of ADC counts (units of energy) was stored. The gain task injected charges on each channel. The measured results were then digitized and stored. From the magnitude of injected charges and the measured value, gains for each amplifier was determined. This process was repeated 32 times and the average value of gains was recorded. A complete description the LAC readout system and their associated electronics is given in reference [25] and [21].

## 3.2 Trigger

The trigger system selected the rare high  $P_T$  events. In the following sections, a simple discussion of the trigger system is given. The trigger type includes Beam, Interaction, Pretrigger, Single Local High, Single Local Low, Two Gamma, Global Low, Global High, and Di-Muon. Most of the triggers were controlled by the NEU PDP. The loading of the trigger parameters such as time delays, prescale factors, and trigger types were operated through Run Control in DA.

The E706 trigger consisted of two parts: the pretrigger and LAC triggers. A description of di-muon trigger can be found in reference [26]. The time needed to form the final trigger was about 800 ns per event in this experiment. This was much longer than the available delay time for the tracking detectors to latch signals. Therefore, a pretrigger was necessary to force the tracking system to hold the information temporarily, while a trigger decision was being made. Besides, the pretrigger provided a tighter constrain on the timing of signals reaching the LAC to prevent firing on the out-of-time interactions (see section 3.3.2). When a pretrigger signal was sent, the hit locations of SSD and PWC as well as the TDCs of straw chambers were latched

and the before signal was sent to the LAC BATS to sample the LAC showers. The trigger system then decided if this event was to be recorded. After the final decision was made, a clear signal was issued so that all apparatus were ready for next event.

### 3.2.1 Beam and Interaction Definition

Before we describe the pretrigger and the LAC trigger, the definitions of "Beam1" and "INT" must be introduced first. Figure 3.2 shows the locations of the scintillation counters used in the trigger system. Right after the veto walls were three beam hodoscopes (BX, BY, and BU) and a beam hole counter, BH. The interaction counters, SE1, SE2, SW1, and SW2, were located before and after the dipole magnet. When the beam was delivered from the accelerator, the accelerator control sent out the signals to indicate the beginning and the end of beam spills. These signals were used to generate a BMGATE signal. Each spill was around 23 ns in duration. The RF\_CLOCK was a pulser sent out by the accelerator control to simulate the beam structure. The accelerator control was running at a frequency of 53 MHz to produce 19 ns wide time bucket in phase with the accelerator. The informations of veto walls, beam hodoscopes, beam hole counter, and interaction counters were latched by the Minnesota latches which sent out the latched information in 15 time buckets. The trigger BEAM1 was defined as

$$BEAM1 = BMGATE \otimes (BX \otimes BY \oplus BY \otimes BU \oplus BU \otimes BX) \\ \otimes RF\_CLOCK.$$

In other words, a BEAM1 signal required that at least two beam hodoscope elements had signals in the same time bucket while the BMGATE was on.

The interaction signal, *INT* required that at least two interaction counters fired in the same time bucket in coincidence with *BEAM1*. To minimize confusion in the detectors, a clean (*CLN*) signal was checked afterwards, where

$$CLN = CLEAN\_EARLY \otimes CLEAN\_LATE.$$

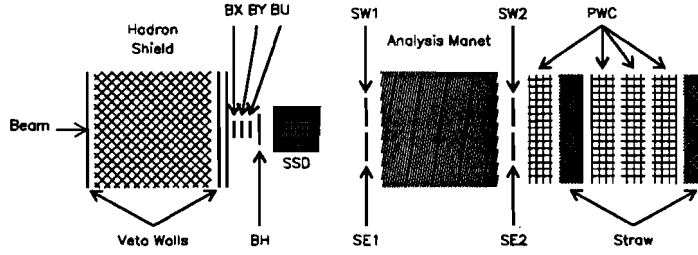


Figure 3.2: Layout of counters in the trigger system.

CLEAN\_EARLY meant that there were no interactions in the previous 3 time buckets of the in-time bucket, while CLEAN\_LATE indicated the same thing for following 3 time buckets. When an event was accepted, our computer issued a busy signal which it maintained until the information from all the subsystem was read out. Once this process was completed, a computer ready signal (*CMPRDY*) was issued and the system was ready for the next event. The final live interaction definition was

$$LIVE\_INT = INT \otimes \overline{BH} \otimes CMPRDY \otimes CLN.$$

The  $\overline{BH}$  was required to identify the beam particle as not a beam halo particle.

### 3.2.2 The Pretrigger

A pretrigger was set up to rapidly reject low  $P_T$  events. The trigger  $P_T$  was calculated from the sum of the weighted energies per octant in the radial strips of the

EMLAC. It could be mathematically expressed as follows:

$$\begin{aligned}
 P_t(\text{trigger}) &= \frac{2}{Z_{lac}} \sum_i E_i r_i \\
 &= \sum_i (P_T)_i.
 \end{aligned}
 \tag{3.1}$$

The factor 2 in equation 3.1 came from the assumption that only half of the energy was deposited in the  $r$  view strips.  $Z_{lac}$  represented the  $z$  distance between the front face of the LAC and the center of target, while "i" was the  $i$ 'th strip and "r" was its radial position in the LAC. In hardware, a  $P_T$  card determined the  $P_T$  for each strip and added the  $P_T$  of 8 strips together to produce "sum-of-8"  $P_T$ . There were 32 sum-of-8 modules per octant. The sum-of-8 signals were then sent to the  $P_T$  adding card to form Trigger  $P_T$ . We divided each octant into two parts: inner octant and outer octant, each of which contained 16 sum-of-8 modules. Figure 3.3 displays the operations of  $P_T$  summing module. The final trigger  $P_T$  signal for each half octant was sent to a zero-crossing timing discriminator to check its timing with the beam and interaction signals. The zero-crossing timing discriminator operated by first copying the original  $P_T$  signal, delaying and inverting the copy, then adding the original one with the copy to give a zero crossing time. If the original signal at this zero crossing time was above the threshold, a 120 ns wide ECL pulse was generated. The zero crossing time is relatively insensitive to the original pulse shape or energy. It thus provides a more s timing reference than the one issued by a time-over-threshold discriminator.

The other signals used to determine the pretrigger were EARLYPT, SCRKILL and the veto wall information. If there were events occurring within 300 ns of the current event and the global  $P_T$  in an octant was above 1.5 GeV/c, an EARLYPT signal was generated. The SCRKILL signal indicated the presence of coherent noise from the 400 Hz low voltage supplies of the LAC amplifiers. Although the noise in each amplifier was small, the sum of coherent noises would mimic a LAC signal and cause a pretrigger. The SCRKILL signal could thus inhibit this fake signal. Veto walls were set up to tag halo muons which could be misidentified as high  $P_T$  photons.

If the upstream veto wall fired in coincidence with one or two downstream veto walls at the same quadrant, we claimed that veto walls fired. This logic can be written as:

$$VETO\_WALL = (VETO\_WALL1 \oplus VETO\_WALL2) \otimes VETO\_WALL3.$$

The final pretrigger definition was

$$PRETRIGGER = \overline{VETO\_WALL} \otimes \overline{SCRKILL} \otimes \overline{EARLYPT} \otimes LIVE\_INT1 \\ \otimes LAC.$$

LAC indicated whether the trigger  $P_T$  of either an inner octant or outer octant was above some threshold values, about 1.5 GeV/c and 0.8 GeV/c for 1990 data. The higher value was used for Single Local High, Global High, and Global Low triggers, while the lower value was for Two Gamma and Single Local Low triggers.

### 3.2.3 The Lac Triggers

With the pretrigger satisfied, different octant signals were used in the event selection. There were three definitions of  $P_T$  in the LAC triggers: local  $P_T$ , 1/2 global  $P_T$ , and global  $P_T$ . The local and global triggers had low and high thresholds associated with them. Local  $P_T$  corresponded to the  $P_T$  detected in two adjacent sum-of-8 modules (16 channels) in an octant. Global  $P_T$  was the total trigger  $P_T$  in an octant. Half global  $P_T$  had the same definition used in the pretrigger ( $P_T$  sum of inner or outer 16 sum-of-8 modules). Different LAC triggers had different criteria and they were defined as follows:

- **LOCAL•GLOBAL\_HIGH**: the global  $P_T$  exceeds the global high threshold and the local  $P_T$  is above the local low threshold in the same octant;
- **LOCAL•GLOBAL\_LOW**: the global  $P_T$  exceeds the global low threshold and the local  $P_T$  is above the local low threshold in the same octant;
- **LOCAL•HALF GLOBAL\_HIGH**: the global  $P_T$ , either in the inner half octant or in the outer half octant, exceeds the global high threshold and the local  $P_T$  is above the local low threshold in the same half octant;

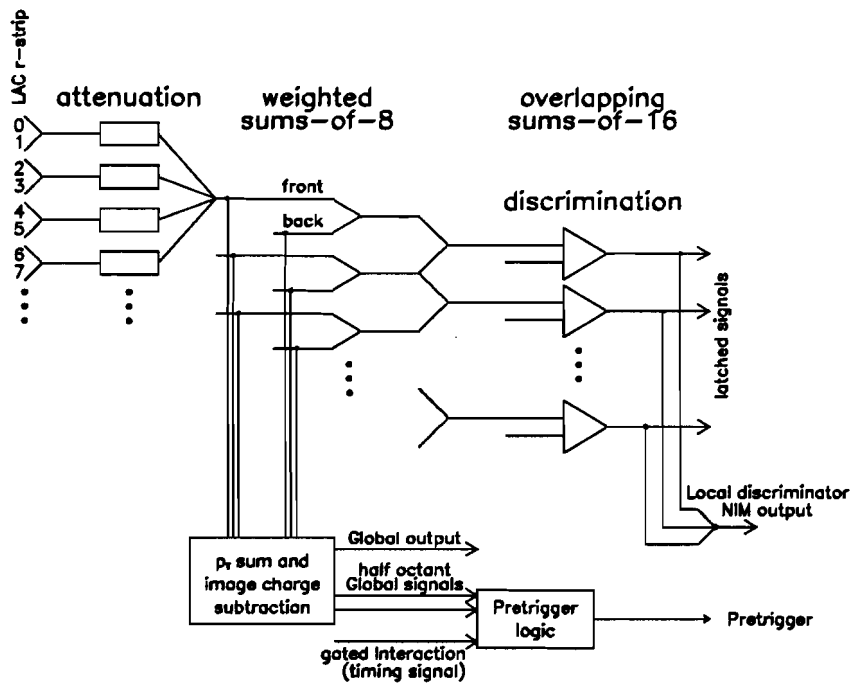


Figure 3.3: The E706  $P_T$  Summing Module



Table 3.2: The statistics of different trigger sets for 1990 Data

Trigger Set	Run Number Range	Number of Events	Data Taking period
1	9181-9434	5,904,433	8/14 - 8/27
2	8989-9180	4,051,049	8/3 - 8/14
3	8629-8988	5,839,137	7/18 - 8/3
4	8240-8628	3,931,743	7/1 - 7/18
5	8055-8239	2,864,491	6/23 - 7/1
6	7594-8054	4,966,478	6/5 - 6/23

- **LOCAL•HALF GLOBAL LOW:** the global  $P_T$ , either in the inner half octant or in the outer half octant, exceeds global low threshold and the local  $P_T$  is above local low threshold in the same half octant;
- **SINGLE LOCAL HIGH:** the local  $P_T$  exceeds the local high threshold;
- **SINGLE LOCAL LOW:** the local  $P_T$  exceeds the local low threshold;
- **TWO GAMMA:** there are at least two distinct octants which satisfy the single local low requirement and the octant pair must be separated from each other by at least two octants.

### 3.3 The SINGLE LOCAL HIGH Trigger

The SINGLE LOCAL HIGH trigger was implemented to detect high  $P_T$  photons which generated local showers in the EMLAC. It aimed to select direct photons and high  $P_T$   $\pi^0$ 's and  $\eta$ 's. During the 1990 run, the SINGLE LOCAL HIGH and the TWO GAMMA triggers performed rather well. Almost every octant was active in each trigger set. Trigger sets were defined by trigger threshold changes or trigger hardware changes. Therefore, the trigger turn-on curves were assumed unchanged during the same trigger set period. There were six different trigger sets analyzed in this thesis. Table 3.2 shows all the trigger sets, run number range, number of events, and corresponding data taking time.

The SINGLE LOCAL HIGH trigger required the pretrigger high fired. When the zero-crossing time discriminator generated a 120 ns wide ECL pulse, this pulse

was first delayed and stored in order to check if the signals of veto walls, SCRKILL, and EARLYPT were within this 120 ns pulse. Therefore, the pretrigger not only distinguished the amplitude of the trigger  $P_T$  signal, but also checked its timing. The standard pretrigger turn-on curves are shown in Fig. 3.4. These turn-on curves were determined with respect to trigger  $P_T$  and reconstructed  $P_T$  ( $\pi^0$  PT). In this thesis, the reconstructed  $P_T$  of  $\pi^0$ 's used in the SINGLE LOCAL HIGH triggers exceeds 4 GeV/c; hence, the corresponding correction for the pretrigger high efficiency is negligible.

### 3.3.1 Trigger Weight

Since the SINGLE LOCAL HIGH trigger was determined on an octant by octant basis, the turn-on probability depended not only on a single photon in a given octant, but also on the other photons (showers) in that octant. Each octant contained a local trigger discriminator card which checked 31 sum-of-8 pairs/footnote There are 32 sum-of-8  $P_T$  card in an octant, which has 31 combinations of two adjacent sum-of-8 modules. If the turn-on characteristics for each sum-of-8 pair is known, the trigger probability for each octant can be calculated from these turn-on curves, assuming linear superposition. The following procedure was used to measure the turn-on curves of sum-of-8 pairs (sections).

- Book two histograms in  $P_T$  bins for each section;
- For each trigger set, select the events in which the SINGLE LOCAL HIGH or the TWO GAMMA fired;
- Choose the appropriate octants to investigate: the triggering octants of the TWO GAMMA triggers and the opposite 3 octants of the triggering octant in the SINGLE LOCAL HIGH triggers;
- Calculate the trigger  $P_T$  for each of the 31 sections in the selected octant;
- Examine the Nanometric trigger banks to see which sections fired;

Table 3.3: The twelve combinations of the TWO GAMMA trigger

Directly Opposite	1-5	2-6	3-7	4-8
Adjacent-Opposite	1-4	1-6	2-5	2-7
	3-6	3-8	4-7	5-8

- Increment the first histogram (the denominator histogram) by 1 for each section and do the same thing in the second histogram (the numerator histogram) only for those sections which fired.

The ratio of the numerator histogram and the denominator histogram gives the turn-on curve. Figure 3.5 shows the turn-on curves of four sections in a typical octant. The fitted function in the plots is

$$\begin{aligned} \text{erf}(x) &= \frac{2}{\pi} \int_0^x e^{-t^2} dt \\ x &= \frac{\tau}{\sigma} \end{aligned}$$

where  $\tau$  is the threshold, 50% point, and  $\sigma$  is the gaussian width. The trigger probability,  $P_i$ , of the  $i$ 'th section can be calculated from the fitted function and the trigger  $P_T$ . Therefore, the octant trigger probability can be derived from the probability sum of the trigger probability in the 31 sections. We can write it as

$$P_{\text{octant}} = 1 - [\prod_{i=1}^{31} (1 - P_i)]. \quad (3.2)$$

### 3.4 The TWO GAMMA Trigger

The TWO GAMMA trigger was designed to select the events which had at least two high  $P_T$  electromagnetic showers in nearly opposite octants. This trigger aims to study double direct photons, high mass  $\pi^0$  pairs, and heavy mesons which decay

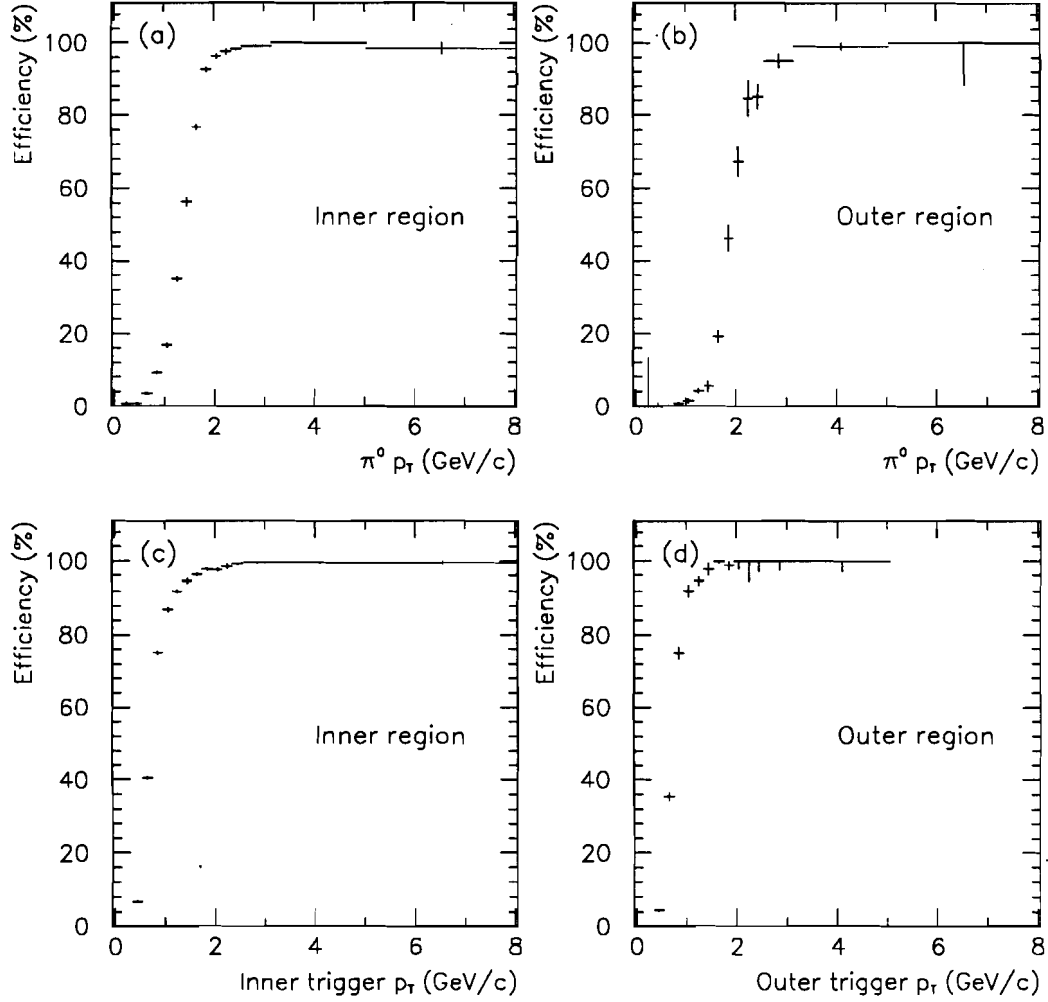


Figure 3.4: The Pretrigger High Turn-on Curves. (a) Turn-on efficiency versus  $\pi^0 P_T$  in inner region, (b) Turn-on efficiency versus  $\pi^0 P_T$  in outer region, (c) Turn-on efficiency versus trigger  $P_T$  in inner region, (d) Turn-on efficiency versus trigger  $P_T$  in outer region.

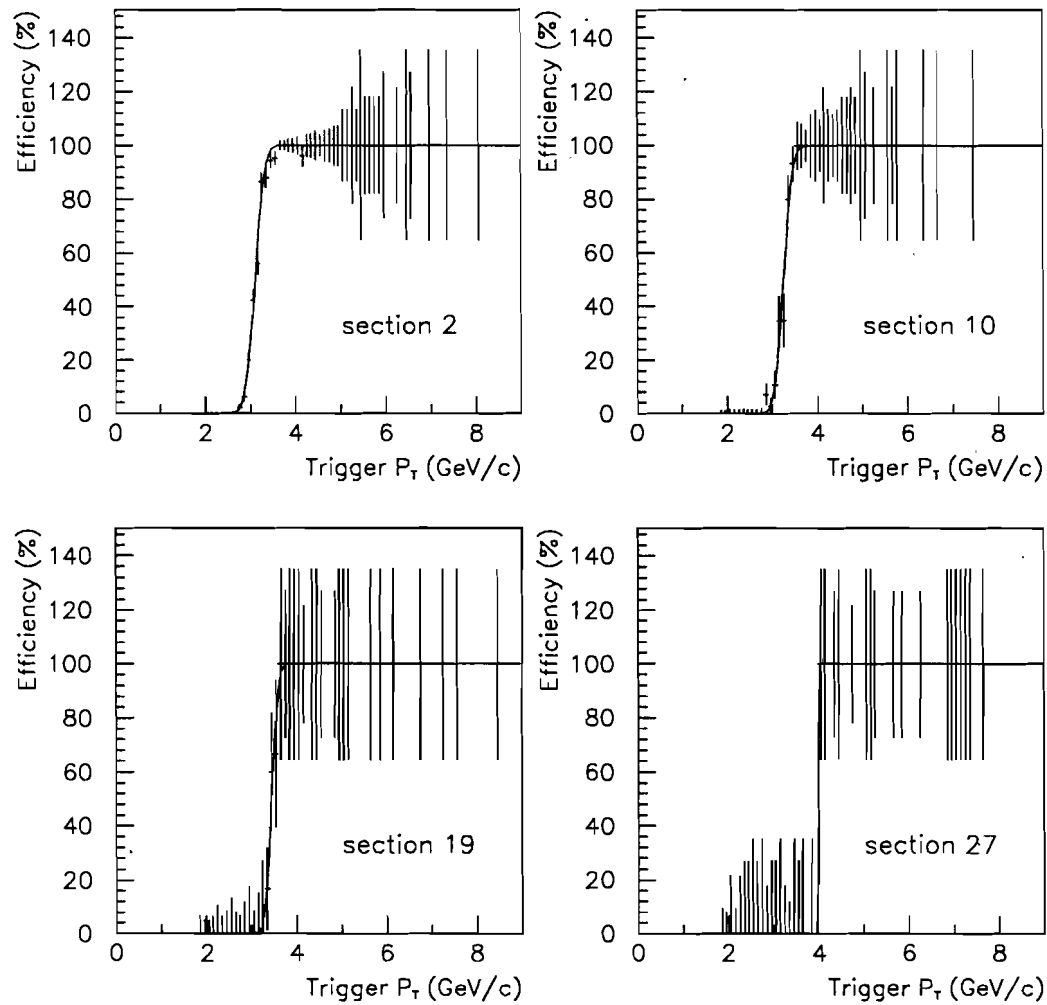


Figure 3.5: The Single Local High turn-on curves of four different regions in a typical octant. Smaller section numbers correspond to sum-of-8 pairs with smaller radial locations.

to electron-positron pairs. There are twelve different octant combinations selected by the TWO GAMMA trigger, as listed in Table 3.3.

The TWO GAMMA triggers required that the pretrigger low and two SINGLE LOCAL LOW triggers fired. The threshold of pretrigger low was below the minimum  $P_T$  of  $\pi^0$ 's used in this analysis (see Fig. 3.6). The corresponding correction is thus negligible. The SINGLE LOCAL HIGH triggers and the SINGLE LOCAL LOW triggers were almost identical except that their thresholds were different. The method employed to measure the local high turn-on curves was also applied to study the turn-on characteristics of the local low triggers. In order to choose unbiased samples, the data from the TWO GAMMA triggers were excluded in this study. Figure 3.7 shows the turn-on curves of four different sections in an octant. These turn-on curves are again very sharp, indicating that reconstructed trigger  $P_T$  was very close to what trigger hardware saw. Equation 3.2 was also used to determine the trigger probability of a given octant. The product of two local low trigger probabilities gave the trigger probability for the TWO GAMMA triggers.

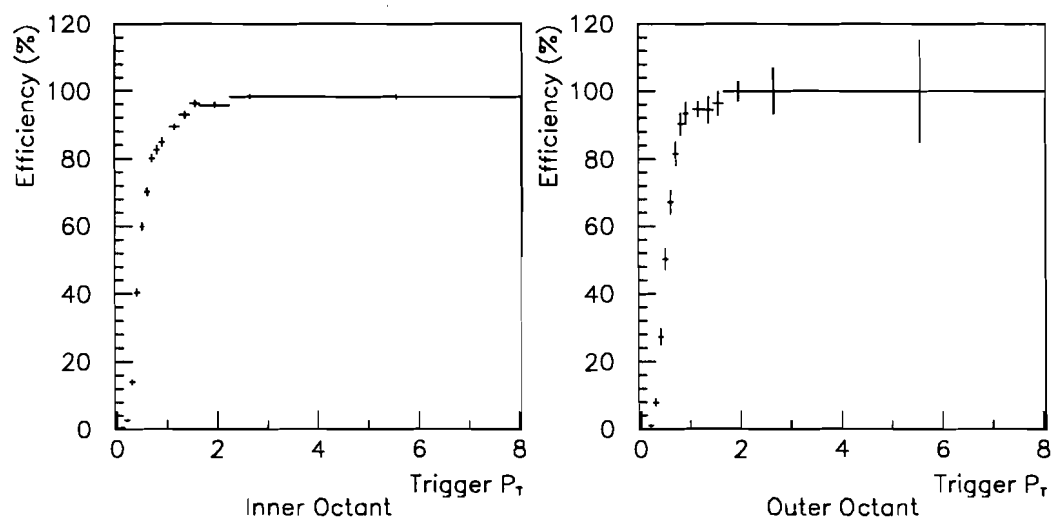


Figure 3.6: The Pretrigger Low Turn-on Curves.

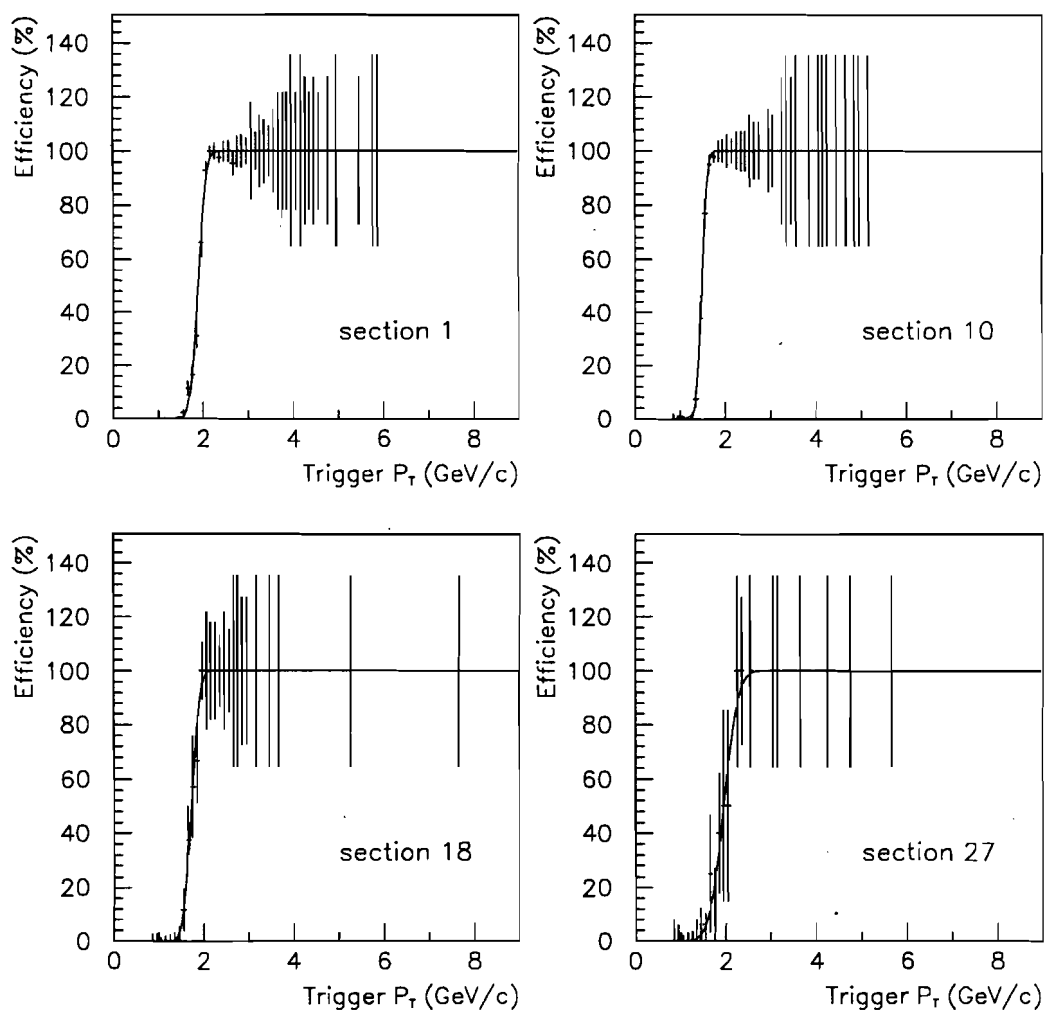


Figure 3.7: The Local low Turn-on Curves in Four Different Regions of an Octant.



# Chapter 4

## Event Reconstruction

This chapter focuses on the event reconstruction in software. It describes how the charged and neutral particles were measured from the raw data. The software architecture and the reconstruction algorithm are also given here.

The main reconstruction code, MAGIC, written in FORTRAN-77, controlled the data reconstruction in each element of the spectrometer. After reading in the raw data, MAGIC unpacked the data and then reconstructed the event through a set of control cards. The users had the liberty to turn on and off the unpackers and reconstructors, to specify the number of runs and the number of events to be processed, and to write out the selected events. In addition to the above functions, Magic could also write out the reconstructed data directly into the Data Summary Tapes (DSTs).

MAGIC used a CERN computer software package—PATCHY—as the code management system. PATCHY accepted the internal switches for machine specific computer code, like VAX, AMDAHL, and SGI. MAGIC employed ZEBRA, also a CERN software package, as the dynamic memory management package. ZEBRA also provided portability of output between various computer platforms. The data structure supported by ZEBRA, called banks, had linear and parallel structure. The input data, output reconstructed data, and run constants were all ZEBRA formatted to allow users to access the same data tapes on computers with different operating system. Six different reconstructors in MAGIC are listed as follows:

- DLREC, which loaded the trigger and Cherenkov informations into banks;
- PLREC, which reconstructed the charged tracks in the tracking system;
- EMREC, which reconstructed the photons in EMLAC;
- HCREC, which reconstructed the hadrons in HALAC;
- FCREC, which reconstructed the energies in FCAL;
- MUREC, which reconstructed the charged tracks in the E672 tracking system.

The 1990 data were processed through the computers (farms) operated by Fermilab. These computers, designed for parallel event processing and composed of Silicon Graphics computers (SGI farms), employed UNIX as their operating system. Each farm contained a host node, which controlled the I/O and distributed events into the processing nodes. When a processing node finished reconstructing an event, it returned the reconstructed results to the host node and began processing the next event assigned from the host. The host node, then, wrote the output from each processing node onto disks or 8mm tapes. Three SGI farms were used in processing the 1990 data sample. The output data were first stored in the spool disk and were copied into 8mm tapes afterwards.

## 4.1 Charged Particle Reconstruction

The charged particle reconstruction program (PLREC) contains the following parts: beam tracking, PWC tracking, STRAW tracking, SSD tracking, linking at the center of the magnet, and vertex finding routines. Before PLREC was called, an unpacker handled the raw data and transformed them into hit positions. All these transformation incorporated the corrected alignment offsets in order to take into account the transverse and longitudinal locations of each plane, as well as rotations about x, y and z axes.

### 4.1.1 Beam Tracking

The beam track reconstruction was performed in X and Y views independently. Each view had three planes. At first, we chose two seed planes and made all possible pairs of hits which were not in the same plane. Each pair of hits was connected to form a line and checked to determine whether there was any hit in the third plane within 1.5 strip spacing to this line. If there was, a least-square method was used to find the slope, the intercept, and the  $\chi^2$  per degree of freedom ( $\chi^2/dof$ ) of the track. Any track with  $\chi^2/dof$  greater than 2 was removed. After all 3-hit tracks were found, all unused hits were paired to make 2-hit tracks. Because the beam particles came from the beam line, it's very unlikely that beam tracks had wide angles. As a result, any track with slope greater than 0.01 or less than -0.01 was rejected. The tracks' projections to the target must be within 1.0 cm of the target boundary and their projections to the hodoscope be within 0.7 cm of the hodoscope boundary, since beam particles were focused to hit the target. Any beam track which failed the above cuts was considered fake.

### 4.1.2 PWC Tracking

Since the PWCs had four independent views, PLREC reconstructed view tracks for each view first. In each view, PLREC reconstructed 3-hit or 4-hit view tracks, using the least-square method. Each X-view track was then paired with each Y-view tracks to form a X-Y space tracks. Each X-Y space track was projected into U and V planes to search for hits which were within 1.5 wire spacing of the track's projection. The same step was applied to pairs of U and V view tracks to form U-V space tracks, but the window to select X and Y view hits into U-V space tracks was 1.0 wire spacing. In this first stage, PLREC required that there were at least 13 hits in a space track. All X-Y space tracks and U-V space tracks were refitted using hits from all four views. Any 14, 15, or 16 hit track with  $\chi^2/dof$  greater than three was rejected. As for 13 hit space tracks, the  $\chi^2/dof$  cut was two. Figure 4.1 shows the

distribution of  $\chi^2/dof$  for 13, 14, 15 and 16 hit space tracks. All the refitted X-Y space tracks were compared to the refitted U-V space tracks to search for duplicates. After dropping the duplicate tracks, PLREC loaded the information of these space tracks into banks and started flagging bad quality tracks. The flagging criteria were as follows:

- the Y-view impact parameter to the center of the target was greater than 2.5 cm, and;
- any 16-hit track that shared more than 13 hits with other tracks;
- any 15-hit track that shared more than 11 hits with other tracks;
- any 14-hit track that shared more than 9 hits with other tracks;
- any 13-hit track that shared more than 8 hits with other tracks.

In such a way, PLREC identified those high quality tracks (unflagged) and removed their corresponding hits before starting the second stage reconstruction. PLREC restarted finding view tracks using the remaining hits and reconstructed space tracks using the same technique which reconstructed tracks with at least 13 hits. However, the number of hits required to make a space track decreased because some wide angle tracks might be outside of the acceptance for PWC module 3 or module 4. The minimum number of hits was 11 if the track was within the acceptance of PWC module 4 and 10 if it was within the acceptance of module 3. Once the second stage tracking was finished, track flagging was reactivated to prepare for the third stage PWC track finding. For tracks which had Y view impact parameters less than 2.5 cm, the maximum number of sharing hits changed from 13, 11, 9, and 8 to 14, 13, 11, and 10 for 16 hit, 15 hit, 14 hit, and 13 hit space tracks, respectively. The 10, 11 and 12 hit tracks were required not to share more than 8 hits with other tracks.

After the second stage tracking, PLREC removed all the hits in high quality tracks and reconstructed those wide angle tracks which were outside the acceptance

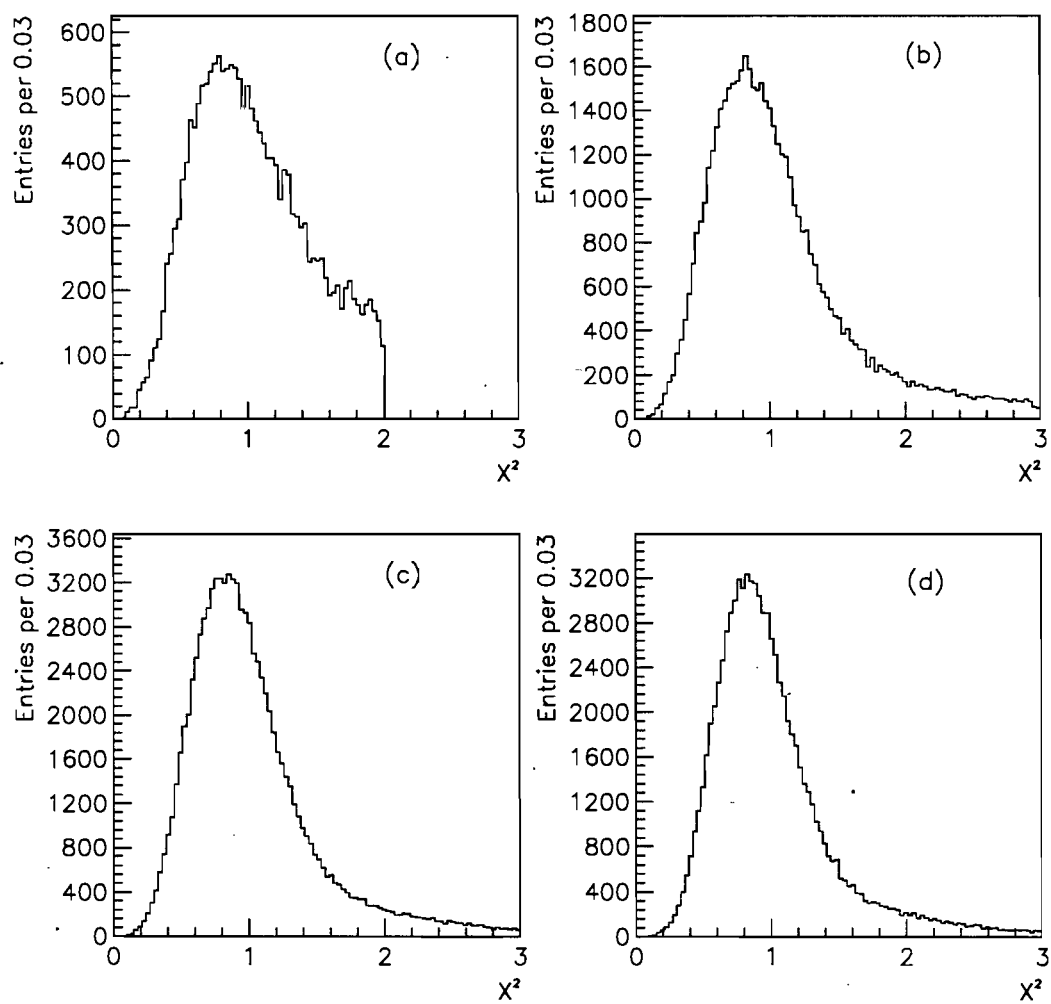


Figure 4.1:  $\chi^2$  per degree of freedom for PWC tracks. (a) 13 hit, (b) 14 hit, (c) 15 hit, (d) 16 hit.

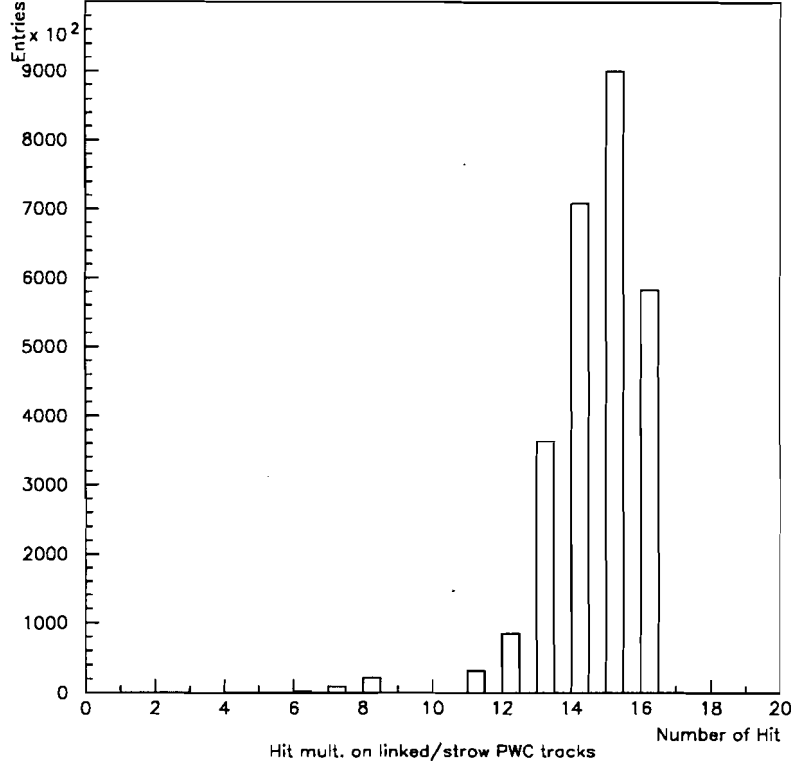


Figure 4.2: Distribution of the number of hits used for PWC tracks

of PWC module 3. In this stage, only hits in PWC module 1 and 2 were used to make 2-hit X and Y view tracks. PLREC made all X-Y space tracks and tried to matched hits in U and V views. The minimum number of hits required in final space tracks was 6 and no shared hits were allowed. The space tracks found in three different stages were stored in the space track bank. Figure 4.2 displays the hit multiplicity for PWC tracks.

### 4.1.3 STRAW Tracking

Since our straw chambers were built in X and Y views, we needed PWC tracks to identify the space tracks. The STRAW reconstructor was executed after PWC tracking was completed. PLREC projected each PWC track into the straw planes to associate straw hits with the PWC tracks. If there were enough straw hits accom-

panying a given PWC track, this track was refitted using those straw hits and all original PWC hits. The above description is the general strategy of straw tracking.

### Time-to-Distance Relation

Unlike the PWC tracking system, the straw tracking system read out the TDC time of straw hits. The translation of the TDC time into distance played an important part in straw tracking. Since the gas pressure and temperature were the similar for each straw tube in the same module, we assumed that all the tubes with the same high voltage supply and same threshold control had the same time-to-distance relation. If there was no high voltage or threshold change within a given time, all the runs within that period was considered in the same STRAW run set. Each straw module had an independent high voltage supply, and there were also four low voltage supplies for thresholds—two for X-view tubes and the other two for Y-view tubes. Therefore, four time-to-distance curves were measured for each run set.

The time-to-distance curves for straw tubes were determined using the TDC "time" recorded in straw chambers and the shortest "distance" between the wire position and the trajectory of a charged track. Since we didn't not have time-to-distance curves for reconstructing the straw tracks, the PWC tracks were first used as the trajectories of charged tracks. We selected 16-hit PWC tracks and projected them into the straw planes. We located the tube in which a PWC track penetrated through and there was a straw hit. Thus, the TDC time as well as the shortest distance between the track's trajectory and the center of tube were entered in the time-to-distance graph. After getting a large statistics, around ten thousand events, the first approximation of time-to-distance curves were measured. From these time-to-distance curves, we reconstructed straw tracks, requiring at least four hits in X/Y view and at least 1 hit in each module. Each straw hit was weighted for reconstructing the straw tracks, according to its resolution in its radial position. The resolution of straw hits are described in the next paragraph. The straw tracks were then projected

to the straw planes to redetermine the time-to-distance curves. These new time-to-distance curves changed the positions of hits and, consequently, gave new straw tracks. Thus, new time-to-distance curves gave new straw tracks and vice versa. We measured the time-to-distance curves after several iterations until these curves stayed unchanged. Figure 4.3 shows the four time-to-distance curves in a typical STRAW run set[27]. Note the hits with the TDC time less than 20 ns were assigned to the wires. The explanation of this assignment is given in the following paragraph in this section.

### The Resolution of Straw Hits

The theoretical resolutions of PWC hits and SSD hits were very straightforward to get. If a PWC wire or a SSD strip gets hit, the hit position is assigned to the center of the wire or the strip. Mathematically, the root mean square of a hit can be written as

$$\sigma^2 = \frac{\sum(\bar{x} - x_i)^2}{N} \quad (4.1)$$

where  $\bar{x}$  is the center position of the wire or a strip, and  $x_i$  is the real hit position of the  $i$ 'th hit. Because every position in the wire or the strip has the equal probability to get hit, equation 4.1 can be expressed as

$$\begin{aligned} \sigma^2 &= \frac{\int_0^L (\frac{L}{2} - x)^2 dx}{\int_0^L dx} \\ &= \frac{L^2}{12} \end{aligned} \quad (4.2)$$

where  $L$  is the width of the wire or the strip. Therefore, once we know the width of a wire or a strip, we know the theoretical resolution. The straw chamber, however, reported which wire got hit, but also recorded the drift time of straw hits to the wire. The resolution of straw hits, in general, was not a constant value but depended on where charged particles hit the tube.

When a charged particle passed through a straw tube, it ionized the argon gas and the electrons drifted to the wire. During this drifting process, more and



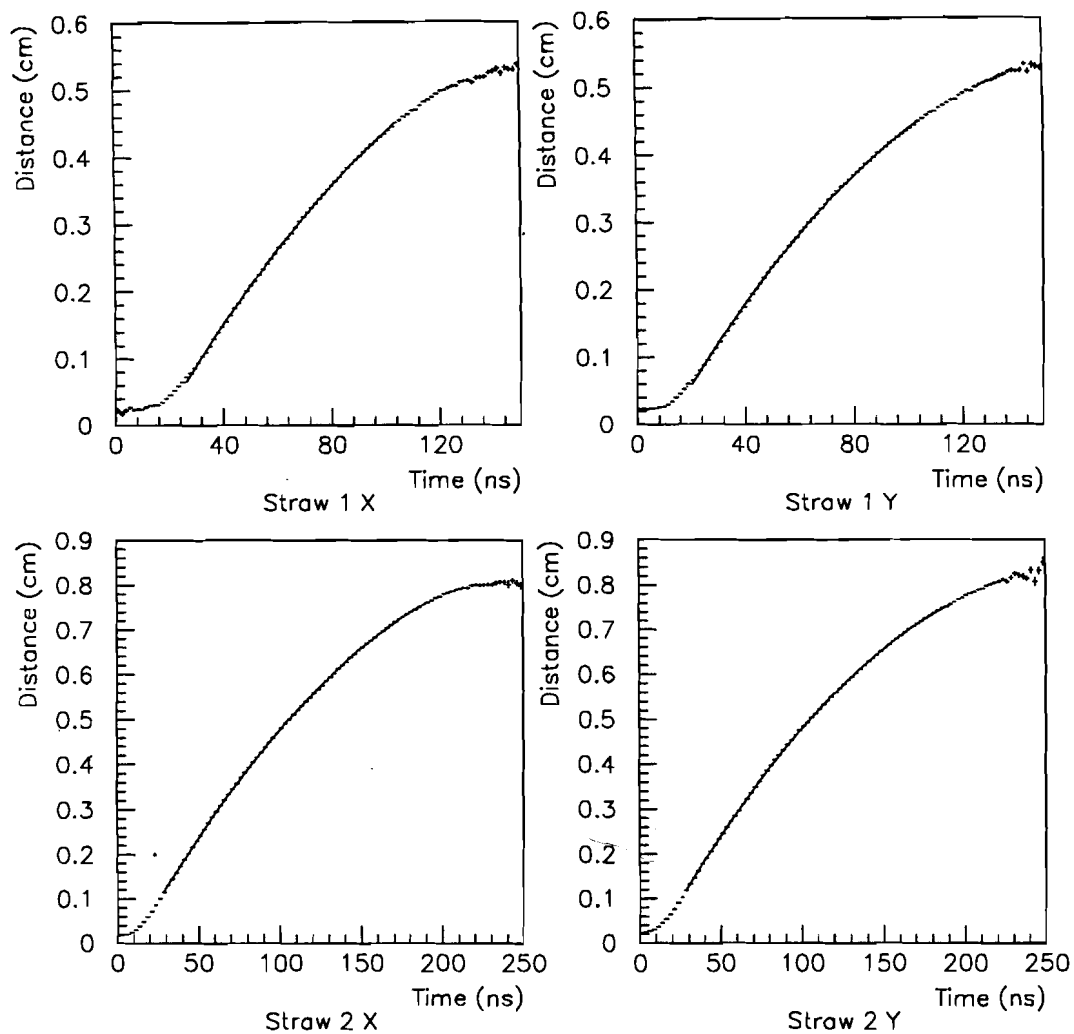


Figure 4.3: The time-to-distance curves for straw chambers in four different modules. The curves are almost flat at small TDC time due to the inefficiency in getting the proper time measurement when charged particles hit close to the wire. If the measured TDC time is less than 20 ns (cutoff value), the hit position is assigned to the wire position.

more electrons were produced by the ionization. When electrons moved closely to the wire, a tremendous amount of electrons were excited by the strong electric field near the wire, which is also known as the avalanche effect. Because there were so many electrons getting to the wire in a short time, they fired the time-voltage (nano) discriminator. If a particle penetrated directly through the wire, the closest electrons were too few to cause the avalanche effect. The nano discriminator, consequently, wouldn't fire until electrons from farther away drifted to the wire to ionize more electrons. The measured TDC time was, therefore, off. The STRAW reconstructor assigned the wire position as the hit position if the TDC time was less than the cutoff value in Fig. 4.3.

After getting the first approximation to the time-distance relation, we began studying the resolutions of straw hits as a function of radius ( $r$ ) within the straw tubes. The following method was applied to measure the hit resolution as a function of  $r$ :

1. Measure the  $r$  position of a straw hit using the time-to-distance curves;
2. Remove this straw hit from its corresponding straw track and refit this straw tracks using the remaining straw hits;
3. Plot the residual of straw hit to the new track and fit it with a gaussian function after getting large statistics.

Figure 4.4 shows the measured  $\sigma$  vs  $r$  for four straw modules. As mentioned in the first paragraph of this section, the new  $\sigma$  (weight) was employed to find straw tracks and, consequently, new time-to-distance curves. The plots in Figure 4.4 were made after several iterations which resulted in stable time-to-distance curves. These plots indicate that the  $\sigma$  is initially decreases when distance increases, but eventually starts rising at larger distances near the straw boundary. This initial decrease can be explained by the resolution in the readout TDC time. At larger distances (longer time), the relative uncertainty due to TDC time resolution is smaller.

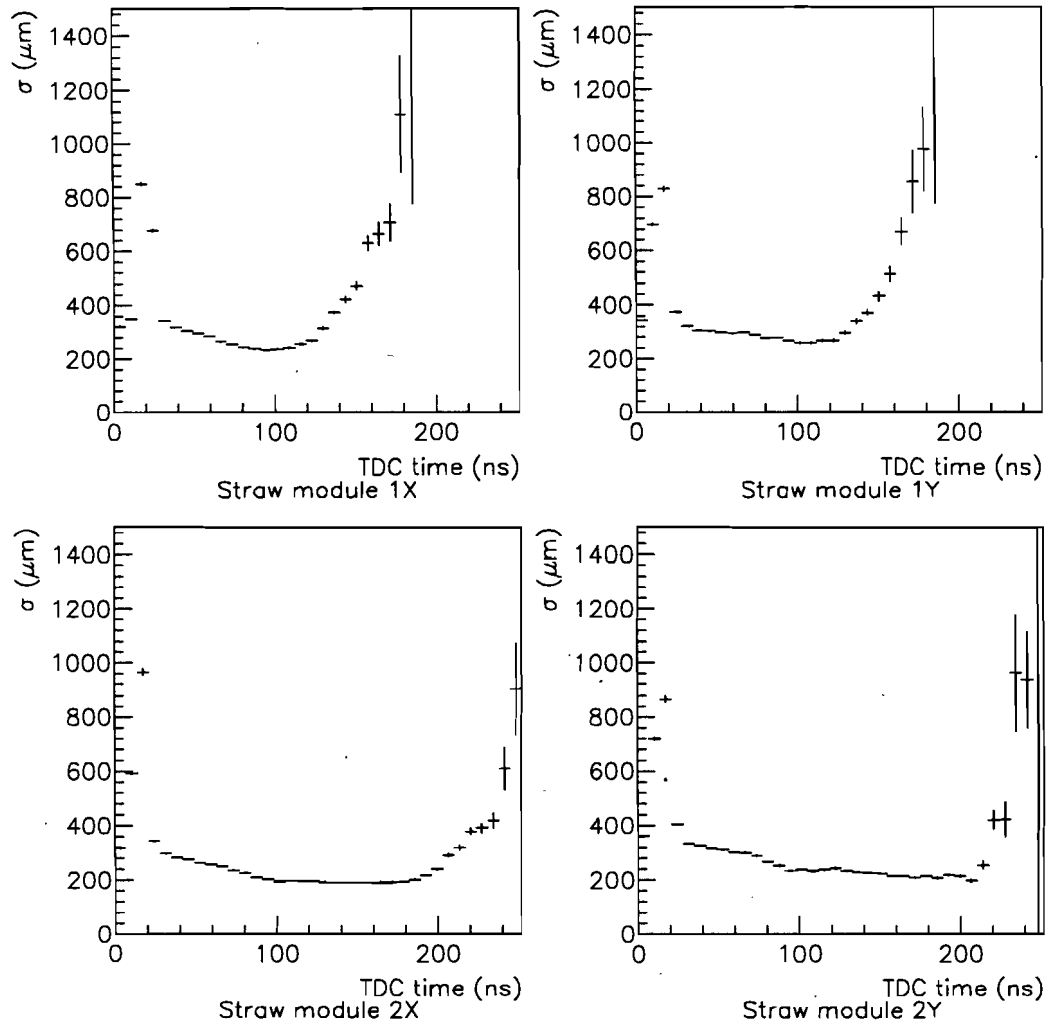


Figure 4.4:  $\sigma$  versus  $r$ . The straw  $\sigma$  (gaussian width) is measured by fitting the residual of the straw hits to the straw tracks at a certain radial position.

#### 4.1.4 SSD Tracking

The SSD tracking was done independently in the X and Y views. To avoid generating many fake tracks, PLREC reconstructed 4-hit and 5-hit view tracks first and called the linking routine (see next section) to mark the quality of these 4-hit and 5-hit tracks. All the hits in the linked SSD tracks were then eliminated prior to the second level tracking. In the second level tracking, PLREC reconstructed 3-hit SSD tracks and re-evaluated the linking. All unlinked 3-hit tracks were deleted afterwards. A detail description of the track cleaning and the track fitting algorithm can be found in [28].

#### 4.1.5 Linking

PLREC called the linking routine to associate the upstream and downstream tracks. The linking code served three different functions: selecting high quality SSD tracks, pairing X and Y view SSD tracks, and connecting track segments of charged particles before and after entering the magnet. PLREC was able to calculate the momentum of these tracks and determine the sign of their charges. Because the momentum impulse provided by the magnetic field was much smaller than the momenta of most charged particles of interests in this experiment, the projections of the downstream and the upstream tracks associated with the same particles were assumed to intersect at the center of the magnet. In addition, the Y-slope differences between the downstream and the upstream tracks were small due to the small changes in  $P_y$  and  $P_z$ . A detailed description of these assumptions and the corresponding corrections are in appendix A.

Because charged particles suffered minimal deflection in the Y view, the extension of the Y-view downstream tracks should be inside the SSD acceptance if the vertices of these tracks occurred before the third downstream SSD module. The linking subroutines, therefore, searched for links for each downstream track by first checking whether their Y projections were inside the SSD acceptance. If their Y pro-

jections at the third SSD module were within 1.65 cm of the edge of the instrumented region, it was likely that the charged particle which generated the downstream track also passed within the acceptance of the SSD's. The value of 1.65 cm, was added into the acceptance window to accommodate the resolution of PWC/STRAW tracks, the coulomb-scattering effect, and the small change of Y-slope experienced by the tracks. This value is determined by projecting the downstream Y-tracks to the primary vertex. Most of the downstream tracks came from the primary vertex. Because the Z position difference between the third SSD module and the primary vertex were small with respect to the downstream tracks, the projection uncertainties were close. In this way, we estimated the projection uncertainty of downstream tracks. The downstream tracks which passed the SSD acceptance cut were projected to the center of the magnet to search for links to the SSD tracks. If the projection differences ( $\Delta X$  in the X view and  $\Delta Y$  and  $\Delta YSL$  in the Y view) between the downstream and the upstream tracks at the center of the magnet were inside the linking windows, PLREC declared that those tracks as linked.  $\Delta YSL$  is the projection difference of Y-slope.

The linking windows were momentum dependent. The larger the momenta, the narrower the windows. Figure 4.5 and 4.6 shows the gaussian width of  $\Delta X$ ,  $\Delta Y$ , and  $\Delta YSL$  for PWC-SSD as well as STRAW-SSD pairs in different momentum bins. Those pairs were chosen by requiring one and only one SSD track projection within the 1.5 cm of a given PWC/STRAW track projection. From the momenta of tracks and the curves in figures 4.5 and 4.6, one may extract the appropriate linking windows. Since the momenta of tracks were not measured prior to linking, PLREC estimated the upstream X-slopes associated with the downstream tracks by assuming the charged particles emerged from the center of target. The momenta of tracks were estimated using their upstream and downstream X-slopes and the downstream Y-slopes. Note that we assumed every downstream track was coming from the target at this stage. In this method, the uncertainty in the estimated momentum increases as the actual momentum increases. Figure 4.7 plots the estimated momentum vs

the measured momentum for isolated linked tracks. In the low momentum region, the estimated momentum and the measured momentum agreed quite well, but the discrepancy becomes larger in the high momentum region. Fortunately, the curves in figures 4.5 and 4.6 were flat for high momentum tracks, indicating that the resolutions of  $\Delta X$ ,  $\Delta Y$ , and  $\Delta YSL$  did not change in high momentum region. Even though the momenta were not well estimated for high momentum particles, this method, as a result, still provides a rather good estimation of the linking windows. The linking windows in this analysis were chosen to be  $3.3 \times \sigma$  plus  $100/0.015$  microns/mrad to accommodate the uncertainty of the tracking alignment.  $\sigma$  is defined in Fig. 4.5.

The other important parameter in the linking code was the Z position of the center of the magnet (or the optimal location for linking). Because positively and negatively charged particles were bent in opposite directions in the X view, we may use this feature to determine where the center of the magnet was. As linking was less sensitive to Z location of the center of the magnet for high energy tracks, the low momentum tracks with isolated links were chosen in this study. Figure 4.8 shows the  $\Delta X$  distributions of positively and negatively charged tracks projected to different Z positions. These two distributions clearly merged with each other and, then, departed from each other with increasing Z. The Z position of the center of the magnet was defined as the location where the two distributions merged. Using the tracks with momenta between 3 to 8 GeV/c, we located the Z position of the center of the magnet as 197.73 cm for 1990 data.

After PLREC linked the SSD tracks to each PWC-STRAW track, it started ordering the SSD links for each downstream track because one downstream track might have more than one SSD link. The linking code selected at most five candidate SSD tracks per PWC/STRAW track in each view and stored them in hierarchy into the bank, based on the linking  $\chi^2$  defined as:

$$\chi_x^2 = \left( \frac{\Delta X}{\sigma_{\Delta X}} \right)^2 \quad (4.3)$$

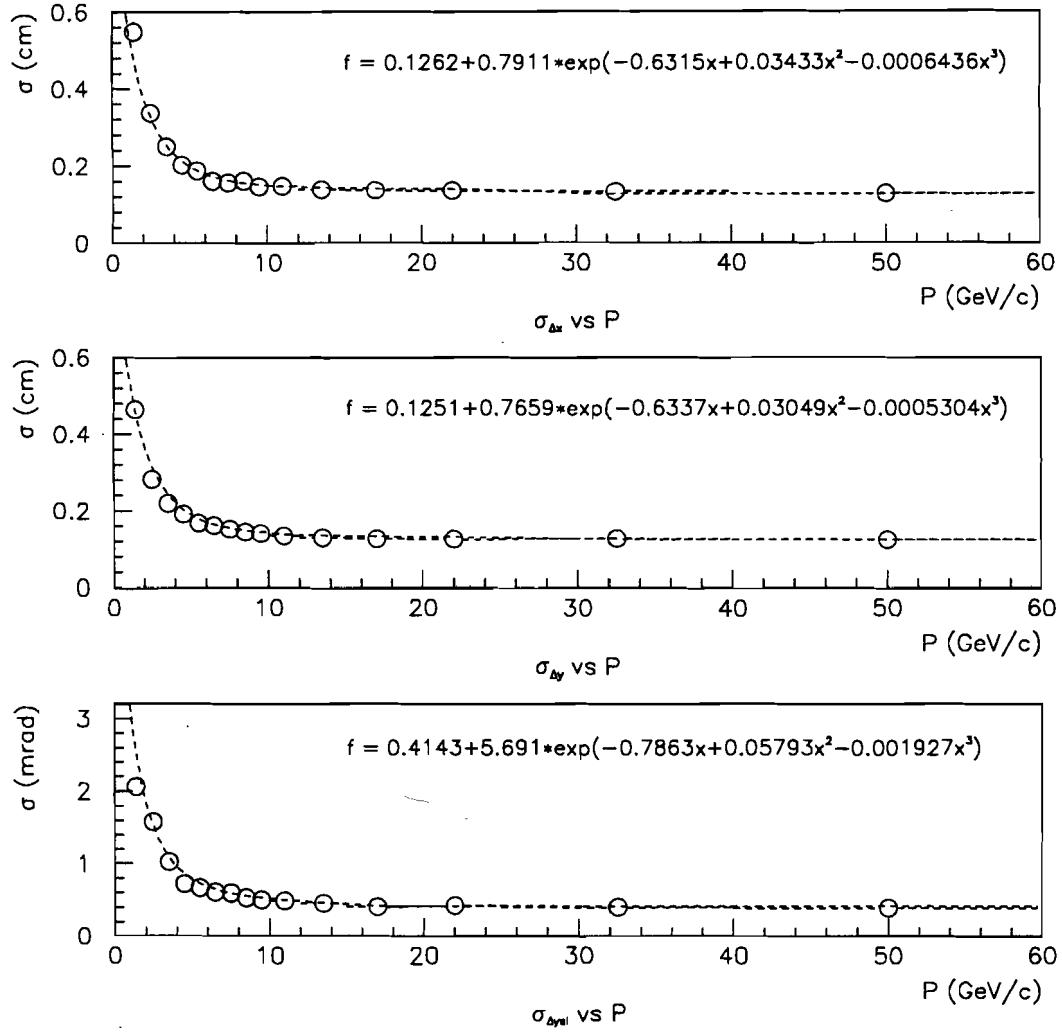


Figure 4.5:  $\sigma$ 's of  $\Delta X$ ,  $\Delta Y$ , and  $\Delta YSL$  vs  $P$  for PWC-SSD pairs.  $\sigma$ 's are the fitted gaussian width of  $\Delta X$ ,  $\Delta Y$ , and  $\Delta YSL$  distributions. The function  $f$  is fitted to the data points.

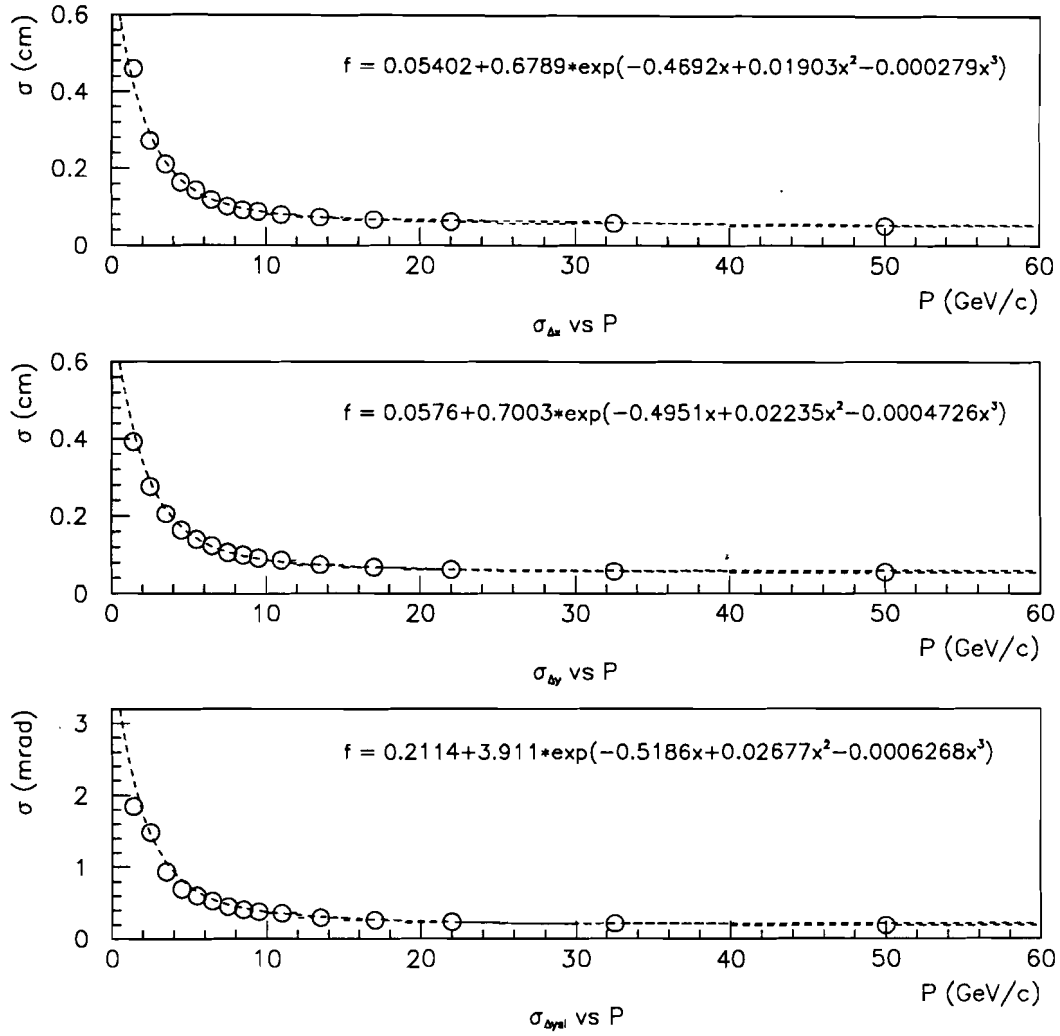


Figure 4.6:  $\sigma$ 's of  $\Delta X$ ,  $\Delta Y$ , and  $\Delta YSL$  vs  $P$  for STRAW-SSD pairs.  $\sigma$ 's are the fitted gaussian width of  $\Delta X$ ,  $\Delta Y$ , and  $\Delta YSL$  distributions. The function  $f$  is fitted to the data points.



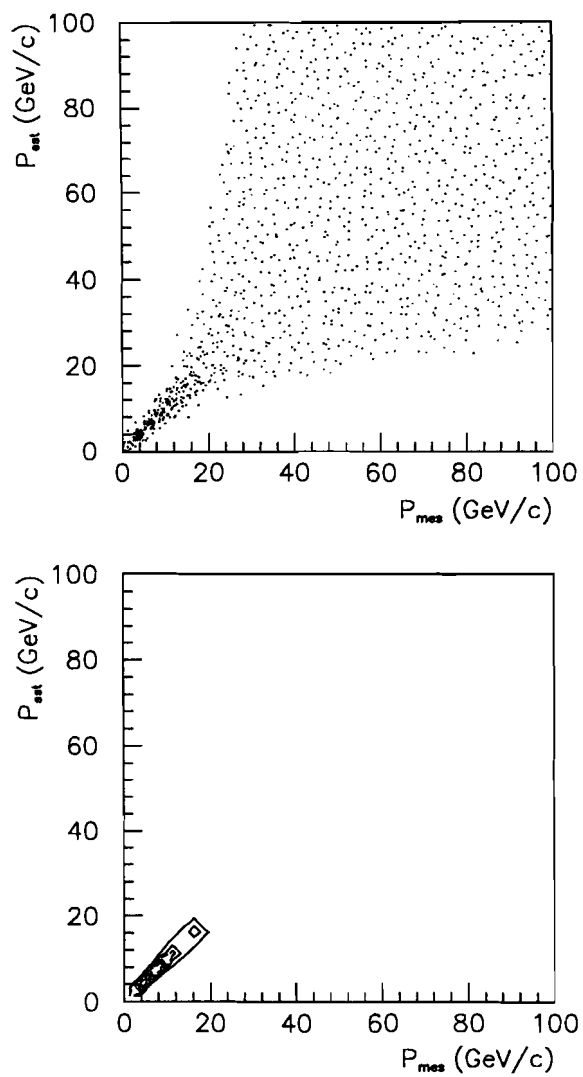


Figure 4.7: The estimated momentum versus the momentum measured from the linked tracks. The top plot is a scatter plot and the bottom one is a contour plot.

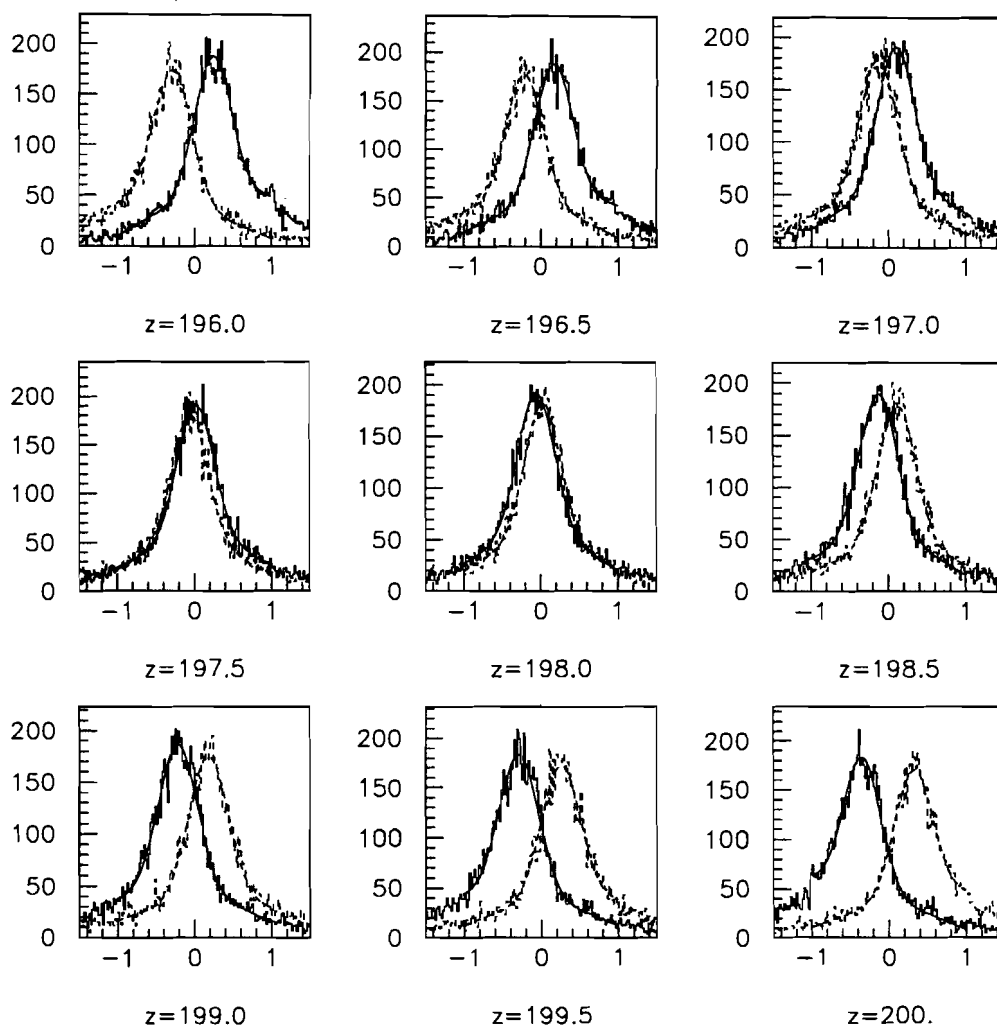


Figure 4.8:  $\Delta X$  distributions in different  $Z$ . Solid line is for positively charged tracks and dash line is for negatively charged tracks.

$$\chi_y^2 = \left(\frac{\Delta Y}{\sigma_{\Delta Y}}\right)^2 + \left(\frac{\Delta YSL}{\sigma_{\Delta YSL}}\right)^2. \quad (4.4)$$

$\sigma_{\Delta X}$ ,  $\sigma_{\Delta Y}$  and  $\sigma_{\Delta YSL}$  were determined from the curves in Figures 4.5 and 4.6. At this stage, the smallest  $\chi^2$  represented the best link. After the primary vertex (the most upstream vertex) was found, the relinking code was called to re-evaluate the linked tracks, using the vertex as another constraint. The relinking code first examined whether the downstream tracks were from the primary vertex by checking their impact-parameters in the Y view. If the downstream Y impact-parameters were not within 0.2 cm or the impact-parameter of the best linked SSD was within 80  $\mu\text{m}$ , the relinking was not operated. Otherwise the linking  $\chi^2$ 's were applied to rearrange the order of SSD links. They were redefined as,

$$\chi_x^2 = \left(\frac{\Delta X}{\sigma_{\Delta X}}\right)^2 + \left(\frac{dx}{\sigma_{imx}}\right)^2 \quad (4.5)$$

$$\chi_y^2 = \left(\frac{\Delta Y}{\sigma_{\Delta Y}}\right)^2 + \left(\frac{\Delta YSL}{\sigma_{\Delta YSL}}\right)^2 + \left(\frac{dy}{\sigma_{imy}}\right)^2 \quad (4.6)$$

where  $dx$  and  $dy$  were the SSD impact-parameters in X and Y views.  $\sigma_{imx}$  and  $\sigma_{imy}$  were the uncertainties of the SSD impact parameters. Again, the SSD track with the smallest  $\chi^2$  for a PWC/STRAW track was considered the best link.

#### 4.1.6 Determination of Momentum and Vertex Reconstruction

The momentum determination relied on the bending angles of charged particles. These bending angles were determined from the upstream and downstream X-slopes. PLREC employed the best link SSD tracks for the the upstream X-slopes associated with the linked downstream tracks. For those downstream tracks which did not have any links in X view, the upstream X-slopes were determined by drawing lines from the primary vertex to the tracks' projections at the center of the magnet. If no vertex was found either, the center of target was chosen as the location of the primary vertex. The bending angle could also reveal the sign of the charges of the tracks. The sign of

charges and the momenta were determined by the following equations:

$$Q = \text{sign}(\theta_1 - \theta_2) \cdot \text{sign}(B_0) \quad (4.7)$$

$$\sqrt{P_x^2 + P_y^2} = \frac{P_T^{kick}}{\sin\theta_1 - \sin\theta_2} \quad (4.8)$$

$$\frac{P_x}{P_z} = \tan\theta_1 \quad (4.9)$$

$$\frac{P_y}{P_z} = \tan\theta_y \quad (4.10)$$

where  $\theta_1$  and  $\theta_2$  were the arc tangent of the upstream and downstream X-slopes.  $\tan\theta_y$  was the slope of the upstream track in Y view. The  $P_T^{kick}$  was adjusted so that the  $K_s^0$  and  $J/\psi$  masses measured in E706 tracking system were consistent with the nominal values. Figures 4.9 and 4.10 shows the results of these two mass spectrum, where the  $\pi$ 's tend to have lower momenta while the  $\mu$ 's generally have higher momenta. Because the majority of charged hadrons and leptons carry one magnitude of electric charge, the magnitude of each charged track is assumed to be 1.

After finding the SSD tracks, PLREC reconstructed the vertices in each view. At first, all the 5-hit and 4-hit linked SSD tracks were used to fit a vertex by minimizing the fitting  $\chi^2$ . If there were less than three linked tracks available, unlinked tracks were also used in the vertex finding. If there were still less than 3 tracks available, 3-hit tracks were then used. Once all x-view and y-view vertices were found, a re-fitting process was executed to determine a matched vertex by using the tracks in one view and the Z-position of the vertex in the other. If there were more than one vertex found in an event, the most upstream one was considered as a primary vertex. A detailed description of the vertex finding algorithm can be found in [29].

## 4.2 The Electromagnetic Shower Reconstruction

EMREC, the electromagnetic shower reconstructor, reconstructed the energies and positions of the photons and electrons which showered in the EMLAC. A detailed description of the reconstruction program was given elsewhere in [30][31]. This section will describe briefly the reconstruction algorithm. As mentioned in chapter 2, the

EMLAC was divided into a front section and a back section. The energies (ADC counts) above a cutoff value, -180 MeV, from the same strips in the front and back sections were added in software to form a summed section. All the energies and positions were reconstructed in this summed section.

EMREC transformed the ADC counts deposited in each strip into energies, based on equation 4.11.

$$E_i = A_{EM}G_i(N_i - N_i^0) \quad (4.11)$$

where  $N_i$  was the ADC counts recorded in strip  $i$ ,  $N_i^0$  was the pedestal for that strip,  $G_i$  was the relative value of channel gain, and  $A_{EM}$  was the nominal normalization factor determined from the electron beam calibration. After loading each strip energy into banks, EMREC reconstructed photons via in the following steps:

1. Find *groups* and *peaks*;
2. Reconstruct *gammas* from *groups* and *peaks*;
3. Correlate  $r$  and  $\phi$  *gammas* into *photons*.

### 4.2.1 Groups and Peaks

EMREC found *groups* in four different views per quadrant: (1) left-R, (2) right-R, (3) inner- $\phi$  and (4) outer- $\phi$ . A *group* was defined as a series of continuous strips with energies above a pre-defined value. In order for strips to form a group, the following criteria were applied:

- For views 1, 2, and 3, at least 3 strips had energies above 80 MeV. As for view 4, two strips were required with a 95 MeV threshold;
- The total energy in the group was at least 600 MeV;
- The average energy per strip was above 150 MeV;

- The strip with the maximum energy contained at least 300 MeV for first three views, and 350 MeV for view 4.

All groups which satisfied the above criteria were stored into the data bank.

When all the groups were located, EMREC searched for peaks in each group. A *peak* occurred where the slope of the energy distribution as a function of strip position changed from positive to negative. There were *valleys* in each side of the peak. A valley was either the strip which had the lowest deposited energy between two groups or the end strip of the group if the the peak was in the first, the last, or the only peak in the group. Because low energy showers tend to deposit most of their energy in the front section, the peak finding algorithm was also applied independently in the front section to recover the peaks that were lost when adding the front and the back energies to form the summed section. This was done by searching for peaks in the front section between any two valleys in the summed section. A quality factor was checked for every peak in order to determine if this peak was significant or just attributed to an energy fluctuation. If a peak was found in the front section of r view, the program tried to search for the corresponding peak in the back section. The front and back radial positions were used to calculate the *directionality* of particles. The directionality helps us identify those showers which did not emanate from the target. Section 5.2 will discuss directionality in more detail.

## 4.2.2 GAMMAS and PHOTONS

EMREC reconstructed "gammas" from groups based on the number of peaks involved. The gammas and the peaks were similar except that the energies and positions of the gammas were determined from the shower shape. For a single-peak group, EMREC considered it a gamma and determined its energy and position by fitting it with the parametrized shower shape. The individual shower shape could be written as

$$E_f(r) = \frac{1}{r}(f_1 e^{-f_2 r} + f_3 e^{-f_4 r} + f_5 e^{-f_6 r}) \quad (4.12)$$

$$E_b(r) = b_1 e^{-b_2 r} + b_3 e^{-b_4 r} + b_5 e^{-b_6 r} \quad (4.13)$$

where  $E_f$  and  $E_b$  were the energies in the front and back sections, respectively;  $r$  was the radial distance from the shower center. The parameters  $f_1$  through  $f_6$  and  $b_1$  through  $b_6$  were determined from the Geant Monte Carlo. We also compared this parametrized shower shape with data, using the isolated shower at  $R=60$  cm. The results were very consistent. As for multiple-peak groups, the program split the group into separated gammas and performed a global fit. The energies and positions were calculated on the corrected pulse distributions from this global fit.

After all the gammas were found, EMREC correlated them in the  $r$  and  $\phi$  views to form final photons. The correlation operated based upon energy matching in these two views. As mentioned in chapter 2, the readout boards of the EMLAC alternated between  $r$  and  $\phi$  views. The energies of individual shower in  $r$  and  $\phi$  views were, therefore, similar. The ambiguity of correlating gammas first occurred when  $r$  gammas were on the inner-outer boundary or  $\phi$  gammas were on the left-right boundary. If there were gamma on these boundary, we first summed the energies of all gammas near the same boundary in one view and split the energies according to the gamma energies in the other view. However, this algorithm might not perform a correct correlation in very complicated cases.

Inner  $\phi$  gammas were correlated with  $r$  gammas that had radial positions less than 40 cm, while outer  $\phi$  gammas were correlated with  $r$  gammas that had radial positions greater than 40 cm. The simplest case was there was only one  $\phi$  gamma and one  $r$  gamma to be correlated. This correlation was named a 1-1 correlation. Sometimes there were two photons overlapped in one view to produce one gamma in this view and two gammas in the other. This type of correlation was named 1-2 correlation. In this case, the program attempted to split the energy of this single gamma into two using the energies of the two gammas. Even more complicated correlations, such as 1-3 and 1-4 correlations, were pursued after all 1-1 and 1-2 cases were completed. The total energy of a photon was the energy sum of the  $r$  gamma and the  $\phi$  gamma. The  $r$  position and  $\phi$  position formed the two dimensional positions

for photons.

### 4.3 Hadron Shower Reconstruction

The hadron reconstruction code, HCREC, was rather simple when compared to EMREC. Because each pad gave its X and Y positions simultaneously, HCREC reconstructed hadrons directly in two dimensions. The zero suppression (see [21]) window was not used in 90-91 data. The corresponding correction in HCREC was, hence, turned off.

Equation 4.11 was also applied to convert the measured ADC counts into energies. HCREC then selected the pads which had at least 4 GeV, and loaded them into banks for the front and back sections. Although HCREC had the ability to reconstruct hadrons respectively in the front, back, and summed sections, all hadrons in 1990-1991 data were reconstructed in the summed section only. In the next step, HCREC searched for "groups" which consisted of adjacent pads with energies above threshold. Each group was required to contain two or more pads, one of which had energy above 7.5 GeV. A group might be resolved into more than one hadron. HCREC first identified the peak pad (the pad having highest energy in a group) and defined its 1st, 2nd, and 3rd neighbors (see figure 4.11). A group was considered as one hadron, if it satisfied the following requirements:

1. Total number pads in a group did not exceed 10;
2. No more than 3 pads in a group carried more than a fraction (0.4) of the energy in the peak pad;
3. No other pads beyond the 12 closest neighbors of the peak pad had energies greater than the average energy of the 12;
4. The energies of 2nd and 3rd neighbors were less than the average energy of the 1st neighbors.



The energy sum in the group gave the energy of the hadron; the energy weighted vector sum of pad's center position defined the position of that hadron. If there was an isolated pad with energy above 7.36 GeV, it automatically formed a hadron whose position was the center of the pad.

The reconstruction of multi-hadron cases in a group was similar to the reconstruction multi gammas in a group. HCREC picked the second highest energy pad as the center of second hadron to start resolving hadrons. The detailed description of resolving this pattern recognition problem can be found in [32]. The basic assumption was that the energy deposited by a hadron became smaller and smaller when one looked away from the central peak pad. Therefore, HCREC used the energy distributions to resolve hadrons in a group. However, the more hadrons in a group, the lower the quality of the resolution of those hadrons. The energy, position, and quality factor, which were based on number of hadrons resolved in a group, for each hadron were at last loaded into data bank.

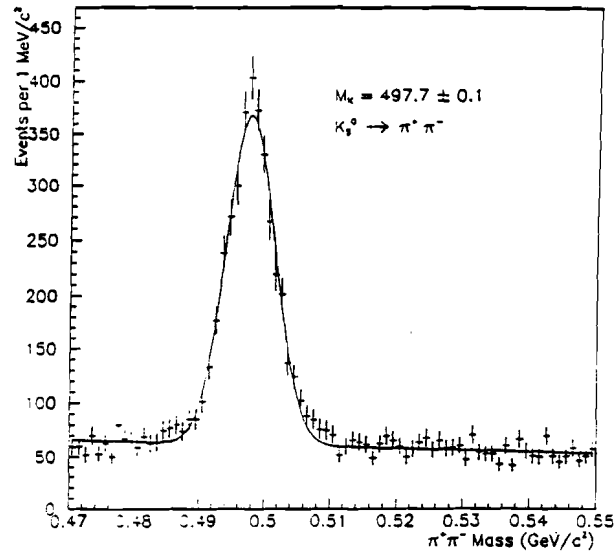


Figure 4.9:  $\pi^+\pi^-$  mass spectrum

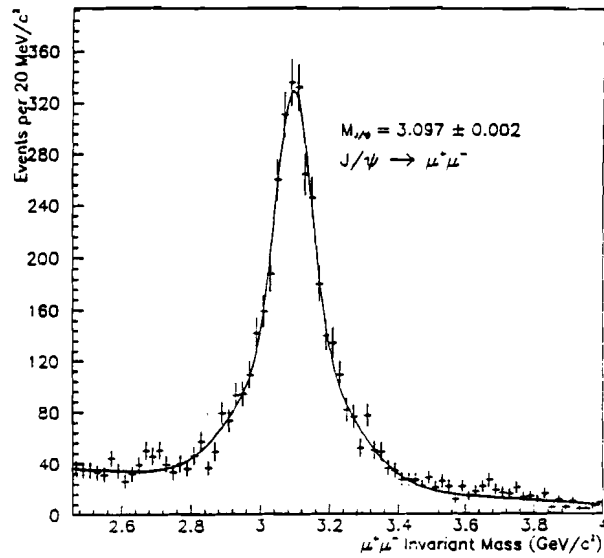
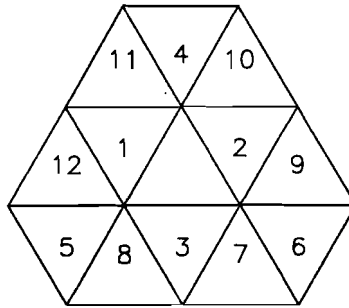
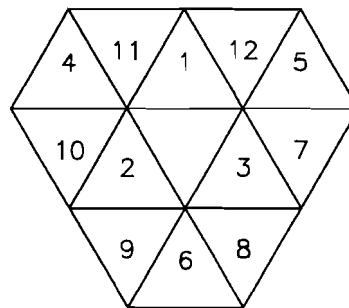


Figure 4.10:  $\mu^+\mu^-$  mass spectrum



Case 1



Case 2

Figure 4.11: The twelve neighbors of the peak pad (center pad). The first neighbors are labeled as pads 1, 2, and 3. The second neighbors contained pads 4, 5, and 6. The rest were the third neighbors.

# Chapter 5

## Electrons, Photons, and Hadrons

This chapter describes the techniques used in this thesis to define photons, electrons, and hadrons. It discusses various methods to identify muons, which are a background for high  $P_T$  photons, and the charged tracks which do not have proper momentum measurement in PLREC. A brief description of the momentum redetermination and the study of the photon energy scale are also summarized.

### 5.1 Electrons

The standard way to identify an electron is to check if a track is pointing to an electromagnetic shower and determine whether the energy and total momentum measured by the EMLAC and the tracking system are similar. However, if electrons are derived from the photon conversions, one may identify them just from the tracking system alone. Those electrons, together with their anti-particles, are called zero mass pairs (ZMPs).

#### 5.1.1 Zero Mass Pairs

As photons are massless, the observed opening angles of ZMPs are very small. If a conversion occurs before the magnet, one would see that the ZMP electron tracks are almost overlapped before entering the magnet and that they are separated in  $X$  by the magnetic field afterwards. Thus, if there are two downstream tracks with opposite charges which have similar  $Y$  slopes and their projections at the center of

magnet are very close, this pair is regarded as a ZMP candidate. In this analysis, we required that the  $Y$  slope difference of a ZMP must be less than 3 mrad and its  $ZX$  intersection is within 10 cm of the center of the magnet in  $Z$ . Figure 5.1 displays the  $Y$ -slope difference and the distribution of  $ZX$  intersections of track pairs with opposite charges before and after these two requirements. The ZMP signal is clearly seen in these plots after these two cuts.

ZMP electrons turned out to be very useful in studying the performance of the EMLAC. They became a bridge to connect the tracking and the LAC information. Together with  $\pi^0$ 's, ZMPs helped us calibrate the EMLAC energy scale. Besides, ZMPs accompanying photons to form  $\pi^0$ 's, provide another channel to measure the  $\pi^0$  cross section, which can be used to check the cross section determined directly from the two-photon mode.

### 5.1.2 LAC Electrons

Since the EMLAC has a similar response to electrons and photons, one would expect that electrons, with reasonable energies, which hit the LAC will shower the LAC, and the energy measured by the LAC, after calibration, would be close to that measured by the tracking system. Before comparing the energy measured by these two systems, the matching of tracks and photons must be studied first. Figure 5.2 shows the distributions of  $\Delta X$ ,  $\Delta Y$ , and  $\Delta R^2$  ( $\Delta R^2 = \Delta X^2 + \Delta Y^2$ ) between the projections of ZMP tracks and the positions of photons at the front face of the EMLAC. The cut for the matching is 1.5 cm in  $R$ . Note that the background of the  $\Delta X$  distribution is smaller than that of  $\Delta Y$  distribution. Because the charged particles are bent in the X view into the region where photons are less populated, the background in the  $\Delta X$  distribution decreases. This effect is illustrated in Figs. 5.3 and 5.4.

The other two variables which help us to identify electrons are  $E/P$  and  $E_f/E_t$ , where  $E/P$  is the ratio of the energy measured by the EMLAC and the momentum

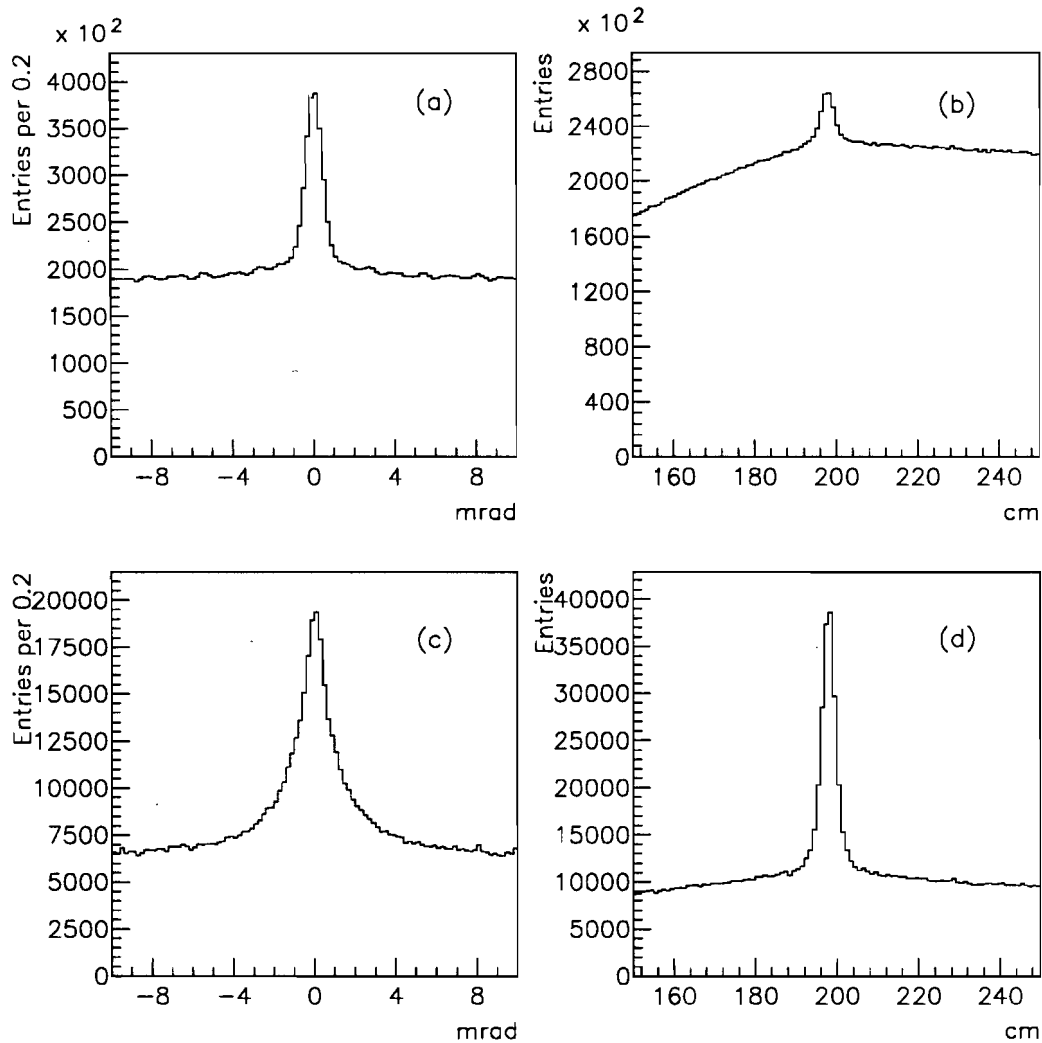


Figure 5.1: (a) Y-slope difference, (b) ZX intersection, (c) Y-slope difference after ZX intersection cut, (d) ZX intersection after Y-slope difference cut.

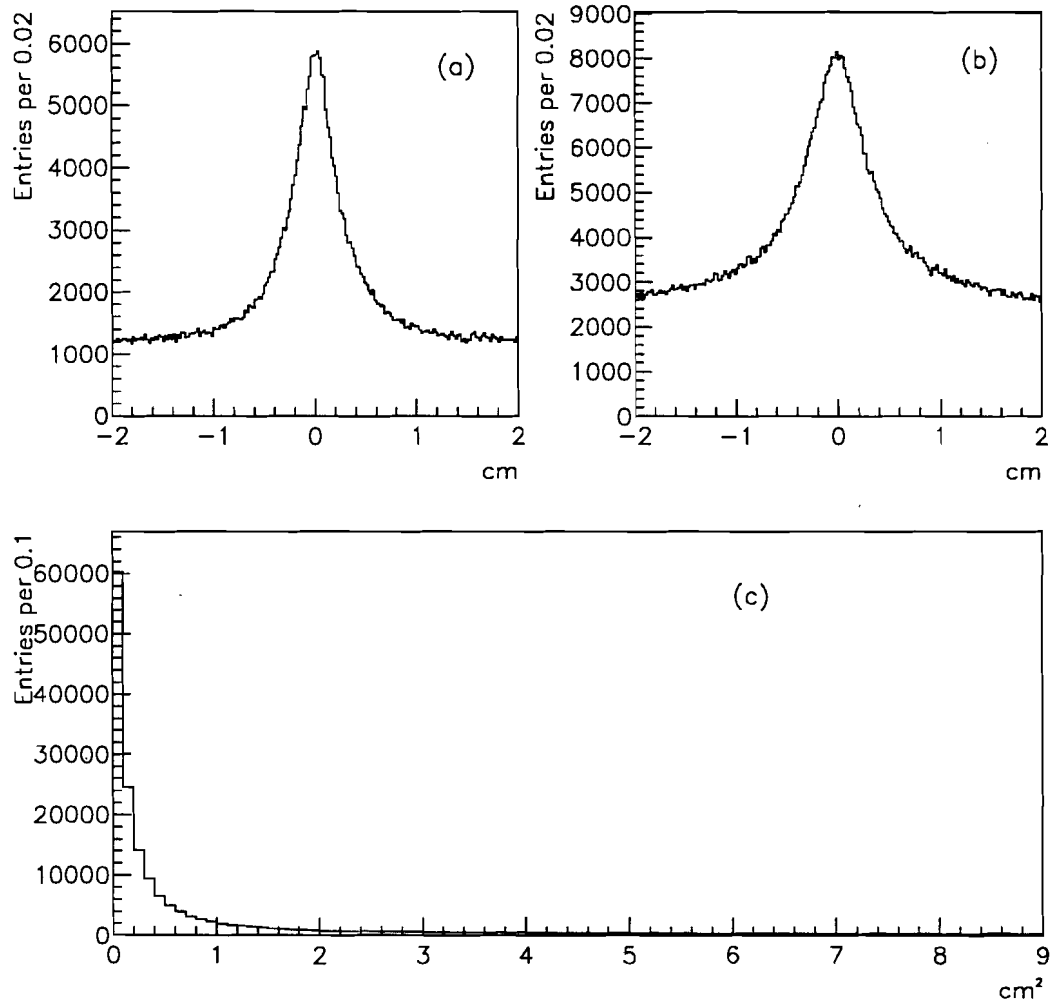


Figure 5.2: The differences between tracks' projections and photons for ZMPs. (a)  $\Delta X$ , (b)  $\Delta Y$ , (c)  $\Delta R^2$ .

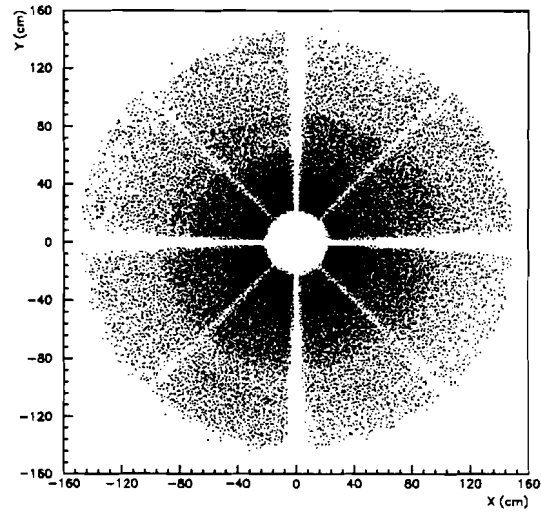


Figure 5.3: The positions of photons at the front face of the EMLAC. The LAC fiducial cut is applied.

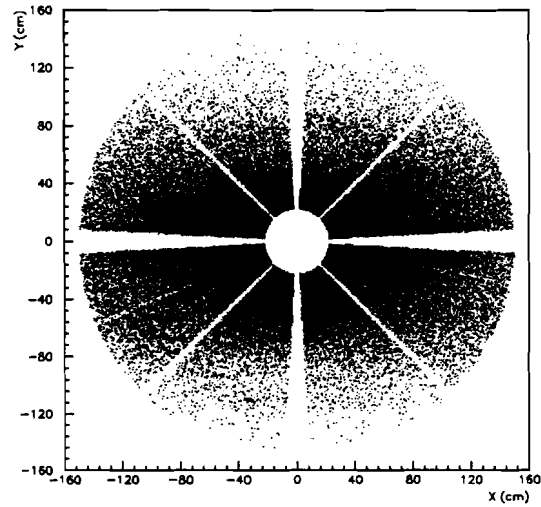


Figure 5.4: The positions of electrons at the front face of the EMLAC. The LAC fiducial cut is applied.



measured by the tracking system.  $E_f/E_t$  means the fraction of the total energy deposited in the front section. The top two plots in Fig. 5.5 shows the distributions of  $E/P$  and  $E_f/E_t$  for all matched tracks, while the bottom two plots are for ZMPs only. Two distributions in each of these top two plots indicate that electrons and charged hadrons have different characteristics in terms of  $E/P$  and  $E_f/E_t$ . The electron showers are likely to deposit most of their energies in the front section, and their  $E/P$  values tend to be close to 1. But the hadron showers tend to deposit their energies in the back section and their  $E/P$  values are likely to be less than 0.5. From these differences between hadrons and electrons, we use the following criteria to identify the LAC electrons:

1. The distance between the track's projection and the nearest electromagnetic shower must be less than 1.5 cm;
2.  $0.7 \leq E/P \leq 1.3$ ;
3.  $0.5 \leq E_f/E_t$ .

## 5.2 Photons

Based on the discussion in the previous section, all electromagnetic showers which match the projections of charged tracks are identified as either electrons or charged hadrons. The other cut we use in our analysis is the  $E_f/E_t$  cut to discriminate against hadron-like showers. In this thesis, 0.2 is chosen as the minimum value for photons. Since halo muons are a background to high  $P_T$  photons, identifying those muons is important to this experiment. A short summary of the muon-rejection cut is given in the following section.

### 5.2.1 Muon Rejection

When the primary beam hit the primary target, in addition to producing the desired secondary beam with negative 515 GeV/c momentum, numerous muons were

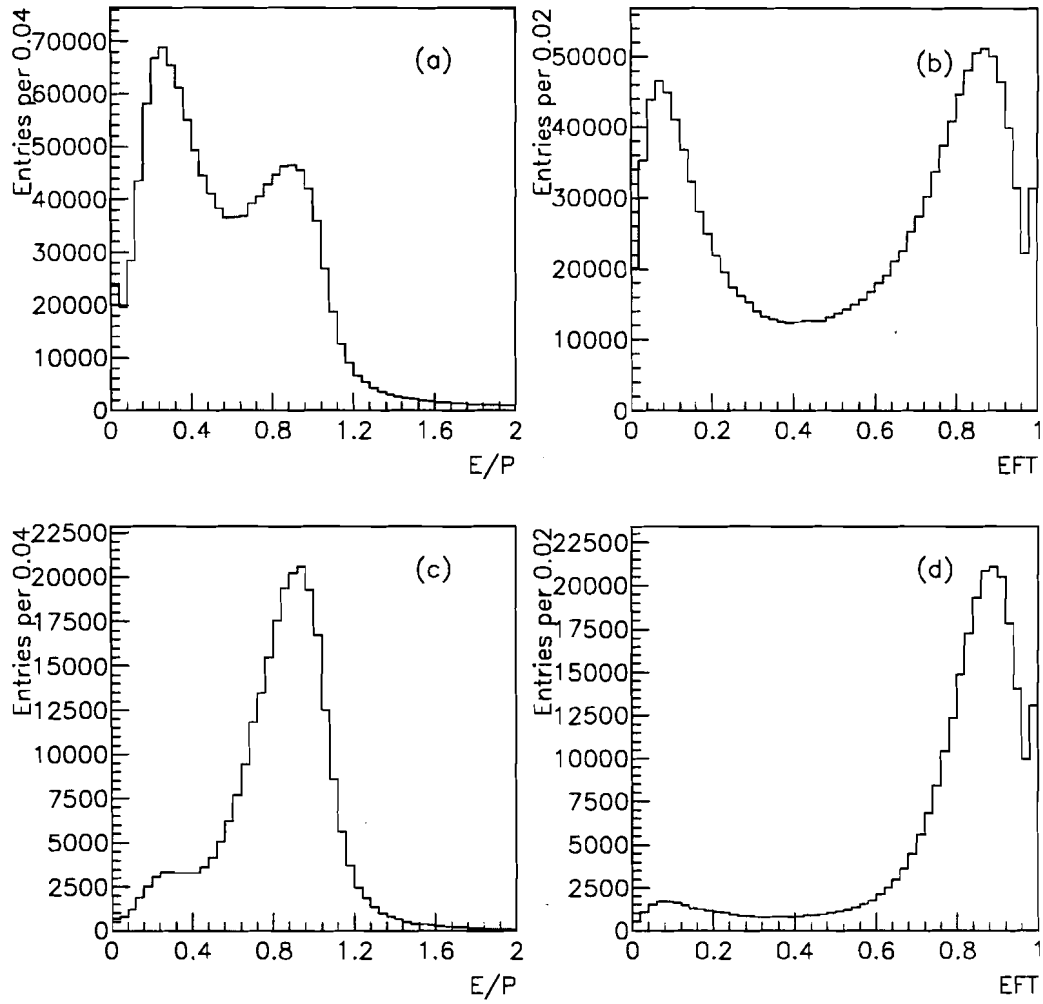


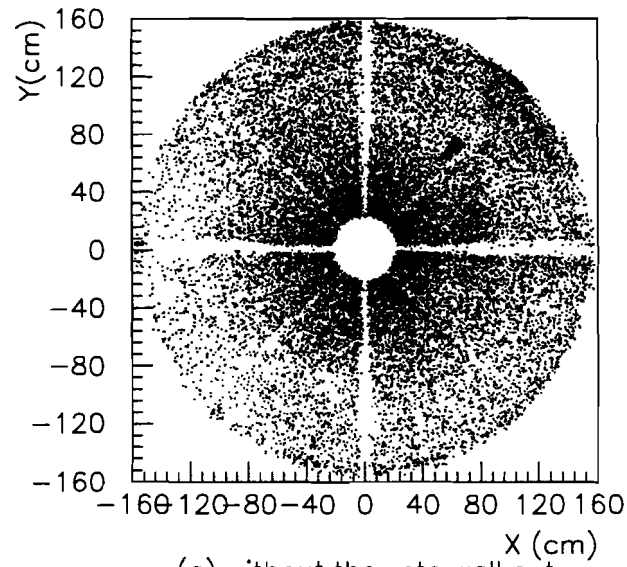
Figure 5.5: (a)  $E/P$  for tracks, (b)  $E_f/E_t$  for tracks, (c)  $E/P$  for ZMP tracks, (d)  $E_f/E_t$  for ZMP tracks.

produced via the decay of pions produced from the primary target. Some of these muons eventually intersected our spectrometer. Although the veto wall was designed to veto the events with the halo muons on line, there were still many muon triggered events, due to the counter inefficiencies of the veto wall. The information from the veto wall counter was read out via Minnesota latches. We have used this information to define the off-line veto wall cut. If there was a hit in a veto wall within  $\pm 3$  time buckets to the in-time bucket, the veto wall is declared fired in the hardware (on-line). In this analysis, we changed the timing constrain from  $\pm 3$  time buckets to time buckets 3 to 13. If there was a hit in a veto wall quadrant in between time bucket 3 to 13, the veto wall of that quadrant was declared fired. If veto wall 1 or 2 fired and veto wall 3 also fired in the same quadrant, we defined that there's a muon in that quadrant. Hence, any photon in that quadrant is disregarded in the analysis. Figure 5.6 shows the positions of single high  $P_T$   $\pi^0$  candidates at the front face of the EMLAC before and after applying the offline veto wall cut. (The definition of a  $\pi^0$  is discussed in the next section.)

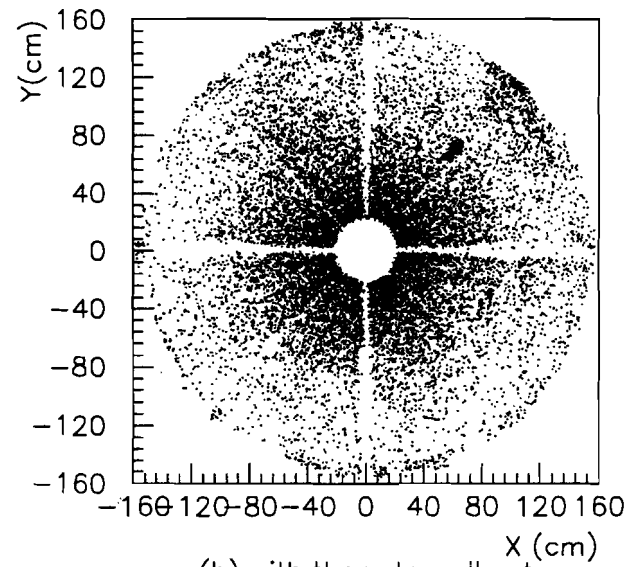
Muons can also be identified via directionality. Directionality ( $Dr$ ) is defined as

$$Dr = R_f - \frac{Z_{front}}{Z_{back}} R_b \quad (5.1)$$

where  $R_f$  and  $R_b$  are the reconstructed front and back radial positions of a shower;  $Z_{front}$  and  $Z_{back}$  are the  $Z$  positions in the front and back sections of the EMLAC, respectively. Figure 5.7 illustrates the concept of directionality. Since muons from the primary target are nearly parallel to the secondary beamline, their directionalities are not zero but positive; however, those of photons from the E706 target are near zero. Figure 5.8 displays the photon  $P_T$  distributions vs their directionality with and without veto wall firing in the same quadrant[33]. A lot of entries for the positive value of directionality occur when the veto walls fire, which is consistent with beamline muons. Since those muons mimicked the high  $P_T$  photons and since the distribution of directionality was broader for low  $P_T$  photons, the directionality cut was only applied



(a) without the veto wall cut



(b) with the veto wall cut

Figure 5.6: The position of  $\pi^0$  candidates with  $P_T$  above 5 GeV/c. (a) before the offline veto wall cut, (b) after the offline veto wall cut.

to showers with  $P_T$  above 5.5 GeV/c. Moreover, showers with small radial values in the EMLAC did not have clearly determined directionality. For muons, the larger the radial value, the larger the directionality. Therefore, the directionality cut is R dependent. The cut used was:

$$\begin{aligned} DRCUT &= 0.2, \text{ if } R \leq 40 \text{ cm} \\ &= 0.0048 \times R, \text{ if } R \geq 40 \text{ cm}. \end{aligned} \quad (5.2)$$

Another method used to tag muons is the tracking cut. Unlike the electrons from the target, the halo muons had different distance-matching distributions between the electromagnetic showers and the charged tracks at the front face of the EMLAC. The matching cut is 3 cm for muons instead of 1.5 cm for electrons. Since the halo muons were not from the target, we used the track's downstream impact parameter in the  $Y$  view to help distinguish the halo muons. If a photon matched a charged track and the downstream  $Y$  impact parameter of this track was greater than 1.5 cm, we regarded this photon as a muon.

Since this thesis is based upon a study of two high  $P_T$  particles which were at least  $90^\circ$  apart in azimuthal angle, muons did not cause a serious problem as they did for single high  $P_T$   $\pi^0$ 's. As a matter of fact, it was very rare to have high  $P_T$  particles on one side and muons on the other in the same event. This is illustrated in Fig. 5.9, which displays the mass spectrum of two photons without the offline veto wall cut in two different types of events. Although the two photon mass had less muon background in di- $\pi$  events, muons still had impact on  $\pi^0$ 's in the high  $P_T$  region. In this analysis, we only applied the muon cuts to  $\pi^0$ 's with  $P_T$  above 9 GeV/c.

### 5.2.2 The Definition of $\pi^0$ 's

98.8% of  $\pi^0$ 's decay into two photons. In this experiment  $\pi^0$ 's can be reconstructed via the effective mass of two photon pairs. The momentum four vector of each photon can be determined from its energy and position in the EMLAC, and the vertex in

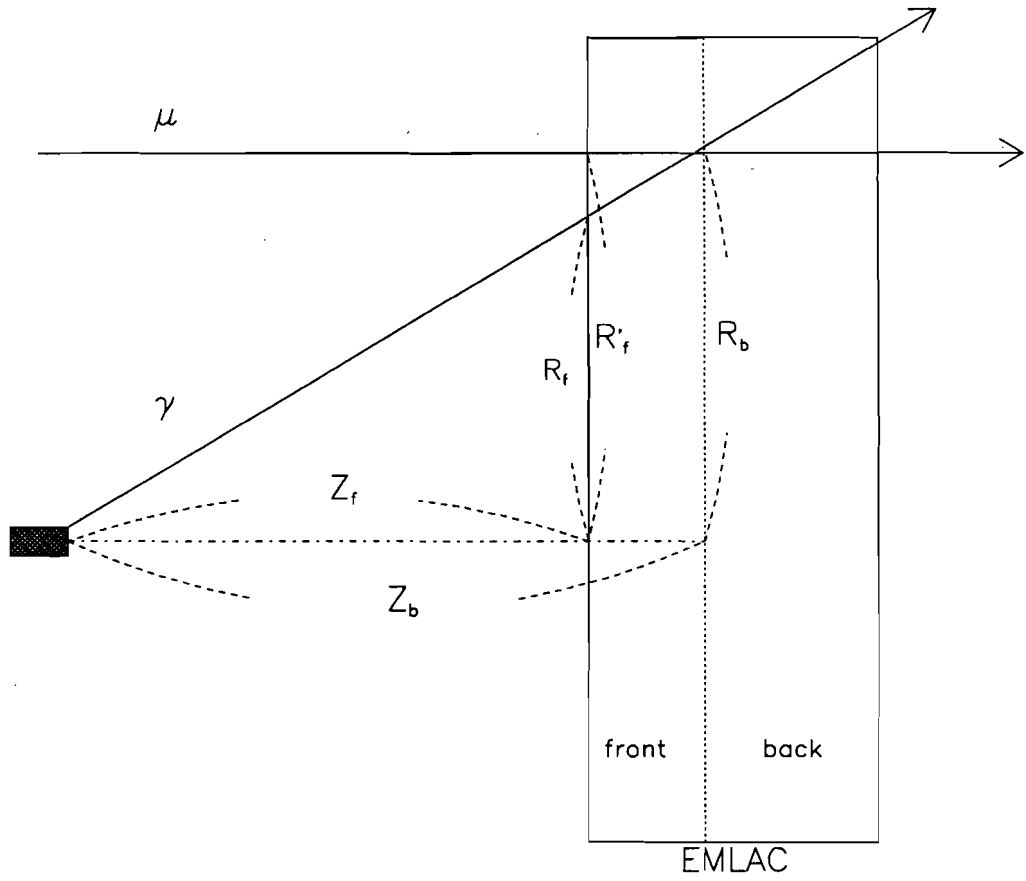


Figure 5.7: The idea of directionality. If photons come from a target, then  $\frac{R_f}{R_b} \simeq \frac{Z_f}{Z_b}$ , implying the directionality is near zero. For muons, the directionality is positive because  $R_f \simeq R_b$ .

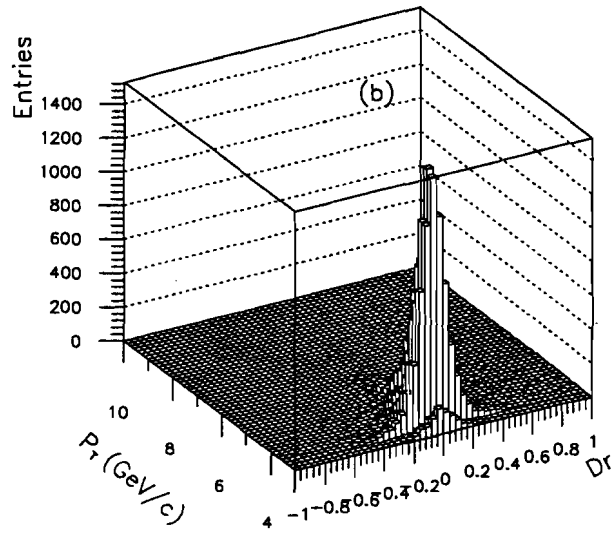
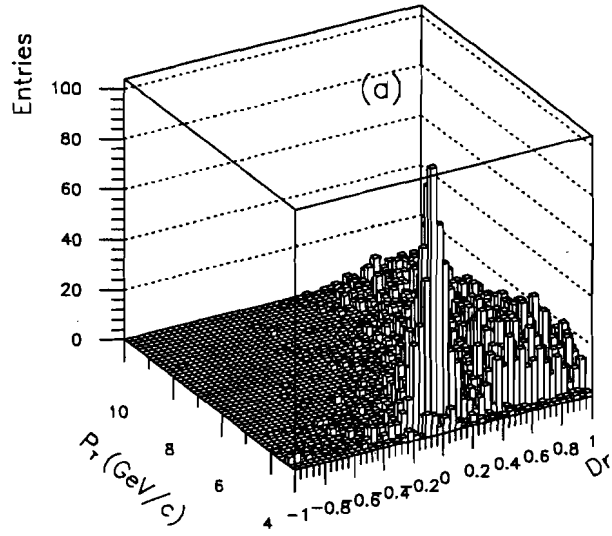


Figure 5.8:  $P_T$  versus directionality. (a) Veto walls fired in the same quadrant, (b) Veto walls did not fire in the same quadrant.

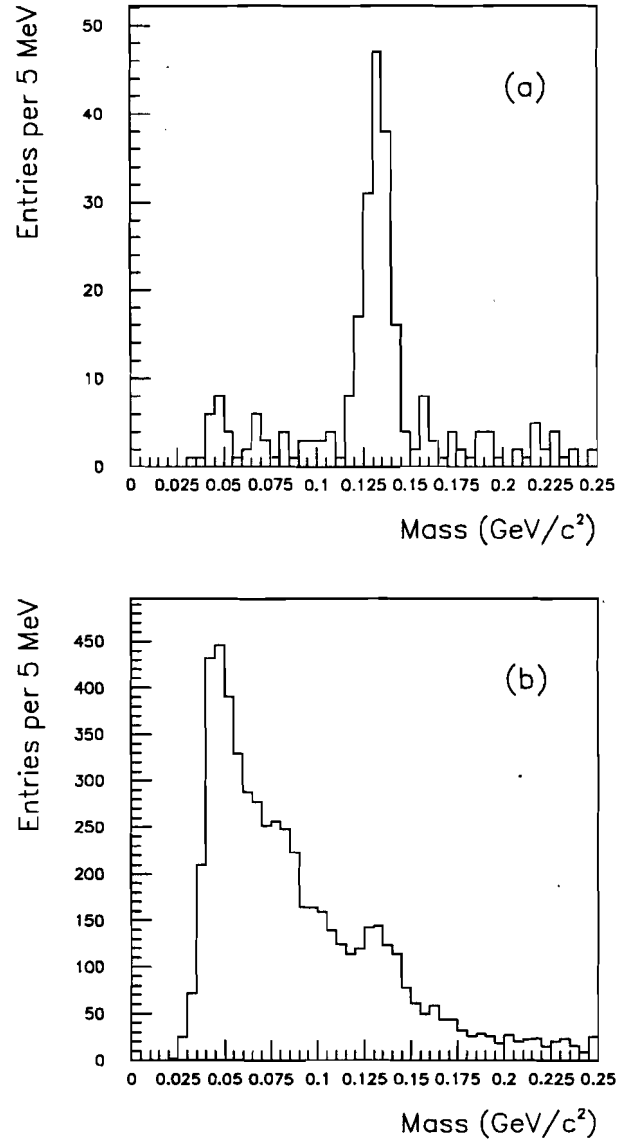


Figure 5.9: The two-photon mass spectrum with  $P_T$  ranging from 7 to 9 GeV/c: (a) Two Gamma trigger, (b) Single Local High trigger.



that event. Only photons from the same octant were combined to reconstruct the effective mass. In addition to the previous cuts in defining photons, two other cuts were applied in reconstructing  $\pi^0$ 's. They were,

- $P_T \geq 1.5 \text{ GeV}/c$ ;
- Asymmetry  $\leq 0.75$  for  $\pi^0$ 's.

Figure 5.10 shows the two photon mass with and without the asymmetry cut. The  $\pi^0$  peak is clearly seen in this plot. Since  $\pi^0$ 's are spin 0 particles, the decay directions in their rest frame ( $\theta^\dagger$ ) is isotropic. For a  $\pi^0$  near the speed of light ( $\beta = 1$ ), the cosine of its decay angle with respect to its original direction equivalents to the "asymmetry" defined in the lab frame. It can be expressed as follows:

$$\begin{aligned} A &= \frac{|E_1 - E_2|}{E_1 + E_2} \\ &= \beta \cos \theta^\dagger. \end{aligned} \tag{5.3}$$

where  $E_1$  and  $E_2$  are the energies of two photons, and  $\theta^\dagger$  is the decay angle with respect to the direction of the  $\pi^0$ . Therefore, the distribution of asymmetry is flat. Low energy photons in highly asymmetric decay do not have much contribution in triggering the event and they are difficult to reconstruct. As a result, the measured asymmetry distribution starts falling at large asymmetry due to the loss of low energy photons. The combinatorial background of the reconstructed  $\pi^0$ 's would be reduced when the asymmetry cut was applied because there weren't many of them at high asymmetry were reconstructed. Figure 5.11 shows the asymmetry distributions in the  $\pi^0$  mass and its sideband region. After the sideband subtraction, the falling spectrum appears in the plot. In this thesis, the highest asymmetry value for  $\pi^0$ 's was 0.75. The definition of  $\pi^0$ 's and their sidebands are expressed in Fig. 5.12, where region A is defined as  $\pi^0$  mass region, and region B as well as region C are defined as two sidebands of  $\pi^0$ 's. Because not every pair in the  $\pi^0$  mass region is a real  $\pi^0$ , two photons in the sideband region are treated as the  $\pi^0$  background. Note that the mass

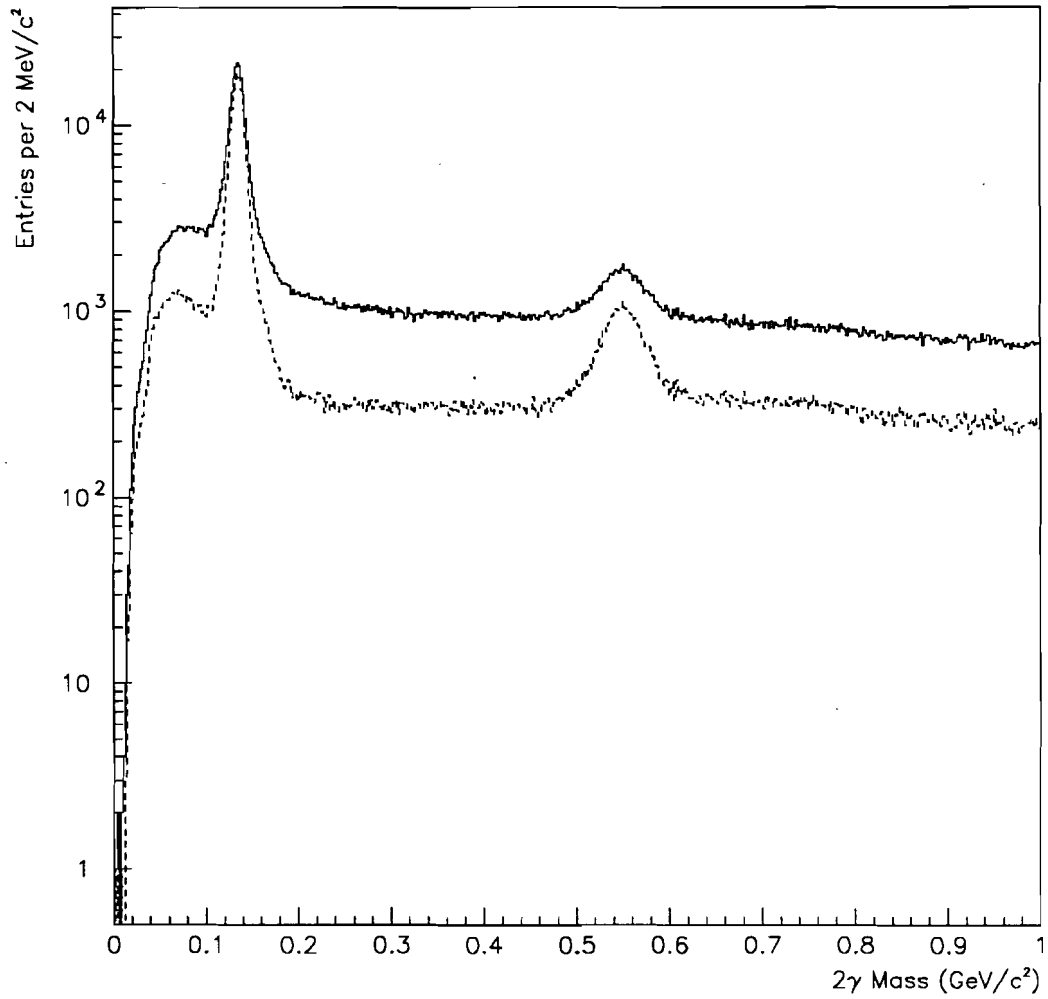


Figure 5.10: Two photon mass distribution with  $P_T$  above 4 GeV/c. Dash line is after applying the asymmetry cut.

range in regions B and C is only half of the  $\pi^0$  mass range. When we count the number of  $\pi^0$  background entries, we multiply the number of entries in regions B and C by 2.

## 5.3 Hadrons

All particles which were not identified as photons or electrons were considered as hadrons. Since most neutral hadrons decayed before reaching the calorimeter and those neutral hadrons detected by the calorimeter were not used in this analysis, we will emphasize the charged hadrons in this section.

The strategy of PLREC was to find as many of the charged tracks as possible. The final cleaning of these track candidates was performed at the DST level. The track cleaning, based on hit sharing, was very similar to the one used to flag tracks (see section 4.1.2). Any downstream track which used straw hits was considered a good track. In addition to the hit sharing, electromagnetic shower matching, vertex matching, and track's  $\chi^2$  were also used in cleaning tracks. A detailed discussion of this cleaning strategy is given in reference [29].

### 5.3.1 Downstream Y Impact Parameter Cut

A category of tracks which were not used in this analysis is that of tracks which did not emerge directly from the primary vertex. Those tracks most likely won't have SSD links and we should not measure the momentum assuming that they came from the primary vertex. The downstream impact parameter in the Y view (non-bend view) was used to do the check. This parameter was measured by projecting the downstream tracks into the primary vertex and by calculating the Y difference between the projection and the vertex. The uncertainty in the downstream impact parameter comes from the resolution of the tracking chambers, the momentum, and hit configuration of tracks. At first, we assumed the projection uncertainty can be

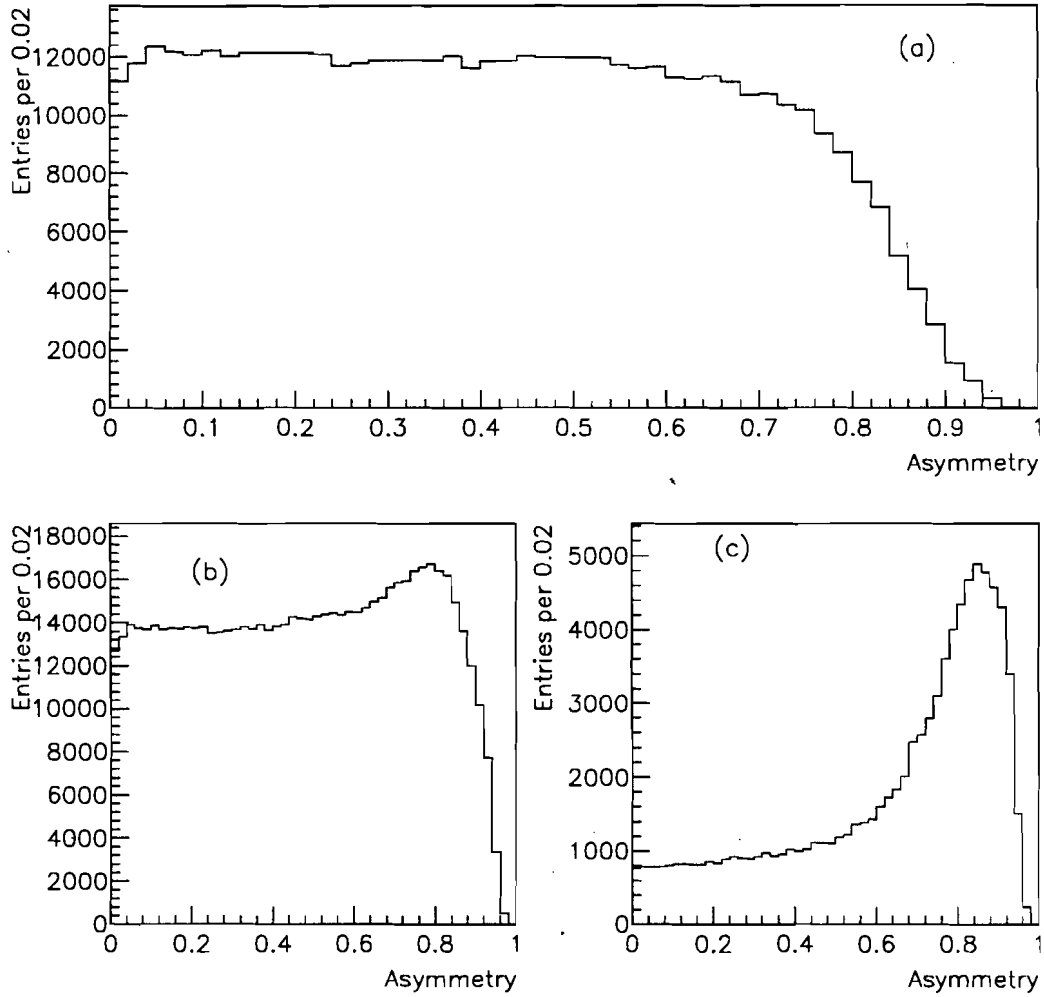


Figure 5.11: Asymmetry distribution of  $\pi^0$ 's at  $P_T \geq 2$  GeV/c. (a) After the side band subtraction, (b) Before the side band subtraction, (c) Asymmetry distribution for the side bands of  $\pi^0$ 's.

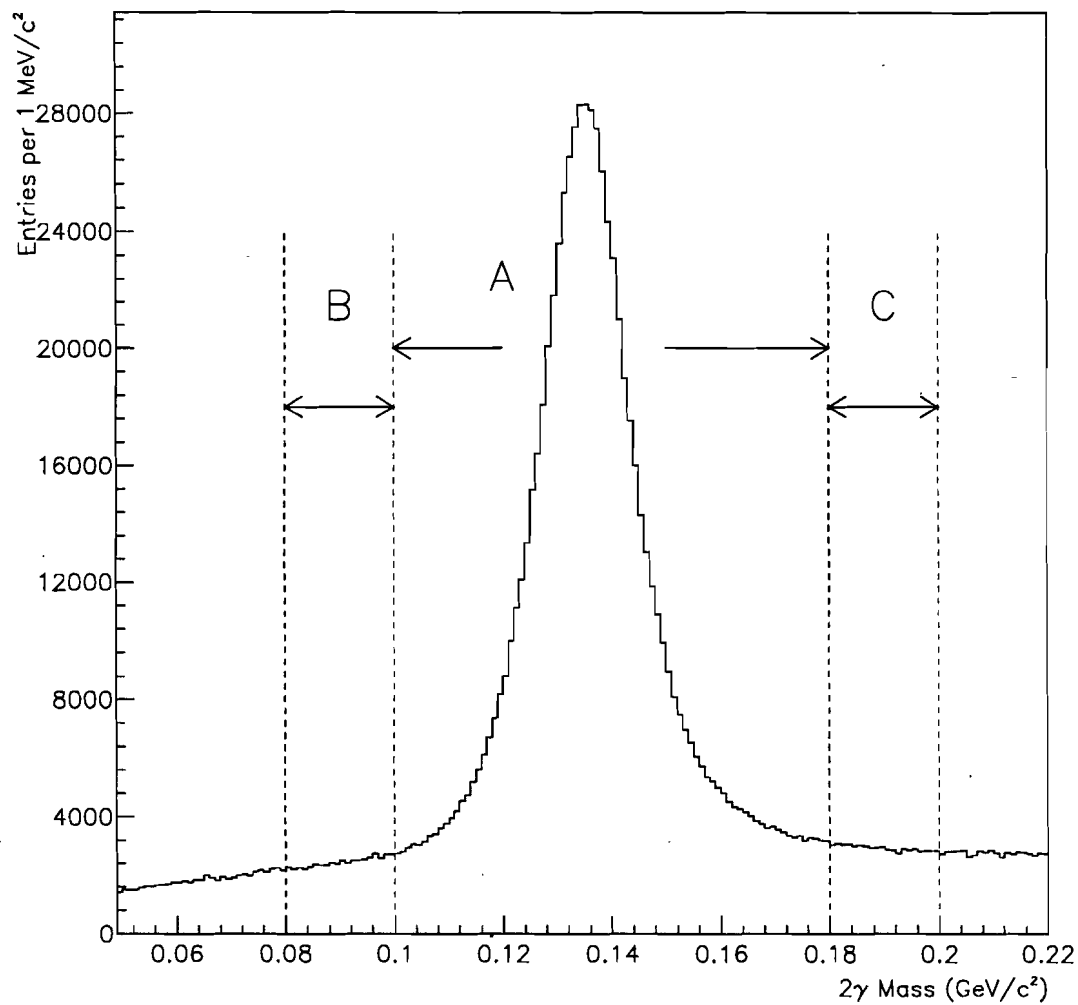


Figure 5.12: The definition of  $\pi^0$  mass region and the sideband region. Region A is the  $\pi^0$  region while region B and C are the sideband regions. The minimum  $P_T$  for each  $\pi^0$  is 2  $\text{GeV}/c$ .

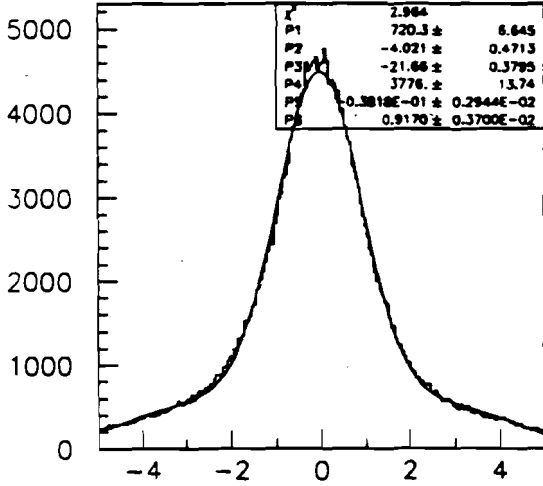
separated into two parts.

$$\sigma_{proj}^2 = \sigma^2(p) + \sigma_{th}^2 \quad (5.4)$$

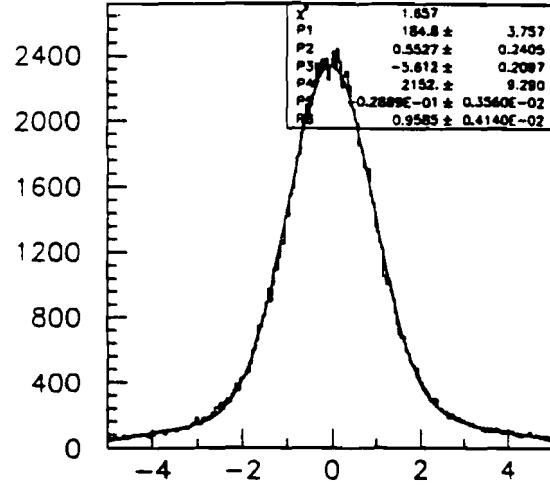
where  $\sigma(p)$  accounted the multiple scattering effect and could be measured from the experiment.  $\sigma_{th}$  accounted for the resolution of the charged tracks and could be calculated using the error matrices of tracks, which depend on the uncertainty of hits ( $\sigma_{hit}$ ). However, the accuracy of alignment also plays an important role. One can not simply use the theoretical  $\sigma_{hit}$  discussed in section 4.3 to obtain  $\sigma_{th}$ . Therefore, we first measured  $\sigma_{proj}$  and calculated  $\sigma_{th}$  using the theoretical  $\sigma_{hit}$  for the 16 (8) hit PWC (STRAW) linked tracks. From  $\sigma_{proj}$  and  $\sigma_{th}$ , the functions  $\sigma(p)$  were determined: one for PWC tracks and the other one for STRAW tracks. We then checked if Eq. 5.4 was also valid for the tracks with different numbers of hits using the  $\sigma(p)$  and the same  $\sigma_{hit}$ . We adjusted  $\sigma_{hit}$  to measure  $\sigma_p$  from 16 (8) hit PWC (STRAW) linked tracks, and evaluated the validity of Eq. 5.4 for tracks with different number of hits. It appeared that if the uncertainty of PWC (STRAW) hits were 1.5 (1.6) times the intrinsic resolution of PWC (STRAW) hits, equation 5.4 worked well. The intrinsic resolution is 750  $\mu\text{m}$  for PWC hits and 250  $\mu\text{m}$  for STRAW hits for this study. Therefore, we are able to estimate the  $Y$ -projection uncertainty of all downstream tracks. Figures 5.13 and 5.14 display the distributions of  $Y$  impact parameter divided by the predicted uncertainty in different momentum regions. The fitted gaussian widths of these ratios were around 1, indicating that the predicted values were close to the measured values. Any track whose downstream  $Y$  impact parameter was 5 times bigger than the predicted value was excluded from this analysis.

### 5.3.2 ZMP Electrons Revisited

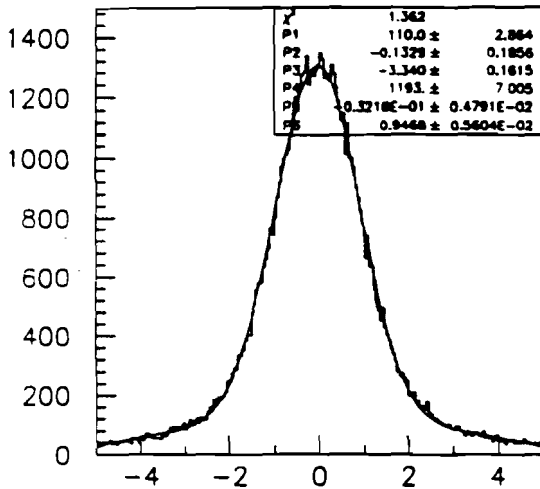
Even after the above cuts to clean charged tracks, some of the remaining charged tracks do not have a proper momentum measurement. Figure 5.15 shows the  $P_T$  and rapidity spectrum of charged tracks with  $P_T$  above 1.5 GeV/c. There is a spike in



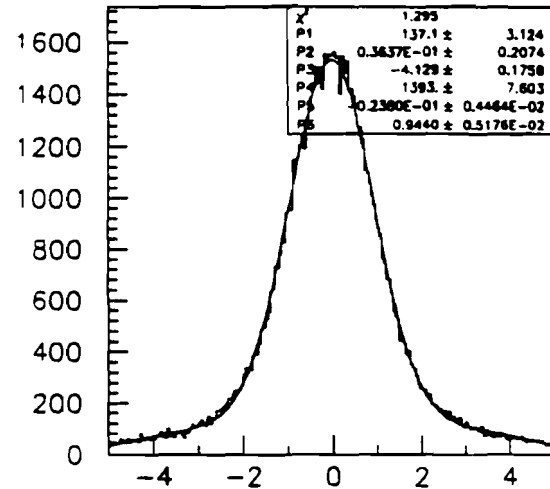
PWC YIMP/ $\sigma_{theo}$ ,  $P < 5$



PWC YIMP/ $\sigma_{theo}$ ,  $5 < p < 10$



PWC YIMP/ $\sigma_{theo}$ ,  $10 < p < 15$



PWC YIMP/ $\sigma_{theo}$ ,  $15 < p < 25$

Figure 5.13: PWC Y impact parameter over the predicted value in four different momentum regions. The function of the fit is a second order polynomial plus a gauss function. p6 is the gaussian width.

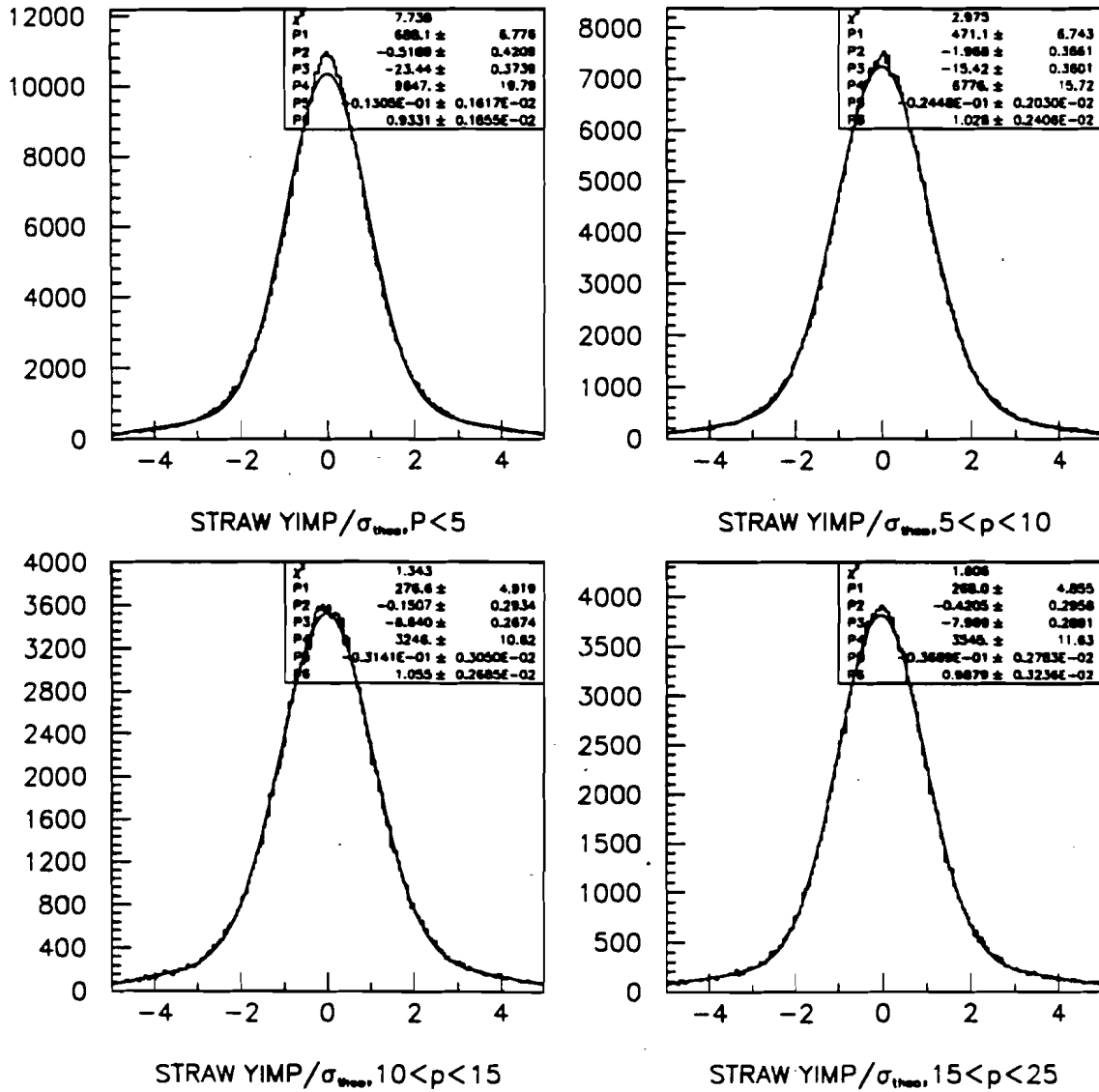


Figure 5.14: STRAW Y impact parameter over the predicted value in four different momentum regions. The function of the fit is a second order polynomial plus a gauss function. p6 is the gaussian width.



the backward rapidity region and a large tail in the high  $P_T$  region. We investigated this problem from the Monte Carlo (MC). In the MC data, the same tail in the reconstructed  $P_T$  spectrum also appeared, but that tail did not exist in the generated  $P_T$  spectrum. It turns out that a large fraction of those “high  $P_T$ ” tracks in the MC data are from photon conversions or secondary interactions after the dipole magnet. Figure 5.16 shows the generated Z-vertex position of charged tracks which, in combination with a high  $P_T$   $\pi^0$ , form a very high mass state. The peaks in this plot are the positions of the helium bag, downstream interaction counters, the first PWC module, straw chamber 1, and the second PWC module. Those tracks (ZMPs) from photon conversions in the material situated after the magnet point back directly to the vertex, due to the small opening angle. They, therefore, can not be ruled out by the  $Y$  impact parameter cut, and since they show little bend in the magnet their “measured” momenta are huge. Even though such tracks with poor momentum measurement are rare, so are the high  $P_T$  charged particles. These ZMPs would mimic high  $P_T$  charged hadrons and caused a severe problem in measuring  $\pi^0\pi^\pm$  cross sections. An extra cleaning was needed to get rid of these tracks.

The first cut used to eliminate these ZMPs is to require at least three hits in the first PWC module (PWC1 cut). Figure 5.17 shows the distribution of the number of hits in the first PWC module. The majority of tracks have more than two hits in the first PWC module, but those suspected tracks tend to have fewer hits. Therefore, we require that each downstream track with  $P_T$  greater than 1.5 GeV/c must contain three or four hits in the first PWC module. Although this cut will also cut out some real tracks, it eliminates about 65% of downstream ZMPs. Since we are dealing with ZMP tracks which mimic high  $P_T$  particles, the calorimeter can also be used to veto them. The calorimeter veto is not necessarily the same for all tracks because linked tracks have a better chance of coming from the primary vertex. The following constraints are applied to eliminate tracks with improperly determined momentum.

- Any track which hits the LAC and has measured momentum greater than 80

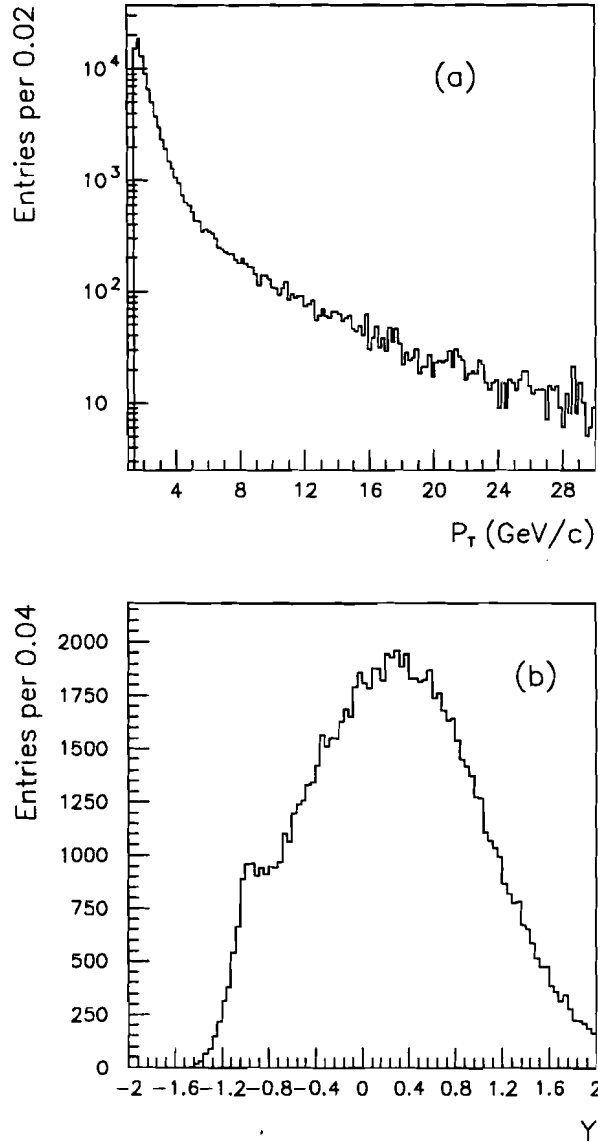


Figure 5.15: The  $P_T$  and rapidity spectrum of charged tracks. (a)  $P_T$  distribution on semi-logarithmic scale, (b) rapidity distribution. The long tail in the  $P_T$  spectrum and the spike at  $-1$  in rapidity indicate that some tracks do not have proper momentum measurement.

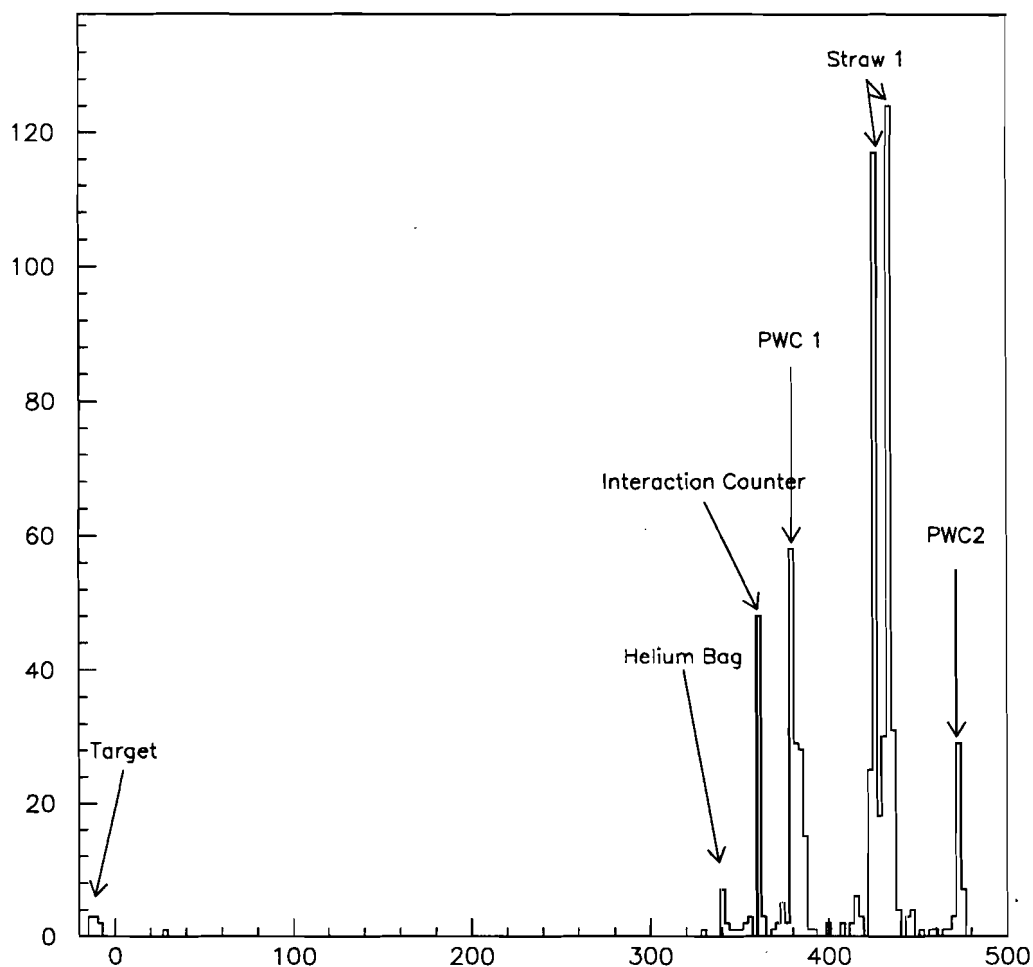


Figure 5.16: The generated Z position of MC tracks. Each track combines with a high  $P_T \pi^0$  in the same event to form a high mass state above  $20 \text{ GeV}/c^2$ . Since the total energy in the hadron-hadron center of momentum frame is  $31 \text{ GeV}$ , it's very unlikely to have dihadron mass greater than  $20 \text{ GeV}/c^2$ . The momenta of these tracks are probably not properly measured.

GeV/c must shower in the LAC, either the EMLAC or the HALAC. In addition, the energy measured by the LAC divided by the momentum measured by the tracking system ( $E/P$ ) must be above certain values. They are

$$E/P \geq \begin{cases} 0.15 & \text{if a track only showers in the EMLAC} \\ 0.2 & \text{if a track only showers in the HALAC} \\ 0.19 & \text{if a track only showers in both parts of the LAC} \end{cases}$$

- If a track with measured momentum greater than 55 GeV/c has only X-view or Y-view links and it hits the LAC, this track must either shower in the HALAC or have  $E/P$  ( $E$  from the EMLAC) greater than 0.1.
- If a track has measured momentum above 45 GeV/c and does not link in either view, this track must shower the LAC.

This calorimeter veto eliminates an additional 25% of the downstream converted ZMPs.

A kinematic cut is also implemented to distinguish tracks with poor momentum measurement from other tracks. Any particle produced by the collisions in the 1990 E706 run can have at most 15.5 GeV/c energy in the  $\pi^-$ -nucleon center of momentum frame. Hence, we boost all charged tracks back to the  $\pi^-$ -nucleon center of momentum frame and check their measured momentum. All tracks with measured momentum above 15 GeV/c are cut out of this analysis. Figure 5.18 shows the  $P_T$  spectrum before and after the cuts used in the analysis. The same cleaning cuts are also applied in the MC data to check the effect. Figure 5.19 shows the generated Monte Carlo  $P_T$  spectrum overlapped with reconstructed  $P_T$  distribution before and after the cleaning cuts. About 95% of tracks with mismeasured momentum are cut out.

### 5.3.3 Momentum Redetermination

The momentum measured by the tracking system mainly depends on the upstream and downstream tracks in the X view. It is easier to get the wrong X links than Y links, since the x link is determined solely via  $\Delta X$  at the center of the magnet (see

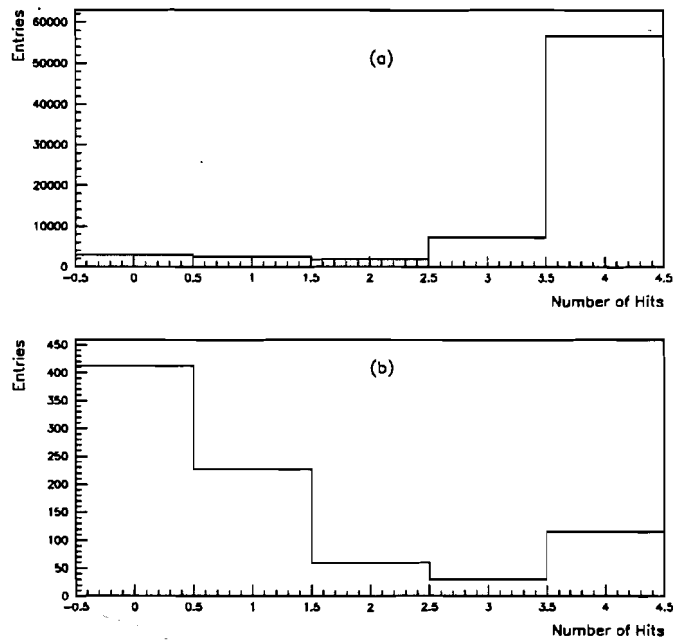


Figure 5.17: The distribution of number of hits in the first PWC module. (a) All tracks with  $P_T$  greater than 1.5 GeV/c, (b) The mass of  $\pi^0$ s and charged tracks are greater than 20 GeV/c<sup>2</sup>.

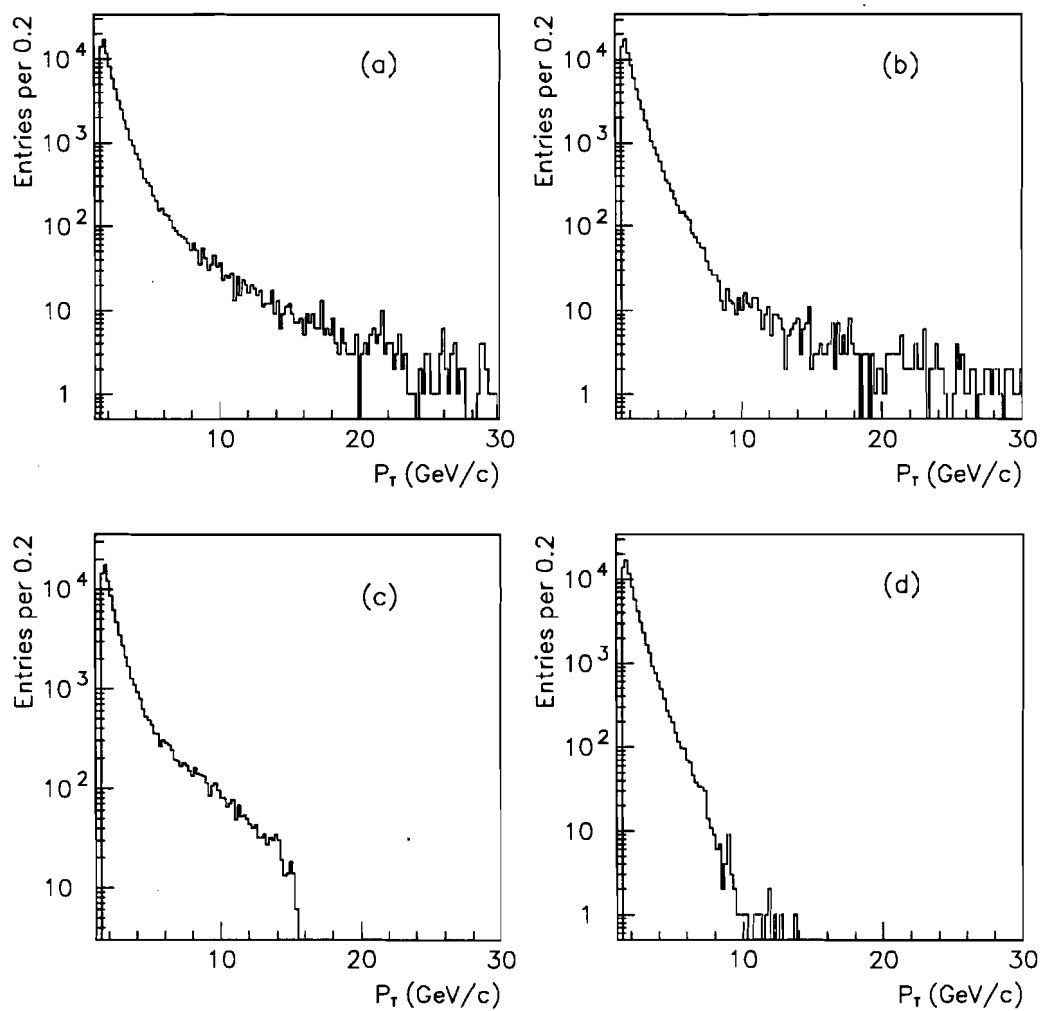


Figure 5.18: Charged track  $P_T$  distribution after different cuts for 1990 data. (a) PWC1 cut, (b) LAC cut, (c) kinematic cut, (d) PWC1, LAC, and kinematic cuts.

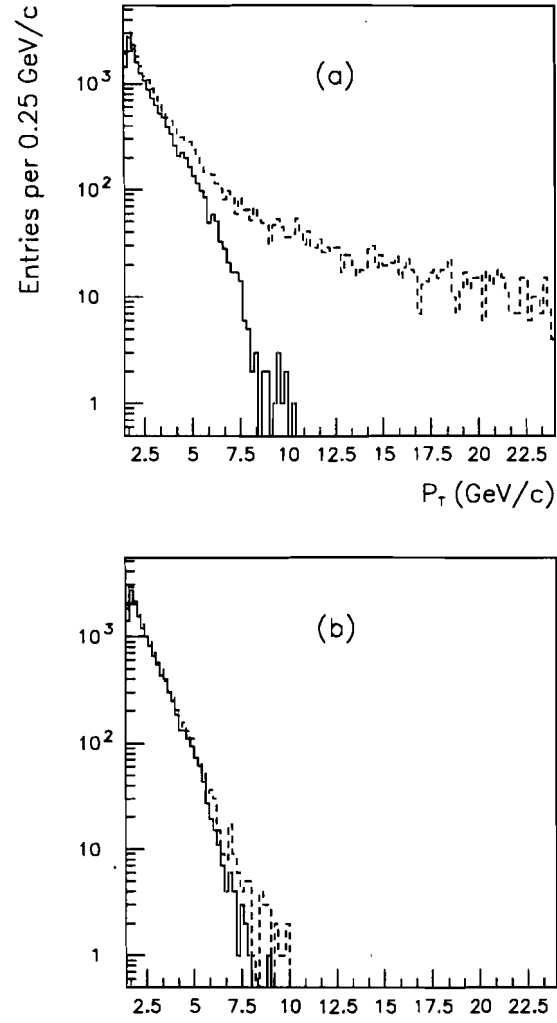


Figure 5.19: The reconstructed  $P_T$  distribution (dashed) compared to the generated distribution (solid) in the MC data. (a) Before the cuts, (b) After the cuts.

section 4.2.5). If a given downstream track comes from the primary vertex in an event, its upstream slope can be estimated by connecting its projection at the center of the magnet with the primary vertex. Thus, we can estimate the momentum ( $P_e$ ) and check whether it agrees with the measured value ( $P_m$ ). The variables,  $\frac{\Delta P}{P_m^2}$  and  $\frac{\Delta P}{P_e^2}$  were used in this study, where  $\Delta P$  is the difference between  $P_e$  and  $P_m$ . The distribution of  $\frac{\Delta P}{P_e^2}$  is similar to that of  $\Delta\theta$ , where  $\Delta\theta$  is the bending angle due to the magnetic field. The uncertainty of  $\Delta\theta$  comes from the resolution of the track chambers, which is momentum independent. Therefore,  $\frac{\Delta P}{P_e^2}$  is not sensitive to the momentum itself. Before applying this method, two criteria have to be satisfied: there is a vertex in the event and the downstream Y impact parameter is within five times the predicted value. In Fig. 5.20, a tail appears in plots of both  $\frac{\Delta P}{P_e^2}$  and  $\frac{\Delta P}{P_m^2}$ . The Monte Carlo study showed that the measured momentum gave a better momentum determination in most cases unless  $\frac{\Delta P}{P_e^2}$  was large (greater than 0.01),  $P_m$  and  $P_e$  were not too small (greater than 4 GeV/c), and  $P_e$  was not too large — less than 90 GeV/c. This indicates that our linking code most likely linked to an improper X SSD track when  $\frac{\Delta P}{P_e^2}$  was huge. Therefore, in this thesis, if the following criteria were met, the estimated momentum was used instead of the measured momentum:

1. The downstream track had an X view link and there was a primary vertex in the event.
2. The downstream Y impact parameter was within 5 times the predicted value.
3.  $P_e$  and  $P_m$  were greater than 4 GeV/c.
4. The SSD Y impact parameter was less than 0.015 cm if a track had SSD Y view links.
5.  $\frac{\Delta P}{P_e^2}$  was greater than 0.01/0.005 for PWC/STRAW tracks.
6.  $P_e$  was less than 55 GeV/c.



When we studied tracks as a function of  $\frac{\Delta P}{P^2}$ , we first applied the track cleaning cuts to eliminate the downstream converted ZMPs. There was another class of tracks with large  $\frac{\Delta P}{P^2}$  that called our attention. If  $\frac{\Delta P}{P^2}$  of a track was large ( $> 0.01$ ) and its  $P_e$  was also large ( $> 300$  GeV/c), the MC data showed that this track was the downstream ZMP track. These ZMPs, which passed the three cuts described in the last section, linked to an improper  $X$  SSD track and their measured momenta were less than 100 GeV/c. Therefore, we could use the variables  $\frac{\Delta P}{P^2}$  and  $P_e$  to eliminate the remaining downstream converted ZMPs. If  $\frac{\Delta P}{P^2}$  was larger than 0.01 (0.005) for a PWC (STRAW) track and its  $P_e$  was greater than 300 GeV/c, this track was disregarded in the analysis.

## 5.4 Photon Energy Scale

The energy scale of the EMLAC is crucial in this experiment. Since the  $\pi^0$  cross section has a steeply falling spectrum in  $P_T$  a small uncertainty in  $P_T$  will result in a relative large uncertainty in cross section. However, understanding the energy scale to less than 1% level is also a difficult task.. Since the author was also involved in this project, a brief summary is given here. A detailed discussion is in reference [24].

The uncorrected  $\pi^0$  reconstructed mass was found to increase with time. In Fig. 5.21, the  $\pi^0$  and  $\eta$  mass over their nominal values are plotted versus time. The fitted function in the plot was used to correct this time dependent effect. A similar effect was observed in the hadronic section of the LAC. Figure 5.22 displays the average  $E/P$  versus time, where  $E$  is the energy of charged hadrons which only shower the HALAC, and  $P$  is the corresponding momentum measured by the tracking system. The same function of  $\pi^0$  mass vs time is superimposed on the  $E/P$  plot, implying a consistent increase in the entire LAC. We do not have a fully consistent explanation for this dramatic effect yet. This time dependent correction was applied in EMREC and HCREC to produce the DST output and the corresponding correction factor was also stored in the DST data.

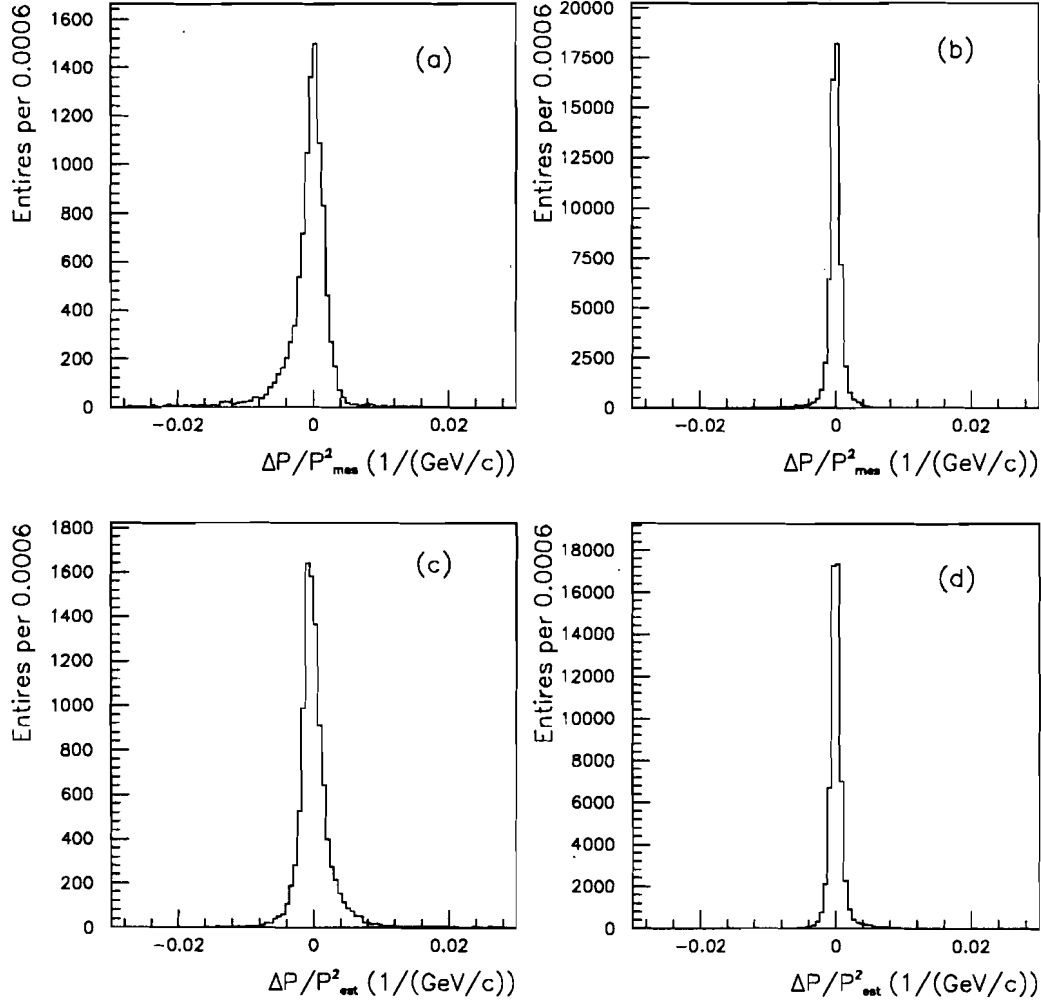


Figure 5.20: The top two plots are the distributions of  $\frac{\Delta P}{P_m^2}$  for (a) PWC tracks and (b) Straw tracks, while the bottom two are the distributions of  $\frac{\Delta P}{P_e^2}$  for (c) PWC tracks and (d) Straw tracks.

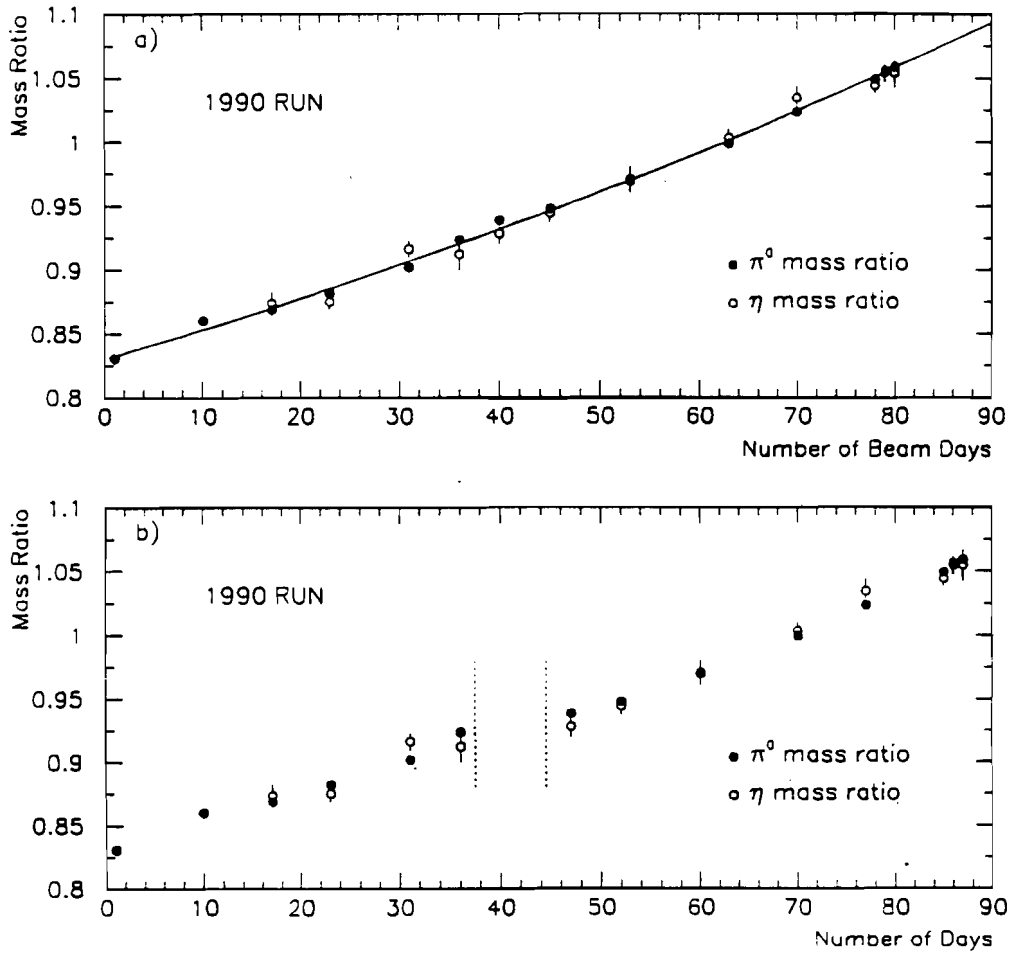


Figure 5.21: Uncorrected  $\pi^0$  and  $\eta$  mass as a function of time during the 1990 run. Both masses are normalized to their nominal values. Beam days was counted when there were beams in those days. The reference day is 31-May-1990. There was a 7-day shutdown, indicated in the vertical lines in (b), during 1990 run. During this shutdown period, the measured  $\pi^0$  mass did not change. This beam-off time was, therefore, subtracted from the fit in (a) to correct this time-dependent effect.

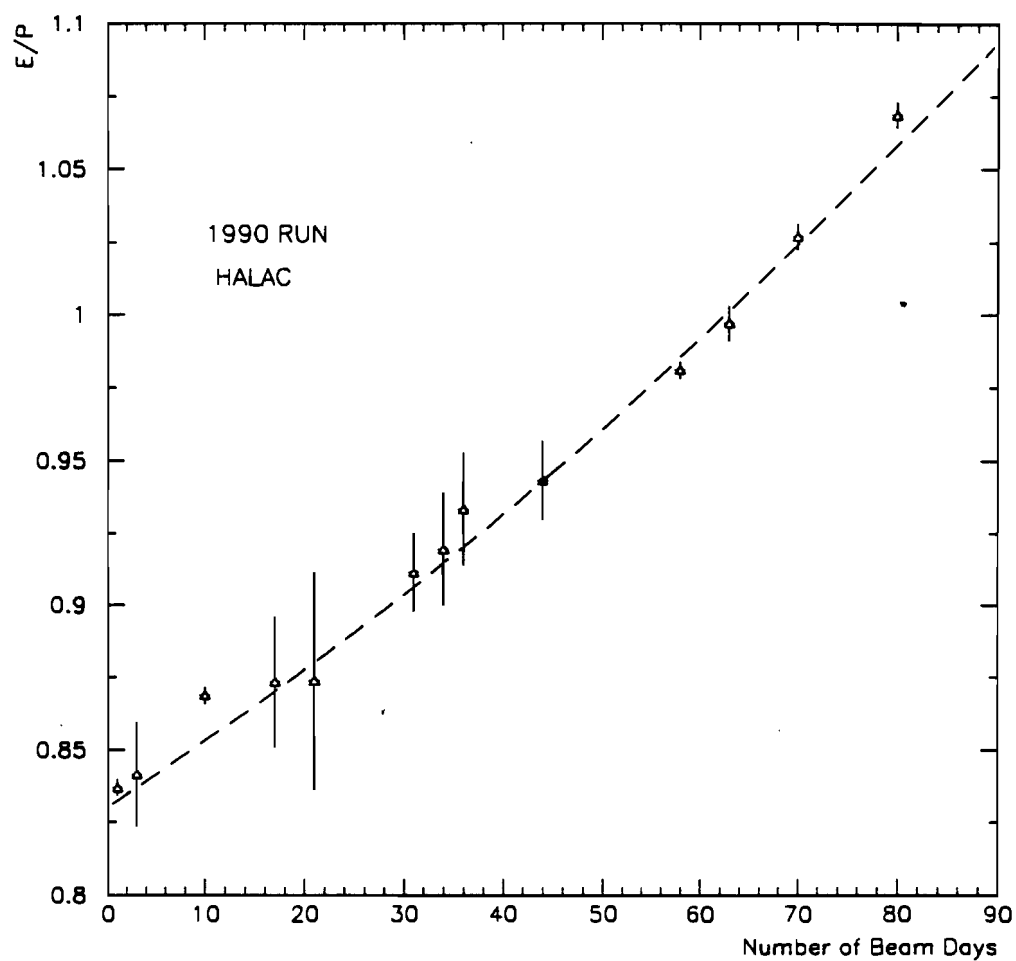


Figure 5.22:  $E/P$  as a function of "beam days" for charged hadrons. The dashed line represents a fit to the data points in Fig. 5.21.

The energy correction of photon-like showers was corrected in the DST and determined in the following steps:

- Determine the initial octant-to-octant corrections. The uncorrected  $\pi^0$  mass, with  $P_T \geq 3.5$  GeV/c, was normalized to the nominal values.
- Apply the corrections to photons near the inner/outer boundary. This was done to account for the overcorrection of  $\phi$  GAMMA energy near the inner/outer boundary. If a photon was within 5 cm of this boundary, the photon energy was assigned as twice the energy measured in the R view instead of the sum of R view energy and  $\phi$  view energy.
- Apply the energy loss corrections to account for the energy lost in the front material of the LAC. The correction factor was determined using Monte Carlo to simulate the energy loss. The energy loss was a monotonically increasing function of the energy.
- Measure the residual energy correction as a function of the radial position. Two samples of data were investigated to determine the correction functions: one was the  $\pi^0$ 's from the TWO GAMMA trigger with  $P_T \geq 2$  GeV/c; the other one was the  $\eta$ 's from the SINGLE LOCAL HIGH trigger with  $P_T \geq 3.5$  GeV/c. This correction function was measured for each octant independently. Figures 5.23 and 5.24 show the radial dependence of the relative  $\pi^0$  mass in each octant. The advantage of using the low  $P_T$   $\pi^0$ 's and  $\eta$ 's is that two photons from these samples tend to have wider separation. Therefore, the uncertainty of  $\pi^0$  mass due to the overlapping showers of two photons is minimized. Figure 5.25 indicates that the  $\pi^0$  and the  $\eta$  have similar radial dependences.
- Redetermine the octant-to-octant energy corrections using the high  $P_T$   $\eta$ 's.
- Check for residual effects on the  $\pi^0$  mass as observed in the  $\gamma e^+ e^-$  sample. After the previous corrections were applied, the  $\gamma e^+ e^-$  mass was used to check

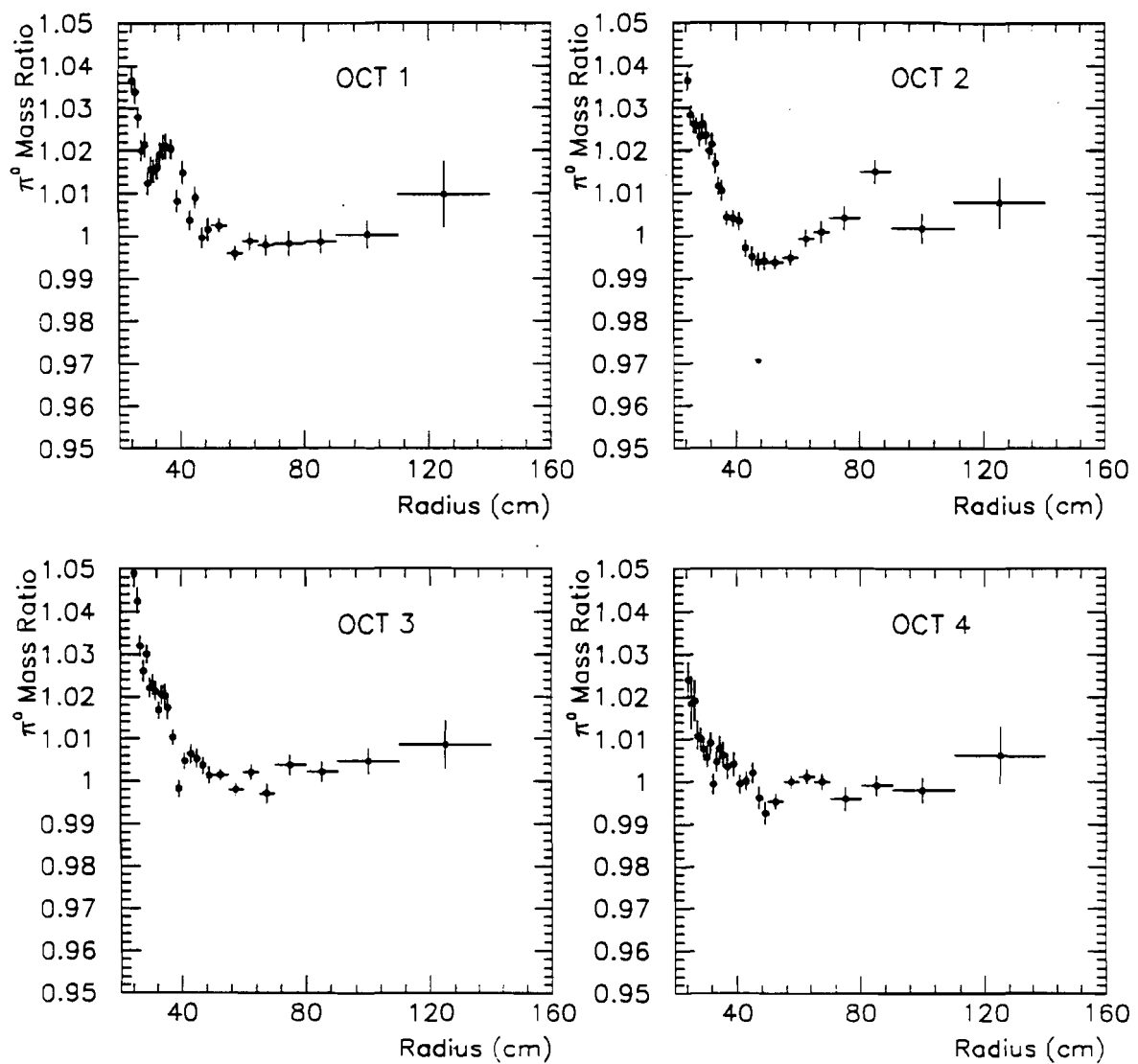


Figure 5.23: Radial dependence of the reconstructed  $\pi^0$  mass over the nominal value in octants 1 through 4.

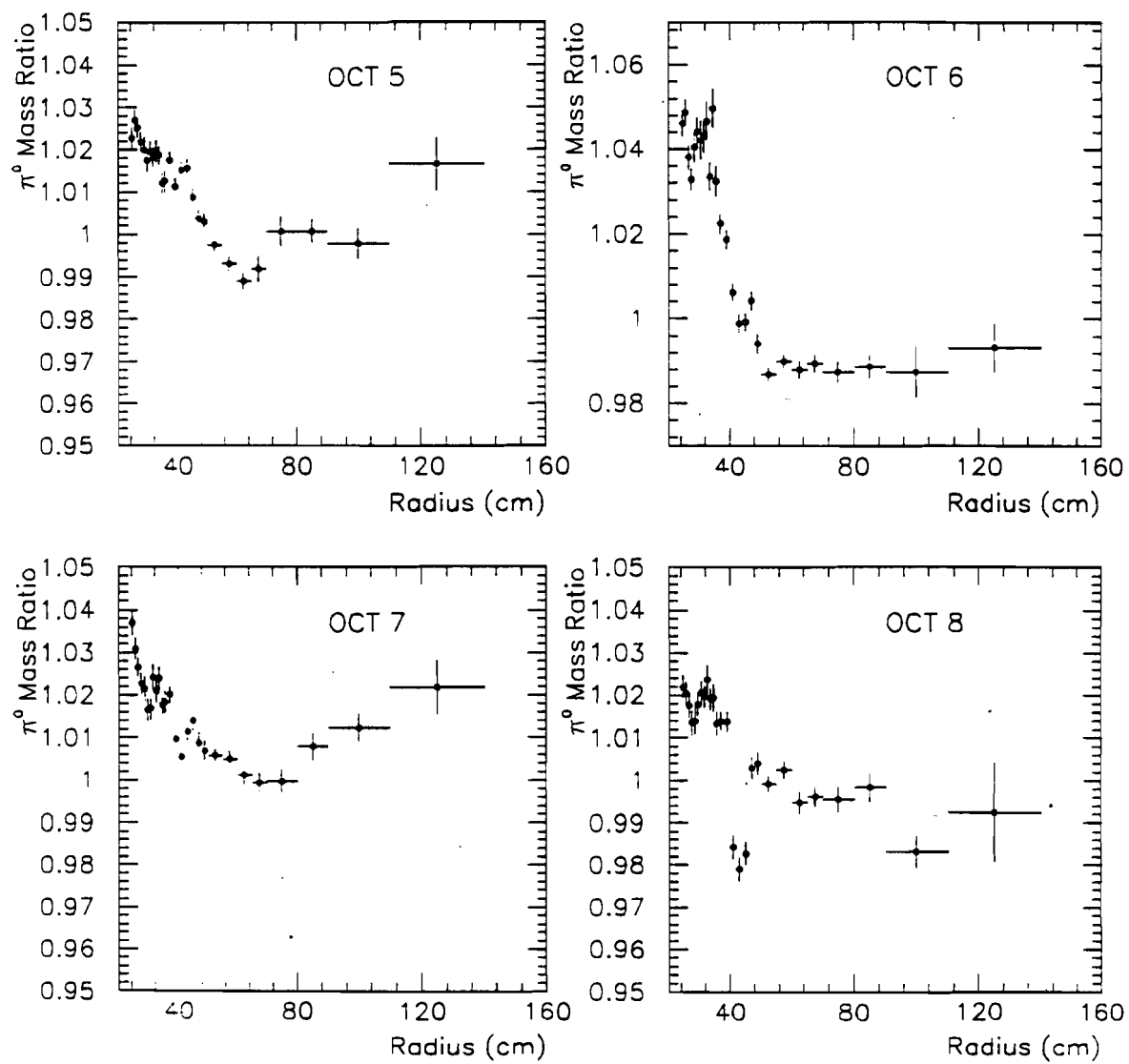


Figure 5.24: Radial dependence of the reconstructed  $\pi^0$  mass over the nominal value in octants 5 through 8.

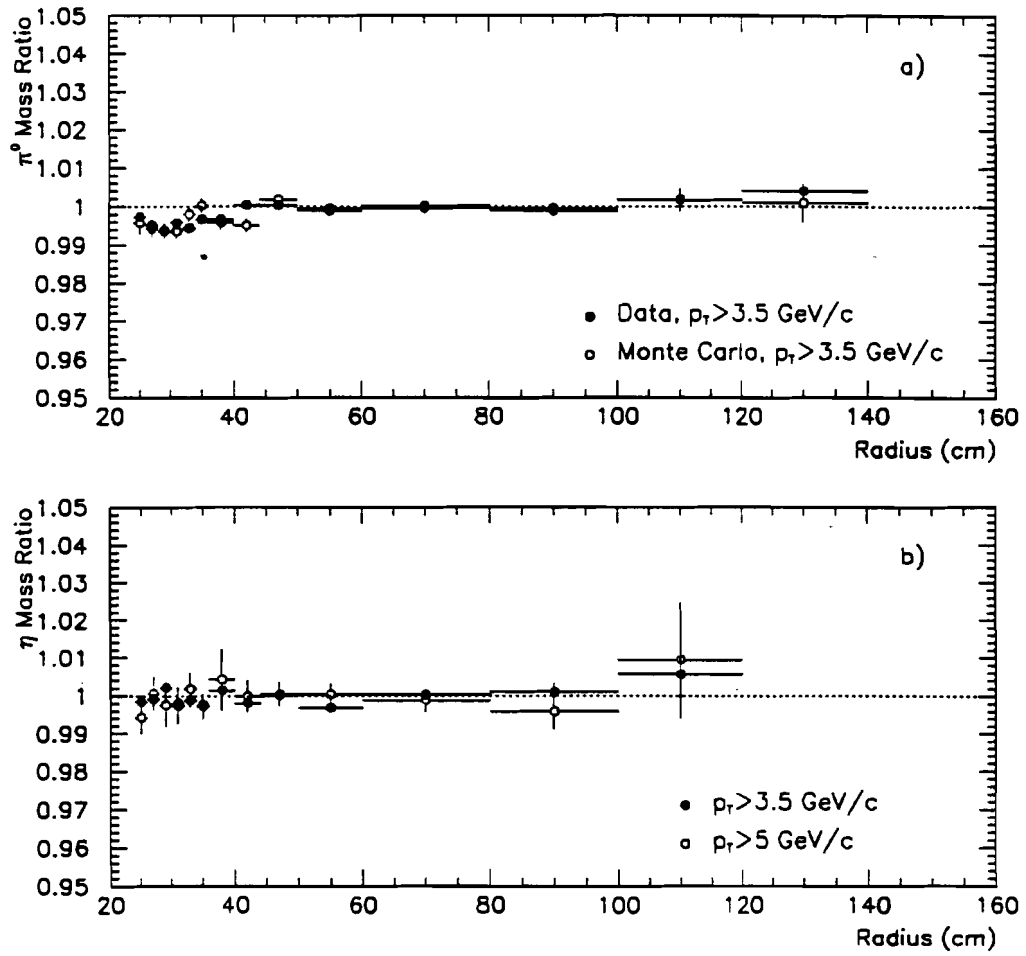


Figure 5.25: Radial dependence of the reconstructed  $\pi^0$  and  $\eta$  mass over their nominal values.



if there was any variation in mass as a function of photon energy. The momenta of the ZMP electrons were determined from the tracking system, while the photon energy was measured from the EMLAC. It turned out that the mass of  $\pi^0 \rightarrow \gamma e^+ e^-$  was nearly independent of photon energy, but the overall mass was about 0.3% lower than the nominal value. This can be explained by the electron's energy lost due to bremsstrahlung. The reconstructed mass of  $\pi^0 \rightarrow e^+ e^- e^+ e^-$  should be even lower. Figure 5.26 shows the invariant mass of  $\gamma e^+ e^-$  and  $e^+ e^- e^+ e^-$ . As expected, the  $\pi^0$  mass from the four electron mode is lower than that from the  $\gamma e^+ e^-$  mode.

After all the corrections were applied, the uncertainty in the energy scale was about 0.5%:

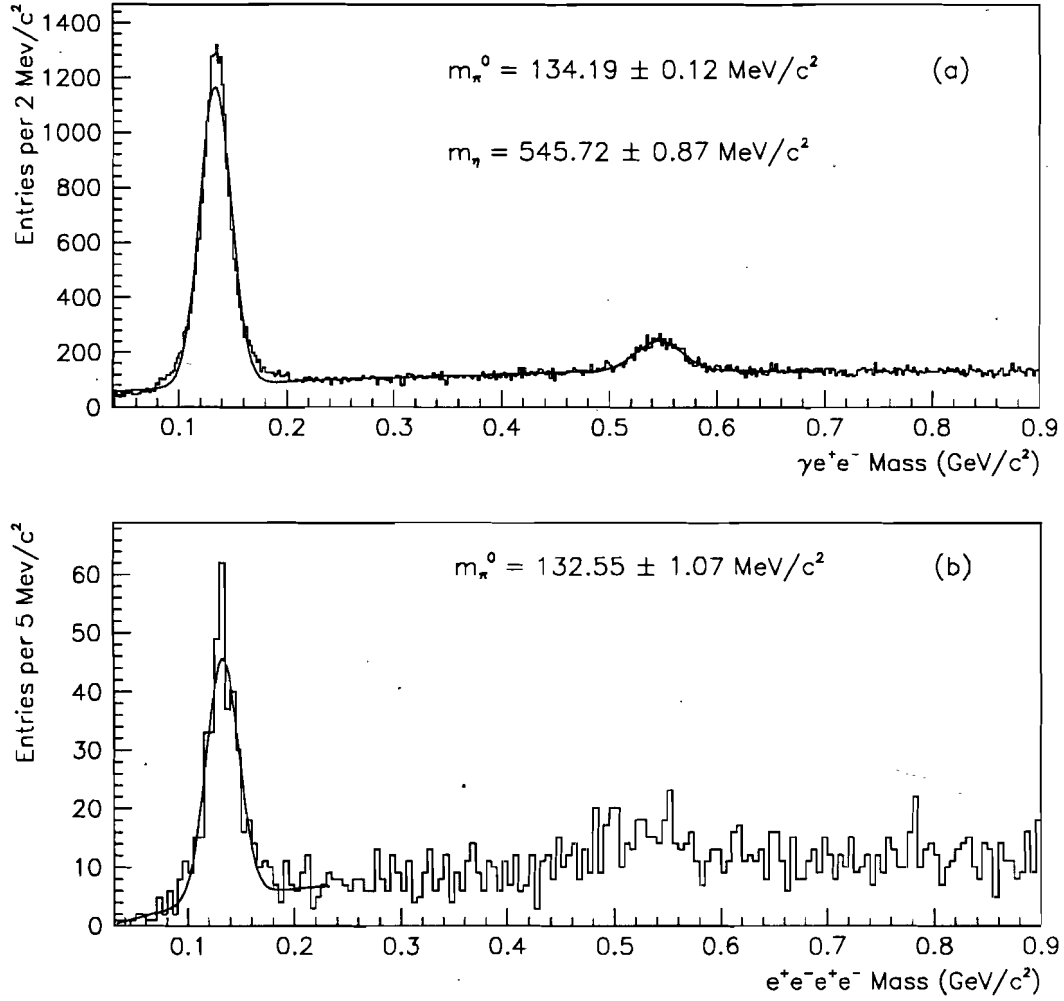


Figure 5.26: The invariant mass of (a)  $\gamma e^+ e^-$  and (b)  $e^+ e^- e^+ e^-$ . The  $P_T$  cut for the  $\gamma e^+ e^-$  sample is 3 GeV/c, while the  $P_T$  cut for the four electron sample is 1 GeV/c.

# Chapter 6

## Data Analysis

This chapter discusses the physics analysis and presents the results for high mass di- $\pi$  production in 515 GeV/c  $\pi^-$  nucleon collisions. It is divided into five sections: data selection and the corresponding corrections for the di- $\pi$  events, cross sections and  $\cos \theta^*$  of di- $\pi$  production, dijet characteristics from the di- $\pi$  events, nuclear dependence, and conclusions.

### 6.1 Data Selection

This thesis uses two different triggers to study the di- $\pi$  events: the SINGLE LOCAL HIGH trigger for  $\pi^0\pi^\pm$  production and the TWO GAMMA trigger for  $\pi^0\pi^0$  production. The trigger corrections and the total number of events processed in the 1990 run were already described in section 3.3. The following sections discuss various cuts used to identify the proper di- $\pi$  events and the correction factors associated with these cuts.

#### 6.1.1 Vertex Cut

Each event was required to have a reconstructed primary vertex within an appropriate fiducial volume. Figure 6.1 displays the Z position of the primary vertex for events which have di- $\pi$  pairs. The Be and Cu targets, along with the SSD planes are clearly visible. The Z position of the primary vertex identifies the target material involved in the interaction. Figure 6.2 shows the X-Y positions of the primary vertices

and the square represents the area covered by the beam hodoscope. The transverse positions of the Be and Cu targets are also shown in this figure. The plots in Fig. 6.2 indicate that the beam hole counter and beam hodoscope, which were used to define incident beam particles, were centered on the beam, but the targets were not. A fraction of beam particles counted by the beam hodoscope, therefore, did not hit the targets. Target fiducial cuts were invoked as follows:

- The reconstructed vertex was inside the area of the beam hodoscope;
- $\sqrt{(V_x + 1.12)^2 + (V_y - 0.07)^2} < 0.96$  cm.  $V_x$  and  $V_y$  are respectively the X and Y positions of the primary vertices.

The corresponding correction for the target fiducial cuts was determined by using the reconstructed vertices in the SSD planes which were large enough to intercept all beam particles. The correction factor results is the ratio of the number of vertices inside the fiducial region to the number of vertices inside the area of the beam hodoscope. This correction was measured as 35% with a 2% systematic uncertainty.

The vertex reconstruction efficiency was measured using the Herwig generated  $\pi^0$  data. The SSD and PWC plane efficiencies and hit noises were parametrized from the experimental data, and were implemented into E706 Monte Carlo. The vertex finding efficiency is determined by counting the number of vertices reconstructed by PLREC compared to the number of generated vertices. It turns out that the vertex finding efficiency was rather uniform in Z with the value 99.6%.

### 6.1.2 LAC Cuts

There are four different cuts applied to  $\pi^0$ 's in this analysis: the *EFT* cut, the energy asymmetry cut, the LAC fiducial cut, and the muon rejection cuts. All these cuts were already described in chapter 5. The corresponding corrections for the *EFT* cut and the LAC fiducial cut were taken into account in the reconstruction efficiency and geometrical acceptance, respectively. The asymmetry cut (0.75) theoretically cut out one fourth of the  $\pi^0$ 's, and the corresponding correction factor is, hence, 4/3.

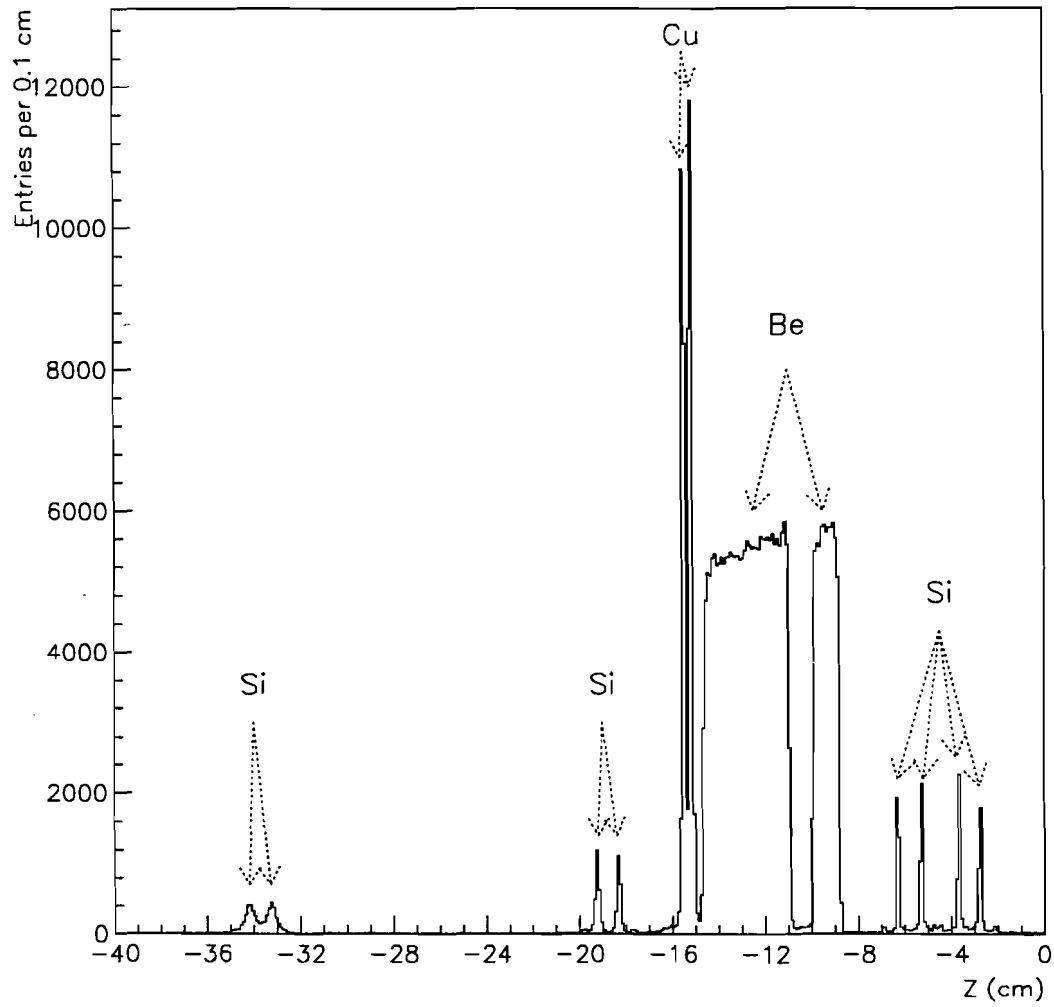


Figure 6.1: Distribution of the reconstructed primary vertices in the di- $\pi$  events. The Silicon SSD planes are labeled Si. No photon conversion correction is applied.

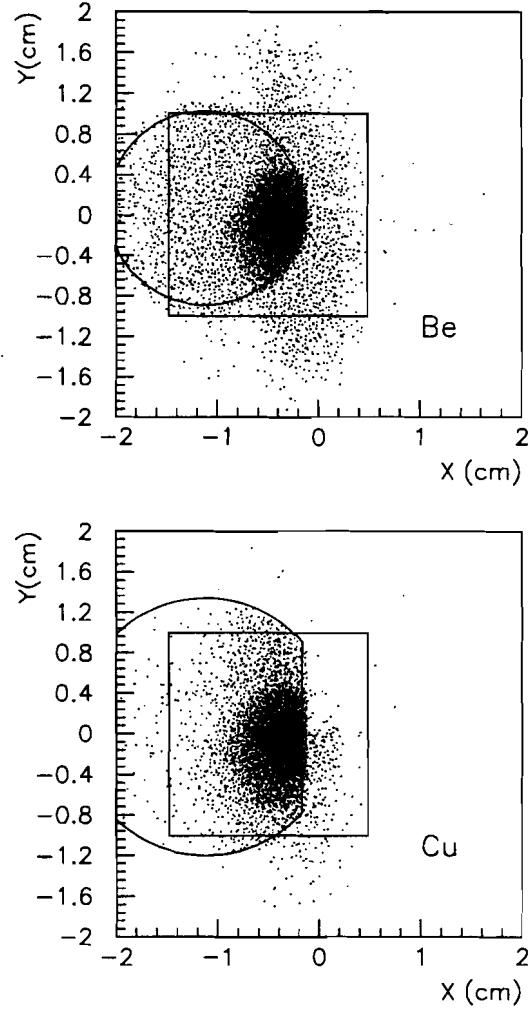


Figure 6.2: X-Y positions of reconstructed primary vertices. The square corresponds to the effective area of the beam hodoscope. The circle in the upper plot shows the shape of Be targets, and the truncated circle in the lower plot indicates the effective region of Cu targets.

The muon rejection cuts deserve some attention here. Muons do not have as much impact on di- $\pi$  production as on single  $\pi^0$  or  $\eta$  production in this experiment. The muon-rejection cuts were applied only for those  $\pi^0$ 's with  $P_T$  above 9 GeV/c. The impact of the muon cuts were studied using  $\pi^0$ 's in the kinematic region where muons had less effect in di- $\pi$  events. Figure 6.3 shows the fraction of the  $\pi^0$ 's which pass the muon cuts in  $P_T$  between 4 to 9 GeV/c. The fitted function in that figure is extrapolated into high  $P_T$  region (above 9 GeV/c) to estimate the losses due to the muon cuts. Although extrapolation is not a pleasant thing to do, the statistical uncertainty of the number of  $\pi^0$ 's in that  $P_T$  range is large enough to accommodate the systematic uncertainty of the fitted function (see Fig. 6.4). Therefore, this extrapolation still provides a good estimate of the event losses. The inverse of the function in  $P_T$  above 9 GeV/c gives the correction factor of the muon cuts.

### 6.1.3 Geometrical Acceptance and Reconstruction Efficiency

Monte Carlo simulation was used to obtain the corrections for the losses of di- $\pi$  events caused by the geometrical acceptance and by the reconstruction efficiency in the spectrometer. The tracking plane efficiency and the noise distribution were first studied in the data and, then, implemented into E706 Monte Carlo package. The electronic noise and the dead channels in the EMLAC were also present in the Monte Carlo. Besides, we compared the multiplicities of charged tracks and photons in our data with the MC data generated by the Herwig generator, and they agreed reasonably well. In order to get the proper weight for each di- $\pi$  event, one may need to generate a large number of MC events, which is very time-consuming. The method used to obtain the corrections was modified.

In the modified method, the physics in scattering processes is assumed to be  $\phi$  (azimuthal angle) independent. The proper weight for a di- $\pi$  (either  $\pi^0\pi^0$  or  $\pi^0\pi^\pm$ ) can be obtained by randomly rotating this pair  $N$  times in  $\phi$  and by checking the

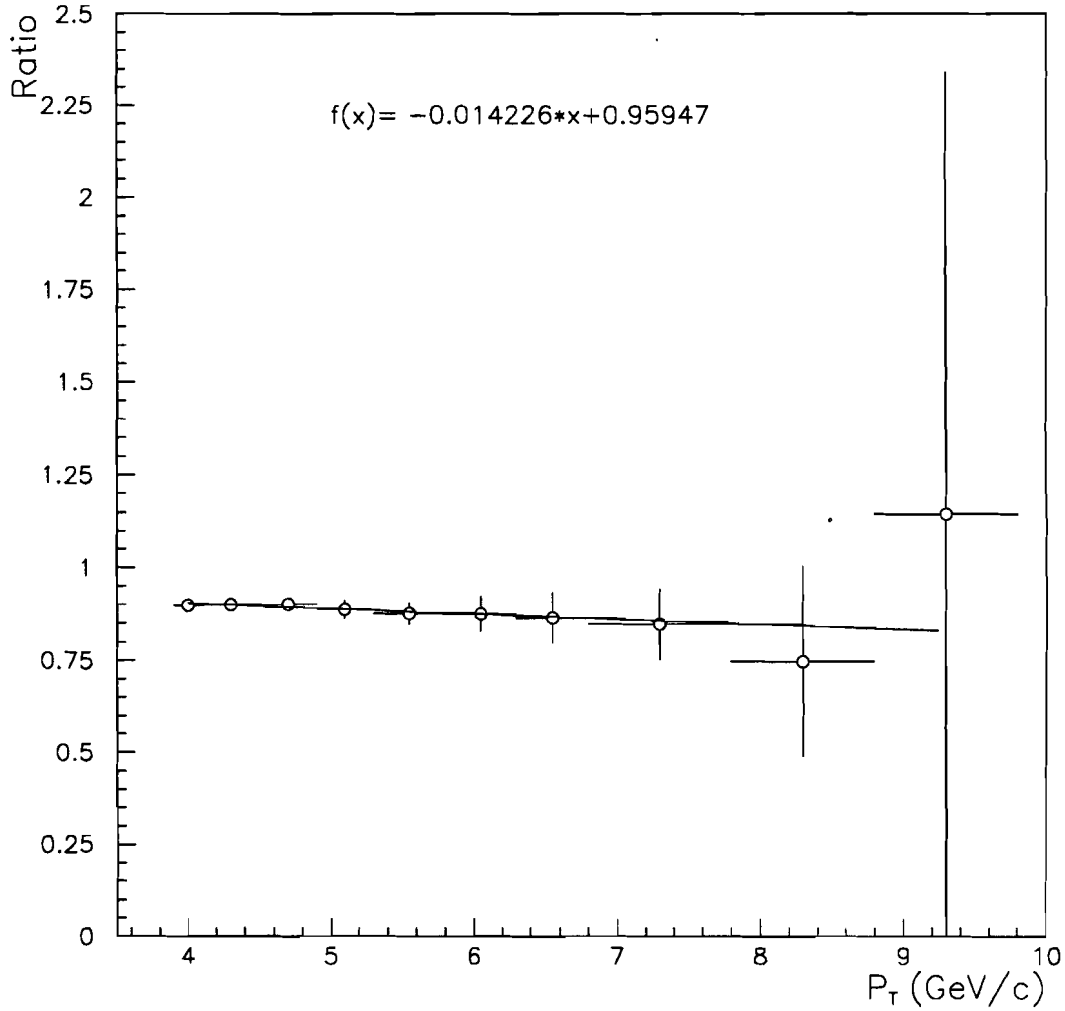


Figure 6.3: The ratio of the number of  $\pi^0$ 's which pass the muon cuts in  $\pi^0$   $P_T$  between 4 to 9 GeV/c. Sideband subtraction is applied when counting the number of  $\pi^0$ 's. The function  $f$  is fitted to these points and implemented to correct for the event losses caused by the muon cuts for high  $P_T$   $\pi^0$ 's ( $P_T > 9$  GeV/c).



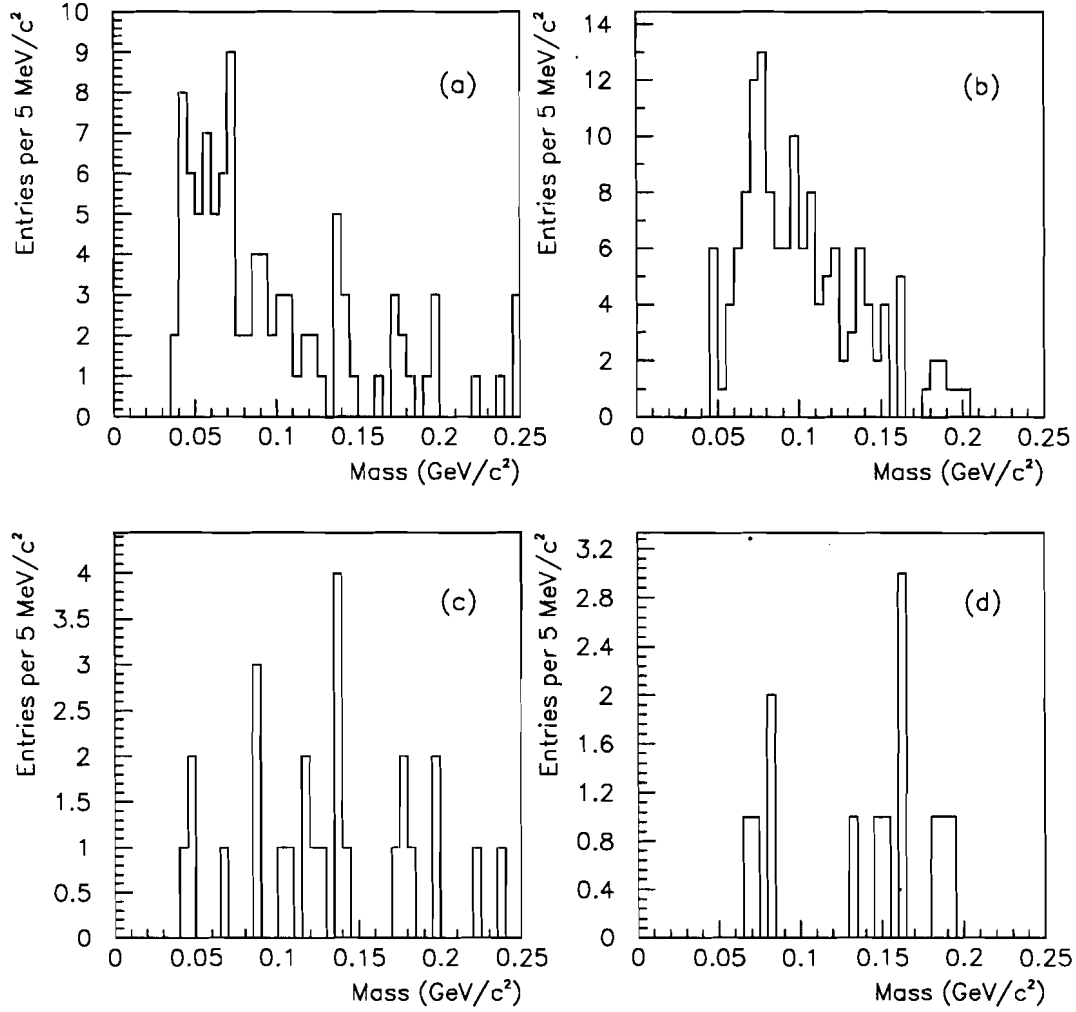


Figure 6.4: Two photon mass spectrum in the di- $\pi$  events with and without the muon cuts. (a)  $9 < P_T < 11$  without the cuts, (b)  $11 < P_T$  without the cuts, (c)  $9 < P_T < 11$  with the cuts, (d)  $11 < P_T$  with the cuts. The number of  $\pi^0$ 's is about  $10 \pm 4.25$  entries in (c), and  $0 \pm 3.464$  events in (d). Therefore, the statistical uncertainty ( $> 30\%$ ) is larger than the systematic uncertainty ( $< 10\%$ ) of the function in Fig. 6.3.

number of times this di- $\pi$  is reconstructed. Mathematically, it can be expressed as:

$$\begin{aligned} W_{di-\pi} &= \frac{\sum_i^N \delta_{1i} P_{1i} \delta_{2i} P_{2i}}{N} \\ &= \frac{N_j}{N} \times \frac{P_{1i} P_{2i}}{N_j} \end{aligned} \quad (6.1)$$

$$N_j = \frac{\sum_i^N \delta_{1i} \delta_{2i}}{N}. \quad (6.2)$$

In equation 6.1,  $\delta_{1i}$  indicates whether particle 1 is inside the detector acceptance in the  $i$ 'th rotation, and  $P_{1i}$  is the reconstruction efficiency if this particle is inside the acceptance. The same expression works for particle 2. Note that  $P_T$  and rapidity of each particle as well as the azimuthal angular difference between them remain unchanged. Equation 6.2 expresses the probability of having this pair inside the acceptance of our detector and the second term on the right side of Equation 6.1 is the reconstruction efficiency.

To get the acceptance correction, we rotated each  $\pi^0\pi^0/\pi^0\pi^\pm$  pair observed in the data a thousand times and simultaneously decayed  $\pi^0$ 's into two photons with asymmetry less than 0.75.  $\pi^0$ 's were decayed according to their reconstructed masses. At each rotation of  $\pi^0\pi^\pm$ , we determined the tracking parameters, such as slopes and intercepts, for charged  $\pi$ 's by applying the momentum impulse to  $P_x$ . We asked:

1. Do the two photons from the  $\pi^0$  decay hit the same octant of the EMLAC?
2. For  $\pi^0\pi^0$  pairs, were the four photons inside the fiducial region? As for  $\pi^0\pi^\pm$  pairs, were the two photons from the  $\pi^0$  decay inside the fiducial region and was the charged  $\pi$  inside the acceptance of the downstream tracking system?

If both answers were "Yes", this pair was deemed accepted. One thousand divided by the number of accepted pairs gave the acceptance correction factor for this  $\pi^0\pi^0$  or  $\pi^0\pi^\pm$  pair. Figure 6.5 shows the average value of the acceptance correction factor as a function of two photon masses. This figure shows that the average correction factor is a linear function of two photon mass. That implies that the mass spectrum of two photons after the acceptance correction is still linear in the sideband region

of  $\pi^0$ 's. Hence, the events in these sideband region can be used as estimations of the background under  $\pi^0$ 's in di- $\pi$  production.

The reconstruction efficiency is not as easy to get, for it requires a large number of Monte Carlo di- $\pi$  events. Note that the reconstruction here is the reconstruction of the di- $\pi$  pair simultaneously instead of two  $\pi$ 's individually. If one calculates the second term on the right side of Eq. 6.1 with the data generated from the event generator, one has to assume the event generator knows the correlations of two  $\pi$ 's. The other approach is to use data-driven Monte Carlo, which takes all measured particles through Geant to produce the output. However, it is usually time consuming and in facts goes beyond our ability at this moment. If the reconstruction efficiency of single particles is  $\phi$  independent,  $P_{1i}$  and  $P_{2i}$  in Eq. 6.1 are uniform in each rotation and Eq. 6.1 can be simplified as:

$$W_{di-\pi} = \frac{N_j}{N} \times P_1 P_2.$$

$P_k$  is the reconstruction efficiency of particle  $k$  at a specific  $P_T$  and rapidity. In other words, the reconstruction efficiency of a di- $\pi$  pair is simply the product of the reconstruction efficiency of each  $\pi$ . The  $\pi^0$  reconstruction efficiency has very little dependence on  $\phi$  in our experiment. Tracks reconstruction efficiency does not depend on  $\phi$  except in very forward or backward regions where tracks were bent out of the acceptance due to the magnetic field. It follows that the reconstruction efficiency of di- $\pi$  pairs can be obtained from the reconstruction efficiency of single  $\pi$ 's.

Figure 6.6 shows the  $\pi^0$  reconstruction efficiency as a function of  $P_T$  and rapidity. This function was measured by generating QCD 2-2 hard scattering events that contained  $\pi^0$ 's, using the Herwig event generator. Only those  $\pi^0$ 's which decayed to two photons with asymmetries less than 0.75 are used. Furthermore, we required that these generated photons were inside the EMLAC fiducial region. The reconstruction efficiency results from having the number of reconstructed  $\pi^0$ 's with  $EFT$  cut divided the number of generated  $\pi^0$ 's. Track reconstruction efficiency was also determined using the Monte Carlo data. We selected the generated charged particles which were

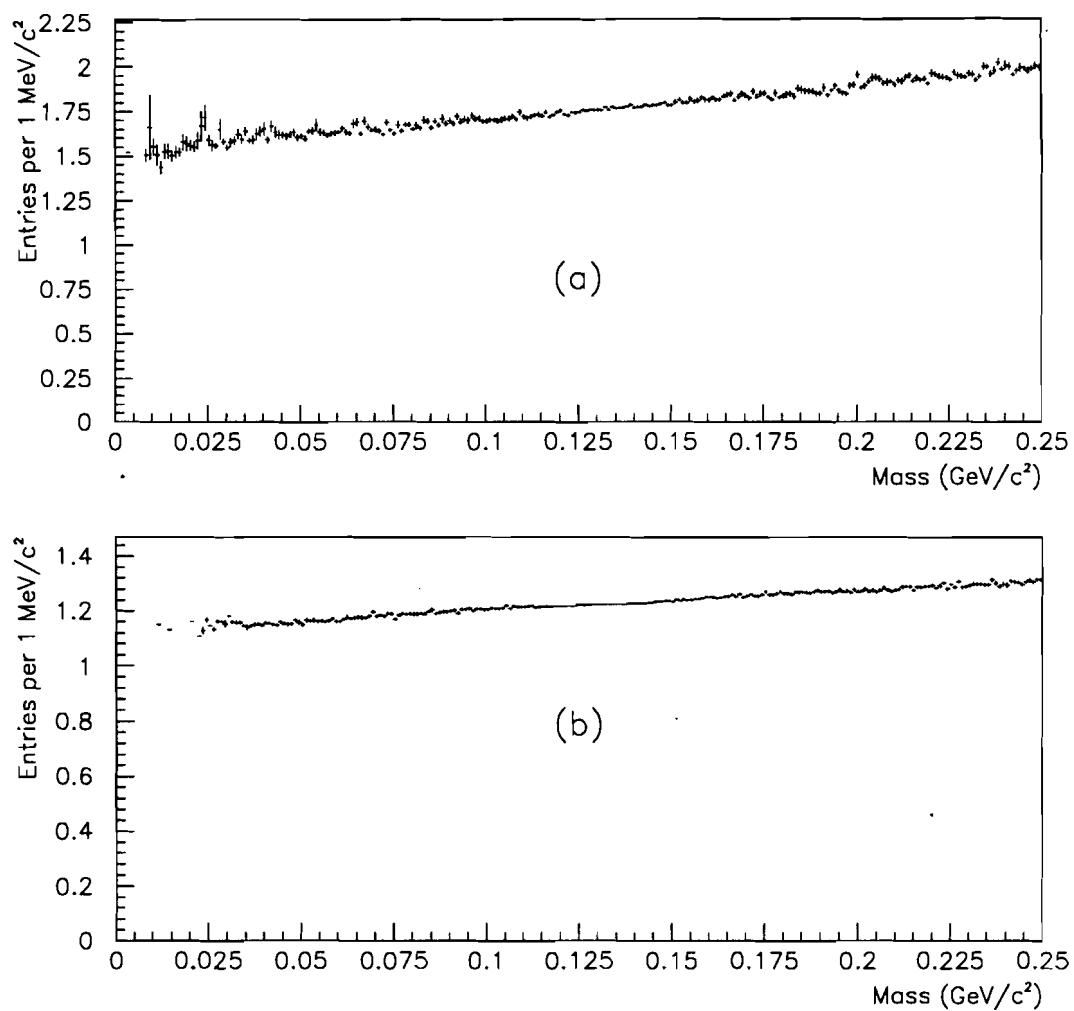


Figure 6.5: The average correction factor of the geometrical acceptance vs the mass of two photons. (a)  $\pi^0\pi^0$ , (b)  $\pi^0\pi^\pm$ .

inside the tracking acceptance and checked how many of them matched reconstructed tracks. Figure 6.7 shows the reconstruction efficiency as a function of rapidity integrated from  $P_T$  above 1.5 GeV/c. The efficiency was measured after applying the track cleaning cuts and the track cuts described in Section 5.3.

#### 6.1.4 Background Subtraction

The background contribution to  $\pi^0\pi^\pm$  pairs can be estimated from the sidebands of  $\pi^0$ 's. Since charged tracks are assumed real after applying all the selection cuts, the background of  $\pi^0\pi^\pm$  is accounted for the combinatorial background of  $\pi^0$ 's. Thus combinations of charged tracks along with any two photons in the  $\pi^0$  sideband region, are employed as an estimation of the background of  $\pi^0\pi^\pm$ . The number of  $\pi^0\pi^\pm$  was counted after subtracting this background.

The background contribution to  $\pi^0$  pairs is more complicated because both  $\pi^0$ 's have significant backgrounds. The  $\pi^0\pi^0$  spectrum can be expressed as:

$$\gamma\gamma_1 \otimes \gamma\gamma_2 = (\pi_1^0 + b_1) \otimes (\pi_2^0 + b_2) \quad (6.3)$$

where  $\gamma\gamma_i$  means two photons in  $\pi^0$  mass region and  $b_i$  is the background of  $\gamma\gamma_i$ . Equation 6.3 can be rearranged as:

$$\begin{aligned} \pi_1^0 \otimes \pi_2^0 &= \gamma\gamma_1 \otimes \gamma\gamma_2 - \gamma\gamma_1 \otimes b_2 \\ &\quad - \gamma\gamma_2 \otimes b_1 + b_1 \otimes b_2. \end{aligned} \quad (6.4)$$

The background of single  $\pi^0$ 's can be estimated from the two photon distribution in the  $\pi^0$  sideband region. Therefore, Eq. 6.4 indicates that the number of  $\pi^0$  pairs can be obtained by subtracting the number of pairs made of a  $\pi^0$  and the two photons in the  $\pi^0$  sideband region, and by adding the number of pairs formed by the two diphotons in the  $\pi^0$  sidebands. In this analysis,  $\pi^0$  pairs were corrected using this method.

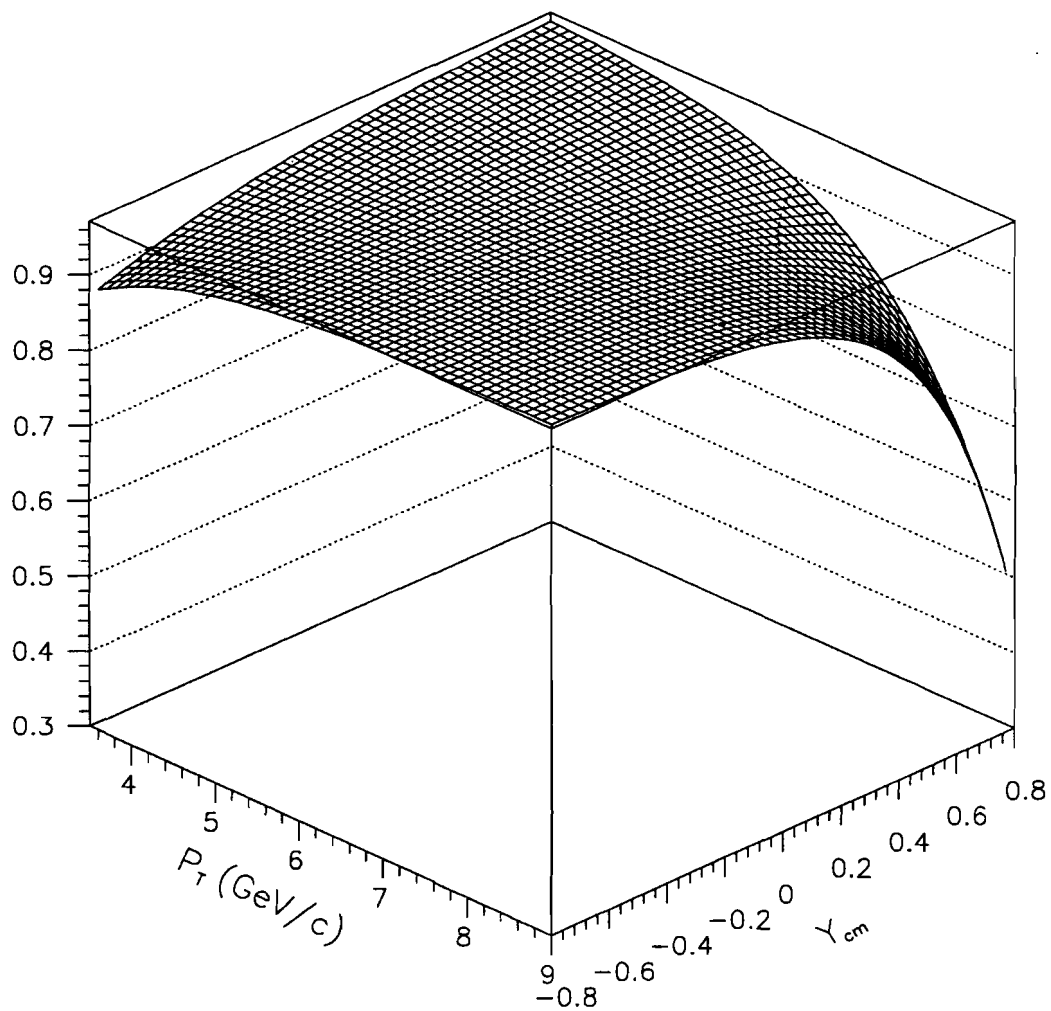


Figure 6.6:  $\pi^0$  reconstruction efficiency as a function of  $P_T$  and rapidity in the  $\pi^-$ -nucleon center of mass frame.

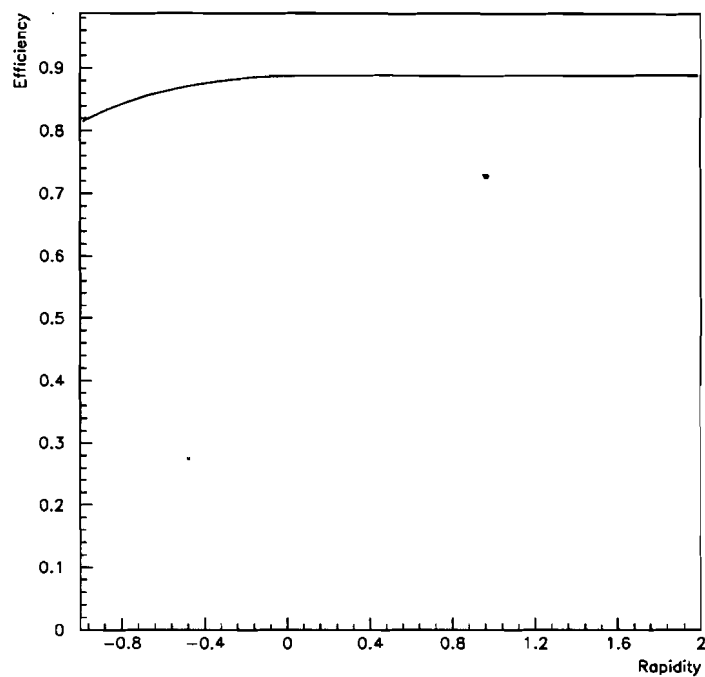


Figure 6.7: Charged particle reconstruction efficiency as a function of rapidity in the  $\pi^-$ -nucleon center of mass frame. The minimum  $P_T$  for each track is 1.5 GeV/c.

### 6.1.5 Live Beam Count

In order to measure cross sections, one has to know the number of beam particles hitting the target when the detectors are ready to take data. The live beam count was calculated using the scaler information, which was recorded for each spill. The *live triggerable beam* (LTB) is expressed in the following form:

$$LTB = BEAM1 \otimes \overline{BH} \otimes (Live\ Fraction) \quad (6.5)$$

where  $BEAM1$  and  $\overline{BH}$  were defined in Section 3.2. And

$$\begin{aligned} (Live\ Fraction) = & (DA\ Live\ Fraction) \otimes \left( \frac{CLEAN\_INT}{INT} \right) \otimes \\ & (Pretrigger\ Live\ Fraction) \otimes \\ & (Veto\ Live\ Fraction). \end{aligned} \quad (6.6)$$

$(DA\ Live\ Fraction)$  and  $(Pretrigger\ Live\ Fraction)$  accounted for the dead time when the computer in the DA system and the pretrigger logic were busy, respectively.  $\frac{CLEAN\_INT}{INT}$  resulted from the requirement that there was no other interactions within  $\pm 60$  ns of the in-time interaction.  $(Veto\ Live\ Fraction)$  accounted for the trigger related dead time caused by the online veto wall cut, SCRKILL, and EARLYPT.

### 6.1.6 Other Correction for Cross Sections

In addition to the corrections described in the previous sections, three other corrections were needed to measure the di- $\pi$  cross sections. They are:

- Photon conversion correction: Since some photons will interact with material to convert to  $e^+e^-$ , each photon was weighted by its conversion probability, which was determined from the amount of material it went through.
- Beam absorption correction: The correction accounted for the loss of beam particles due to the interactions in the material between the beam hodoscopes and the primary vertex.



- Beam muon contamination: Our  $\pi^-$  beam did not contain 100%  $\pi^-$  particles, but had muons in the beam. The muon content was measured using the FCAL [34]. This study suggested that about 0.5% of beam particles were muons. In addition to muon contamination, there were kaons and pbars in our  $\pi^-$  beam. We do not have the measurements for these contaminations yet. However, these particles are believed to compose less than 3% of the beam particles.

## 6.2 Cross Sections and $\cos \theta^*$

In this section, we report the results for the cross sections and  $\cos \theta^*$  distribution for di- $\pi$  production. These results will be compared with the simulated data generated via the Herwig event generator.

### 6.2.1 Di- $\pi$ Cross Section

The di- $\pi$  mass differential cross section per nucleon reported in this thesis can be written as

$$\begin{aligned} \frac{d\sigma}{dM} &= \int dP_T \int d\cos \theta^* \int dY \frac{d\sigma}{dM dY d\cos \theta^* dP_T} \\ &= \frac{1}{\Delta M} \frac{1}{\rho l N_a} \frac{N_{cor}}{LTB} (ABS) \end{aligned} \quad (6.7)$$

where

$$N_{cor} = \sum_{i=1}^{N_{det}} W_i. \quad (6.8)$$

The integrated rapidity and  $\cos \theta^*$  regions are given on page 145.  $N_{det}$  is the total number of di- $\pi$ 's detected per  $\Delta M$  interval, and  $W_i$  is the event weight which is given by:

$$W_i = W_{mu} W_{trig} W_{vtz} W_{geo} W_{rec} W_{conv} W_{beam} W_{asy} W_{bra} W_{tar}. \quad (6.9)$$

The variables in the above expressions are:

- $\rho$ : The density of the target material;

- $l$ : The length of the target material;
- $N_a$ : Avogadro's number;
- ABS: The beam absorption correction ( $ABS = e^{\frac{z}{\lambda}}$ ,  $\lambda$  is the absorption length of the material and  $z$  is the length of the material particles penetrated before interacting with the target);
- LTB: The live triggerable beam;
- $W_{mu}$ : The correction for the muon rejection cuts;
- $W_{trig}$ : The trigger weight of the di- $\pi$  events;
- $W_{vtx}$ : The vertex reconstruction efficiency;
- $W_{geo}$ : The correction for the geometrical acceptance;
- $W_{rec}$ : The correction for the reconstruction efficiency;
- $W_{conv}$ : The correction for  $\pi^0$  loss due to photon conversions;
- $W_{beam}$ : The correction for beam muon contamination;
- $W_{asy}$ : The correction for the  $\pi^0$  asymmetry cut;
- $W_{bra}$ : The correction for the branching ratio of  $\pi^0$  to two photons;
- $W_{tar}$ : The correction for the target fiducial cut.

The above equations for determining di- $\pi$  cross sections can be tested first by using a Monte Carlo (MC) simulation. We generated di- $\pi$  events and compared the generated mass spectrum with the reconstructed mass spectrum in the same kinematic region. Figure 6.8 displays the generated and reconstructed mass spectra of  $\pi^0\pi^-$ ,  $\pi^0\pi^+$ , and  $\pi^0\pi^0$ . Note we interpreted every charged hadron as a charged  $\pi$  meson in the reconstructor as well as in the generator. Among all the MC high  $P_T$  charged

particles (above 1.5 GeV/c) which penetrated through the downstream tracking system in the MC events, 13.8% of them were kaons, 15.9% were protons, 1.2% were electrons, 0.2% were muons, and 0.14% were other charged particles, such as  $\Sigma$  and  $\Xi$  baryons. Since we did not include simulations for our triggers and the interaction points were always generated in the fiducial volume of the target, the corresponding MC corrections were unity. The simulation of the electron veto (See section 5.3) operated simply by checking whether the reconstructed tracks that matched the generated particles were electrons. This simulation was done because we did not simulated the HALAC in our MC and some events contained only the EMLAC information in the triggering octants ( $\pi^0$  octants). The charged tracks loss caused by the LAC veto was counted by measuring the loss of high quality tracks in the data due to the LAC veto. For example, the loss for 80 GeV/c tracks at  $P_T$  above 1.5 GeV/c was about 3%. Although this process did not simulate our detectors perfectly, it still provided a reasonable check in measuring di- $\pi$  cross sections. As for a  $\pi^0\pi^0$  events, we chose the MC data which simulated the electromagnetic shower in all octants. In these data, each event had a  $\pi^0$  with  $P_T$  greater than 6.5 GeV/c.

In general, the generated spectrum matched well with the reconstructed spectrum except in the very high mass region for  $\pi^0\pi^\pm$  pairs where the number of reconstructed  $\pi^0\pi^\pm$  pairs is larger than the number of generated pairs. However, this feature does not appear for  $\pi^0\pi^0$  pairs. The explanations is that the track momentum resolution worsens for high momentum tracks. Since the momentum is determined by the bending angle, whose resolution is gaussian and nearly momentum independent, the distribution of the measured momentum for a given incident momentum has a tail on the large momentum side. This tail increases when the given momentum increases. Therefore, this tail has a strong impact for large momentum cases and, consequently, changes the spectrum of  $\pi^0\pi^\pm$  in the large mass region. Figure 6.9 shows the reconstructed and generated  $\pi^0\pi^\pm$  mass spectrum, where one charged track matches one of the generated charged particles emanated from the target and all corrections are

turned off. The generated (reconstructed) masses of the  $\pi^0\pi^\pm$  pairs were calculated using the measured four vector momenta for  $\pi^0$ 's and the measured (reconstructed) four vectors for charged  $\pi$ 's. The same discrepancy shows up in the high mass region, indicating the momentum resolution is the cause of this feature in high mass region rather than any of the corrections. In order to correct this resolution effect in the high mass region, we used a function to fit the ratio of the generated  $\pi^0\pi^\pm$  spectrum and the reconstructed spectrum at mass greater than 14 GeV/ $c^2$ . Each  $\pi^0\pi^\pm$  event in this high mass region was weighted by this fitted function. Figure 6.10 shows the ratio of the generated and the reconstructed  $\pi^0\pi^\pm$  mass spectrum. In general, this ratio is around one except at mass greater than 14 GeV/ $c^2$ . Since the momentum resolution is charge independent, the MC  $\pi^0\pi^-$  and  $\pi^0\pi^+$  data are added to obtain corrections.

All the  $\pi$  pairs are restricted to the kinematic region determined by the trigger efficiency and the detector acceptance. To summarize, the kinematic cuts in this analysis are follows. For  $\pi^0\pi^0$  production,

- $-0.8 < Y < 0.8$  for each  $\pi^0$
- $P_T > 2$  GeV/ $c$  for each  $\pi^0$
- $|\cos\theta^*| < 0.5$  for the pair
- $-0.3 < Y < 0.7$  for the pair
- $\Delta\phi \geq 96^\circ$

As for  $\pi^0\pi^\pm$  events,

- $-0.8 < Y < 0.8$  for  $\pi^0$ 's and  $-1 < Y < 2$  for  $\pi^\pm$ 's
- $P_T > 4$  GeV/ $c$  for  $\pi^0$ 's and  $P_T > 1.5$  GeV/ $c$  for  $\pi^\pm$ 's
- $|\cos\theta^*| < 0.5$  for the pair

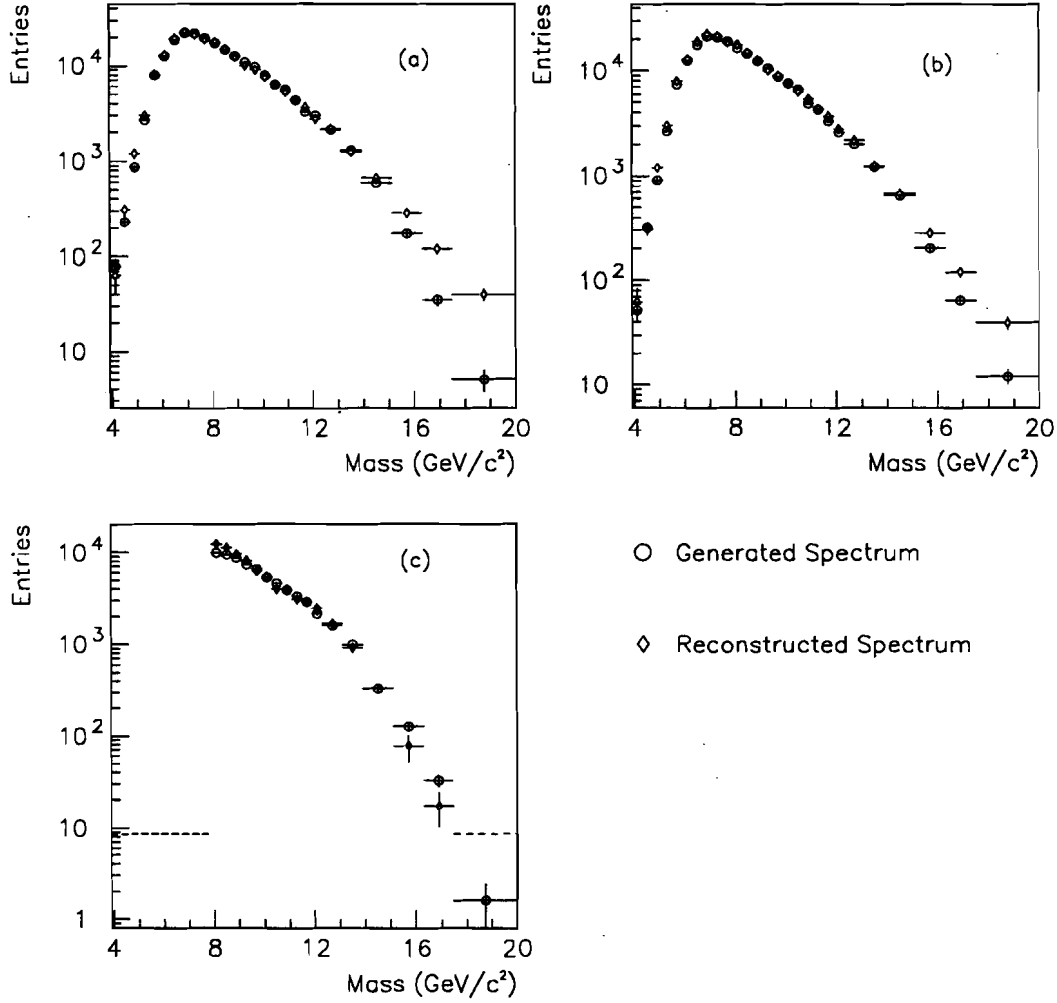


Figure 6.8: The MC generated and reconstructed mass spectra of di- $\pi$  events. (a)  $\pi^0\pi^-$ , (b)  $\pi^0\pi^+$ , (c)  $\pi^0\pi^0$ . The same kinematic cuts were applied for the generated and the reconstructed events. All the corrections except the trigger correction, the target fiducial correction, and the correction for beam muon contamination were turned on.

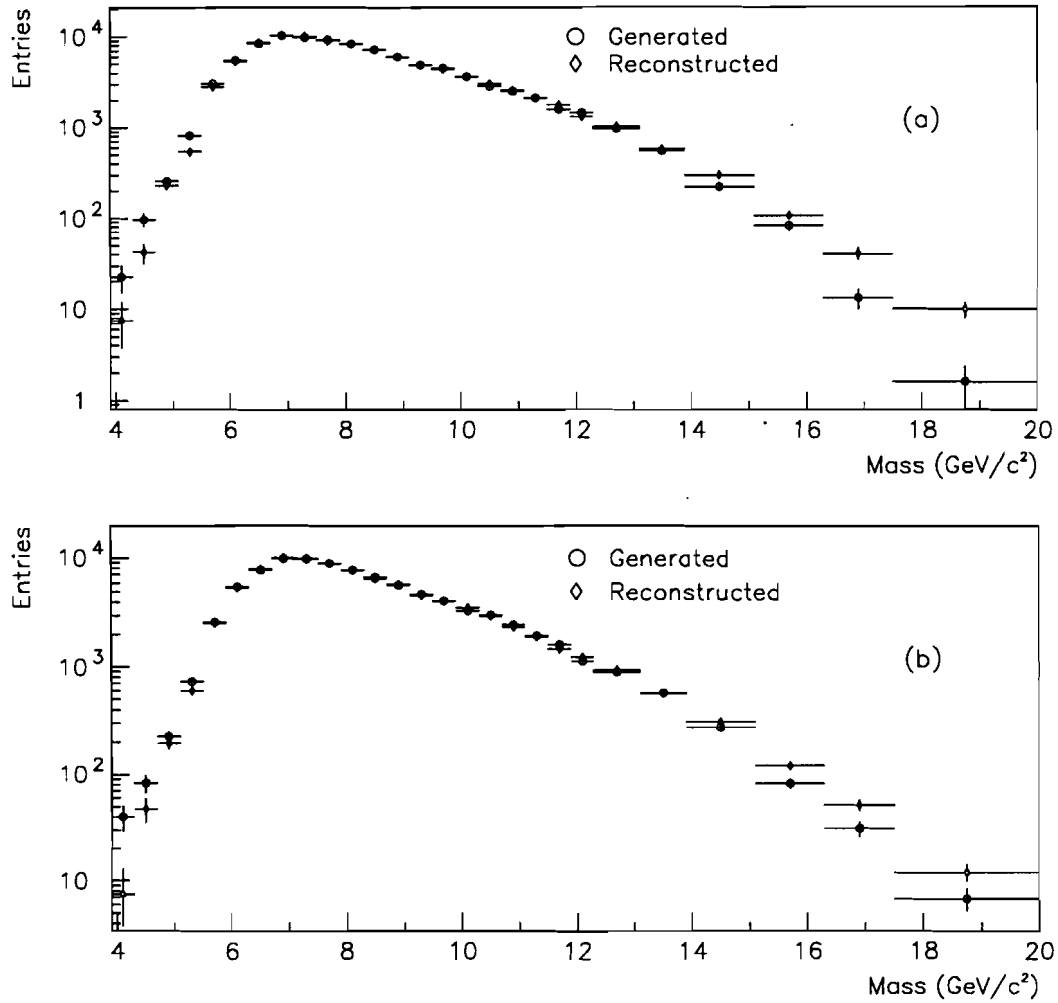


Figure 6.9: The MC generated and reconstructed mass spectra of (a)  $\pi^0\pi^-$  and (b)  $\pi^0\pi^+$ . Every charged track corresponds to a generated particle. All corrections were turned off.

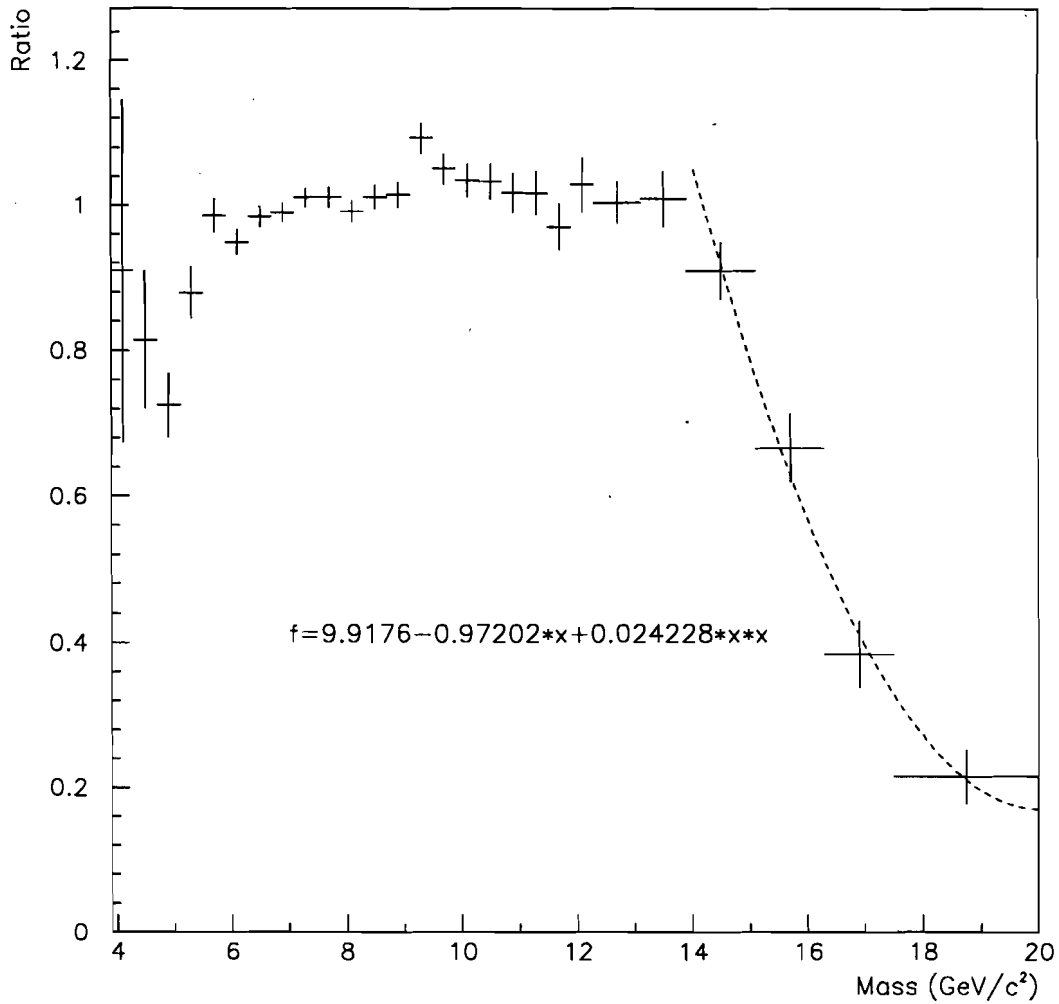


Figure 6.10: The ratio of the MC generated and reconstructed mass spectra of  $\pi^0\pi^\pm$  events. This ratio is around one except at mass greater than 14 GeV/c<sup>2</sup>. The fitted function is used as a correction to measure the  $\pi^0\pi^\pm$  cross sections in the real data.

- $-0.4 < Y < 0.8$  for the pair
- $\Delta\phi > 90^\circ$

The mass differential cross sections for di- $\pi$ 's are shown in Figs. 6.11 and 6.12 using Be and Cu targets. These results are also listed in Tables B.1, B.2, and B.3. In these plots, the data tend to rise in the low mass region because of the  $P_T$  cut for each particle. After the point which stands for the sum of the minimum  $P_T$  required for each particle in the pair is reached, the mass spectra fall as expected. The  $\pi^0\pi^-$  cross section is a little bit larger than the  $\pi^0\pi^+$  cross section in the same kinematic region. This feature may be due to the  $\bar{u}$  and d contents in the beam particles. If the charged  $\pi$ 's are from gluon jets, they have a equal chance to form positive or negative states. But if  $\pi$ 's are from quark jets, the chance of forming a positive or negative state is enhanced by the charge signs of the quarks. For example,  $\bar{u}$  jets have a higher chance to fragment to leading  $\pi^-$ 's particles than to fragment to leading  $\pi^+$ 's. Counting the valence quarks in  $\pi^-$ , p, and n, we find that the cross section of  $\pi^0\pi^-$  should be larger than  $\pi^0\pi^+$ . This feature also shows up in the events generated from the Herwig generator. Figure 6.13 presents the cross section ratio of  $\pi^0\pi^+$  and  $\pi^0\pi^-$ , showing that the ratio decreases when mass increases. What causes this trend is unknown. This trend may suggest that the subprocess of gluon gluon scattering becomes less dominant at high mass.

We now compare our results with expectation from QCD. Figs. 6.14, 6.15, and 6.16 display the measured mass spectrum and the generated mass spectrum from the Herwig event generator for  $\pi^0\pi^0$ ,  $\pi^0\pi^-$ , and  $\pi^0\pi^+$  events, respectively. The generated spectrum is obtained from the leading-log QCD calculation through the Herwig event generator, using Owens set 1.1 as the parton distribution and fragmentation functions. We did not get the absolute differential cross section from Herwig. We normalized the generated spectrum to one point of the measured data and compared the overall mass shape.



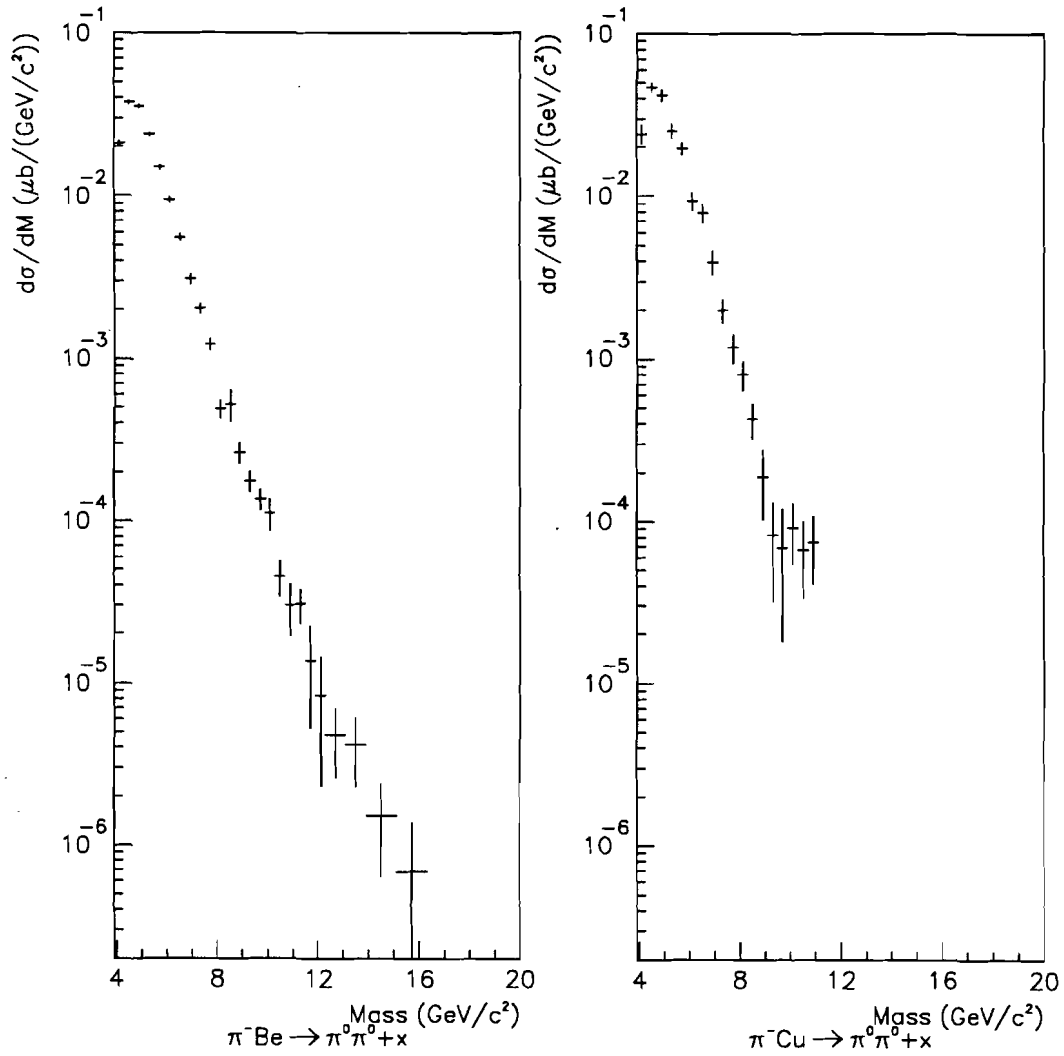


Figure 6.11:  $\pi^0$  pair mass spectra in  $\pi^- \text{Be}$  and  $\pi^- \text{Cu}$  interactions. The spectra rises in the low mass region because of the minimum  $P_T$  requirement for each  $\pi^0$  (2 GeV/c). After the point (4 GeV/c) that stands for the sum of the  $P_T$  of each  $\pi^0$  is reached, the spectra are falling as expected.

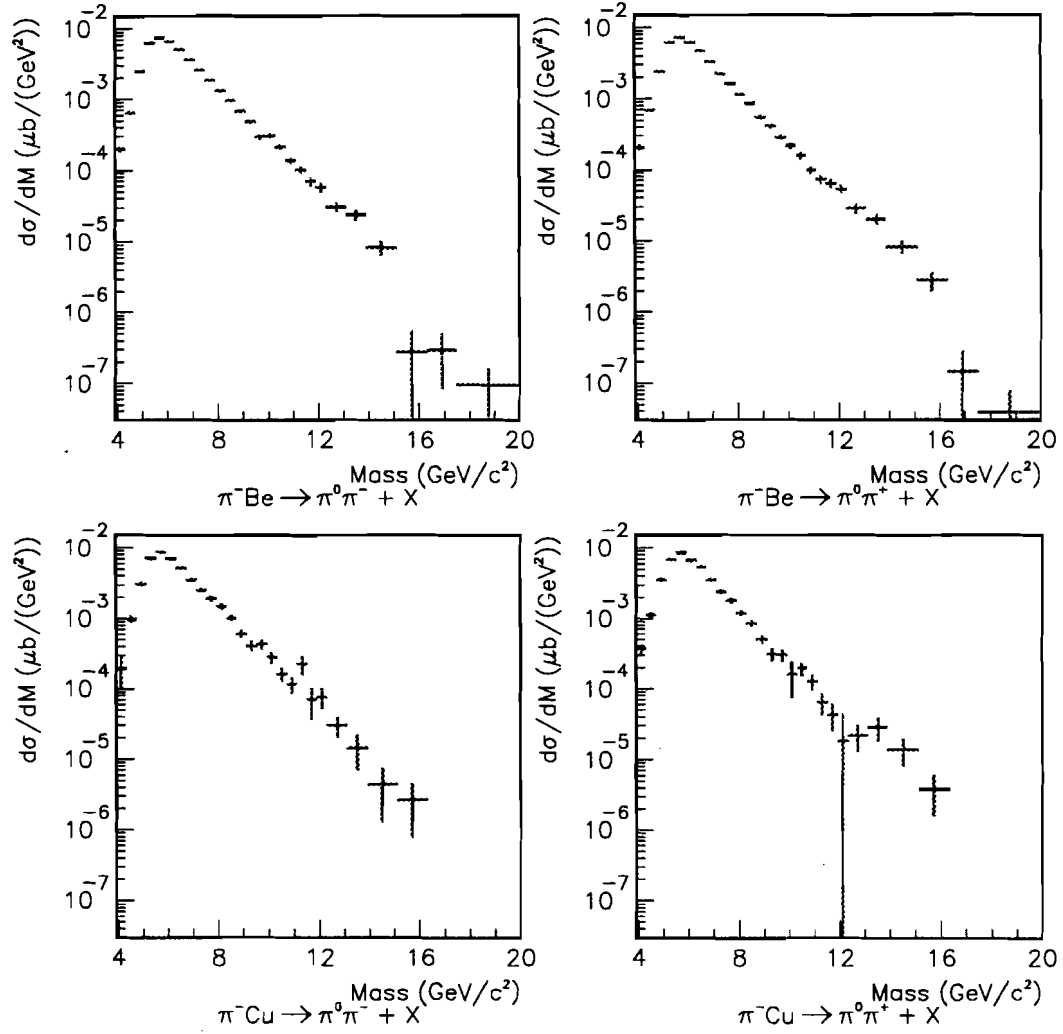


Figure 6.12:  $\pi^0\pi^\pm$  mass spectra in  $\pi^-$ Be and  $\pi^-$ Cu interactions. The spectra rises in the low mass region because of the minimum  $P_T$  requirement for the  $\pi^0$  (4  $\text{GeV}/c$ ) and the  $\pi^\pm$  (1.5  $\text{GeV}/c$ ). After the point (5.5  $\text{GeV}/c$ ) that stands for the sum of the  $P_T$  of each particle is reached, the spectra are falling as expected.

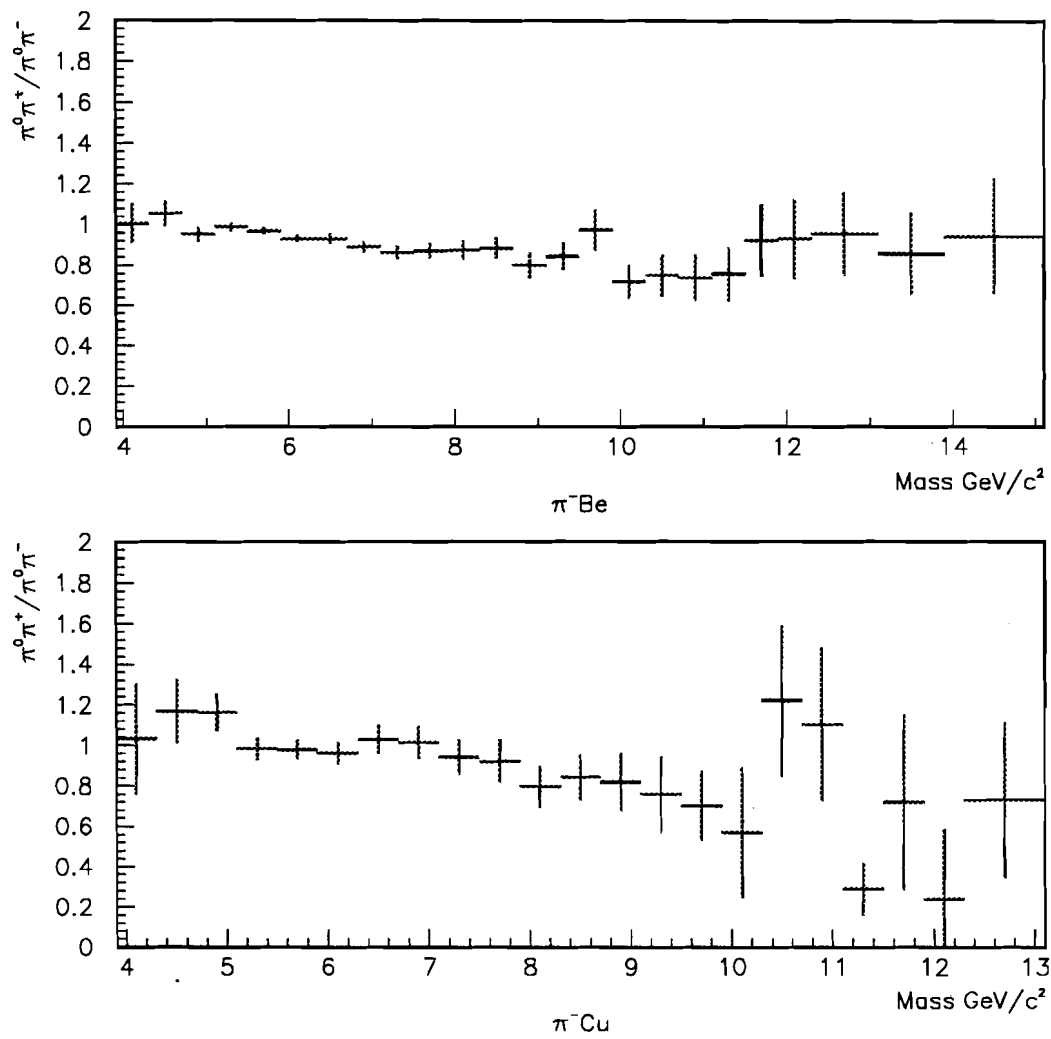


Figure 6.13: The cross section ratio of  $\pi^0\pi^+$  and  $\pi^0\pi^-$  versus mass of the pairs.

The generated  $\pi^0\pi^0$  mass shape agrees with our data very well. However, the generated mass shapes for  $\pi^0\pi^-$  and  $\pi^0\pi^+$  do not exactly match our data. The differences between the generated spectra and the data are visible in the mass region ranging from 10 to 14 GeV/ $c^2$ , indicating either the leading log QCD calculation may not be adequate to explain the hadronic interaction or the Herwig event generator does not simulate the  $\pi^- - p$  interaction correctly.

It is of interests to compare the  $\pi^0\pi^0$  cross section to the  $\pi^0\pi^\pm$  cross sections in the same kinematic region. We required that every  $\pi^0\pi$  event must have a  $\pi^0$  with  $P_T$  above 4 GeV/ $c$  and a  $\pi$  (charged or neutral) with  $P_T$  above 2 GeV/ $c$ . The rapidity and  $\Delta\phi$  ranges are required to be the same as used for  $\pi^0\pi^0$  events. Since the SINGLE LOCAL HIGH trigger is appropriate to use for  $\pi^0$   $P_T$  above 4 GeV/ $c$ , we first compare the measured  $\pi^0\pi^0$  cross section with the SINGLE LOCAL HIGH trigger to that with the TWO GAMMA trigger. This study provides a cross check for the  $\pi^0\pi^0$  cross section. Figure 6.17 shows the measured  $\pi^0\pi^0$  cross sections using these two different triggers. The cross sections measured from the TWO GAMMA trigger is, in average, less than 5/trigger, manifesting a good agreement between these two measurements.

Figs. 6.18 and 6.19 displays respectively the  $\pi^0\pi^-$  and  $\pi^0\pi^+$  mass differential cross sections overlapped with the  $\pi^0\pi^0$  cross section, using the SINGLE LOCAL HIGH trigger. The  $\pi^0\pi^0$  cross section is about 60% of the " $\pi^0\pi^-/\pi^0\pi^+$ " cross section, indicating that a big fraction (40%) of the high  $P_T$  ( $> 2$  GeV/ $c$ ) charged particles comprises other charged particles instead of the charged  $\pi$  mesons. As indicated in Page 143, the Herwig event generator shows that 31% of the high  $P_T$  charged particles are not  $\pi$ 's. The results of the generated  $\pi^0\pi^\pm$  and  $\pi^0\pi^0$  mass spectra are displayed in Fig. 6.20, where every charged particle is regarded as a  $\pi$ . The MC  $\pi^0\pi^0$  mass spectrum is, in general,  $\sim 32\%$  lower than the MC  $\pi^0\pi^\pm$  spectra. The experiment of Cronin *et al.*, have measured, as a function of  $P_T$ , the cross section for the production of  $\pi^\pm$ ,  $K^\pm$ ,  $p$ ,  $\bar{p}$ ,  $d$ , and  $\bar{d}$  in proton collisions with tungsten target

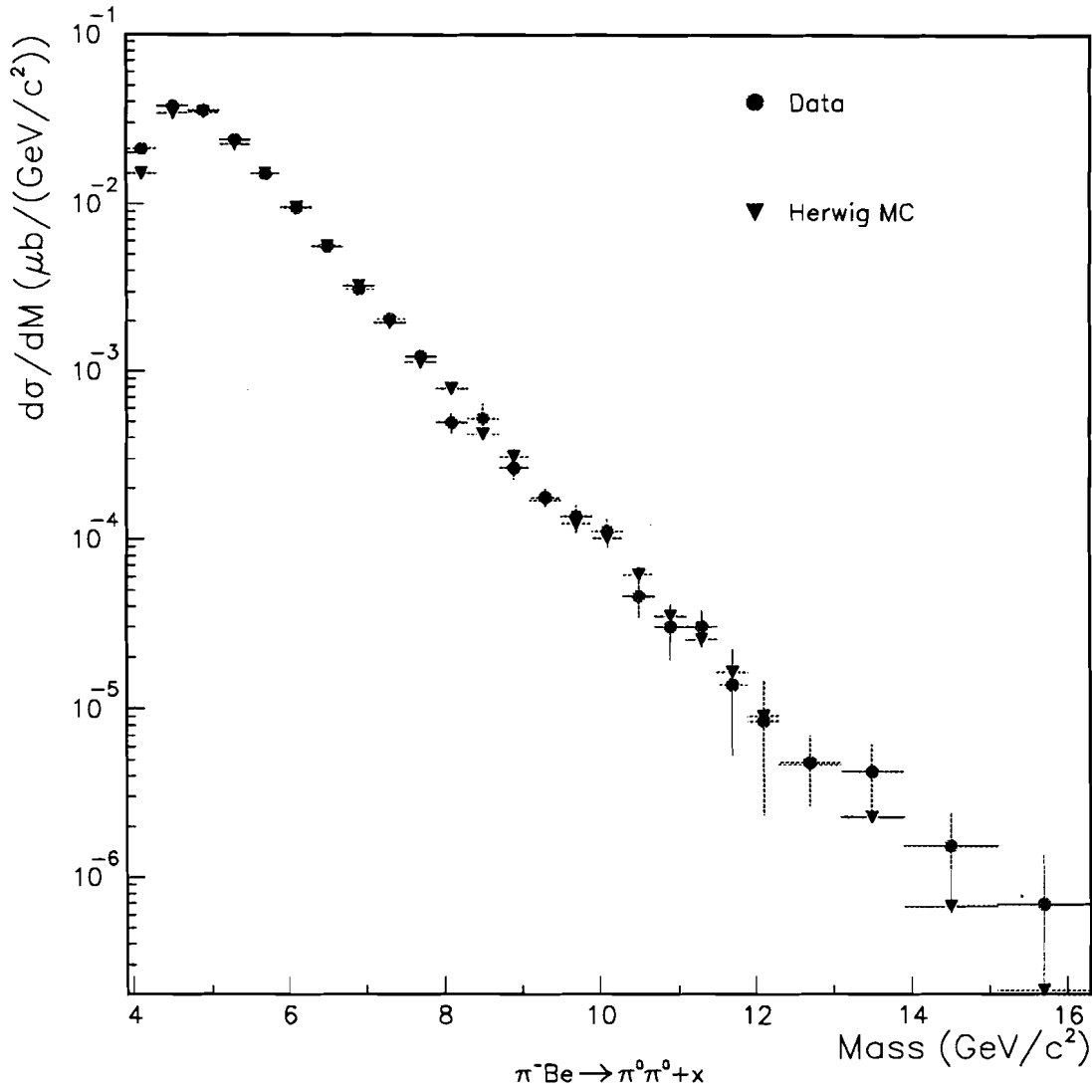


Figure 6.14: The measured  $\pi^0\pi^0$  mass differential cross section compared to the generated result from the Herwig event generator. The Herwig result is normalized to the fifth point of the data spectrum.

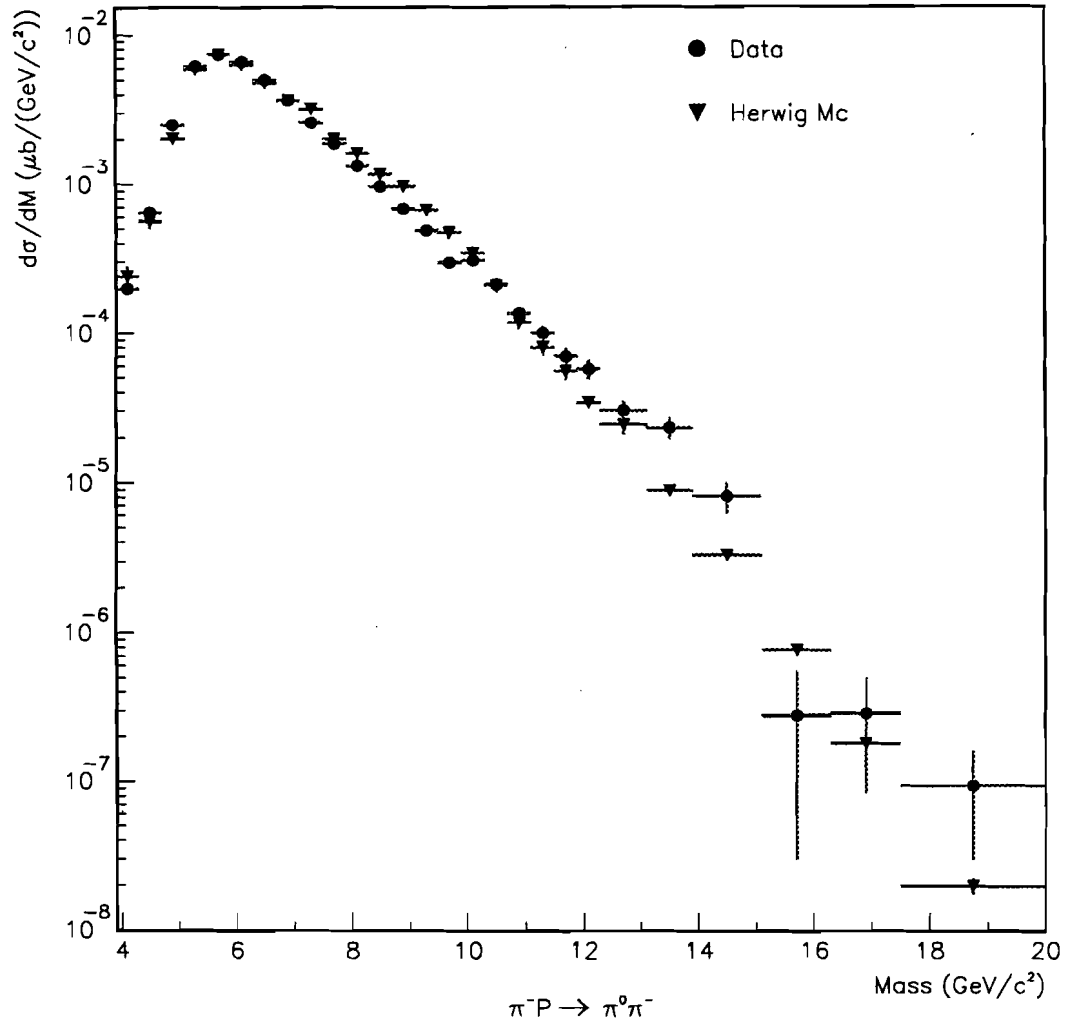


Figure 6.15: The measured  $\pi^0\pi^-$  mass differential cross section compared to the generated result from the Herwig event generator.

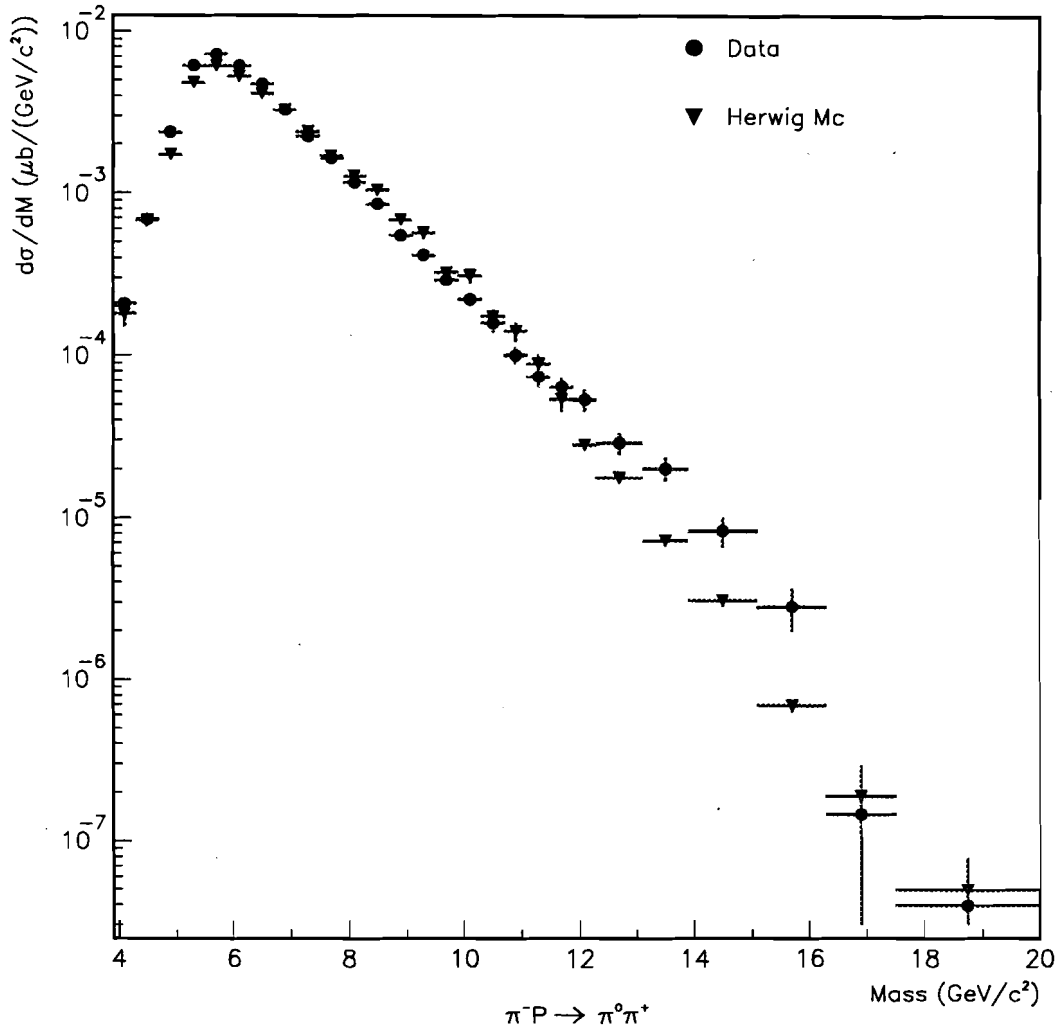


Figure 6.16: The measured  $\pi^0\pi^+$  mass differential cross section compared to the generated result from the Herwig event generator.

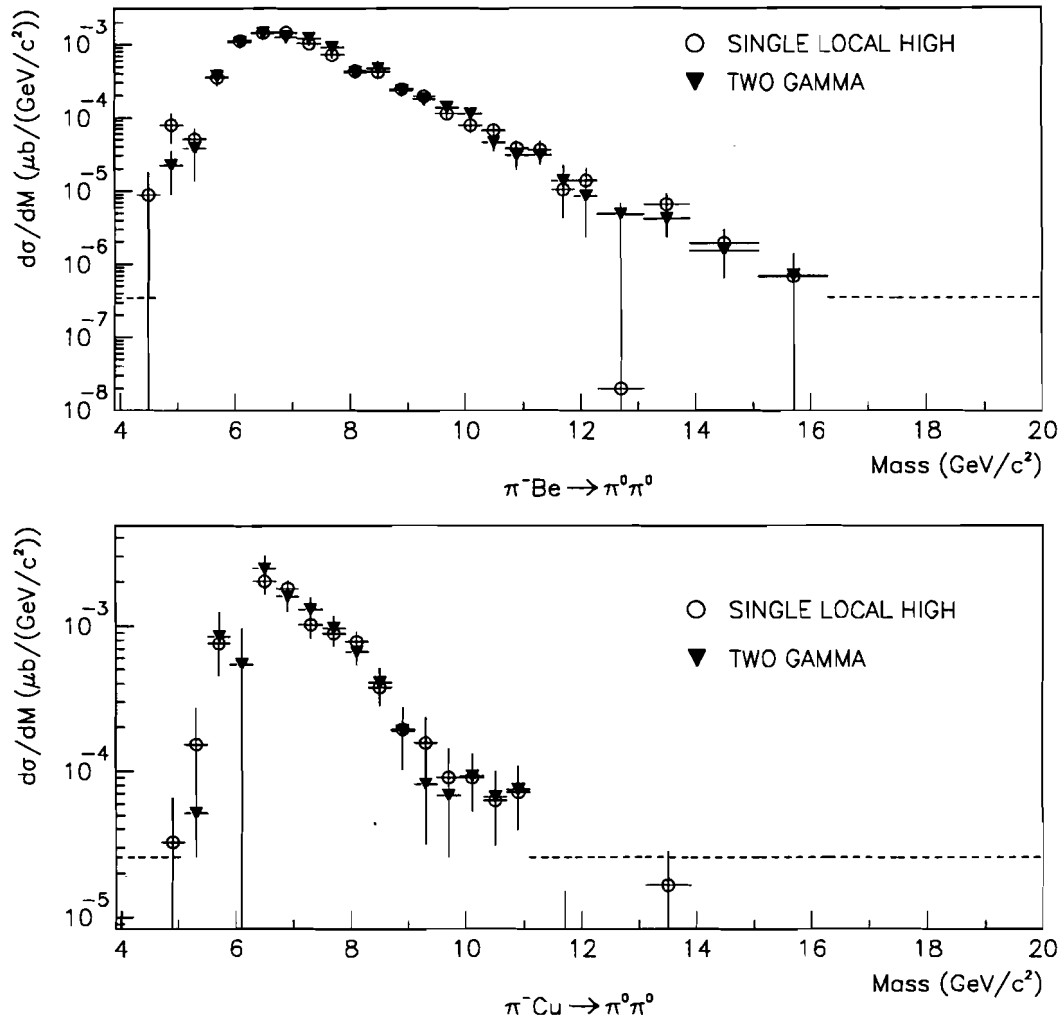


Figure 6.17: The measured  $\pi^0\pi^0$  mass differential cross sections using the SINGLE LOCAL HIGH trigger and the TWO GAMMA trigger.



[14]. The  $K^+/\pi^+$  ( $K^-/\pi^-$ ) and  $p/\pi^+$  ( $\bar{p}/\pi^-$ ) cross section ratios are respectively  $\sim 0.44$  (0.28) and  $\sim 0.811$  (0.14) at  $P_T = 2.29$  GeV/c. Their results indicate that a big fraction of the high  $P_T$  particles are  $K^\pm$ ,  $p$ , and  $\bar{p}$ , which is qualitatively consistent with our observations.

### 6.2.2 $\cos\theta^*$ in Di- $\pi$ 's

The  $\cos\theta^*$  value of each  $\pi$  pair can be calculated from Eqs. 1.26 and 1.27. As introduced in Section 1.3, the mass cut and  $\eta_b$  cut are necessary to get an unbiased  $\cos\theta^*$  distribution. Figure 6.21 shows the  $\cos\theta^*$  distribution of  $\pi^0$  pairs in four different mass regions with  $|\eta_b| < 0.25$ . As expected, the distribution rises for larger  $\cos\theta^*$  values. The number of entries at  $\cos\theta^*=0.5$  is about three to four times more than the number at  $\cos\theta^*=0$  in these four mass regions. Figure 6.22 displays the  $\cos\theta^*$  distribution, normalized at  $\cos\theta^*=0$  and integrated over four mass regions. The fitted function using Eq. 1.23 and the QCD predicted spectrum generated from the Herwig Monte Carlo are also shown in Fig. 6.22. The QCD predicted spectrum agrees with the experimental measurement very well. The parameter  $a$  is determined as  $2.60 \pm 0.20$ .

The same study was done for  $\pi^0\pi^\pm$  events. Since the minimum  $P_T$  requirement for  $\pi^0$ 's is higher (above 4 GeV/c) and the tracking system has larger acceptance coverage, the mass cut and  $\eta_b$  cut are different from those used in  $\pi^0$  pairs. From Eqs. 1.26 and 1.27, as well as the acceptance ranges of  $\pi^0$  and  $\pi^\pm$ , the range of  $\eta_b$  can be derived as follows:

$$\eta_b = \eta_{\pi^0}^* - \eta_{\pi^0} \implies \eta_{\pi^0}^* - 0.8 < \eta_b < \eta_{\pi^0}^* + 0.8 \quad (6.10)$$

$$\eta_b = -\eta_{\pi^0}^* - \eta_{\pi^\pm} \implies -2 - \eta_{\pi^0}^* < \eta_b < 1 - \eta_{\pi^0}^* \quad (6.11)$$

$$\eta_b = -\frac{\eta_{\pi^0} + \eta_{\pi^\pm}}{2} \implies -1.4 < \eta_b < 0.9 \quad (6.12)$$

where

$$\eta_{\pi^0}^* = \frac{1}{2} \times \ln\left(\frac{1 + \cos\theta^*}{1 - \cos\theta^*}\right). \quad (6.13)$$

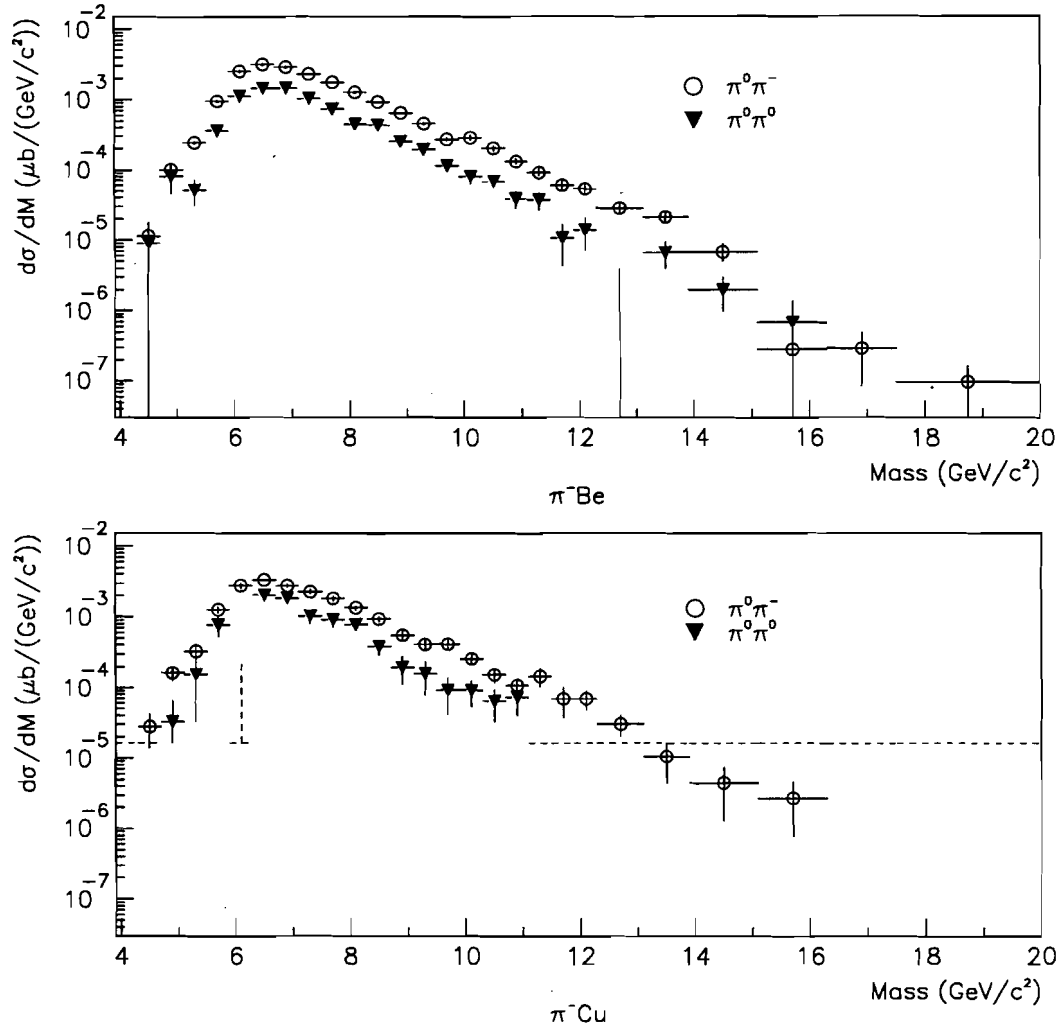


Figure 6.18: The measured  $\pi^0\pi^-$  mass differential cross section overlapped with the  $\pi^0\pi^0$  cross section using the SINGLE LOCAL HIGH trigger.

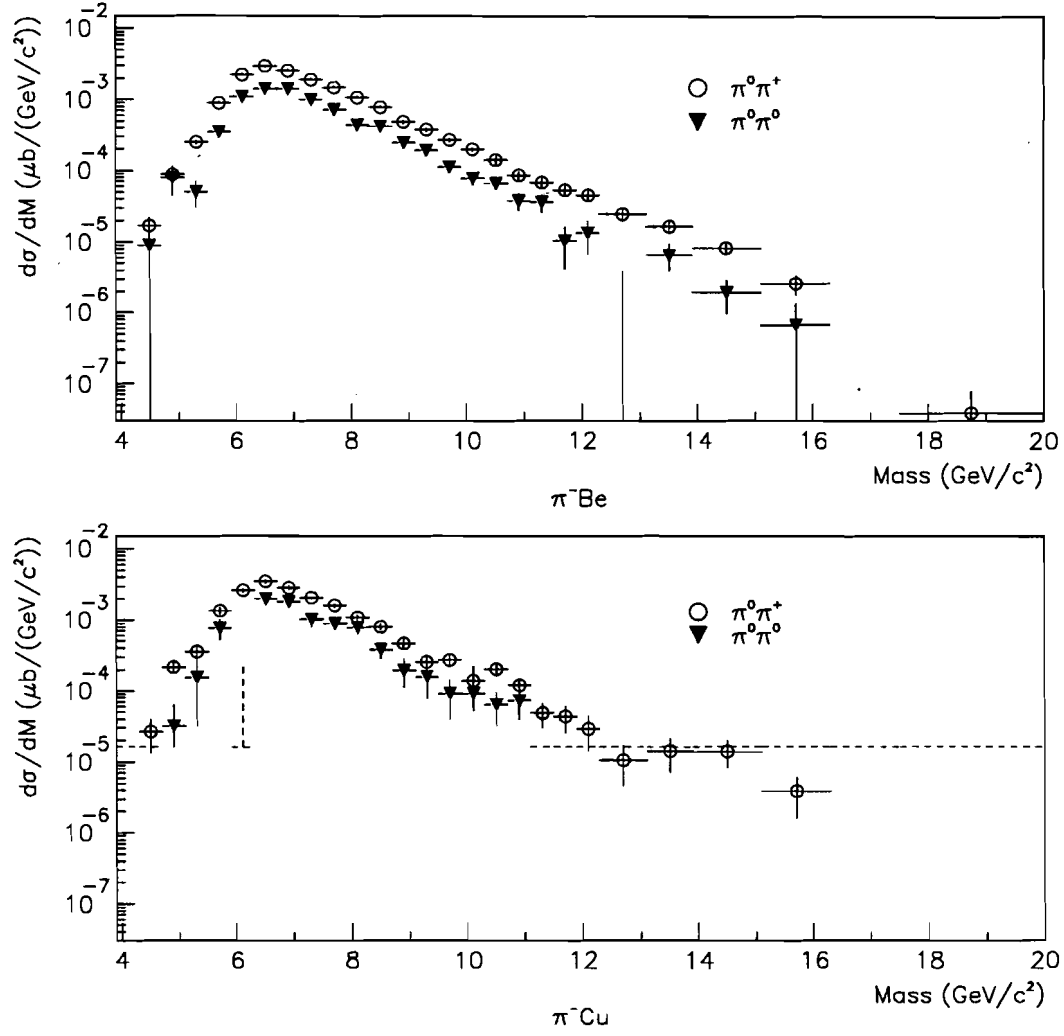


Figure 6.19: The measured  $\pi^0\pi^+$  mass differential cross section overlapped with the  $\pi^0\pi^0$  cross section using the SINGLE LOCAL HIGH trigger.

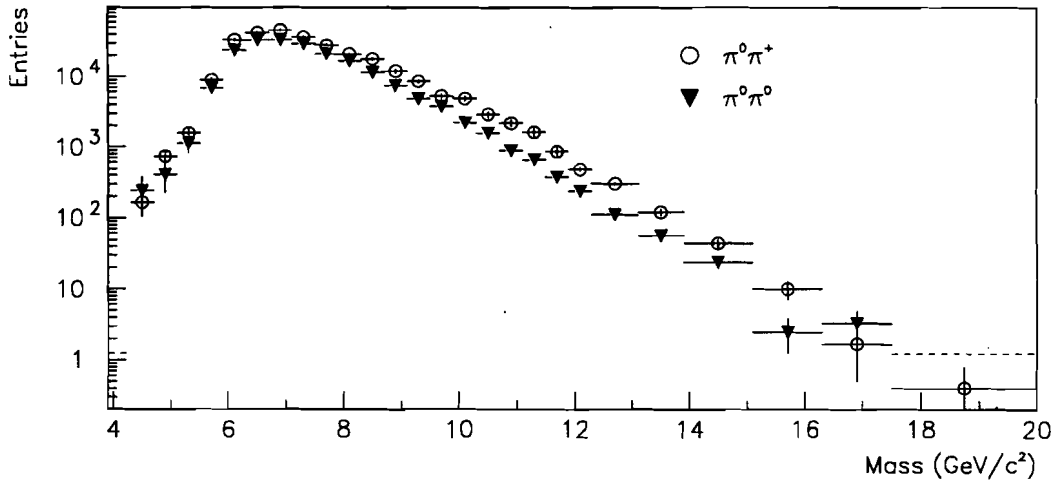
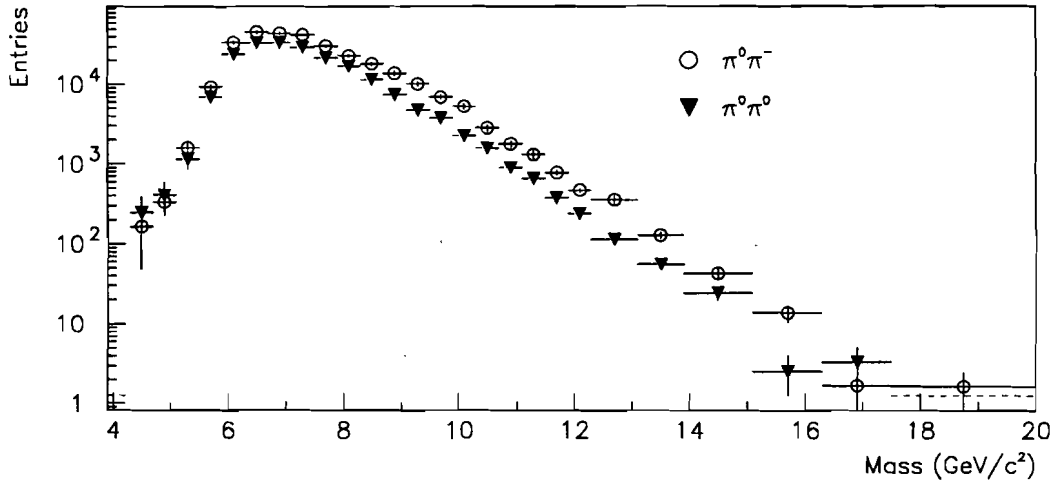


Figure 6.20: The MC generated  $\pi^0\pi^\pm$  mass spectra overlapped with the generated  $\pi^0\pi^0$  mass spectrum.

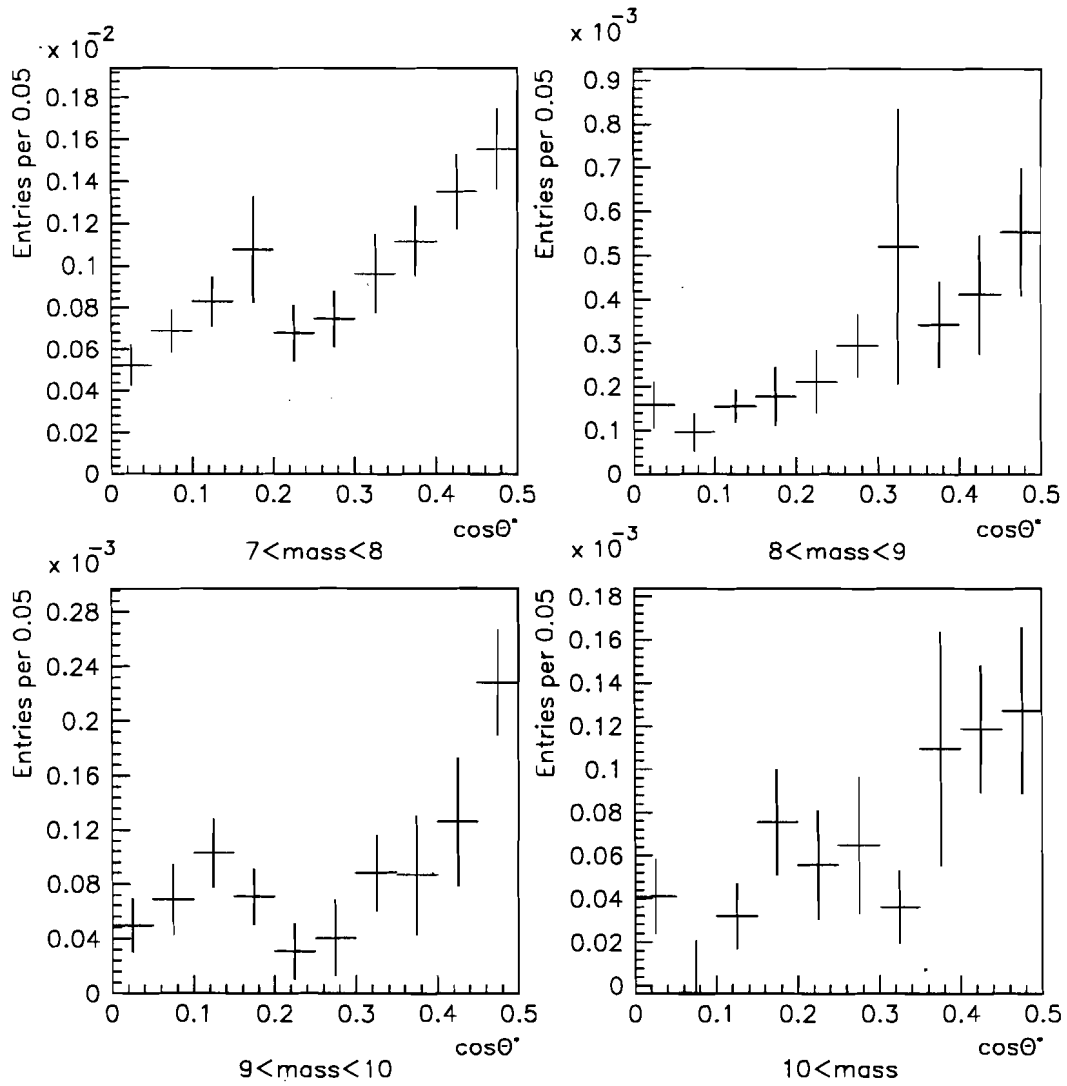


Figure 6.21:  $\cos \theta^*$  distribution of  $\pi^0$  pairs in four different mass regions.

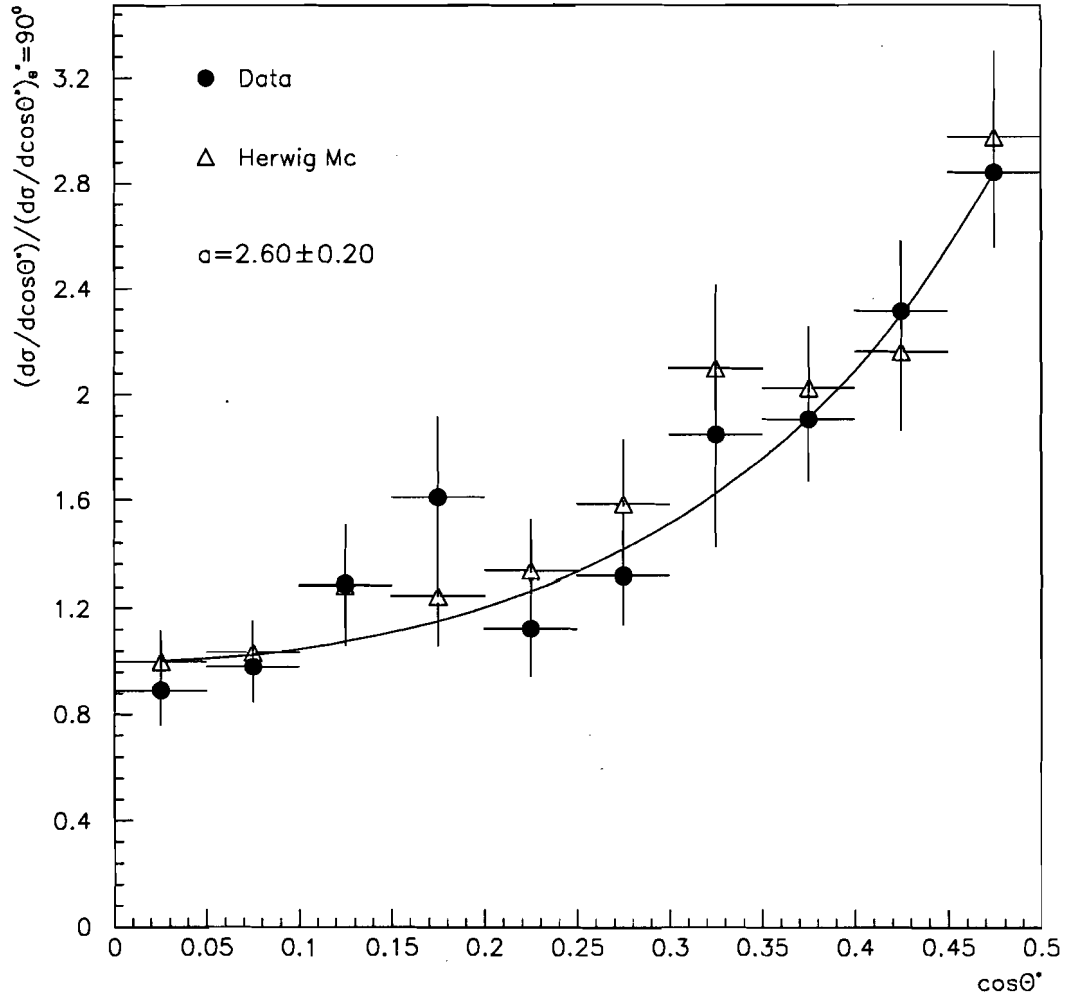


Figure 6.22:  $\cos \theta^*$  distribution of  $\pi^0$  pairs overlapped with the leading-log QCD calculation derived from the Herwig event generator. The fitted function is  $\frac{1}{2} \left[ \frac{1}{(1+\cos \theta^*)^a} + \frac{1}{(1-\cos \theta^*)^a} \right]$ . The parameter  $a$  is determined from the experimental data.

$\cos \theta^*$	minimum $\eta_b$	maximum $\eta_b$
-0.5	-1.400	0.250
-0.4	-1.223	0.377
-0.3	-1.109	0.491
-0.2	-1.080	0.597
-0.1	-0.900	0.700
0.	-0.800	0.800
0.1	-0.700	0.900
0.2	-0.597	0.797
0.3	-0.491	0.691
0.4	-0.377	0.577
0.5	-0.250	0.450

Table 6.1: The minimum and maximum values of  $\eta_b$  in different  $\cos \theta^*$  values with respect to  $\pi^0$ 's in  $\pi^0\pi^\pm$  events. The negative  $\cos \theta^*$  values with respect to  $\pi^0$ 's correspond to the positive values with respect to  $\pi^\pm$ 's. The  $\eta_b$  range is derived from Eqs. 6.11, 6.12, 6.13, and 6.14.

$\cos \theta^*$  in Eq. 6.13 can be positive or negative. Note that  $\cos \theta^*$  referred in di- $\pi$ 's is the absolute value since it has the same magnitude but different signs with respect to the other particle of the pair. For example,  $\cos \theta^*$  is 0.4 with respect to  $\pi^0$  and is -0.4 with respect to  $\pi^\pm$ . Table 6.2.2 lists the  $\eta_b$  range for different  $\cos \theta^*$  values.

The different restricted  $\eta_b$  range in different  $\cos \theta^*$  values distorts the  $\cos \theta^*$  distribution. The  $\eta_b$  cut is, therefore, needed to get the unbiased sample. The  $\eta_b$  cut is ,

$$\begin{aligned}\eta_{\pi^0} < \eta_{\pi^\pm} &\Rightarrow \cos \theta^* < 0, -0.8 < \eta_b < 0.25 \\ \eta_{\pi^0} > \eta_{\pi^\pm} &\Rightarrow \cos \theta^* > 0, -0.25 < \eta_b < 0.45\end{aligned}$$

Figure 6.23 shows the  $\cos \theta^*$  distribution of  $\pi^0\pi^\pm$  events in four different mass regions with the  $\eta_b$  cut. Again, the spectrum is rising as  $\cos \theta^*$  values increase. Fig. 6.24 displays the same distribution integrated in four mass regions with the  $\eta_b$  cut. The fitted function and the QCD prediction are also shown in this plot. The

parameter  $a$  is measured as  $2.82 \pm 0.12$ , which is consistent with the number extracted from the  $\pi^0\pi^0$  data ( $2.60 \pm 0.20$ ). The CCOR experiment and E711 experiment also measured this parameter  $a$  using proton beam [35][36]. In the CCOR experiment,  $a$  was measured to be  $2.97 \pm 0.05$ , while in E711  $a$  was  $3.01 \pm 0.04$  and  $3.30 \pm 0.07$  for opposite sign and same sign dihadrons, respectively. The  $a$  values in our experiment are close to but slightly lower than what these two experiments got.

Fig. 6.24 shows a large discrepancy between the generated  $\cos\theta^*$  distribution and the data for  $\pi^0\pi^\pm$  events. However, it does not show up in  $\pi^0\pi^0$  events. This feature indicates that the Herwig event generator does not simulate our events quite accurately.

## 6.3 Dijets

Dijets in this thesis contain a  $\pi^0$  as the leading particle of one jet and a  $\pi^0$ ,  $\pi^-$ , or  $\pi^+$  as the leading particle of the other jet from the di- $\pi$  events. Two jets are assumed to be nearly back to back in the parton-parton center of momentum frame. This section aims to describe the characteristics of these dijets. A detailed analysis of jets in E706 is given elsewhere in [28][37][38]. We will briefly discuss the jet algorithm employed and present the results of the correlations between jets and their leading particles here.

### 6.3.1 Jet Definition

A cone algorithm is used to define jets. Each cone is defined by two variables: the azimuthal angle difference ( $\Delta\phi$ ) and the rapidity difference ( $\Delta Y$ ). As an outgoing parton fragments into particles, many of these particles are moving more or less in the direction of their parent parton.  $\Delta\phi$  and  $\Delta\eta$  are used to define what “more or less” means. High  $P_T$   $\pi^0$ 's and  $\pi^\pm$ 's, identified as the leading particles of jets, often give a good approximation of the direction of their original partons and, consequently, their directions are employed to classify the rest of the particles in the same jets.



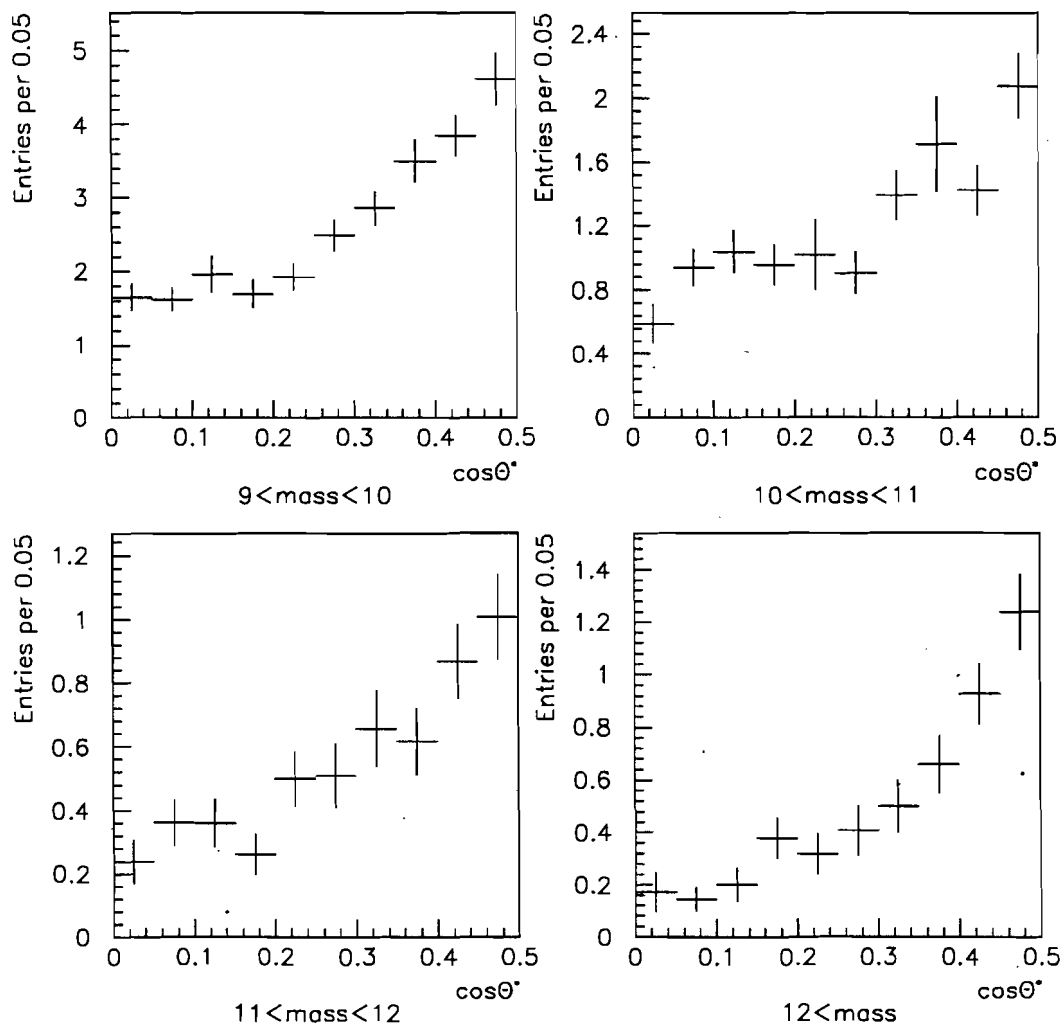


Figure 6.23:  $\cos \theta^*$  distribution of  $\pi^0 \pi^\pm$  in four different mass regions.

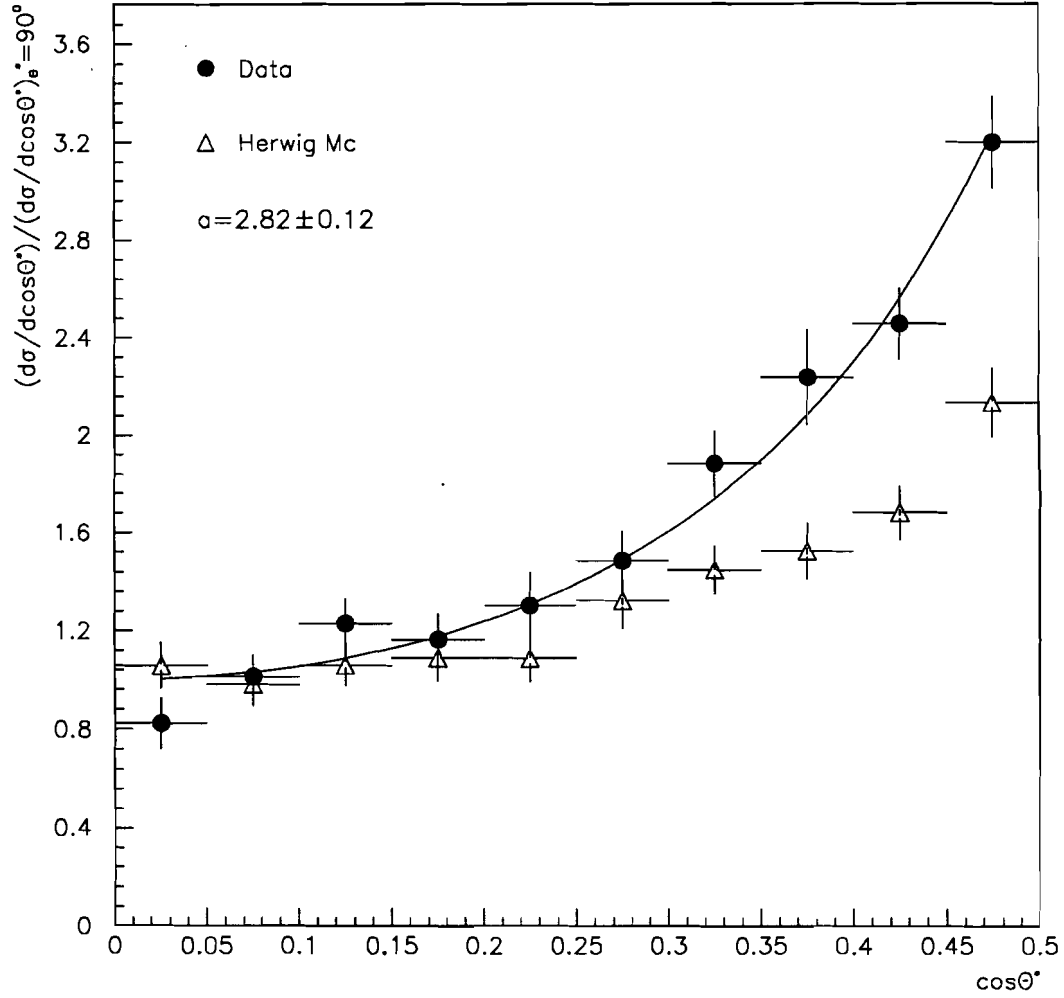


Figure 6.24:  $\cos \theta^*$  distribution of  $\pi^0\pi^\pm$  overlapped with the leading-log QCD calculations derived from the Herwig event generator. The fitted function is  $\frac{1}{2} \left[ \frac{1}{(1+\cos \theta^*)^a} + \frac{1}{(1-\cos \theta^*)^a} \right]$ . The parameter  $a$  is determined from the experimental data.

Figure 6.25 shows the  $\Delta\phi$  between the highest  $P_T$  triggered  $\pi^0$  and the charged tracks in the  $\pi^0\pi^0$  events. The strong enhancement at  $\Delta\phi = 0^\circ$  and  $180^\circ$ , suggests that there are many charged tracks with nearly the same and opposite directions of the highest  $P_T$   $\pi^0$ 's, supporting the hypothesis that two jets tend to be back to back in the azimuthal plane. Moreover, there are apparently more high  $P_T$  particles in the opposite direction from the  $\pi^0$  direction than in the same direction. This phenomenon is consistent with the arguments of the conservation of momentum as well as QCD expectation. A similar study is also conducted for neutral particles detected in EMLAC. Figure 6.26 displays the distributions of  $\Delta\phi$  between the highest  $P_T$  triggered  $\pi^0$  and other electromagnetic showers (photons) in  $\pi^0\pi^0$  events. If the electromagnetic showers match charged tracks at the front face of the EMLAC, or they are the decay photons of the triggered  $\pi^0$ 's, these showers are excluded in the plot. The same  $\Delta\phi$  correlation appears for photons as well.

We also study the  $\Delta\phi$  correlation in for  $\pi^0\pi^\pm$  events for charged and neutral particles, although this time, the direction of high  $P_T$   $\pi^\pm$  in the away side of the triggered  $\pi^0$  is chosen as the reference. This choice is made to avoid the trigger bias. Since particles in the same direction of the triggered  $\pi^0$  helped trigger the events, we preferentially selected those events where particles were populated at  $\Delta\phi = 0$ . Therefore, charged  $\pi^\pm$ 's in the away side is chosen as the reference. The  $\Delta\phi$  distributions are displayed in Fig. 6.27 and 6.28 for charged particles and photons, respectively. The region at  $\Delta\phi=0$  is now more populated, because the  $P_T$  of  $\pi^\pm$  is, in general, less than that of triggered  $\pi^0$  (which is above 4 GeV/c).

These  $\Delta\phi$  plots for  $\pi^0\pi^0$  and  $\pi^0\pi^\pm$  events indicate that there is a strong correlation between the highest  $P_T$  particles and the remaining high  $P_T$  particles in the same events. Moreover, as the  $P_T$  of the particles increases, the correlations become more pronounced.

In addition to the  $\Delta\phi$  correlation, it is of interests to study the rapidity correlation (" $\Delta Y$ ") in the events.  $\Delta Y$  is defined with respect to the highest triggered  $P_T$   $\pi^0$

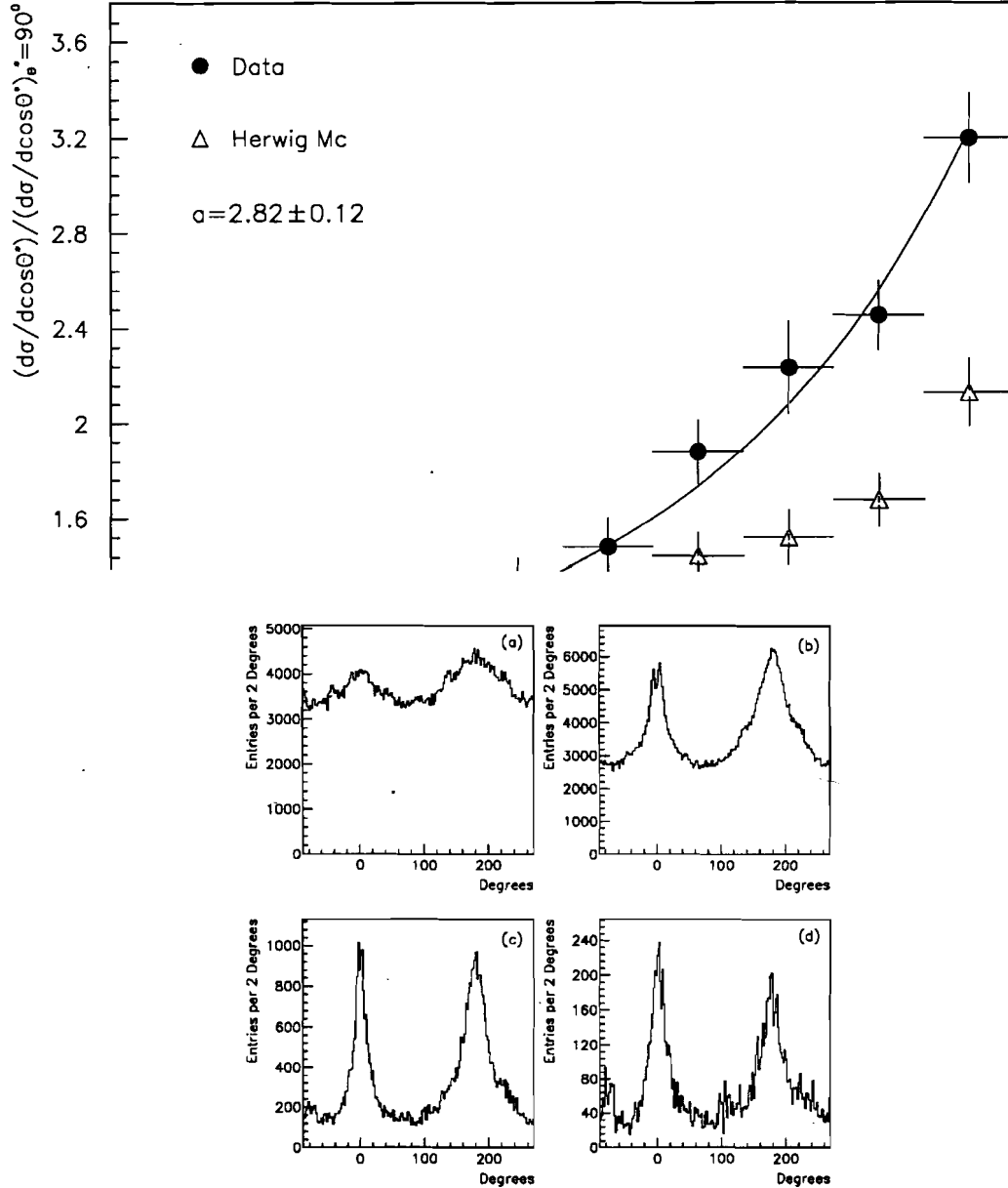


Figure 6.26: Azimuthal Correlations in  $\pi^0\pi^0$  Events.  $\Delta\phi$  is the angle between the highest  $P_T$   $\pi^0$  and photons. For all photons with (a)  $P_T < 0.25$  GeV/c, (b)  $P_T > 0.25$  GeV/c, (c)  $P_T > 1$  GeV/c, (d)  $P_T > 2$  GeV/c.

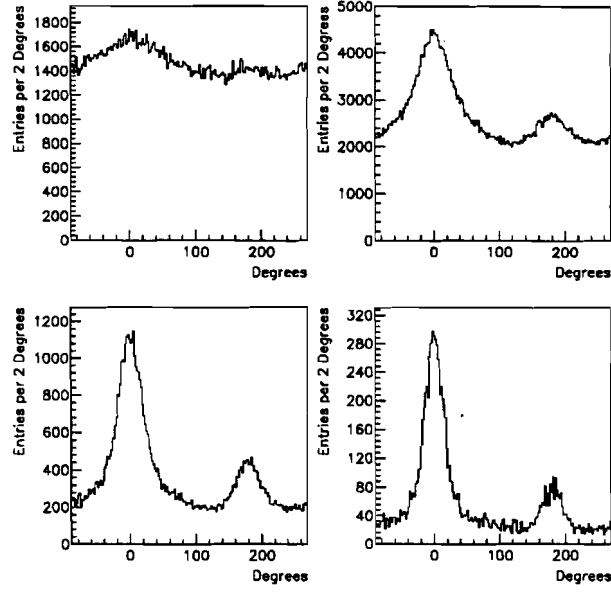


Figure 6.27: Azimuthal Correlations in  $\pi^0\pi^\pm$  Events.  $\Delta\phi$  is the angle between the highest  $P_T$   $\pi^\pm$  and the other charged particles. For all tracks with (a)  $P_T < 0.25$  GeV/c, (b)  $P_T > 0.25$  GeV/c, (c)  $P_T > 1$  GeV/c, (d)  $P_T > 2$  GeV/c.

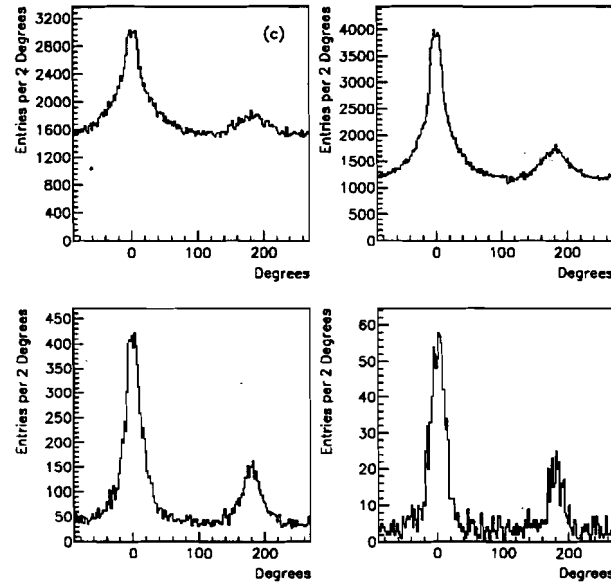


Figure 6.28: Azimuthal Correlations in  $\pi^0\pi^\pm$  Events.  $\Delta\phi$  is the angle between the highest  $P_T$   $\pi^\pm$  and photons. For all photons with (a)  $P_T < 0.25$  GeV/c, (b)  $P_T > 0.25$  GeV/c, (c)  $P_T > 1$  GeV/c, (d)  $P_T > 2$  GeV/c.

for  $\pi^0\pi^0$  events and to the highest  $P_T \pi^\pm$  in the away side of the triggered  $\pi^0$  for  $\pi^0\pi^\pm$  events. The results of  $\Delta Y$  distributions are displayed in Figs. 6.29, 6.30, 6.31, and 6.32. In these plots, the “background curves” are formed by taking the leading  $\pi$ ’s from the previous events and keeping the rest of the particles in the event unchanged. All these figures are normalized to the total number of entries in the plots. Again, as in the  $\Delta\phi$  study, the high  $P_T \pi^\pm$  is chosen to avoid the trigger bias. The enhancement at  $\Delta Y = 0$  above background shows that there are particles, charged and/or neutral, produced in the direction of the leading  $\pi$ ’s. This correlation becomes stronger as the  $P_T$  of the particle increases. This phenomenon agrees with the expectations of QCD, suggesting there are jet-like signals in di- $\pi$  events.

Since particles have correlations with respect to the high  $P_T \pi$ ’s in di- $\pi$  events, we now use these two variables,  $\Delta\phi$  and  $\Delta Y$ , to distinguish particles inside the  $\pi$  “cone”. We define the radius of cone,  $R$ , as:

$$R = \sqrt{(\Delta\phi)^2 + (\Delta Y)^2}. \quad (6.14)$$

Every particle, whose  $R$  is less than 1 with respect to a high  $P_T \pi$ , is assigned to this  $\pi$  cone. In order to exclude the large background from low  $P_T$  particles, each particle is required to have  $P_T$  above 0.25 GeV/c. The particles inside a  $\pi$  cone, including  $\pi$  itself, form a  $\pi$  jet. After getting a  $\pi$  jet, we use its direction instead of the direction of the leading  $\pi$  to reassign particles into this jet, based on the new  $R$  with respect to this jet. Thus, each high  $P_T \pi$  makes a  $\pi$  jet, which more or less represents the original parton.

### 6.3.2 Characteristics of Jets

Using the cone algorithm introduced in the previous section, we now study the characteristics of the jets. Most notably, the number of particles in the jets decrease when the transverse momentum carried by the leading  $\pi$  of the jets increase. This effect is shown in Figs. 6.33 and 6.34. Secondly, when the transverse momentum of the leading  $\pi$  of the jet increases, the fraction of the jet transverse momentum

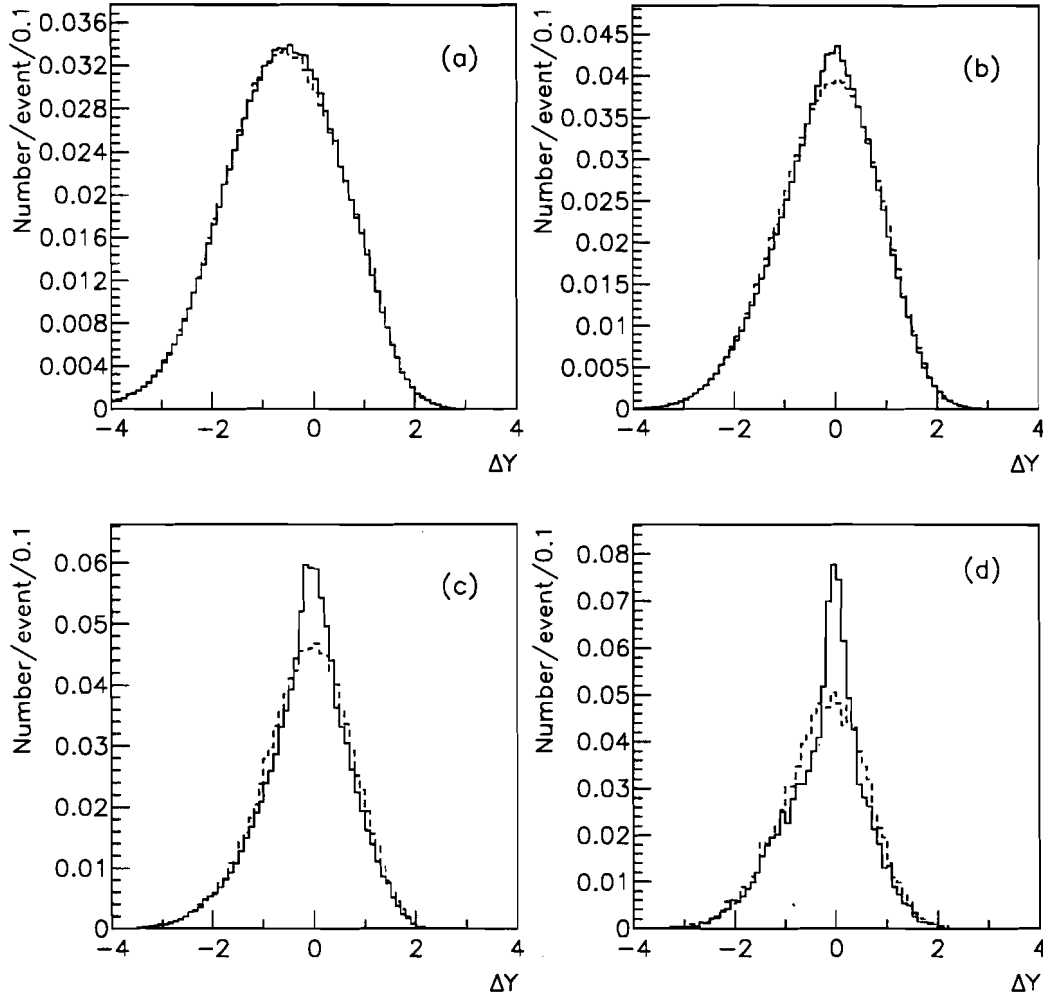


Figure 6.29: Rapidity Correlations in  $\pi^0\pi^0$  Events.  $\Delta Y$  is the rapidity difference between the highest  $P_T$   $\pi^0$  and the charged particles. For all tracks with (a)  $P_T < 0.25$  GeV/c, (b)  $P_T > 0.25$  GeV/c, (c)  $P_T > 1$  GeV/c, (d)  $P_T > 2$  GeV/c. The dash line represents the background of  $\Delta Y$  formed by the leading  $\pi^0$  of the previous event and the particles from the present event. The strong enhancement at zero suggests that there are particles moving in the same direction of the leading particles.

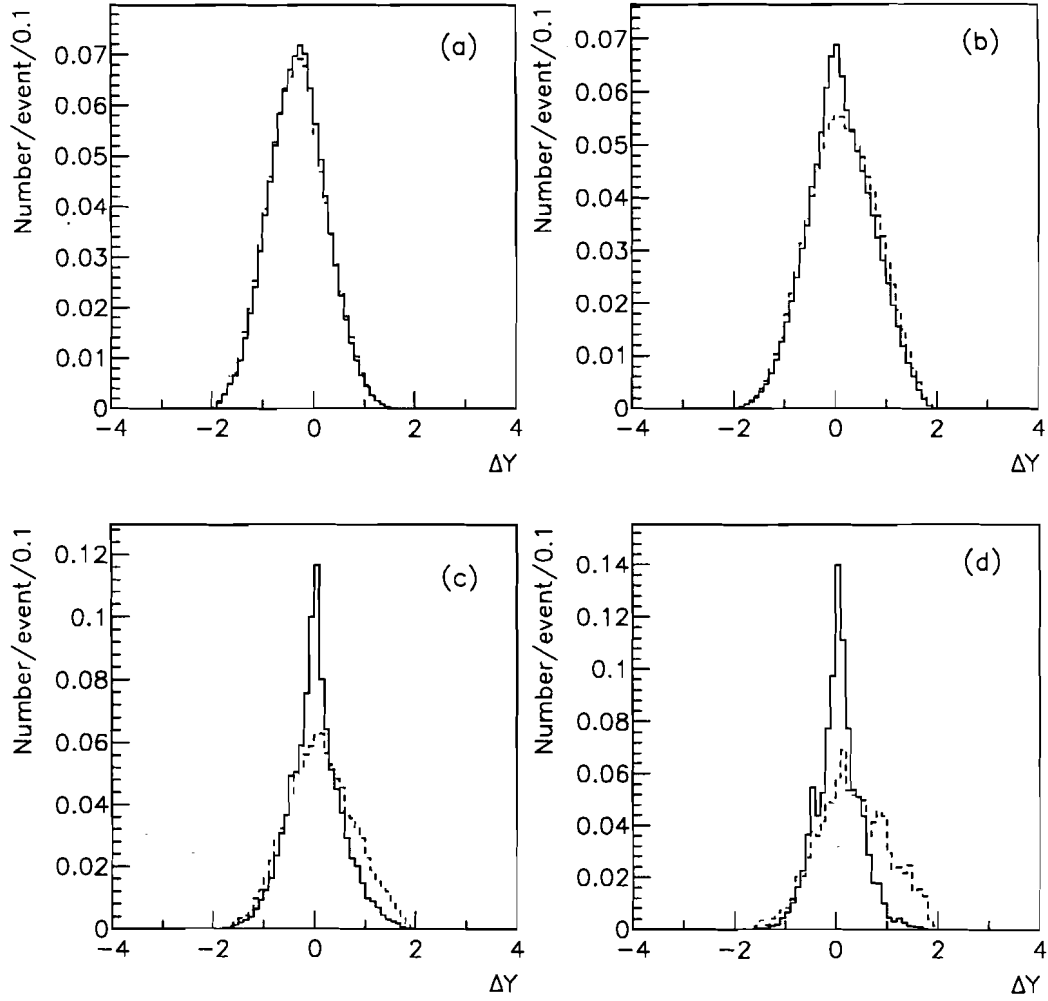


Figure 6.30: Rapidity Correlations in  $\pi^0\pi^0$  Events.  $\Delta Y$  is the rapidity difference between the highest  $P_T$   $\pi^0$  and photons. For all photons with (a)  $P_T < 0.25$  GeV/c, (b)  $P_T > 0.25$  GeV/c, (c)  $P_T > 1$  GeV/c, (d)  $P_T > 2$  GeV/c. The dash line represents the background of  $\Delta Y$  formed by the leading  $\pi^0$  of the previous event and the particles of the present event.



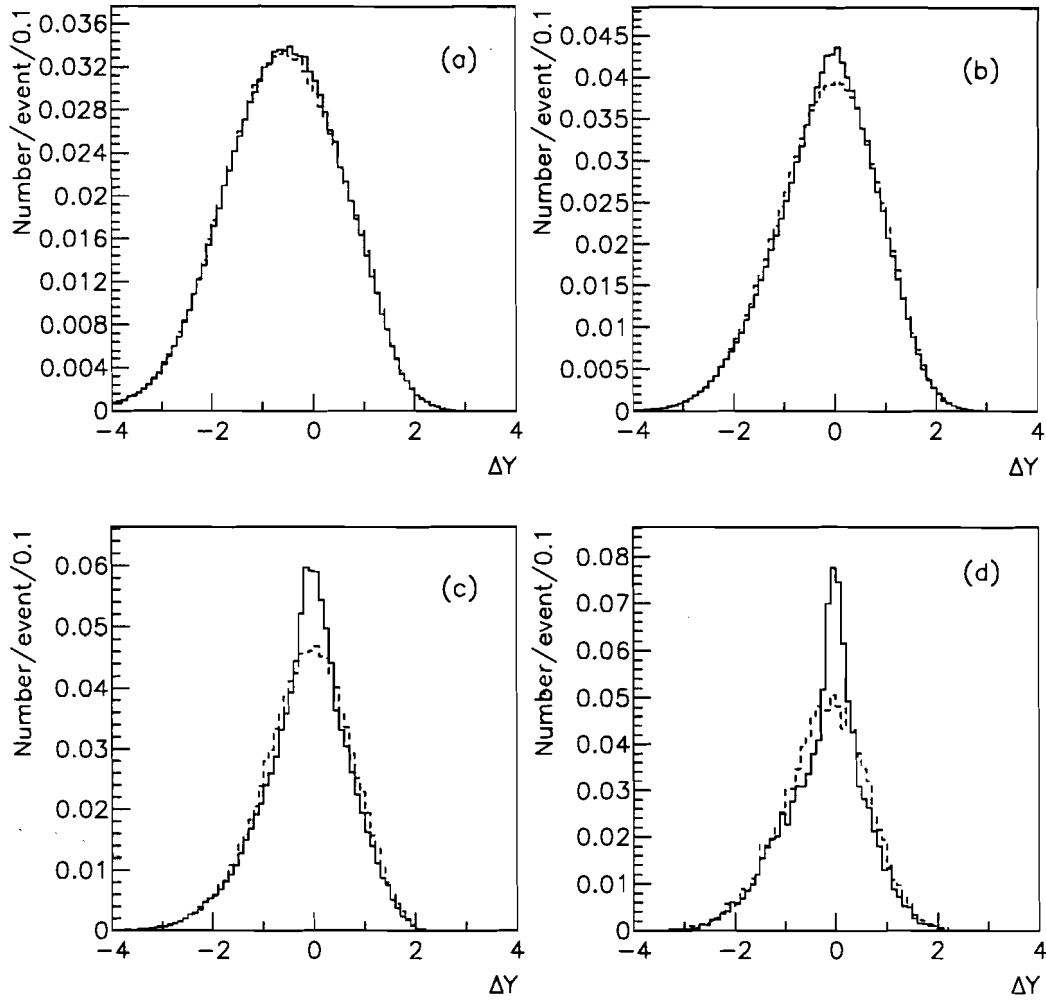


Figure 6.31: Rapidity Correlations in  $\pi^0\pi^\pm$  Events.  $\Delta Y$  is the rapidity difference between the highest  $P_T$   $\pi^\pm$  and the charged particles. For all tracks with (a)  $P_T < 0.25$  GeV/c, (b)  $P_T > 0.25$  GeV/c, (c)  $P_T > 1$  GeV/c, (d)  $P_T > 2$  GeV/c. The dash line represents the background of  $\Delta Y$  formed by the leading  $\pi^\pm$  from the previous event and the particles of the present event.

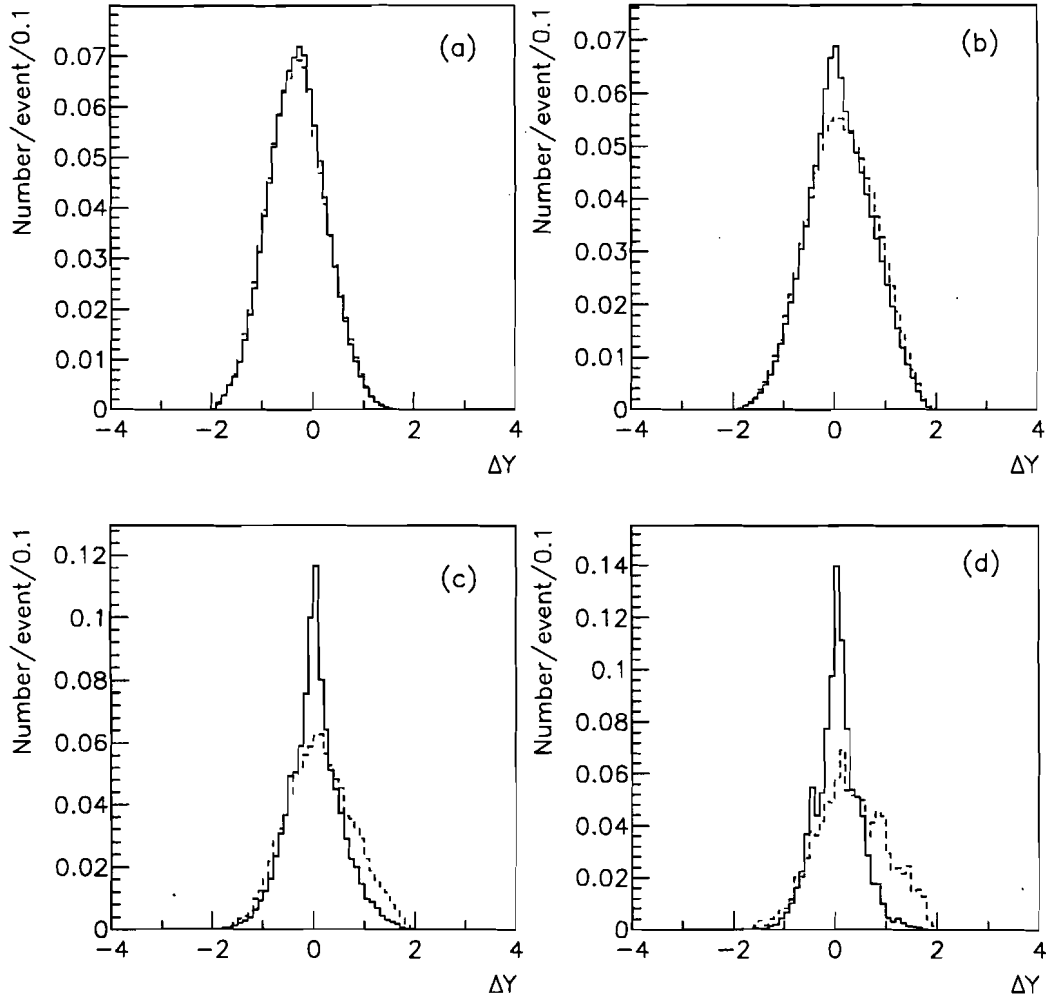


Figure 6.32: Rapidity Correlations in  $\pi^0\pi^\pm$  Events.  $\Delta Y$  is the rapidity difference between the highest  $P_T$   $\pi^\pm$  and photons. For all photons with (a)  $P_T < 0.25$  GeV/c, (b)  $P_T > 0.25$  GeV/c, (c)  $P_T > 1$  GeV/c, (d)  $P_T > 2$  GeV/c. The dash line represents the background of  $\Delta Y$  formed by the leading  $\pi^\pm$  from the previous event and the particles of the present event.

carried by the  $\pi$  meson also increases. Fig. 6.35 displays the average fraction of the jet transverse momentum versus the  $P_T$  of the leading  $\pi$  meson. The variable  $Z$  is defined as the ratio of the  $P_T$  carried by the leading  $\pi$  meson and the  $P_T$  carried by the jet. These two effects can be interpreted as follows:

1. Jet  $P_T$  in average, increases when the  $P_T$  of its leading particle increases. This proportionality, however, is not linear but the ratio between these two is linearly dependent on the  $P_T$  of the leading  $\pi$  at  $P_T$  above 3 GeV/c.
2. The larger the transverse momentum carried by the leading  $\pi$  of the jet, the less energy left for the parton to fragment high  $P_T$  particles ( $P_T > 0.25\text{GeV}/c$ ). Therefore, fewer particles are found in the jets with higher  $P_T$  leading particles.

Knowing the four vectors of jets in dijet events, the momentum fractions,  $x_a$  and  $x_b$ , can be estimated by using Eqs. 1.21 and 1.22. In E706,  $x_a$  is the momentum fraction of  $\pi^-$  carried by partons, while  $x_b$  is the momentum fraction of the target nucleon. Since the net  $P_T$  of dijets may not always be zero, the  $P_T$  of the jet with the larger value is chosen to calculate  $x_a$  and  $x_b$ . We cannot measure the raw  $x_a$  and  $x_b$  distributions because we do not really trigger on jets and the  $x_a$  and  $x_b$  distributions are restricted by our detector acceptance. However, it's still fair to compare the  $x_a$  distribution with the  $x_b$  distribution. In Eqs. 1.20 and 1.21,  $x_a$  and  $x_b$  are determined by three variables,  $y_c$ ,  $y_d$ , and  $P_T$ .  $y_c$  and  $y_d$  are the rapidities of jets (partons) in the  $\pi^-$ -nucleon center of momentum frame. Since the rapidity coverage in our spectrometer for  $\pi^0$ 's is symmetrical about 0 in the  $\pi^-$ -nucleon center of momentum frame, the rapidity coverage for  $\pi^0$  jets is nearly symmetrical about 0. The difference between  $x_a$  and  $x_b$  in Eqs. 1.20 and 1.21 is the sign in  $y_c$  and  $y_d$ . Therefore, the phase space restricted by our apparatus is the same for  $x_a$  and  $x_b$  for  $\pi^0\pi^0$  jets. The rapidity coverage for charged tracks is, however, asymmetrical. In order to get an unbiased sample due to the detector acceptance, the rapidity of the leading charged particles of jets are required to be within  $\pm 0.8$  in studying the  $x_a$

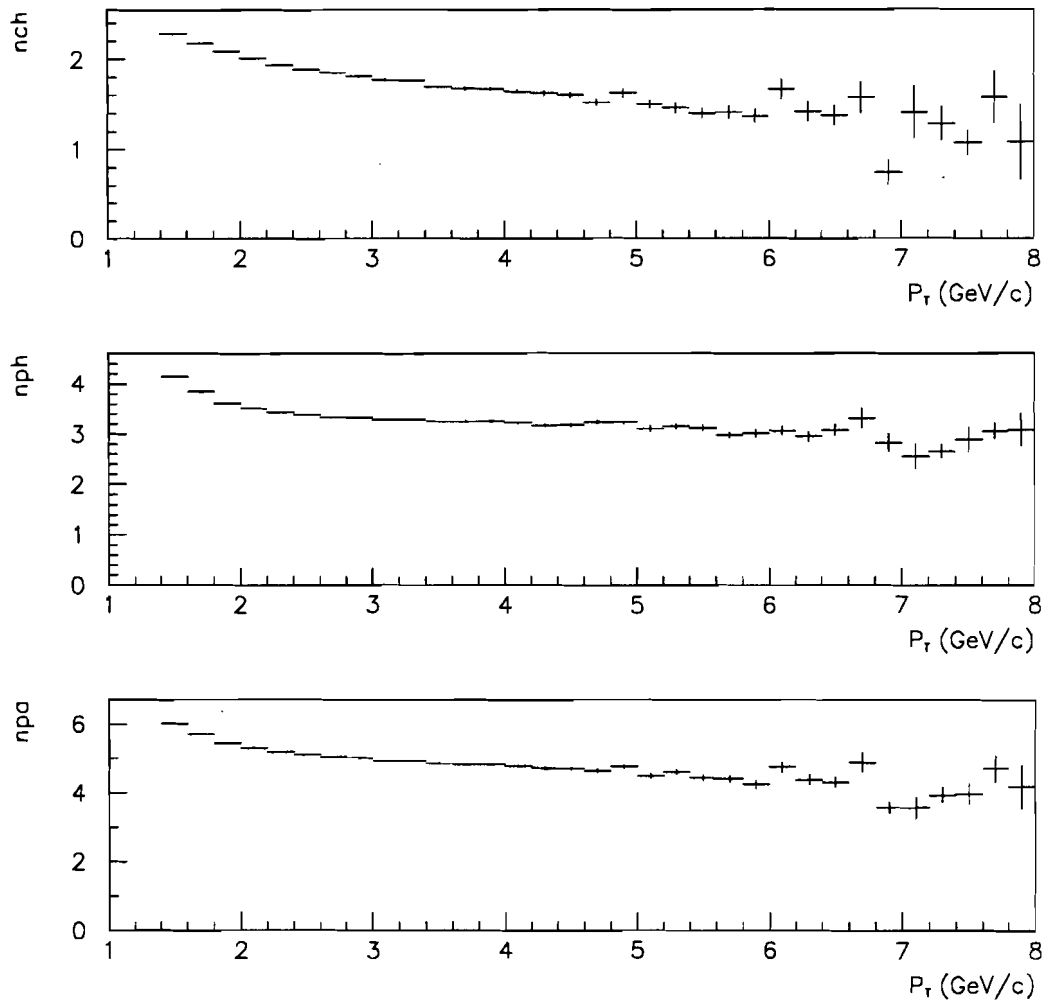


Figure 6.33: The average number of particles in  $\pi^0$  jets versus the  $P_T$  of the leading  $\pi^0$ . The top plot counts charged particles only, the middle one displays the average number of neutral, and the bottom one includes both neutral and charged particles.

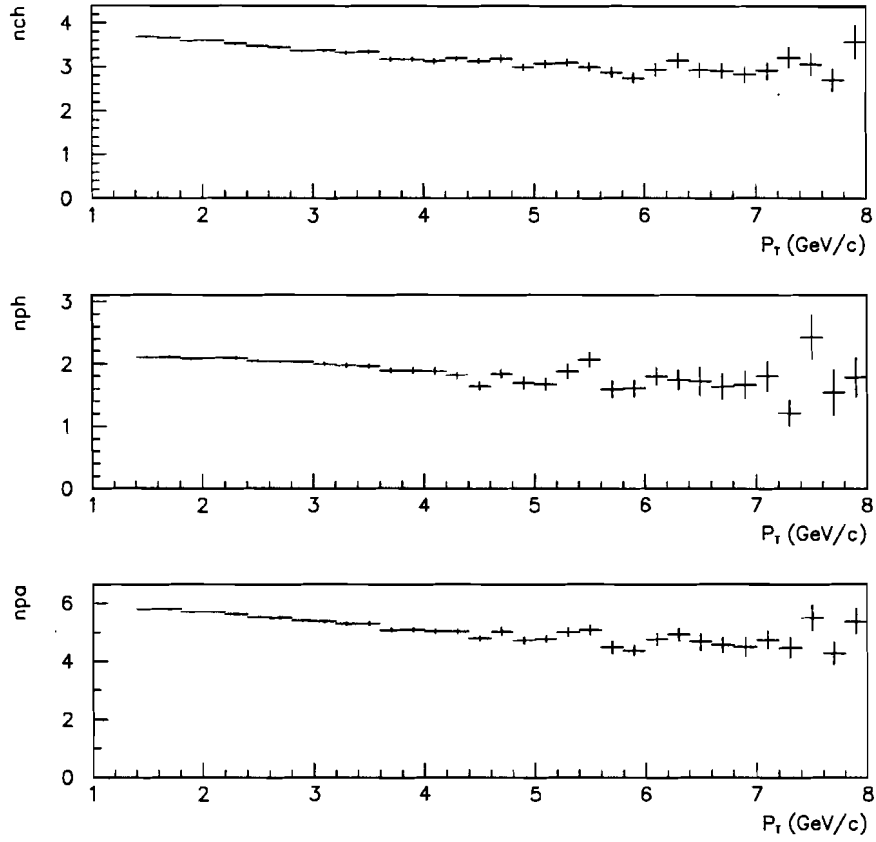


Figure 6.34: The average number of particles in  $\pi^\pm$  jets versus the  $P_T$  of  $\pi^\pm$ . The top plot counts charged particles only, the middle one displays the average number of neutral particles, and the bottom plot includes both neutral and charged particles.

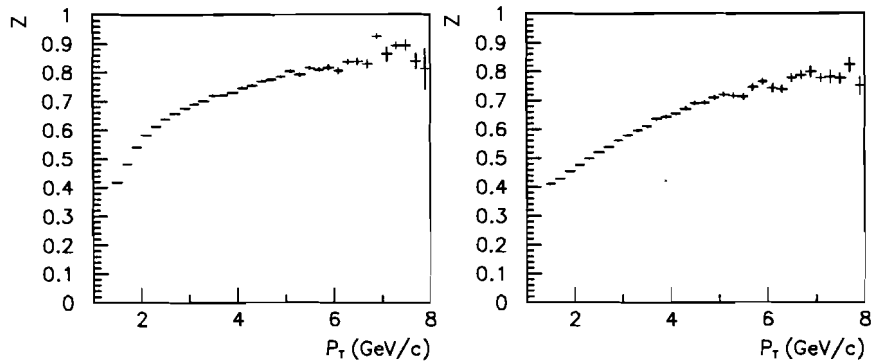


Figure 6.35: The average fraction of the jet  $P_T$  carried by the leading  $\pi$  meson, versus the  $P_T$  of  $\pi$  meson. The leading particle is  $\pi^0$  in the plot to the left and  $\pi^\pm$  in the one to the right.

and  $x_b$  distributions. This  $\pm 0.8$  is introduced to have the same rapidity coverage for the leading charged particles and  $\pi^0$ 's.

We present the  $x_a$  and  $x_b$  distributions of  $\pi^0\pi^0$  jets and  $\pi^0\pi^\pm$  jets in Figs 6.36 and 6.37, respectively. These plots show that the most probable value in the  $x_a$  distribution is larger than that of the  $x_b$  distribution, suggesting that the partons inside the  $\pi^-$ , on average, carry a larger fraction of momentum than the partons inside nucleon. This phenomenon is also consistent with the parton model, since there are two valence quarks in the  $\pi^-$  meson whereas there are three valence quarks per nucleon. The difference in the  $x_a$  and  $x_b$  distributions between Fig. 6.36 and 6.37 is caused by the  $P_T$  difference between the triggered  $\pi^0$ 's. The minimum  $P_T$  of  $\pi^0$ 's for  $\pi^0\pi^0$  events is 2 GeV/c, but the minimum  $P_T$  for  $\pi^0\pi^\pm$  events is 4 GeV/c. The reconstructed  $\pi^0$  jets, hence, also have a difference in  $P_T$ . Since  $x_a$  and  $x_b$  are proportional to the  $P_T$  of jets, the average values of  $x_a$  and  $x_b$  are larger in  $\pi^0\pi^\pm$  events than in  $\pi^0\pi^0$  events.

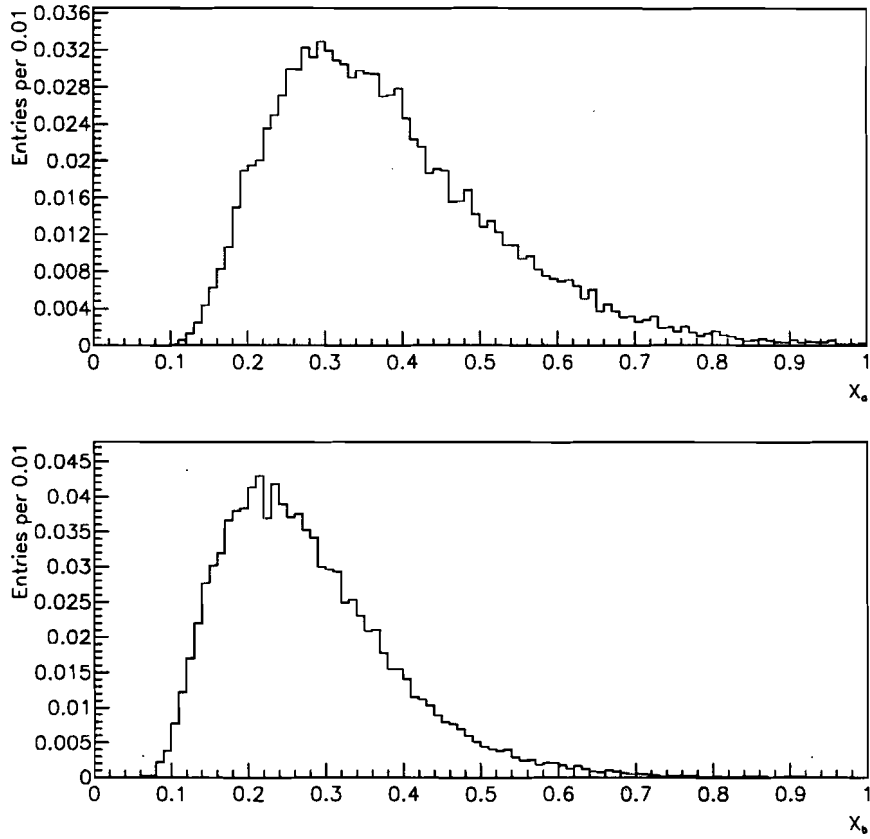


Figure 6.36:  $x_a$  and  $x_b$  distributions in  $\pi^0\pi^0$  jets. These distributions are weighted by all the correction factors described in Section 6.2.

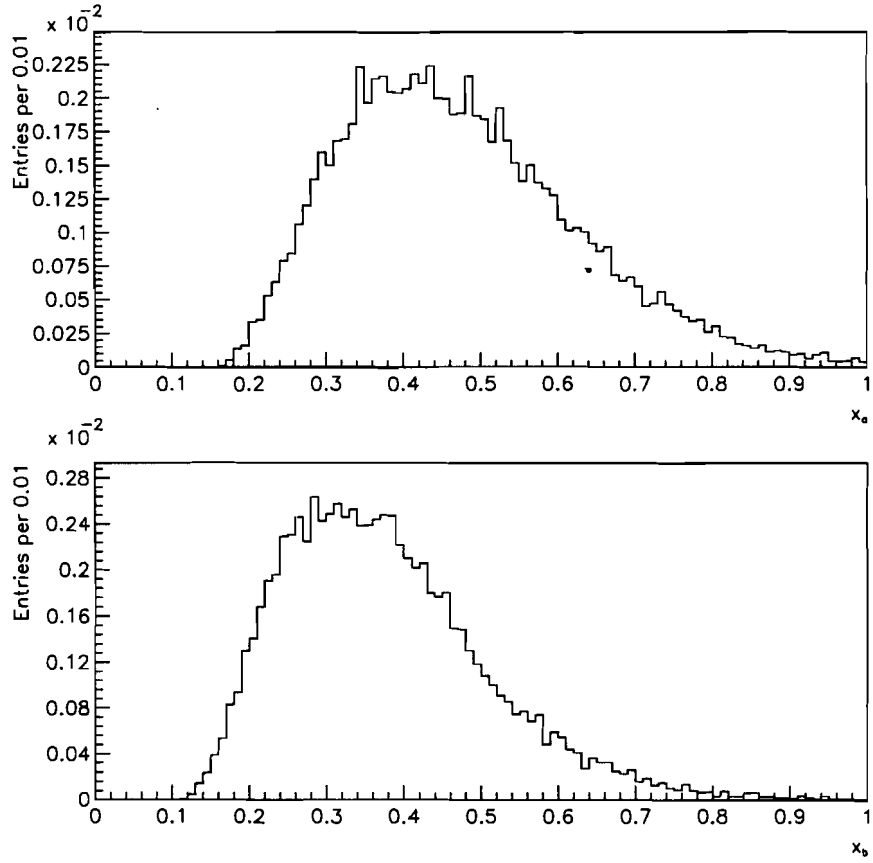


Figure 6.37:  $x_a$  and  $x_b$  distributions in  $\pi^0\pi^\pm$  jets. These distributions are weighted by all the correction factors described in Section 6.2.



## 6.4 Nuclear Dependence

Since the tracking system can determine where the primary interactions occur, we are able to study nuclear effect in our experiment. This section presents the results for the nuclear dependence of the di- $\pi$  events as well as the evidence of multiple scattering in  $\pi^0\pi^0$  jets and  $\pi^0\pi^\pm$  jets. We will also compare our results with other experiments.

### 6.4.1 Nuclear Dependence on Di- $\pi$ Cross Sections

As described in Section 1.4, the cross section per nucleon is often parametrized as  $\sigma(A) = \sigma_0 A^{\alpha-1}$ . The ratio of di- $\pi$  cross sections between  $\pi^-$ -Cu and  $\pi^-$ -Be interactions can be written as:

$$\frac{\sigma_{Cu}}{\sigma_{Be}} = \left(\frac{A_{Cu}}{A_{Be}}\right)^{\alpha-1}. \quad (6.15)$$

where  $\sigma_{Cu}$  and  $\sigma_{Be}$  are the di- $\pi$  cross sections per nucleon for  $\pi^-$ -Cu and  $\pi^-$ -Be interactions, respectively. Therefore,

$$\alpha = 1 + \frac{\ln \frac{\sigma_{Cu}}{\sigma_{Be}}}{\ln \frac{A_{Cu}}{A_{Be}}} \quad (6.16)$$

The top plot of Figure 6.38 displays the parameter,  $\alpha$ , in terms of the mass of di- $\pi$ 's. These  $\alpha$  values are also listed in Tables B.4 and B.5. It's obvious that  $\alpha$  is above one in the region where di- $\pi$  mass is less than  $8 \text{ GeV}/c^2$ , and it tends to decrease when di- $\pi$  mass increases. There have been several other experiments which studied the A dependence of dihadron production [39][40][41][42][43]. All these experiments used proton beams and detected dihadrons with  $+-$  states. Experiments [44] on Drell-Yan dilepton production in hadron-nucleus interactions and the results of A dependence of direct photon production at E706 [45], have shown that initial-state parton experienced very little nuclear scattering. Therefore, it may be reasonable to compare our results with the published data of theirs even though we did not use the same type of beams. The bottom plot of Fig. 6.38 shows the  $\alpha$  values measured in

E706 and other published data. Our results are consistent with the cited experiments within the statistical uncertainties for mass greater than  $4.5 \text{ GeV}/c^2$ .

The Fermilab dihadron experiment of Straub *et al.*, [46] studied the W-to-Be per nucleon cross section ratio in the dihadron mass range similar to ours. Their result indicates that this cross section ratio decreases when the dihadron mass increases. However, this ratio was less than 1 except in the low mass region (mass less than  $8 \text{ GeV}/c^2$ ), indicating that  $\alpha$  dropped to the value less than 1 at high mass. Although we have this decreasing trend in  $\alpha$ , our  $\alpha$  values in high mass region are around 1 with 10-20% statistical uncertainties. At present, we cannot say our di- $\pi$  result is inconsistent with theirs, because of the large statistical uncertainties. This phenomenon of  $\alpha < 1$  can not be explained by the parton multi-scattering model. In their published paper, Straub *et al.* suggested that this nuclear suppression effect may be brought about by the suppression of high- $z$  hadronization. They had this nuclear suppression effect even for single high  $P_T$  hadrons, which agreed with the prediction of the suppression of high- $z$  hadronization. Our data in inclusive  $\pi^0$  and  $\eta$  production[45] showed very little reduction of  $\alpha$  in our high  $P_T$  region. The real reason for this  $\alpha$  decreasing trend is still not clear.

#### 6.4.2 Nuclear Effects on Dijets

We also studied nuclear effect in our di- $\pi$  jets, using the variables— $\Delta\phi$  and  $K_{T\phi}^2$ . Figure 6.39 shows the azimuthal angle difference,  $\Delta\phi$ , between the jet axes in di- $\pi$  events for  $\pi^-$ -Cu and  $\pi^-$ -Be interactions. This plot indicates that the  $\Delta\phi$  distribution for the Cu data is somewhat broader. The same effect has been reported by Fermilab E609 [47], which used H and Pb as their targets. This broadening effect is more dramatic in E609 data probably because of the larger A difference between H and Pb.

The second variable,  $K_{T\phi}$  (see Fig. 1.6), gives us another view of this nuclear effect. Figure 6.40 shows these  $K_{T\phi}$  distributions for Be, Cu, and Si data in di- $\pi$

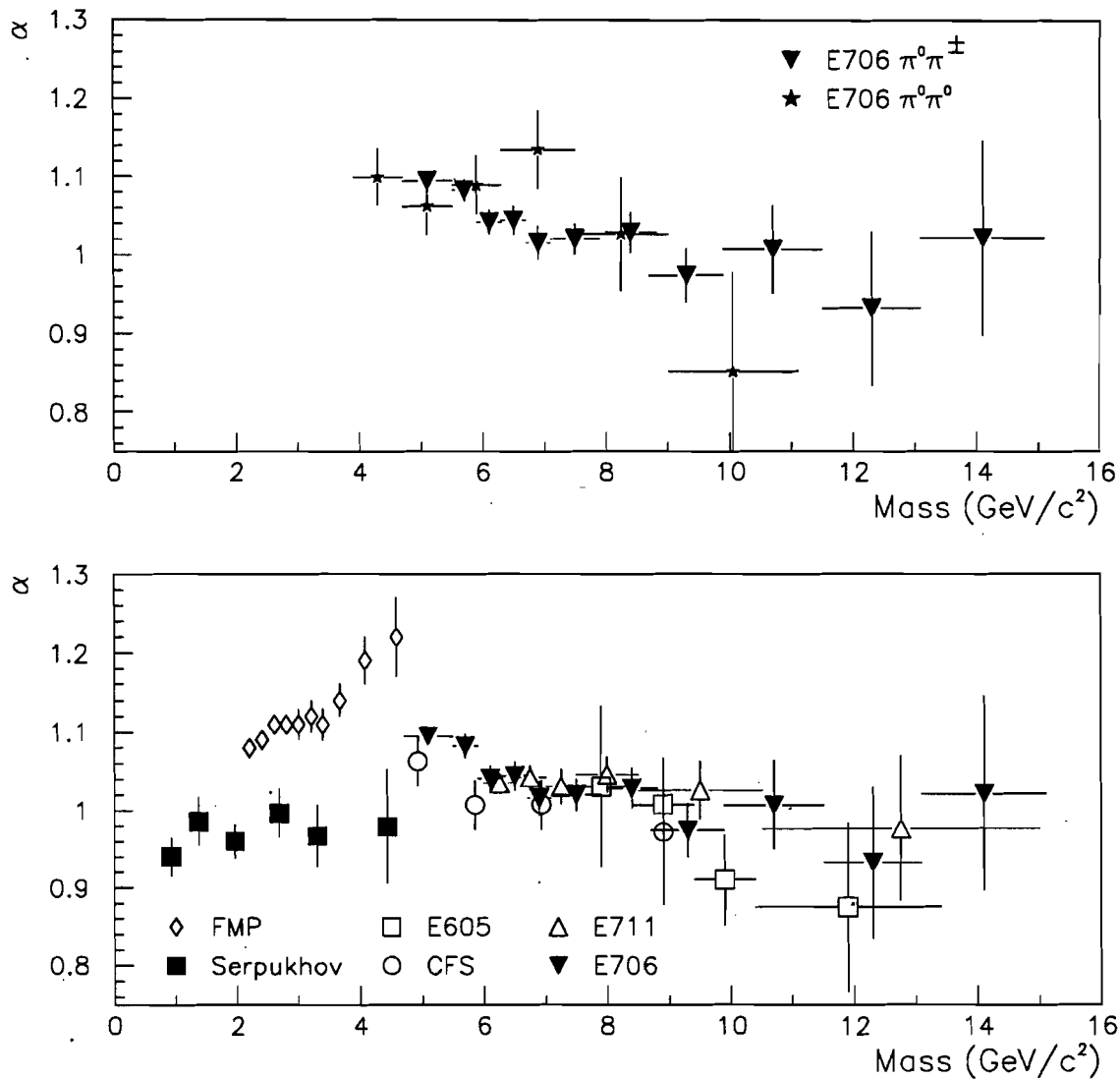


Figure 6.38:  $\alpha$  vs dihadron mass. The top plot shows the results of  $\pi^0\pi^0$  and  $\pi^0\pi^\pm$  events. The bottom one shows all published data of  $\alpha$  as a function of mass. All experiments except E706 measured dihadrons in  $+-$  states. FMP (Ref. [40]), CFS (Ref. [39]), and E605 (Ref. [42]) used 400 GeV/c proton beams. Experiment E711 (Ref. [43]) used 800 GeV/c proton beams while Serpukhov (Ref. [41]) used 70 GeV/c proton beams.

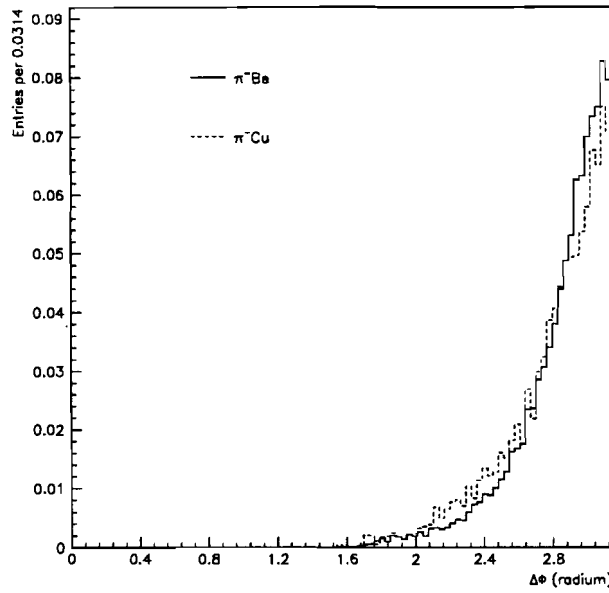


Figure 6.39:  $\Delta\phi$  between jet axes for  $\pi^-$ -Be and  $\pi^-$ -Cu interactions.

jets. Since we are able to reconstruct the primary vertices in the silicon detectors, Si becomes our third “target”. It turns out that this  $K_{T\phi}$  distribution has different shapes in the different targets. The larger the nucleus number, the broader the  $K_{T\phi}$  distribution. This phenomenon is manifested in Fig. 6.41, which displays the ratio of the  $K_{T\phi}$  distribution for Cu and Be targets. This ratio increases with the increasing absolute value of  $K_{T\phi}$ . One may argue that the shape difference of the  $K_{T\phi}$  distribution is caused by the coulomb scattering between outgoing hadrons and targets instead of the parton rescattering with the nuclear matter, especially since the Cu target is in front of the Be target in this experiment. To address this issue, we studied this  $K_{T\phi}$  shape from sections of targets of the same material. Figure 6.42 shows this ratio of the  $K_{T\phi}$  distribution in the same target material. These distributions are all flat, indicating that the coulomb scattering effect is small. Therefore, we conclude that the nuclear enhancement in the  $K_{T\phi}$  distribution is not caused by the coulomb scattering but by parton rescattering.

Fermilab experiment E683 has already observed the nuclear enhancement in

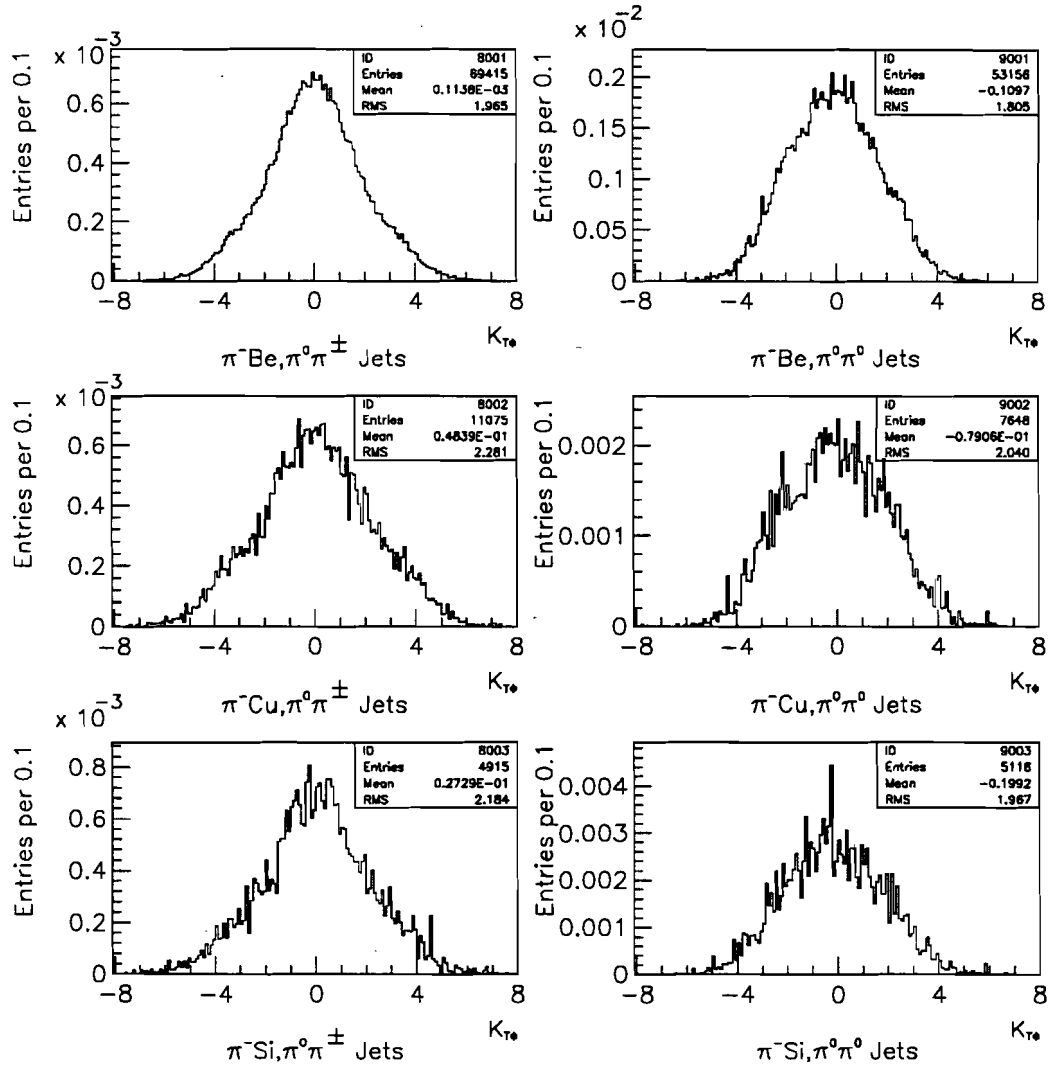


Figure 6.40:  $K_{T\phi}$  distributions in Be, Cu, and Si data.

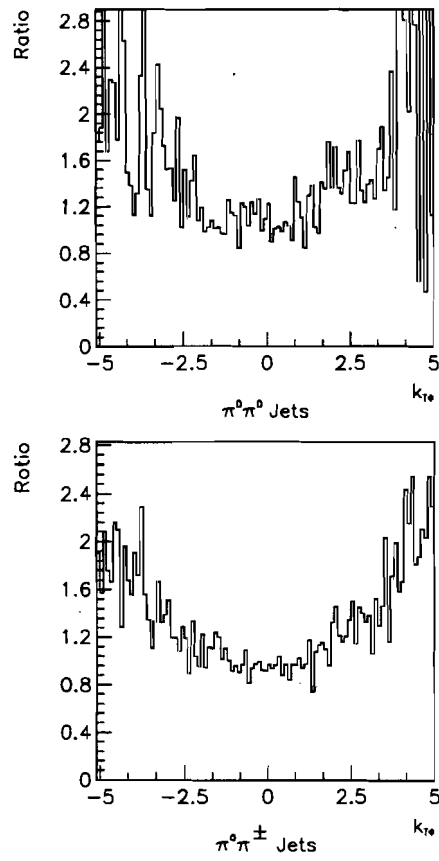


Figure 6.41: Cu-to-Be ratio of the  $K_{T\phi}$  distribution in  $\pi^0\pi^0$  jets and  $\pi^0\pi^\pm$  jets

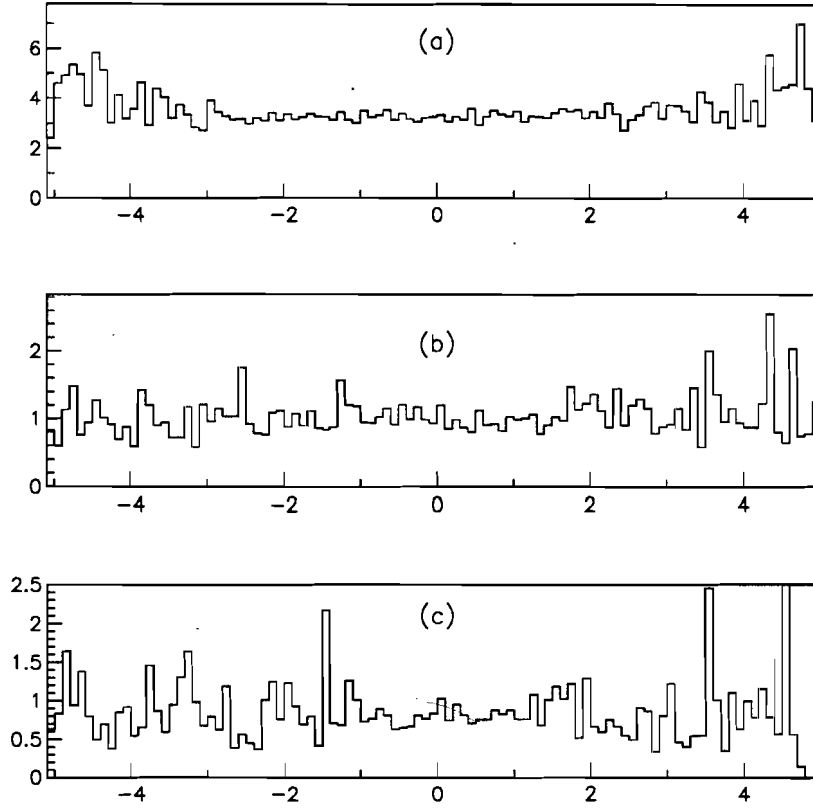


Figure 6.42: Ratios of the  $K_{T\phi}$  distributions for (a) first piece of Be to second piece of Be, (b) first piece of Cu to second piece of Cu, (c) upstream Si to downstream Si.

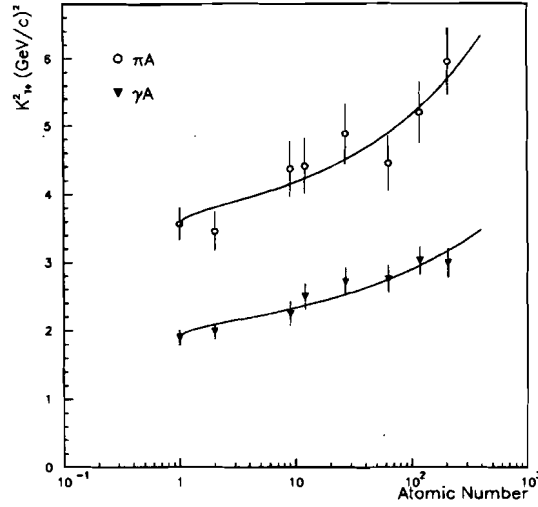


Figure 6.43:  $\langle K_{T\phi}^2 \rangle$  as a function of atomic weight for photon-nucleus ( $\gamma A$ ) and pion-nucleus ( $\pi A$ ) data in E683 experiment. The curves shown are the best power law fits to the form  $\langle K_{T\phi}^2 \rangle = C_0 + C_1(A - 1)^\alpha$ . For the photon data the minimum  $\chi^2$  fit yields  $C_0 = 1.85 \pm 0.10$ ,  $C_1 = 0.24 \pm 0.10$ ,  $\alpha = 0.32 \pm 0.08$ , and for pion data the fit yields  $C_0 = 3.54 \pm 0.22$ ,  $C_1 = 0.27 \pm 0.21$ ,  $\alpha = 0.39 \pm 0.15$ .

terms of this variable  $K_{T\phi}$ [48]. They studied photon and  $\pi$  beam on 8 different targets, and found that the mean value of  $K_{T\phi}^2$  ( $\langle K_{T\phi}^2 \rangle$ ) increased when the atomic number increased (see Fig. 6.43). They also reported that the difference of this  $\langle K_{T\phi}^2 \rangle$  between different targets became larger as the beam energy increased. These two phenomena are also consistent with the results in E706. Since the mean value of the  $K_{T\phi}$  distribution is zero, the mean value of  $K_{T\phi}^2$  mathematically equals the square of the RMS of the  $K_{T\phi}$  distribution ( $\sigma^2$ ). Figure 6.44 displays the  $\sigma^2$  of  $K_{T\phi}$  for three different atomic numbers. Our result shows a clear picture of nuclear enhancement in this  $\sigma^2$  variable. The difference of the  $\sigma^2$  value of  $K_{T\phi}$  between Cu and Be targets in our data is larger than what E683 measured. Since E706 has higher beam energy, the trend supports the second phenomenon observed in E683.

Fig. 6.44 also shows that the  $\sigma^2$  of the  $K_{T\phi}$  distribution are smaller for  $\pi^0\pi^0$  jets than for  $\pi^0\pi^\pm$  jets. This feature can also be explained by the  $P_T$  difference of the leading  $\pi^0$  in these two types of events: 2 GeV/c for  $\pi^0\pi^0$ 's and 4 GeV/c for



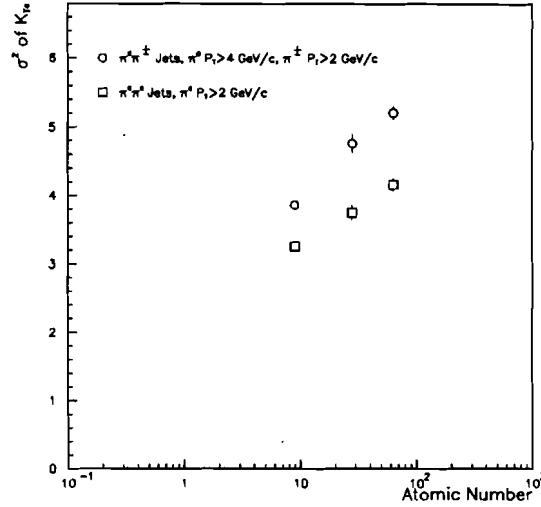


Figure 6.44:  $\sigma^2$  as a function of atomic number for pion-nucleus data in E706 experiment.  $\sigma$  is the RMS of the  $K_{T\phi}$  distribution.

$\pi^0\pi^\pm$ .  $K_{T\phi}$  is calculated by the average  $P_T$  of two jets multiplied by the sin value of the azimuthal angular difference. Therefore, the higher  $P_T$  jets give the higher  $K_{T\phi}$  value. Jets with higher  $P_T$  leading particles potentially have higher reconstructed  $P_T$ . Therefore, the  $\sigma^2$  of the  $K_{T\phi}$  distribution is smaller for  $\pi^0\pi^0$  jets.

## 6.5 Conclusion

In this thesis, we use the data from 515 GeV/c  $\pi^-$  beam incident on Cu and Be targets to measure the cross sections for the production of high mass  $\pi^0\pi^0$ ,  $\pi^0\pi^-$ , and  $\pi^0\pi^+$  pairs. The overall mass spectra of these processes have been compared with QCD predictions generated from the Herwig event generator. The MC generated spectrum agreed with our data for  $\pi^0\pi^0$  production but has a discrepancy for  $\pi^0\pi^-$  and  $\pi^0\pi^+$  production. The  $\cos\theta^*$  distributions for di- $\pi$  events are also measured in the range between 0 to 0.5. In order to get an unbiased sample to measure this  $\cos\theta^*$  distributions, a mass cut and an  $\eta_b$  cut are introduced. The  $\cos\theta^*$  distributions can

be parametrized as

$$\frac{1}{2} \left[ \frac{1}{(1 + \cos \theta^*)^a} + \frac{1}{(1 - \cos \theta^*)^a} \right].$$

The parameter,  $a$ , is measured as  $2.60 \pm 0.20$  in  $\pi^0\pi^0$  events and  $2.82 \pm 0.12$  in  $\pi^0\pi^\pm$  events. The leading-log QCD calculation for  $\cos \theta^*$  distribution shows a consistent results for  $\pi^0\pi^0$ 's but not for  $\pi^0\pi^\pm$ 's. Based on the comparisons of the mass spectra and the  $\cos \theta^*$  distributions, we conclude that the LO QCD calculation via the Herwig event generator is not adequate to explain these measurements.

In studying the azimuthal and rapidity distributions of charged and neutral particles in di- $\pi$  events, we have shown strong correlations of these particles with high  $P_T$   $\pi$ 's, suggesting a jet-like structure in these events. Using the cone algorithm to define jets, the number of particles inside the cone decreases when the  $P_T$  of the leading particle of jets increases. Furthermore, our data also shows that the leading particles of jets tend to carry a large fraction of transverse momenta of jets, and this fraction increases when the  $P_T$  of the leading particles increases. From the dijet events, we compared the distributions of momentum fraction,  $x_a$  and  $x_b$ , carried by partons inside  $\pi^-$ 's and nucleon, respectively. The peak of  $x_a$  distribution is greater than that of  $x_b$  distribution, which is consistent with the quark model since the  $\pi$  has two valence quarks and the nucleon has three.

A nuclear enhancement has been observed in di- $\pi$  production. We parametrize the di- $\pi$  cross section as:

$$\sigma(A) = \sigma_0 A^\alpha$$

where  $A$  is the atomic number of the target nucleus.  $\alpha$  starts about 1.1 at 4 GeV/ $c^2$  mass and decrease to near 1 after 10 GeV/ $c^2$  mass. The reason for this decrease is uncertain. This  $\alpha$  is compared with the results measured from several other dihadron experiments. Our results agreed well with theirs within the statistical uncertainties.

The nuclear enhancement in  $\Delta\phi$  and  $K_{T\phi}$  can be explained by the parton rescattering model. The measured  $\sigma^2$ 's of the  $K_{T\phi}$  distributions in three different

materials are compared with the result of Fermilab E683. In the same range of atomic number, we see a larger nuclear effect than do they. In their results, the difference of  $\langle K_{T\phi}^2 \rangle$  increases when beam energy increases, which is consistent with our data. The nuclear enhancement in this variable,  $\langle K_{T\phi} \rangle$ , suggests that parton rescattering is the reason for the nuclear effect.

# Bibliography

- [1] E. Rutherford, *Philosophical Magazine* 21, 669 (1911)
- [2] S. H. Neddermeyer and C. D. Anderson, *Physical Review*, 51 (1937)
- [3] J. C. Street and E. C. Stevenson, *Physical Review*, 52 (1937)
- [4] M. Gell-Mann, *Phys. Lett.* 8 (1964), 214.
- [5] G. Zweig, CERN report 8182/Th. 401 (1964).
- [6] M. Breidenbach *et al.*, *Phys. Rev. Lett.* 23, 16 (1969)
- [7] F. Halzen & A. D. Martin, *Quarks & Leptons*
- [8] Raymond *et al.*, *Handbook of Perturbative QCD*, (1993)
- [9] J. F. Owens, *Rev. Mod. Phys.*, 59, 2 (1987)
- [10] J. F. Owens, *Phys. Rev. D* 20, 221 (1979)
- [11] R. Baier, J. Engles, and B. Petersson, *Z. Phys. C* 2, 265 (1979)
- [12] M. Krawczyk & W. Ochs, *Phys. Lett.* 79B, 119 (1978)
- [13] B. Bailey & J. F. Owens, *Phys. Rev. D* 46, 2018 (1992)
- [14] J. W. Cronin *et al.*, *Phys. Rev. D* 11, 3105 (1975)
- [15] L. Kluberg *et al.*, *Phys. Rev. Lett.* 38, 670 (1977)

- [16] M. Lev. and B. Petersson, Z. Phys. C 21, 155 (1983);  
K. Kastella, J. Milana and G. Sterman, Phys. Rev. D 39, 2586 (1989)
- [17] K. Hartman, *unpublished* Ph.D. Thesis, Pennsylvania State University, University Park, Pennsylvania (1990).
- [18] L. Apanasevich, private communication.
- [19] C. Bromberg *et al.*, NIM A307, 292 (1991).
- [20] W. Desoi, Ph.D. Thesis, University of Rochester, Rochester, New York (1988).
- [21] R. Roser, *unpublished* Ph.D. Thesis, University of Rochester, Rochester, New York (1994).
- [22] C. B. Lirakis, *unpublished* Ph.D. Thesis, Northeastern University, Boston, Massachusetts (1989).
- [23] R. Benson, *unpublished* Ph.D. Thesis, University of Minnesota, Minneapolis, Minnesota (1989).
- [24] N. Varelas, *unpublished* Ph.D. Thesis, University of Rochester, Rochester, New York (1994).
- [25] D. Skow, *unpublished* Ph.D. Thesis, University of Rochester, Rochester, New York (1990).
- [26] R. Jesik, *unpublished* Ph.D. Thesis, University of Illinois at Chicago, Chicago, Illinois (1993).
- [27] J. Bacigalupi, private communication.
- [28] W. Chung, *unpublished* Ph.D. Thesis, University of Pittsburgh, Pittsburgh, Pennsylvania (1994).

- [29] S. Blusk, *unpublished* Ph.D. Thesis, University of Pittsburgh, Pittsburgh, Pennsylvania (1994).
- [30] J. P. Mansour, *unpublished* Ph.D. Thesis, University of Rochester, Rochester, New York (1989).
- [31] W. Dlugosz, *unpublished* Ph.D. Thesis, Northeastern University, Boston, Massachusetts (1994).
- [32] A. P. Sinanidis, *unpublished* Ph.D. Thesis, Northeastern University, Boston, Massachusetts (1989).
- [33] V. Zutshi, private communication.
- [34] G. B. Osborne, E706 Internal Note 197 (1992)
- [35] A.L.S. Angelis *et al.*, Nucl. Phys. B209, 284 (1982)
- [36] H.B. White *et al.*, Phys. Rev. D 48, 3996 (1993)
- [37] D. D. S. Weerasundara, Ph. D. Thesis, University of Pittsburgh, Pittsburgh, Pennsylvania (1993).
- [38] D. Brown, Ph. D. Thesis, Michigan State University, East Lansing, Michigan (1993).
- [39] R.L. McCarthy *et al.*, Phys. Rev. Lett. 40, 213 (1978).
- [40] D. A. Finley *et al.*, Phys. Rev. Lett. 42, 1031 (1979).
- [41] Abramov *et al.*, Pis'ma Zh. Eksp. Teor. Fiz. 38, 296 (1983) [JETP Lett. 38, 352 (1983)].
- [42] Y. B. Hsiung *et al.*, Phys. Rev. Lett. 55, 457 (1985).
- [43] K. Streets *et al.*, Phys. Rev. Lett. 66, 864 (1991).

- [44] D. M. Alde *et al.*, Phys. Rev. Lett. 66, 2285 (1991); P. Bordalo *et al.*, Phys. Lett. B 193, 373 (1987).
- [45] M. Zielinski, Nuclear Effects in High  $P_T$  Production of Nuclear Mesons and Direct Photons, Proceeding of 5th Conference on the Intersections of Particle and Nuclear Physics, St. Petersburg, Florida (1994).
- [46] P.B. Straub *et al.*, Phys. Rev. Lett. 68, 452 (1992).
- [47] M. D. Corcoran *et al.*, Phys. Lett. B 259, 209 (1991).
- [48] D. Naples *et al.*, Phys. Rev. Lett. 72, 2341 (1994).
- [49] F. Lobkowicz and L. de Barbaro, E706 Internal Note 167, (1988).

# Appendix A

## Corrections in Linking

This appendix describes various corrections in the linking code to associate the downstream and upstream tracks. These corrections are important in obtaining correct track matching, and, consequently, make the measured momentum more reliable. In PLREC, the assumption that the upstream tracks (SSD) and the downstream tracks (PWC-STRAW) intersect at the center of the magnet is just a first order approximation. In general, the projection differences ( $\Delta X$  and  $\Delta Y$ ) of the downstream and upstream tracks at the center of the magnet are not zeros. The differences of  $Y$  slopes ( $\Delta YSL$ ) between the downstream and upstream tracks associated with the same particles are also not zero, due to the change of  $P_z$  ( $Z$  component of the momentum) after bending. Two effects need to be taken into account. The first one is the finite curvature of tracks inside the magnet and the second one is the leakage of the magnetic field. In this appendix, we try to determine the offsets of  $\Delta X$ ,  $\Delta Y$ , and  $\Delta YSL$  in a form suitable for our PLREC.

In Reference [46] we parametrize our magnetic field using the measured field strength in different positions inside the magnet and the Maxwell's equations. Moreover, we simulated our magnetic field as a constant field  $B$  in the  $Y$  view with an field length  $L$ . We use this effective field approximation to derive the offsets of  $\Delta X$ ,  $\Delta Y$ , and  $\Delta YSL$



## A.1 Effective Field

Suppose we have an uniform field in Y direction with an field length  $L$ , mathematically it can be expressed as:

$$B_y(z) = \begin{cases} B_0 & \text{if } 0 < z < L \\ 0 & \text{otherwise} \end{cases}$$

We also assume there is no field on X direction and no field Z direction at the median plane ( $Y=0$ ). From  $\nabla \times \vec{B} = 0$ , we get,

$$\frac{\partial B_y}{\partial z} = \frac{\partial B_z}{\partial y} \quad (\text{A.1})$$

$$\frac{\partial B_y}{\partial y} = -\frac{\partial B_z}{\partial z} \quad (\text{A.2})$$

where  $B_y$  and  $B_z$  are the Y and Z components of the magnetic field, respectively.

From Eqs. A.1 and A.2,  $B_z$  can be solved as:

$$\begin{aligned} B_z &= \int \frac{\partial B_y}{\partial z} dy \\ &= yB_0\delta(Z) - yB_0\delta(Z - L). \end{aligned}$$

$\delta(z)$  and  $\delta(Z - L)$  are  $\delta$  functions. In another words, we have an uniform field along the Y direction and a sharp and discontinuous field in the Z direction on both edges of the magnet.

From equation of motion, we can write

$$\frac{d\vec{P}}{dt} = e\vec{V} \times \vec{B}$$

$$\frac{dE}{dt} = 0$$

(E is the energy, P is the momentum). Hence, total energy and total momentum are conserved. When a charge particle moves inside the magnet, the magnetic field is only on Y direction.

$$\frac{dP_y}{dt} = 0 \quad (\text{A.3})$$

$$\frac{d\vec{P}_{zx}}{dt} = e\vec{V}_{zx} \times \vec{B}. \quad (\text{A.4})$$

From equations A.3 and A.4 we get that  $P_y$  and  $P_{zx}$  are constants and the trajectory in Z-X plane is a part of a circle with radius R, where

$$R = \frac{P_{zx}}{eB_0}. \quad (\text{A.5})$$

## A.2 Correction for $\Delta X$

Let's assume that a charged particle enters the magnet with an angle  $\alpha$  and leaves the magnet with an angle  $\beta$  in the Z-X plane. Because of the instantaneous  $B_z$  in the two edges of the magnet, the angle right after the particle entering the magnet is  $\alpha'$  and the angle right before the particle leaving the magnet is  $\beta'$ . The geometrical picture is in Fig. A.1. In the Z-Y plane, we define that the angle right before the particle entering the magnet is  $\eta_1$ , and the angle right after the particle leaving the magnet is  $\eta_2$  (see Fig. A.2). The angle  $\eta$  is defined as the angle between the moving direction of a particle and its projection on Z-X plane (see Fig. A.3).

Let's consider the momentum kick due to the  $B_z$  right on the edges of the magnet.

$$\frac{dP_x}{dt} = eV_y B_z. \quad (\text{A.6})$$

Therefore,

$$\begin{aligned} \Delta P_x |_{z=0} &= \int_{0^-}^{0^+} e y_1 B_0 \delta(z) V_y dt \\ &= e y_1 B_0 \tan(\eta_1) \end{aligned} \quad (\text{A.7})$$

$$\Delta P_x |_{z=L} = -e y_2 B_0 \tan(\eta_2) \quad (\text{A.8})$$

where  $y_1/y_2$  are the Y position where the particle enters/leaves the magnet.

Suppose the trajectory of the charge particle before entering the magnet and after leaving the magnet can be expressed by  $m_1 z + k_1$  and  $m_2 z + k_2$ , respectively. At the two edges inside the magnet, the motion can be expressed as  $m_1' z + k_1'$  and  $m_2' z + k_2'$ . From the continuity of the motion at the two edges, we get

$$m_1 \times 0 + k_1 = m_1' \times 0 + k_1'$$

$$m_2 L + k_2 = m_2' L + k_2'.$$

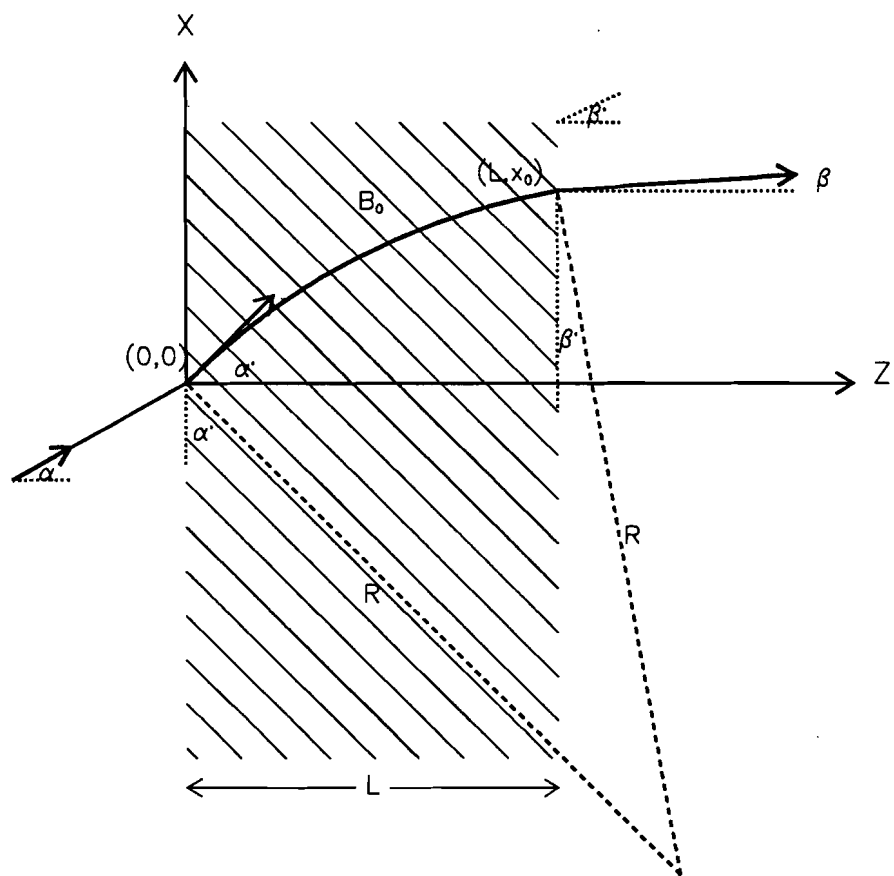


Figure A.1: The trajectory of charged particle inside the magnet in Z-X plane.

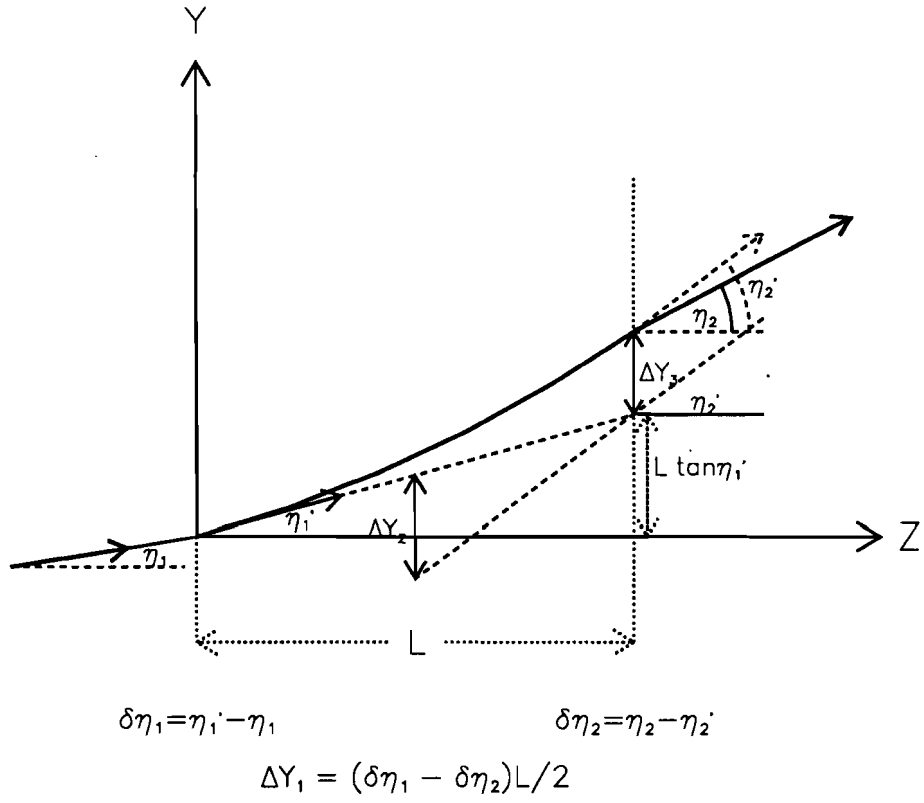


Figure A.2: The trajectory of charged particle inside the magnet in  $Z - Y$  plane

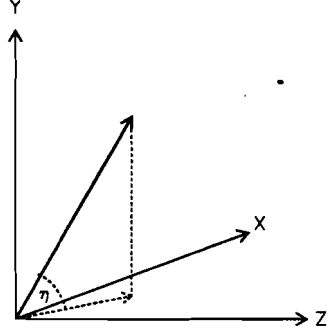


Figure A.3: The illustration of the angle  $\eta$ .

Hence,

$$k_1 = k_1' \quad (\text{A.9})$$

$$k_2 - k_2' = m_2' L - m_2 L. \quad (\text{A.10})$$

The  $\Delta X$  at the center of magnet ( $z=L/2$ ) is

$$\begin{aligned} \Delta x &= m_2 \frac{L}{2} + k_2 - m_1 \frac{L}{2} - k_1 \\ &= m_2 \frac{L}{2} + k_2 - m_2' \frac{L}{2} - k_2' + \\ &\quad m_1' \frac{L}{2} + k_1' - m_1 \frac{L}{2} - k_1 + \\ &\quad m_2' \frac{L}{2} + k_2' - m_1' \frac{L}{2} - k_1' \\ &= \Delta X_1 + \Delta X_2 \end{aligned} \quad (\text{A.11})$$

where

$$\Delta X_1 = ((m_2' - m_2) + (m_1' - m_1)) \frac{L}{2} \quad (\text{A.12})$$

$$\Delta X_2 = m_2' \frac{L}{2} + k_2' - m_1' \frac{L}{2} - k_1'. \quad (\text{A.13})$$

$\Delta X_1$  is attributed to the fringe field on both ends, and  $\Delta X_2$  is from the geometrical

effect.  $m_1$ ,  $m_2$ ,  $m_1'$ , and  $m_2'$  can be expressed as  $\tan\alpha$ ,  $\tan\beta$ ,  $\tan\alpha'$ , and  $\tan\beta'$ , respectively.

### A.2.1 Geometrical Correction

From Fig. A.1, two equations can be written as follows:

$$L = R \sin \alpha' - R \sin \beta' \quad (\text{A.14})$$

$$x_0 = R \cos \beta' - R \cos \alpha'. \quad (\text{A.15})$$

$\Delta X_2$  becomes

$$\Delta X_2 = x_0 - \frac{L}{2} \tan \alpha' - \frac{L}{2} \tan \beta'. \quad (\text{A.16})$$

However, we measure  $\alpha$  and  $\beta$  rather than  $\alpha'$  and  $\beta'$  in PLREC. Since the momentum impulse on the edges of the magnet are much smaller than the momenta of the particles of interest, we use the approximations,  $\alpha \approx \alpha'$  and  $\beta \approx \beta'$ , in Eqs. A.14 and A.15.  $\Delta x_2$  is expressed as:

$$\Delta X_2 = \frac{L(\cos \beta - \cos \alpha)}{(\sin \alpha - \sin \beta)} - \frac{L}{2}(\tan \alpha + \tan \beta). \quad (\text{A.17})$$

### A.2.2 Fringe Field Correction

In general,  $P_z$  is much larger than  $P_x$  for the charge particles which penetrate through our downstream tracking system. Besides, The change of  $P_z$  inside the magnet is rather small for these particles. Therefore, we use  $P_z \approx P_{zx}$  in Eq. A.12. Equation A.12 can be expressed as:

$$\begin{aligned} \Delta X_1 &= \frac{L}{2} \left( \frac{P_x}{P_z} \Big|_{z=L^-} - \frac{P_x}{P_z} \Big|_{z=L^+} + \frac{P_x}{P_z} \Big|_{z=0^+} - \frac{P_x}{P_z} \Big|_{z=0^-} \right) \\ &\approx \frac{L}{2P_{zx}} (-\Delta P_x \Big|_{z=L} + \Delta P_x \Big|_{z=0}) \\ &\equiv \frac{1}{2}(\sin \alpha - \sin \beta) \left( \frac{y_2 \tan \eta_2}{\cos \beta} + \frac{y_1 \tan \eta_1}{\cos \alpha} \right). \end{aligned} \quad (\text{A.18})$$

Since the linking routine is executed in the X view first, and the SSD tracking system can not give us 3-dim tracks, we are not able to find  $y_1$  and  $\eta_1$  in X-view linking.

Assuming that Y slope does not change much, we have  $\eta_1 \approx \eta_2$  and  $y_1 \approx y_2 - L \tan \eta_2$ .

Equation A.18 becomes

$$\Delta X_1 = \frac{1}{2}(\sin \alpha - \sin \beta) \left( \frac{y_2 \tan \eta_2}{\cos \beta} + \frac{y_2 \tan \eta_2}{\cos \alpha} - \frac{L \tan^2 \eta_2}{\cos \alpha} \right). \quad (\text{A.19})$$

### A.3 Correction for $\Delta YSL$

The y-slope difference can be also divided into two parts: one is due to the fringe field on the edges, and the other one is for the  $P_z$  change.

$$\begin{aligned} \Delta YSL &= \frac{P_y}{P_z} \Big|_{z=L^+} - \frac{P_y}{P_z} \Big|_{z=0^-} \\ &= \frac{P_y}{P_z} \Big|_{z=L^+} - \frac{P_y}{P_z} \Big|_{z=L^-} \\ &\quad + \frac{P_y}{P_z} \Big|_{z=0^+} - \frac{P_y}{P_z} \Big|_{z=0^-} \\ &\quad + \frac{P_y}{P_z} \Big|_{z=L^-} - \frac{P_y}{P_z} \Big|_{z=0^+}. \end{aligned} \quad (\text{A.20})$$

The first two lines in eq. A.20 are due to fringe field effect and the third line is because of the change of  $P_z$  inside the magnet. From  $\frac{dP_z}{dt} = -qV_x B_z$ , we get

$$\Delta P_y \Big|_{z=0} = -ey_1 B_0 \tan \alpha \quad (\text{A.21})$$

$$\Delta P_y \Big|_{z=L} = ey_2 B_0 \tan \beta. \quad (\text{A.22})$$

Using Eqs. A.21, A.22, and A.5, Equation A.20 becomes

$$\begin{aligned} \Delta YSL &= \frac{\sin \alpha - \sin \beta}{L} \left( \frac{y_2 \tan \beta}{\cos \beta} - \frac{y_1 \tan \alpha}{\cos \alpha} \right) \\ &\quad + \tan \eta (\sec \beta - \sec \alpha). \end{aligned} \quad (\text{A.23})$$

### A.4 Correction for $\Delta Y$

The  $\Delta Y$  in the center of the magnet can also be divided into fringe field part and geometrical part. The fringe field part is easy to get.

$$\Delta Y_1 = \frac{L}{2}(\delta \eta_1 - \delta \eta_2)$$

$$\begin{aligned}
&= -\frac{L}{2R} \left( \frac{y_1 \tan \alpha}{\cos \alpha} + \frac{y_2 \tan \beta}{\cos \beta} \right) \\
&= -\frac{1}{2} (\sin \alpha - \sin \beta) \left( \frac{y_1 \tan \alpha}{\cos \alpha} + \frac{y_2 \tan \beta}{\cos \beta} \right). \tag{A.24}
\end{aligned}$$

where we used Eqs. A.21, A.22, and A.5 in expressing  $\delta\eta_1$  and  $\delta\eta_2$ .

The geometrical part is a little bit complicated. In Fig. A.2, we divide the geometrical part into two terms:  $\Delta Y_2$  is due to slope difference at the two edges, and  $\Delta Y_3$  is for the spiral motion of the particle inside the magnet. In the following calculation, we use the approximations,  $\alpha \approx \alpha'$  and  $\beta \approx \beta'$ . Therefore,  $\tan \eta_1'$  and  $\tan \eta_2'$  can be expressed as  $\frac{\tan \eta}{\cos \alpha}$  and  $\frac{\tan \eta}{\cos \beta}$ . According to the geometry in Fig. A.2,  $\Delta Y_2$  can be written as:

$$\begin{aligned}
\Delta Y_2 &= \frac{L}{2} \tan \eta_2' - \frac{L}{2} \tan \eta_1' \\
\Delta Y_2 &= \frac{L}{2} \tan \eta (\sec \alpha - \sec \beta). \tag{A.25}
\end{aligned}$$

$\Delta Y_3$  can also be written as:

$$\Delta Y_3 = \int dy - \frac{L \tan \eta}{\cos \alpha}. \tag{A.26}$$

We can express  $dy$  in terms of  $\tan \eta$ .

$$\begin{aligned}
\tan \eta &= \frac{P_y}{P_{zx}} = \frac{P_y}{P_z} \cos \theta \\
&= \frac{dy}{dz} \cos \theta.
\end{aligned}$$

Therefore,

$$\begin{aligned}
\Delta Y_3 &= \int \frac{\tan \eta}{\cos \theta} dz - \frac{L \tan \eta}{\cos \alpha} \\
&= -\int_{\alpha}^{\beta} R \tan \eta d\theta - \frac{L \tan \eta}{\cos \alpha} \\
&= L \tan \eta \frac{\beta - \alpha}{\sin \beta - \sin \alpha} - \frac{L \tan \eta}{\cos \alpha}. \tag{A.27}
\end{aligned}$$

where we use the expressions,  $P_z = P_{zx} \cos \theta$  and  $z = -R \sin \theta$ . Since  $\eta$  is not measured in the Y-view linking, we use  $\eta_1$  as an approximation of  $\eta$ . The sum of  $\Delta Y_1$ ,  $\Delta Y_2$ , and  $\Delta Y_3$  give the offset of  $\Delta Y$ .



# Appendix B

## Cross Sections and A Dependence

This appendix presents the tables for the invariant cross sections of  $\pi^0\pi^0$ ,  $\pi^0\pi^-$ , and  $\pi^0\pi^+$  in 515 GeV/c  $\pi^-$ -Be and  $\pi^-$ -Cu interactions. It also contains the tables for the  $\alpha$  and RMS of  $K_{T\phi}$  in di- $\pi$  productions.

Mass $\text{GeV}/c^2$	Be Target	Cu Target
3.9 - 4.3	$21.06 \pm 0.92$	$24.20 \pm 3.30$
4.3 - 4.7	$37.65 \pm 1.10$	$47.07 \pm 3.30$
4.5 - 5.1	$35.62 \pm 0.95$	$41.82 \pm 3.64$
5.1 - 5.5	$23.84 \pm 0.72$	$25.18 \pm 2.71$
5.5 - 5.9	$15.04 \pm 0.52$	$19.74 \pm 1.59$
5.9 - 6.3	$9.44 \pm 0.42$	$9.38 \pm 1.22$
6.3 - 6.7	$5.54 \pm 0.31$	$7.93 \pm 1.00$
6.7 - 7.1	$3.10 \pm 0.22$	$3.95 \pm 0.67$
7.1 - 7.5	$2.04 \pm 0.13$	$1.99 \pm 0.34$
7.5 - 7.9	$1.22 \pm 0.11$	$1.18 \pm 0.23$
7.9 - 8.3	$0.49 \pm 0.07$	$0.80 \pm 0.16$
8.3 - 8.7	$0.52 \pm 0.12$	$0.43 \pm 0.10$
8.7 - 9.1	$0.263 \pm 0.039$	$0.189 \pm 0.086$
9.1 - 9.5	$0.176 \pm 0.0262$	$0.082 \pm 0.050$
9.5 - 9.9	$0.137 \pm 0.0199$	$0.069 \pm 0.051$
9.9 - 10.3	$0.112 \pm 0.0240$	$0.093 \pm 0.038$
10.3 - 10.7	$0.0453 \pm 0.0111$	$0.0670 \pm 0.034$
10.7 - 11.1	$0.0301 \pm 0.0108$	$0.0747 \pm 0.034$
11.1 - 11.5	$0.0302 \pm 0.0075$	
11.5 - 11.9	$0.0137 \pm 0.0084$	
11.9 - 12.3	$0.0084 \pm 0.0061$	
12.3 - 13.1	$0.0047 \pm 0.0021$	
13.1 - 13.9	$0.0042 \pm 0.0019$	
13.9 - 15.1	$0.0015 \pm 0.00087$	
15.1 - 16.3	$0.00068 \pm 0.00068$	

Table B.1: Invariant differential cross section per nucleon in units  $\text{nb}/(\text{GeV}/c^2)$  for  $\pi^0\pi^0$  production in 515  $\text{GeV}/c$   $\pi^-$ -Be and  $\pi^-$ -Cu interactions. The cross sections are integrated from -0.3 to 0.7 in  $Y_{cm}$  and from 0 to 0.5 in  $\cos\theta^*$ .

Mass $\text{GeV}/c^2$	Be Target	Cu Target
3.9 - 4.3	$0.199 \pm 0.016$	$0.192 \pm 0.087$
4.3 - 4.7	$0.646 \pm 0.030$	$0.972 \pm 0.110$
4.7 - 5.1	$2.498 \pm 0.063$	$3.085 \pm 0.169$
5.1 - 5.5	$6.180 \pm 0.095$	$7.001 \pm 0.264$
5.5 - 5.9	$7.421 \pm 0.105$	$8.694 \pm 0.315$
5.9 - 6.3	$6.581 \pm 0.097$	$7.032 \pm 0.301$
6.3 - 6.7	$5.064 \pm 0.089$	$5.243 \pm 0.235$
6.7 - 7.1	$3.663 \pm 0.076$	$3.534 \pm 0.198$
7.1 - 7.5	$2.590 \pm 0.065$	$2.543 \pm 0.151$
7.5 - 7.9	$1.875 \pm 0.053$	$1.941 \pm 0.157$
7.9 - 8.3	$1.330 \pm 0.048$	$1.485 \pm 0.133$
8.3 - 8.7	$0.965 \pm 0.041$	$1.024 \pm 0.095$
8.7 - 9.1	$0.679 \pm 0.030$	$0.616 \pm 0.077$
9.1 - 9.5	$0.488 \pm 0.027$	$0.412 \pm 0.065$
9.5 - 9.9	$0.295 \pm 0.021$	$0.434 \pm 0.068$
9.9 - 10.3	$0.305 \pm 0.023$	$0.280 \pm 0.049$
10.3 - 10.7	$0.209 \pm 0.016$	$0.160 \pm 0.034$
10.7 - 11.1	$0.136 \pm 0.013$	$0.115 \pm 0.029$
11.1 - 11.5	$0.099 \pm 0.010$	$0.222 \pm 0.066$
11.5 - 11.9	$0.0692 \pm 0.0091$	$0.0687 \pm 0.0321$
11.9 - 12.3	$0.0573 \pm 0.0088$	$0.0763 \pm 0.0230$
12.3 - 13.1	$0.0303 \pm 0.0046$	$0.0302 \pm 0.0101$
13.1 - 13.9	$0.0234 \pm 0.0039$	$0.0145 \pm 0.0073$
13.9 - 15.1	$0.0081 \pm 0.0019$	$0.0044 \pm 0.0031$
15.1 - 16.3	$0.00028 \pm 0.00028$	$0.0027 \pm 0.0019$
16.3 - 17.5	$0.00029 \pm 0.00021$	
17.5 - 20.0	$0.000094 \pm 0.000068$	

Table B.2: Invariant differential cross section per nucleon in units  $\text{nb}/(\text{GeV}/c^2)$  for  $\pi^0\pi^-$  production in 515  $\text{GeV}/c$   $\pi^-$ -Be and  $\pi^-$ -Cu interactions. The cross sections are integrated from -0.4 to 0.8 in  $Y_{cm}$  and from 0 to 0.5 in  $\cos\theta^*$ .

Mass $\text{GeV}/c^2$	Be Target	Cu Target
3.9 - 4.3	$0.208 \pm 0.018$	$0.369 \pm 0.056$
4.3 - 4.7	$0.686 \pm 0.032$	$1.112 \pm 0.100$
4.7 - 5.1	$2.379 \pm 0.063$	$3.558 \pm 0.210$
5.1 - 5.5	$6.118 \pm 0.097$	$6.874 \pm 0.272$
5.5 - 5.9	$7.176 \pm 0.112$	$8.467 \pm 0.303$
5.9 - 6.3	$6.138 \pm 0.094$	$6.762 \pm 0.245$
6.3 - 6.7	$4.716 \pm 0.090$	$5.422 \pm 0.268$
6.7 - 7.1	$3.263 \pm 0.067$	$3.581 \pm 0.202$
7.1 - 7.5	$2.235 \pm 0.059$	$2.410 \pm 0.168$
7.5 - 7.9	$1.637 \pm 0.051$	$1.782 \pm 0.152$
7.9 - 8.3	$1.158 \pm 0.043$	$1.190 \pm 0.108$
8.3 - 8.7	$0.856 \pm 0.033$	$0.854 \pm 0.087$
8.7 - 9.1	$0.547 \pm 0.036$	$0.503 \pm 0.063$
9.1 - 9.5	$0.414 \pm 0.025$	$0.312 \pm 0.060$
9.5 - 9.9	$0.289 \pm 0.022$	$0.304 \pm 0.057$
9.9 - 10.3	$0.220 \pm 0.018$	$0.159 \pm 0.084$
10.3 - 10.7	$0.158 \pm 0.018$	$0.194 \pm 0.042$
10.7 - 11.1	$0.100 \pm 0.012$	$0.126 \pm 0.030$
11.1 - 11.5	$0.0737 \pm 0.0101$	$0.0639 \pm 0.0214$
11.5 - 11.9	$0.0640 \pm 0.0089$	$0.0431 \pm 0.0176$
11.9 - 12.3	$0.0534 \pm 0.0078$	$0.0185 \pm 0.0257$
12.3 - 13.1	$0.0289 \pm 0.0044$	$0.0219 \pm 0.0090$
13.1 - 13.9	$0.0201 \pm 0.0034$	$0.0291 \pm 0.0103$
13.9 - 15.1	$0.0083 \pm 0.0017$	$0.0139 \pm 0.0058$
15.1 - 16.3	$0.0028 \pm 0.0008$	$0.0039 \pm 0.0023$
16.3 - 17.5	$0.00014 \pm 0.00014$	
17.5 - 20.0	$0.000039 \pm 0.000039$	

Table B.3: Invariant differential cross section per nucleon in units  $\text{nb}/(\text{GeV}/c^2)$  for  $\pi^0\pi^+$  production in 515  $\text{GeV}/c$   $\pi^-$ -Be and  $\pi^-$ -Cu interactions. The cross sections are integrated from -0.4 to 0.8 in  $Y_{cm}$  and from 0 to 0.5 in  $\cos\theta^*$ .

Mass (GeV/ $c^2$ )	$\alpha$
4.7 - 5.5	$1.095 \pm 0.0124$
5.5 - 5.9	$1.082 \pm 0.0141$
5.9 - 6.3	$1.041 \pm 0.0154$
6.3 - 6.7	$1.044 \pm 0.0182$
6.7 - 7.1	$1.015 \pm 0.0216$
7.1 - 7.9	$1.020 \pm 0.0198$
7.9 - 8.7	$1.028 \pm 0.0259$
8.7 - 9.9	$0.974 \pm 0.0341$
9.9 - 11.5	$1.007 \pm 0.0563$
11.5 - 13.1	$0.931 \pm 0.0978$
13.1 - 15.1	$1.021 \pm 0.1249$

Table B.4:  $\alpha$  values in different  $\pi^0\pi^\pm$  masses. Only statistical uncertainty is included.

Mass (GeV/ $c^2$ )	$\alpha$
3.9 - 4.7	$1.099 \pm 0.036$
4.7 - 5.5	$1.061 \pm 0.036$
5.5 - 6.3	$1.089 \pm 0.038$
6.3 - 7.5	$1.134 \pm 0.050$
7.5 - 9.0	$1.026 \pm 0.072$
9.0 - 11.1	$0.851 \pm 0.125$

Table B.5:  $\alpha$  values in different  $\pi^0\pi^0$  masses. Only statistical uncertainty is included.

Target	Atomic Number	RMS of $K_{T\phi}$ for $\pi^0\pi^0$ jets	RMS of $K_{T\phi}$ for $\pi^0\pi^\pm$ jets
Be	9.01	$3.258 \pm 0.028$	$3.865 \pm 0.029$
Si	28.09	$3.755 \pm 0.108$	$4.765 \pm 0.136$
Cu	63.55	$4.166 \pm 0.089$	$5.208 \pm 0.100$

Table B.6: RMS of  $K_{T\phi}$  for di- $\pi$  jets in the interactions of different targets.